Controlling Extended Structures in Spread Polyelectrolyte/Surfactant Films at the Air/Water Interface

A thesis submitted to The University of Manchester for
the degree of Doctor of Philosophy in the Faculty of
Biology, Medicine and Health

2023

Javier Carrascosa Tejedor

SCHOOL OF HEALTH SCIENCE

DIVISION OF PHARMACY AND OPTOMETRY

List of contents

Total word count: 54090

List of acronyms

Acronym	Explanation	Appearance in the text
ACMW	air contrast matched water	77
AT	Andrea Tummino	58
BAM	Brewster angle microscopy	41
cac	critical aggregate concentration	32
CCD	charge coupled device	73
cmc	critical micelle concentration	24
cpp	critical packing parameter	25
CTAB	hexadecyltrimethylammonium bromide	22
d-DTAB	dodecyl-d25-trimethylammonium bromide	65
d-SDS	sodium dodecyl-d25 sulfate	65
DTAB	dodecyltrimethylammonium bromide	18
ESs	extended structures	18
FIGARO	Fluid Interfaces Grazing Angles ReflectOmeter	58
IV	Imre Varga	58
JCT	Javier Carrascosa-Tejedor	58
LB	Langmuir-Blodgett	92
LbL	layer-by-layer	92
LMM	Laura M. Miñarro	58
LS	Langmuir-Schaeffer	92
ME	Marina Efstratiou	58
NaPSS	poly(sodium styrene-sulfonate)	18
NR	Neutron reflectometry	36
Pdadmac	poly(diallyldimethylammonium chloride)	26
PEI	poly(ethylenimine)	26
PLA	poly(L-arginine)	30
PLL	Poly(L-lysine)	30

PP/S	polypeptide/surfactant	18
P/S	polyelectrolyte/surfactant	18
RAC	Richard A. Campbell	58
SDS	sodium dodecyl sulfate	18
SLD	Scattering length density	76
TOF	time-of-flight	79
TTAB	tetradecyltrimethylammonium bromide	22

List of figures

List of tables

Abstract

In this project, a recently developed methodology for the formation of spread oppositely charged polyelectrolyte/surfactant (P/S) films at the air/water interface has been extended. This methodology involves the dispensing of P/S aggregates onto a bare air/water interface, which results in their dissociation due to Marangoni spreading and the formation of a kinetically-trapped film as a result of counterion release into the bulk. Initial research had shown that successive spreading or surface area compression of poly(sodium styrene-sulfonate) (NaPSS)/ dodecyltrimethylammonium bromide (DTAB) films can form extended structures (ESs).

The aim of this PhD project is to gain precise control of the structures self-assembled in P/S films at the air/water interface prepared by the aggregates spreading methodology under static and dynamic conditions with the ambition of tuning the film properties in three dimensions and with a focus on biocompatible systems. For this purpose, various optical and neutron reflectometry techniques have been used to determine the dynamic behaviour, structure and morphology of films created by four different systems: poly(L-lysine)/sodium dodecyl sulfate (SDS), poly(L-arginine)/SDS, poly(ethyleneimine)/SDS and NaPSS/DTAB.

Self-assembled structures of spread P/S films have been resolved in three dimensions for the first time. Various approaches for tuning the properties, morphologies and structures of the films have been explored and validated with respect to different physicochemical variables. It has been shown that ESs form spontaneously in some systems regardless of the aggregate charge used in the spreading processes; others require the use of overcharged aggregates. Also, changes in the polyelectrolyte charge density results in films with different morphologies. Furthermore, the stability of the material self-assembled in ESs varies according to the system studied, with the most stable and tunable reservoirs originating in spread polypeptide/surfactant (PP/S) films, where interactions related to secondary structures may be preserved in the ESs.

The results suggest a need for more experiments on different systems under different conditions to understand better the physicochemical properties of these films, and in turn help develop biomedical or film transfer applications with potential economic and environmental advantages.

Declaration

The author hereby declares no portion of the work referred to in the thesis has been submitted in support of an application for another degree or qualification of this or any other university or other institute of learning.

Copyright statement

i. The author of this thesis (including any appendices and/or schedules to this thesis) owns certain copyright or related rights in it (the “Copyright”) and they have given the University of Manchester certain rights to use such Copyright, including for administrative purposes.

ii. Copies of this thesis, either in full or in extracts and whether in hard or electronic copy, may be made only in accordance with the Copyright, Designs and Patents Act 1988 (as amended) and regulations issued under it or, where appropriate, in accordance with licensing agreements which the University has from time to time. This page must form part of any such copies made.

iii. The ownership of certain Copyright, patents, designs, trademarks and other intellectual property (the “Intellectual Property”) and any reproductions of copyright works in the thesis, for example graphs and tables (“Reproductions”), which may be described in this thesis, may not be owned by the author and may be owned by third parties. Such Intellectual Property and Reproductions cannot and must not be made available for use without the prior written permission of the owner(s) of the relevant Intellectual Property and/or Reproductions.

iv. Further information on the conditions under which disclosure, publication and commercialisation of this thesis, the Copyright and any Intellectual Property and/or Reproductions described in it may take place is available in the University IP Policy (see http://documents.manchester.ac.uk/DocuInfo.aspx?DocID=2442 0), in any relevant Thesis restriction declarations deposited in the University Library, the University Library’s regulations (see http://www.library.manchester.ac.uk/about/regulations/) and in the University’s policy on Presentation of Theses.

Acknowledgements

These three and a half years of PhD have been one of the most beautiful stages of my life, in which I have learned a lot on a professional level, but much more on a personal level. And all of this has been thanks to all the people who have supported me during this time. I would like to start by thanking my supervisors Richard, Armando, Jayne and Philipp for giving me the opportunity to do this PhD, for teaching me many things during these years and for always supporting me by being patient. But I have to give special thanks to Richard, without your help I am sure it would not have been possible for me to carry out this project. You have been a great supervisor, attentive, understanding, positive, organised... and always ready to help.

I would like to thank the Institut Laue-Langevin and the University of Manchester for the funding. I would also like to thank all the people from these two institutions with whom I have worked over the years. Thanks to Glenn and Marina for their warm welcome in Manchester and their help during beamtimes and various experiments. On the ILL side, thanks to Larissa, Giacomo, Andrea, Daniel, Laura, Samantha, Martina, Sandrine, Simon, Benoit, Leo and those I have unfortunately forgotten to include. In some way you all helped me during this project to bring it forward. But I need to thank especially Andreas, who always listened to me and helped me with both thesis-related and personal problems. It has been a pleasure to work with you over these years. I will never forget the latin music that could be heard all over the hall... Thanks to Imre for his support and the interesting discussions about the various manuscripts during the last stages.

And of course, I couldn't be more grateful to have such a wonderful family. Many thanks to my parents, who despite the fear I had, encouraged me to start this PhD and have supported me unconditionally during all these years. Many thanks also to my parents in-law for their help, encouragement and support over these years, but especially during the last months.

And the most special thanks of this thesis go to my wife, Sara. Thank you for being patient, loving, empathetic, for encouraging me always, especially in the most difficult moments, and, in short, for loving me as I am. And I cannot forget my two children, the two greatest gifts I have received over these years and who have helped me so many times to get out stress and work.

And lastly, but most importantly, I thank God for having accompanied me during these wonderful years in the good times and in the suffering, helping me to accept it without giving up everything.

1 Introduction

1.1 Surfactants

Surfactants are amphiphilic molecules composed of a hydrophilic or polar moiety soluble in water known as the head (or headgroup) and a hydrophobic or nonpolar moiety insoluble in water known as the tail. They are generally classified depending on the nature of the headgroups which can be non-ionic (aliphatic alcohol ethoxylates), cationic (dodecyltrimethylammonium bromide), anionic (sodium dodecyl sulfate) or zwitterionic (dipalmitoylphosphatidylcholine). The tail is often composed of one or more hydrocarbon chains, but fluorocarbon chains are also used. Surfactants find application in a wide range of industries such as cosmetics, detergents, food, pharmaceuticals, paints or oil recovery. Several textbooks include detailed descriptions of their characteristics, properties, uses and importance in colloid and surface science.[1–3] The chemical structure of the most common surfactants studied in this field is depicted in Figure 1.1.

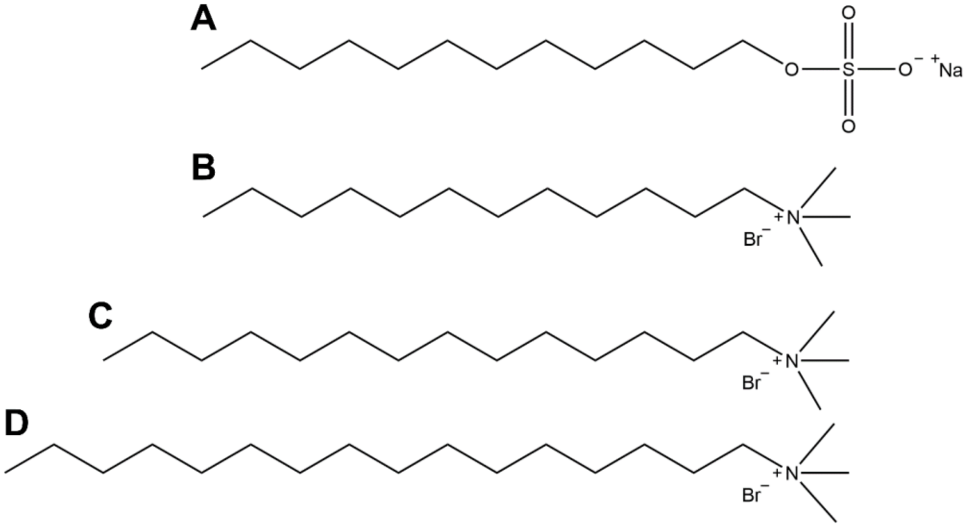

Figure 1.1. Chemical structures of (A) SDS, (B) DTAB, (C) tetradecyltrimethylammonium bromide (TTAB) and (D) hexadecyltrimethylammonium bromide (CTAB).

The spontaneous adsorption at a hydrophobic/hydrophilic interface reducing the interfacial tension is one of the main characteristics of these molecules. The term surface tension (γ) is generally used in the studies of phenomena at the air/water interface, so this terminology is adopted for the air/water interface hereinafter. Water molecules in solution are stabilised by attractive intermolecular interactions such as hydrogen bonding and polar interactions between neighbours. At the interface, though, the absence of neighbouring water molecules above the outmost layer results in the formation of stronger bonds (due to cohesion) and a higher energy state with respect to molecules in the bulk. Thus, surface tension is a thermodynamic property defined as the variation of free energy (*G*) per unit area (*A*) of a system at a constant temperature (*T*) and composition (n_i):

$$\gamma = \left(\frac{\partial G}{\delta A}\right)_{T,n_i} \tag{1.1}$$

Additionally, changes in the surface tension $d\gamma$ can be linked to the surface excess of the *ith* component (Γ_i) and its chemical potential (μ_i) by the well-known Gibbs equation:[4]

$$d\gamma = -\sum_i \Gamma_i d\mu_i \tag{1.2}$$

Γ_i is defined as the excess of surfactant molecules at the interface per unit area over the same volume in the bulk, and as the latter is negligible it can be approximated to zero, and then it is the amount of surfactant molecules per unit area. Γ_i can be expressed in terms of molarity or mass, i.e., $\mu mol/m^2$ or mg/m^2, with the latter being particularly useful when comparing species with different molecular masses such as proteins and surfactants. In the case of polymers, a way to define their concentration is in terms of monomer units, which detaches the definition from the molecular weight of the polymer. This is particularly useful for polyelectrolytes where it can be helpful to compare the stoichiometry of binding in terms of charges on monomers of the polyelectrolyte with opposite charges on surfactant molecules irrespective of the polyelectrolyte molecular weight. Γ is positive for surface active molecules in aqueous systems, and negative for aqueous solutions of electrolytes, which means they do not adsorb at interfaces. This is a critical point in this project because it will allow one to understand the significance of the synergy between polyelectrolytes and surfactants in conferring unique properties to their mixtures.

Surfactant molecules in aqueous solutions are in dynamic equilibrium between the bulk, the interface and any self-assembled structure. Figure 1.2 depicts a typical variation in surface

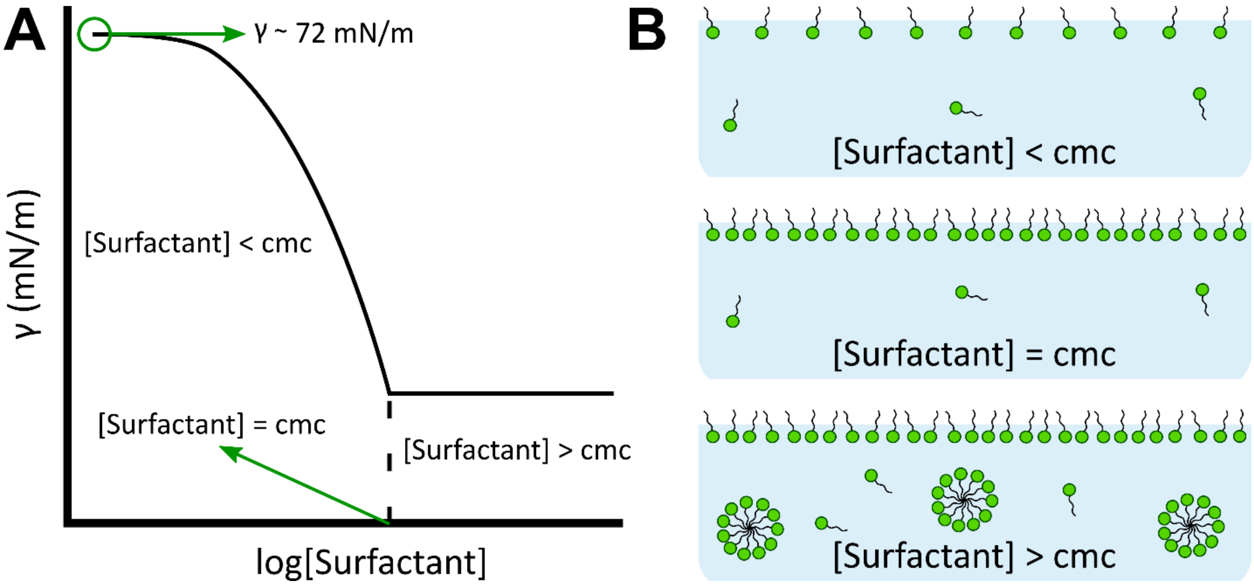

Figure 1.2. (A) Idealised variation of the equilibrium surface tension of water/surfactant systems with the logarithm of the total surfactant concentration. (B) Illustration of the aggregation state of surfactant molecules at three different concentration ranges.

tension as a function of the logarithm of surfactant concentration, as well as an illustration of three distinct concentration ranges. In the range of low concentrations, the adsorption of individual surfactant molecules (monomers) at the interface with the hydrophobic tail pointing towards the air and the hydrophilic head immersed in water leads to a decrease in the surface tension until the interface is saturated. The surface tension remains approximately constant after this point, known as the critical micelle concentration (cmc), and monomers start to form self-assembled supramolecular aggregates, typically spherical micelles. The hydrophobic tails accumulate in the interior of these aggregates to minimise their contact with water, whereas the hydrophilic heads orient themselves on the outer region to maximise their contact with water (and any counterions present in the solution). This is what Tanford described for the first time as the hydrophobic effect.[5] This effect, in turn, is related to the entropic contribution explained below, which also applies to monomer adsorption at the interface when the surfactant concentration is lower than its cmc. The introduction of surfactant molecules into an aqueous solution results in the disruption of the hydrogen bond network and a reorganisation of water molecules around the tails that maximises the number of hydrogen bonds. This causes the water structure to become more ordered, which is an entropically unfavourable process. As a result, the adsorption of surfactant molecules at the interface when [Surfactant] < cmc and their self-assembly into supramolecular aggregates when [Surfactant] > cmc is entropically more favourable because the hydrogen bond network is less disturbed and the hydrophobic tails can interact with each other.

Each surfactant molecule has a characteristic cmc value that depends on the length of the tail, the nature of the headgroup, temperature and ionic strength. The form and shape of the micelles depend on the concentration and the molecular architecture of the surfactant. The latter can be approximated by the area occupied by its hydrophilic headgroup, a_0, the volume of its hydrocarbon chain, v, and the maximum effective length of the chains or critical chain length, l_c. Indeed, Israelachvili et al. introduced the critical packing parameter (cpp) defined as

$$cpp = v/a_0 l_c \tag{1.3}$$

which can be used to predict the shape of the micelles formed by a given surfactant.[6,7] Figure 1.3A shows the typical preferred supramolecular aggregates formed by surfactants depending on the cpp. Finally, as the surfactant concentration increases significantly above the cmc, the form and shape of micelles change, and the formation of liquid crystalline phases such as cubic, hexagonal or lamellar phases (Figure 1.3B) may be favoured at very high surfactant concentrations.

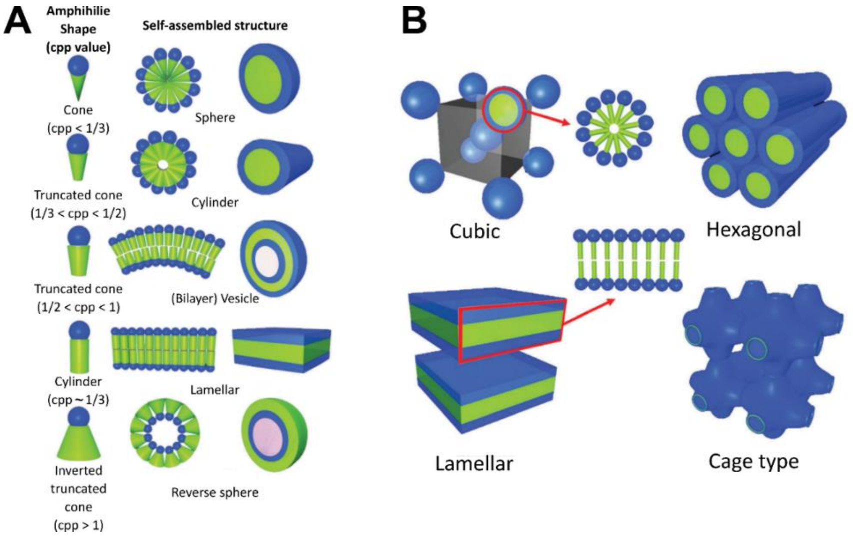

Figure 1.3. (A) Molecular architecture and preferred self-assembled structure of surfactants with different cpp. (B) Examples of liquid crystalline phases found in surfactant solutions. Figures adapted from Ramanathan et al, 2013.[8]

1.2 Polyelectrolytes

Polyelectrolytes are macromolecules composed of one or more chemical units (monomers) that are repeated throughout a chain and either present ionisable groups that may dissociate in polar solvents like water, or ions from the solution can bind to them. Polyelectrolytes have been investigated extensively owing to their numerous applications in everyday products,[9] industry,[10–12] and biomedicine.[13–15] Furthermore, because many biologically relevant molecules such as proteins or nucleic acids are polyelectrolytes, a greater knowledge of their behaviour might lead to novel applications of these macromolecules, particularly in biocompatible systems. The advances in synthetic methods allow nowadays precise control of the polydispersity and architecture of these molecules, which range from the most basic, linear polyelectrolytes, to more sophisticated ones such as cross-linked, branched or dendritic polyelectrolytes. In addition, the introduction of groups with specific properties such as photoresponsive,[16] thermoresponsive[17] or hydrophobic units[18] can be used to control their functionality. Polyelectrolytes can be classified according to various properties.[15,19,20] Based on their origin they can be natural (e.g. nucleic acids, proteins or polysaccharides), synthetic (e.g. poly(acrylic acid) or poly(styrene)) or chemically modified (N-trimethyl chitosan or pectin). They can be composed of repeating units of single (homo-polyelectrolytes) or various (co-polyelectrolytes) monomers. They can be polyanions, polycations or polyampholytes depending on the charge of the ionisable groups. Lastly, depending on the degree of dissociation they can be strong when they dissociate completely in solution, and weak when they dissociate partially. The chemical structure of the most common polyelectrolytes studied in this field is depicted in Figure 1.4.

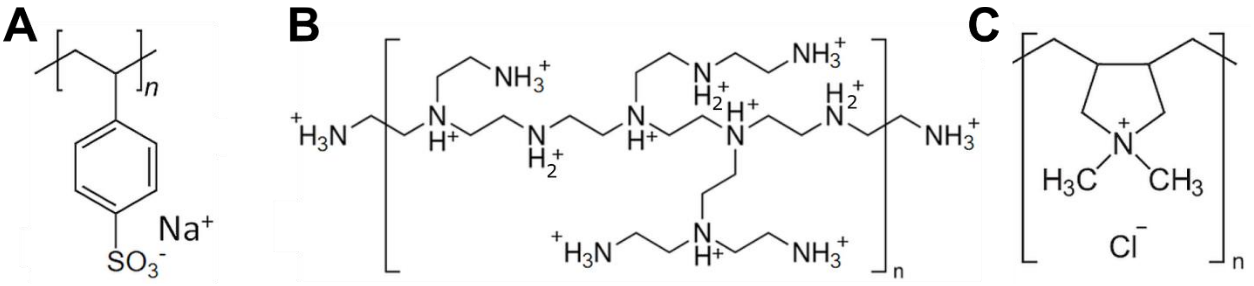

Figure 1.4. Chemical structures of (A) NaPSS, (B) hyperbranched (PEI) and (C) poly(diallyldimethylammonium chloride) (Pdadmac). The protonation degree of PEI varies depending on the pH of the medium.

Generally, polyelectrolytes exhibit excellent water-solubility and strong electrostatic interactions with oppositely charged ions, molecules or surfaces.[19,21,22] Their dissociation in water leaves charges on the polyelectrolyte chains and releases counterions to the solution the fraction of these charges is balanced between the strong electrostatic interactions and the reduction of translational entropy caused by the localisation of the counterions. This phenomenon can lead to counterion condensation and was described by Manning.[23–26] The presence of charges in the polyelectrolyte chains generally leads to swelling of the polyelectrolyte coil in dilute solutions. Although to a lesser extent than in uncharged polymers, the stiffness of the polyelectrolyte can have a significant impact on the molecule's conformation[27] and its ability to bind to other molecules or surfaces.[28–31] This property is usually quantified as the persistence length (l_P), which is an important parameter in polymer science as it determines the rigidity of a polymer chain. It is defined as the extent to which the direction of a polymer (or polyelectrolyte) is correlated or, in other words, the extent to which the polymer chain can be considered as a random coil. It varies from a few nanometres for flexible polyelectrolytes such as NaPSS,[27] to tens or hundreds of nanometers for rigid polyelectrolytes such as DNA[32] or xanthan.[33]

Several factors can influence the structure of polyelectrolytes in the bulk solution. Dobrynin et al.[34] explained how properties of polyelectrolyte solutions rely not only on the molecule's characteristics (e.g., molecular weight, chain length and charge density) and concentration but also on the ionic strength and pH of the solution.[34–37] Polyelectrolytes with high charge density present generally an extended conformation due to the electrostatic repulsion between charged monomers, whereas those with low charge density present a more compact structure due to a decrease of the repulsive interactions and, in some cases, the emergence of hydrophobic interactions. In terms of the ionic strength of the medium, the greater the ionic force, the greater the charge screening in the polyelectrolyte coil. Thus, a large increase in the ionic strength produces a dramatic contraction of the polyelectrolyte coils, which may overlap resulting in phase separation at high ionic strengths chains.[37–39] Varying the pH of the solution has a similar effect on weak polyelectrolytes. Their charge density depends on the acidity constant of the monomer and the pH of the solution. Thus, changing the pH might result in sudden changes in the structure of the polyelectrolyte.[40,41]

In addition to the behaviour of polyelectrolytes in solution, numerous studies have focused on their behaviour at interfaces.[19,22,37,42–45] On the one hand, if the polyelectrolyte chains are amphiphilic, they can adsorb spontaneously at fluid interfaces as long as the hydrophobic sections can be rearranged to minimise interaction with the hydrophilic phase or vice versa. On the other hand, although the vast majority of polyelectrolytes lack surface activity, they can be modified by introducing hydrophobic units into the chain,[9,46,47] or by interacting with surface-active species.[48–57]

1.2.1 Polypeptides

Polypeptides are polymers whose repeating units are amino acids linked by peptide bonds between the carboxyl group of one amino acid and the amide group of the next amino acid in the sequence. There are 20 natural amino acids present in proteins depicted in Figure 1.5, which, along with a wide variety of synthesised amino acids, provide the possibility of synthesizing a huge number of polypeptide sequences with varying lengths.

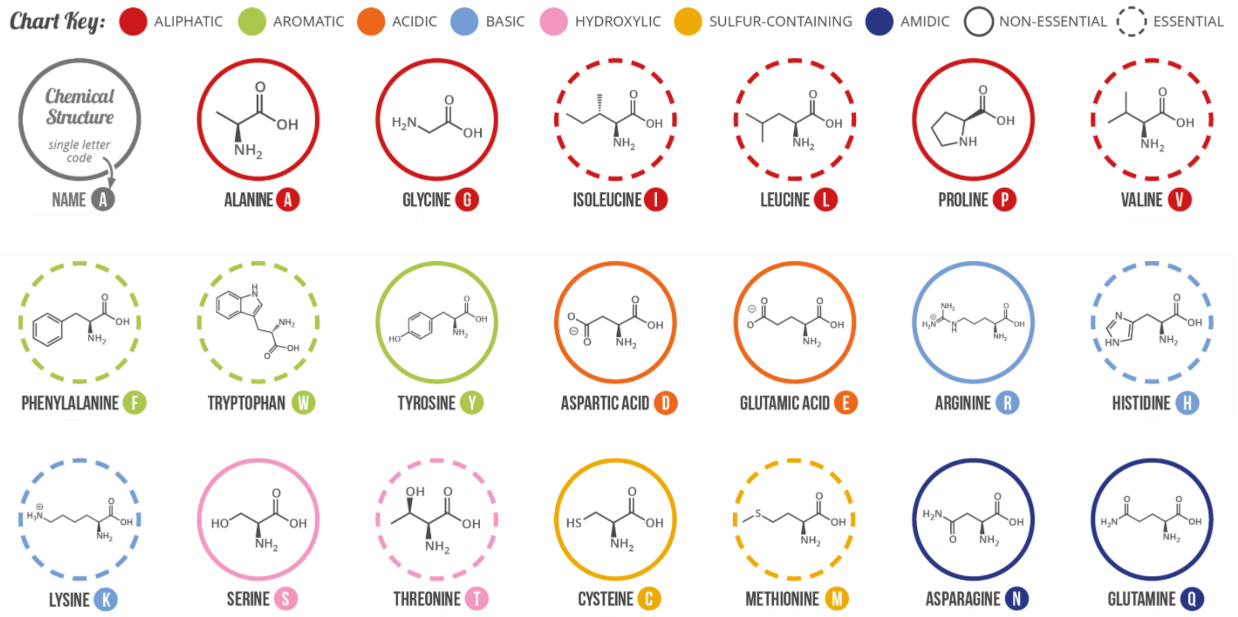

Figure 1.5. Chemical structure, name, and single letter code of the 20 natural amino acids present in proteins. The chart key provides information about the side chains. Figure adapted from https://www.compoundchem.com/2014/09/16/aminoacids/.[58]

The primary structure, the most basic level of polypeptide structure, refers to the linear sequence of amino acids that make up the chain. Each polypeptide has a unique sequence that determines its function. Folding of local regions of the polypeptide chains into structural elements stabilised by hydrogen bonds is referred to as secondary structure. The two main types of secondary structures are α-helices and β-sheets. On the one hand, α-helices are right-handed spirals stabilised by intramolecular hydrogen bonds between each carbonyl oxygen atom and the amide hydrogen of another amino acid four residues ahead in the chain. The side chains of the amino acids point outwards the helix. β-sheets, on the other hand, are flat and extended structures composed of a series of parallel or anti-parallel β-strands stabilised by hydrogen bonds between the carbonyl oxygen and the amide hydrogen of peptide bonds on adjacent strands. In this case, the amino acid side chains points above or below the plane of the sheet. A schematic illustration of these two types of secondary structures is shown in Figure 1.6.

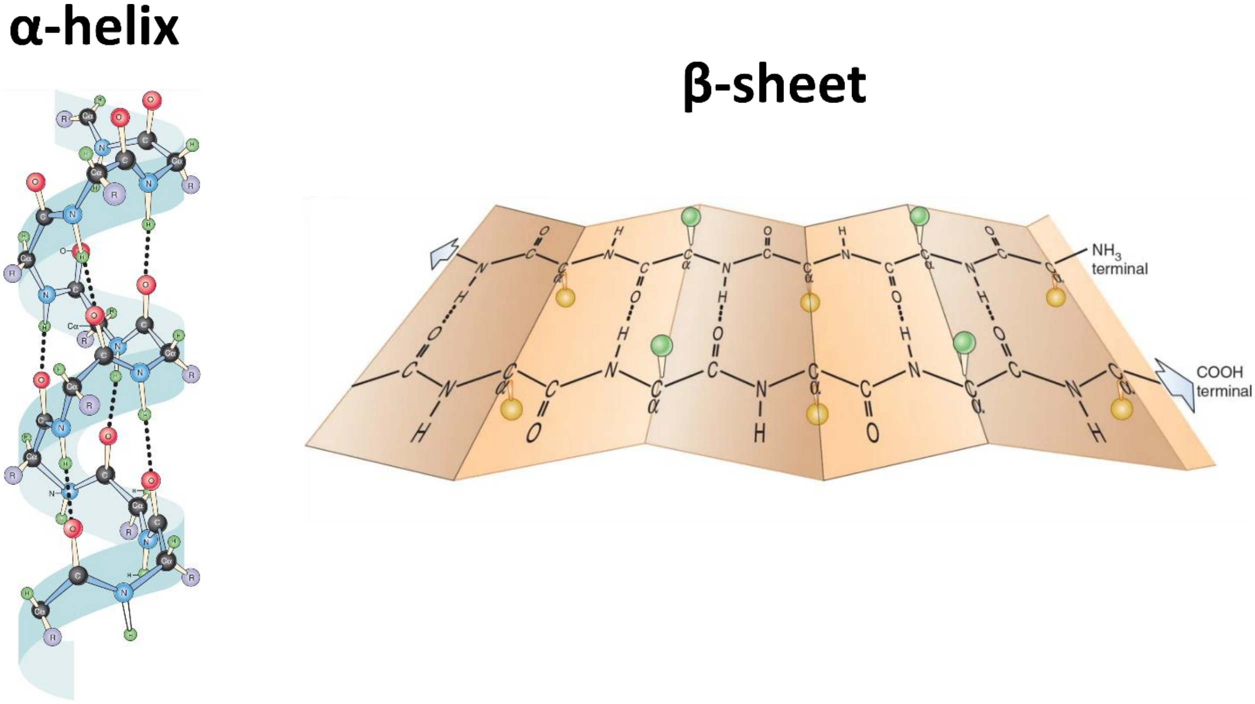
α-helix

β-sheet

Figure 1.6. Schematic illustration of the α-helix (left) and β-sheet (right) secondary structures. The black dots indicate the intramolecular or intermolecular hydrogen bonds formed in α-helices and β-sheets, respectively. Figure adapted from https://basicmedicalkey.com/structure-function-relationships-in-proteins.[59]

The ability of polypeptides to adopt secondary structures make them unique compared to other synthetic polyelectrolytes such as NaPSS, PEI or Pdadmac. Because of this ability, polypeptides can be used as building blocks to create a variety of self-assembled supramolecular structures.[60,61] For example, super-helices[62] can be formed by the winding of α-helices and interactions between β-sheets can occur through the formation of hydrogen bonds between their βedges and other polypeptide chains.[63,64] These interactions between secondary structure elements give rise to a vast array of structural possibilities, including the formation of nanotubes,[65–67] and nanofibrils.[64,68,69] The secondary structure of a polypeptide is sometimes critical in defining its properties and function to the extent that it can control its antibacterial activity,[70] the stiffness of a gel,[71] or the morphology of self-assembled vesicles.[72] It also affects its stiffness, with the order of decreasing stiffness being α > β > random coil.[73]

Aside from their designability and ability to form secondary structures, polypeptides have important properties such as biocompatibility, biodegradability, and biomimicry. Therefore, they are widely used molecules with applications in tissue engineering,[74–78] drug[79] and gene delivery,[80] or cancer therapy.[81] In this work only homopolypeptides have been used, i.e. polypeptides formed by the repetition of a single amino acid. The chemical structure of some of the most common homopolypeptides used in biomedical applications is depicted in Figure 1.7.

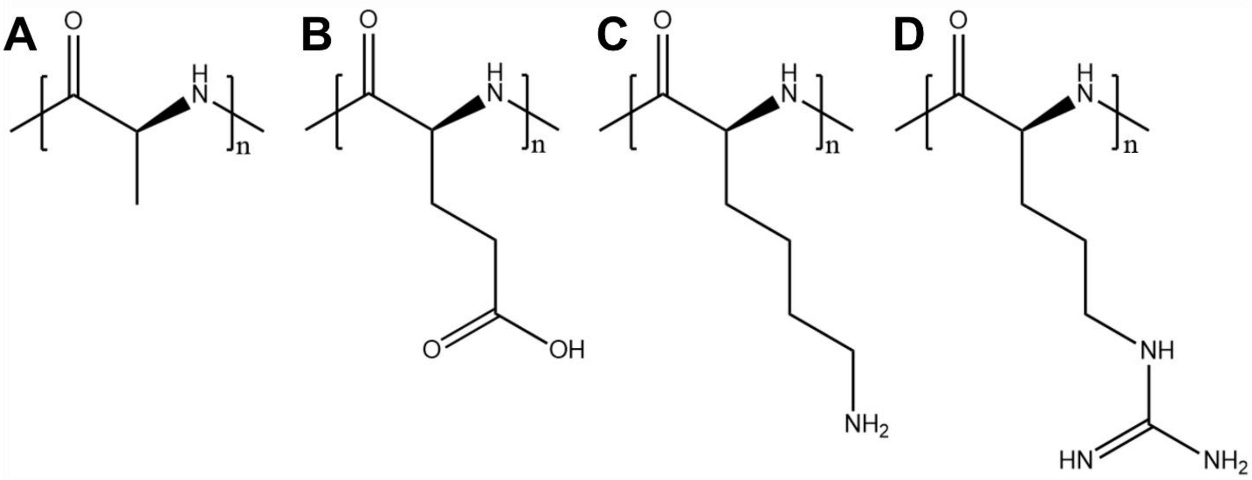

Figure 1.7. Chemical structures of (A) poly(L-alanine), (B) poly(L-glutamic acid), (C) poly(L-lysine) (PLL) and (D) poly(L-arginine) (PLA).

1.3 Oppositely charged polyelectrolyte/surfactant mixtures

1.3.1 Background

In the last decades, the properties and behaviour of oppositely charged polyelectrolyte/surfactant mixtures have been extensively studied by several active groups including Campbell and Varga,[49,50,82–84] von Klitzing,[48,85–87] Braunschweig,[88–90] Guzmán and Rubio[9,52,91–94] and Richdmond.[95–97] Surfactants reduce the interfacial tension while polymers enhance the viscoelastic and rheological properties of the system. Most polyelectrolytes are not surface-active on their own, but their interactions with surfactants allow tuning of their adsorption properties. Indeed, synergy to lower the surface tension comes from increasing surfactant packing by neutralising the charge layer of the headgroups, which results in an enhancement of the surface properties of P/S mixtures at much lower concentrations than either component alone. The simplest interfacial structure formed by these systems is referred to as 'surface monolayer', which is defined as a single monolayer of surfactant in contact with air (hydrophobic driving force) with hydrated polyelectrolyte bound to the headgroups (electrostatic force). Nevertheless, these systems may present more complex structures such as multilayers depending on the materials used and the conditions (pH, temperature, ionic strength, etc.). The structure, rheological properties and phase behaviour of these systems enable them to be used as stabilisers of foams and emulsions, in the cosmetic[9,98] and detergent industry,[99] for wastewater treatment[10] or food processing.[100,101] Furthermore, the use of biocompatible P/S mixtures in pharmacy and medicine has become very interesting in order to reduce the toxicity of many drugs and useful materials in these fields, as well as to develop new drug delivery and coating fabrication systems.[102,103]

1.3.2 Bulk phase behaviour

Numerous studies have shown that understanding the bulk behaviour of P/S mixtures is critical for fully understanding their interfacial behaviour.[9,48,52,55,104,105] Indeed, many applications of these systems involve the adsorption or deposition of P/S complexes or supramolecular aggregates previously formed in the bulk solution.[50,53,106,107]

The bulk phase behaviour of polymer/surfactant mixtures depends on the type of interactions (Van der Waals forces, hydrophobic interactions, hydrogen bonds, electrostatic interactions) between polymer chains and surfactant molecules or micelles. These interactions are determined by the nature of the components of the mixture. Thus, factors such as polymer charge density, molecular weight or stiffness, and surfactant concentration, chain length or nature of the head, have a significant impact on the properties of these systems.

Uncharged polymer/surfactant systems associate mainly through hydrophobic interactions leading to a cooperative association.[9,52,108,109] This means that surfactant molecules remain free in the solution until a certain surfactant concentration, known as the critical aggregate concentration (cac), is reached, several orders of magnitude below the cmc of the surfactant.[110,111] Once the cac is reached, the attractive forces that cause surfactant molecules to bind to other surfactant molecules that are already bound to the polymer chains start to contribute to the cooperative association. At this point, micelle-like structures begin to self-assemble on the polyelectrolyte chains, resulting in the commonly known as 'pearl necklace' structure.[112] Finally, as surfactant concentration increase further, polymer chains become saturated and surfactant molecules begin to self-assemble in the solution forming micelles.

In addition to Van der Waals and London forces, hydrogen bonds or hydrophobic interactions, oppositely charged P/S mixtures exhibit strong electrostatic interactions between the surfactant headgroups and the charged monomers of the polyelectrolyte, rendering the previous description of the bulk phase behaviour not completely applicable in this case.[9,48,52,104,113] Furthermore, the P/S association releases counterions to the solution increasing the entropy, which is typically the driving force for the assembly. In this case, at low surfactant concentrations, free surfactant molecules are in equilibrium with P/S complexes formed as a consequence of the association of micelle-like supramolecular surfactant aggregates with single polyelectrolyte chains. Since these complexes still have a high charge density, they are soluble, and the solution is in a one-phase region. Beyond the cac, polyelectrolyte chains become saturated decreasing the net charge of P/S complexes; hence, electrostatic repulsions between complexes are reduced and they lose colloidal stability leading to the formation of macroscopic P/S aggregates involving many polyelectrolyte chains. Consequently, the solutions become increasingly cloudy due to the presence of particles suspended in the bulk solution. When the surfactant concentration in the system approaches the point at which charge neutralisation of polyelectrolyte chains occurs, the aggregates become highly insoluble due to reduced colloidal stability and associative separation occurs.[114] Eventually precipitation and sedimentation (if aggregates are denser than the solvent) or creaming (if aggregates are less dense than the solvent) of macroscopic flocks occurs. Finally, additional surfactant molecules added to the system are adsorbed onto P/S aggregates giving rise to overcharged aggregates that retain colloidal stability but themselves are present as kinetically-stabilised colloidal dispersions.[57,115]

Over the last decade, numerous studies have paid special attention to the non-equilibrium effects that P/S systems present and their influence in both their bulk and the interfacial behaviour. Aside from the P/S ratio, many other factors can affect the properties of these systems, ranging from the specific characteristics of the polyelectrolyte and surfactant used to the mixing protocol.[48] When solutions of polyelectrolyte and surfactant are mixed to get a P/S solution in the equilibrium one-phase region, local concentrations in the equilibrium two-phase region can lead to the formation of non-equilibrium (kinetically-trapped) P/S aggregates. These kinetically-trapped aggregates can persist in solution over extended time scales. Indeed, such non-equilibrium effects are inherent to the underlying nature of the experiments that will be conducted in this PhD project.

There are important parameters that can affect the non-equilibrium characteristics of these systems. Mészáros et al. have dedicated many efforts to this topic, and some of their most important contributions are summarised below. They have shown that the mixing protocol followed to prepare P/S solutions (order of addition,[116,117] speed of the P/S mixing[115,117,118] or surfactant and polyelectrolyte concentration[119,120]) has strong influences on the physical state, the size and the structure of P/S aggregates. A good and visual example is presented in Figure 1.8. In this work, they studied the influence of the order of addition on the final state of PEI/SDS solutions at high surfactant concentrations. The rapid addition of the polyelectrolyte solution to the surfactant one prevented the aggregation of P/S complexes because the adsorption of the excess SDS kinetically-stabilised the dispersion. On the other hand, the slow addition of SDS to the PEI solution resulted in a cloudy solution as a result of precipitation.[116] Later, they investigated systematically the effects of two different protocols on the same P/S system: i) the 'stop-flow mixing protocol', in which the mixture is obtained rapidly, and ii) the 'gentle mixing protocol', in which the components mixing is less efficient.[115] They found that the size and the structure of resulting P/S aggregates are affected by the protocol used, and that it is possible to have a greater range of kinetically-stable colloidal dispersion (i.e., avoid precipitation) when an appropriate mixing protocol is applied. A similar study carried out with a poly(vinylamine)/SDS mixture also showed that the bulk properties of the system are affected by the mixing protocol used.[118]

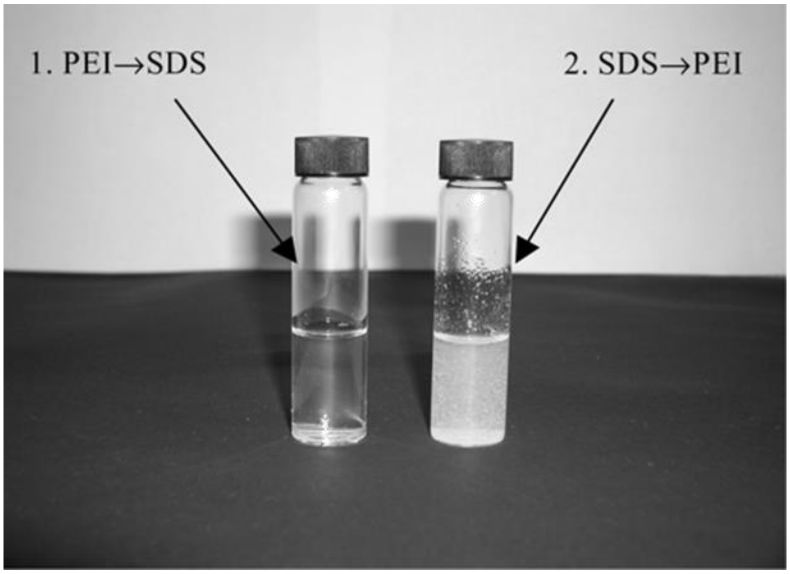

Figure 1.8. Appearance resulting from two solutions with the same final concentration of PEI and SDS prepared by different protocols. A transparent solution results from the addition of the PEI solution to the SDS solution, while in the opposite case the slow precipitation of P/S aggregates manifested as high turbid samples. Figure reproduced from Mészáros et al., 2003.[116]

The ionic strength of the solution, which is strongly affected by the presence of an additional electrolyte in P/S solutions, causes the screening of polyelectrolyte and surfactant charges. As a result, high ionic strength can lead to the total screening of polyelectrolyte charges, suppressing electrostatic interactions with surfactant. Therefore, ionic strength is another important factor to consider when studying the equilibrium vs. non-equilibrium nature of P/S interactions. Similarly, the charge density of weak polyelectrolytes depends on the pH of the solution. Thus, a modification of the pH influences also the non-equilibrium features of P/S mixtures.[121] Mészáros et al. showed that the addition of moderate concentrations of salt resulted in a narrower concentration range where kinetically-trapped aggregates were observed compared to that in the absence of salt. Furthermore, the formation of kinetically-trapped aggregates was suppressed at high ionic strength, showing therefore the high impact of salt concentration on the non-equilibrium nature of P/S association.[122] Naderi et al. found that compact P/S aggregates formed at high surfactant concentrations were more stable to the addition of NaCl than larger aggregates obtained a low surfactant concentrations.[57] Hence, the size and state of the aggregates and their stability in the solution can be tuned by carefully controlling the mixing protocol, the ionic strength and the pH of the medium. It can be concluded then that, in general, an increase in ionic strength promotes equilibrium whilst the entropy associated with counterion release in samples without added inert electrolyte promotes kinetically-trapped states.

Varga and Campbell recently reported a general physical description of the behaviour of P/S mixtures at the air/water interface.[49] They showed that the nature of the bulk binding interactions and the characteristics of the precipitate may be used to explain the interfacial properties of P/S mixtures, but we will return to this point in the following section. Turbidity measurements were performed to characterise the bulk behaviour of three different P/S systems as a function of surfactant concentration and sample age. The results are presented in Figure 1.9 and exhibit similar features. At low surfactant concentrations, the low turbidity detected is associated with the presence of soluble and stable P/S complexes in the one-phase region. The equilibrium two phase region is indicated by high turbidity of freshly-prepared mixtures, which decreases with time due to precipitation as a consequence of the lack of colloidal stability of P/S aggregates near to charge neutralisation. At surfactant concentrations near to the phase boundaries, the P/S mixture showed high turbidity during extended time scales, which is related to the formation and persistence of kinetically-trapped aggregates. Finally, at higher bulk surfactant concentrations, the turbidity generally remains higher than at low bulk surfactant concentrations because of the presence of kinetically-stabilised colloidal dispersion of aggregates.

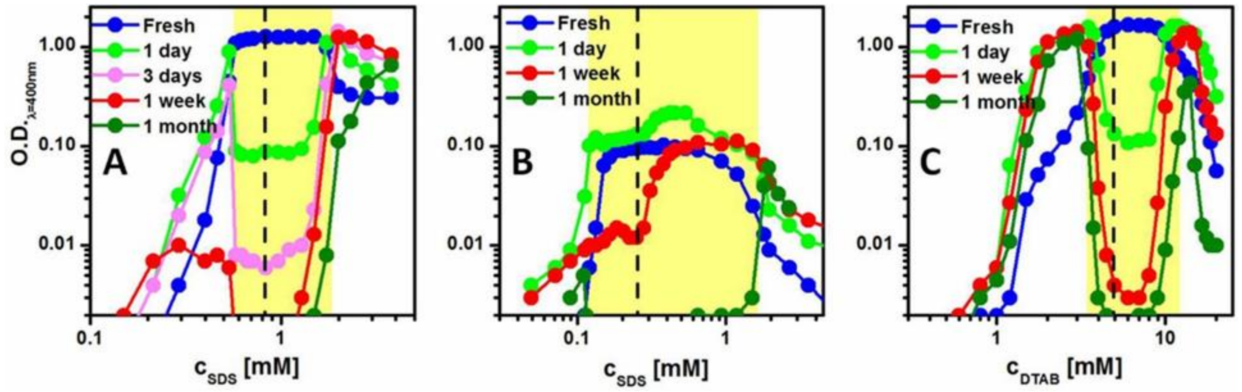

Figure 1.9. Variation of the optical density at 400 nm (turbidity) with respect to the total concentration of surfactant and the sample age recorded using UV-vis spectroscopy: (A) 100 and (B) 10 ppm Pdadmac/SDS in 0.1 mM NaCl and (C) 100 ppm NaPSS/DTAB in pure water. Two-phases regions are indicated with shaded areas. Figure reproduced from Varga and Campbell, 2017.[49]

1.3.3 Air/water interface

1.3.3.1 Background

Goddard and co-workers noted for the first time the differences in the interfacial behaviour of uncharged polymer/surfactant and P/S mixtures showing that the addition of a small amount of polyelectrolyte can result in a significant lowering of the interfacial tension of dilute surfactant solutions.[123,124] Consequently, a large number of studies to explain the interfacial properties of P/S systems began to emerge. However, the dominant influence that non-equilibrium effects could have on the behaviour of these systems at interfaces remained not fully appreciated for many years,[104,125] leading to some misinterpretation in the studies conducted.

Thomas, Penfold and co-workers dedicated many efforts to understanding the surface tension isotherms of P/S mixtures through the use of neutron reflectometry (NR), which allows for determining the composition and structure of mixed layers formed at the air/water interface (a detailed description of the NR technique is presented in section 3.3.5).[51,84,126,127] Thus, they related the surface tension isotherms with the structure and composition of the interface obtained using NR.[46,56,104,128–130] They proposed a general classification[104] of P/S mixtures according to the type of adsorption they present: type 1, thick layers characterised by very strong adsorption at the air/water interface and a plateau in the surface tension isotherm such as NaPSS/DTAB,[56,130] and type 2, more compact layers characterised by a peak in the surface tension isotherm such as Pdadmac with sodium alkyl sulfates.[128] Despite acknowledging the lack of reproducibility[130] in data recorded or the impossibility of applying a common structural model in the analysis of the different NR isotopic contrasts,[56] which are now known to be non-equilibrium features, they considered that the surface properties of P/S mixtures that had reached steady-state represented true equilibrium. They even elaborated two thermodynamic models to explain the data,[131,132] which was later shown to be an incorrect assumption.[49]

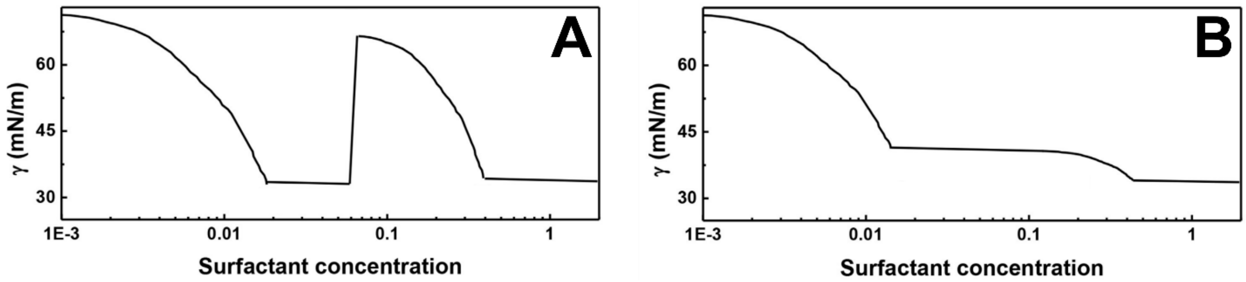

Figure 1.10. Idealised surface tension isotherm of P/S mixtures characterised by the (A) presence and (B) absence of a surface tension peak. Figure adapted from Guzmán et al., 2020.[93]

Over the last decade, it has been demonstrated that many steady-state interfacial properties of P/S mixtures explained in terms of equilibrium adsorption were actually far from the equilibrium.[52,83,88,119,133–135] Guzmán et al. have recently collected in a review the current state of the physical chemistry of P/S mixtures focusing on equilibrium vs. non-equilibrium behaviour.[93]

1.3.3.2 Impact of bulk aggregation on interfacial depletion

Campbell, Varga and co-workers have contributed significantly in recent years to the study of the relation between bulk and interfacial behaviour properties of P/S mixtures by paying special attention to non-equilibrium effects and preparation protocols.[82,83,106,133,136,137] In 2010 they studied the Pdadmac/SDS system to examine the origin of the surface tension peak paying special attention to the influence that non-equilibrium effects can have on the interfacial properties of the system.[82] They demonstrated that the surface tension peak is caused by slow precipitation and the subsequent loss of surface-active material, as well as the possibility to tune the interfacial properties of the mixtures by using different sample handling methods, which are clear indications of the pronounced non-equilibrium nature of the system. Further work showed that the experimental surface tension values agree with the ones calculated from the surface excess obtained by NR.[133] Later it was demonstrated that NaPSS/DTAB mixtures presented a surface tension peak after extremely slow precipitation.[137] This contrasts sharply with Thomas, Penfold and coworkers' classification of NaPSS/DTAB as a type 1 system,[56,130] i.e. a system presenting a plateau in the surface tension isotherm. In this work a new method to predict the surface tension of P/S mixtures was also developed and rigorously tested using NaPSS/DTAB, Pdadmac/SDS and DNA/DTAB systems.

Finally, Campbell and Varga described the general behaviour of P/S mixtures at the air/water interface in terms of equilibrium vs. non-equilibrium extremes.[49] Through a comparison of the bulk phase behaviour (Figure 1.9), a comprehensive characterisation of the surface tension with respect to the sample age, as shown in Figure 1.11 allowed them to demonstrate that freshly-prepared samples of both types of systems presented a plateau in the surface tension isotherm and a surface tension peak appeared after bulk equilibration because of the aggregation of P/S complexes and the consequent depletion of material from the interface.[133] Therefore, they demonstrated that the classification of P/S systems in type 1 and type 2 is redundant.

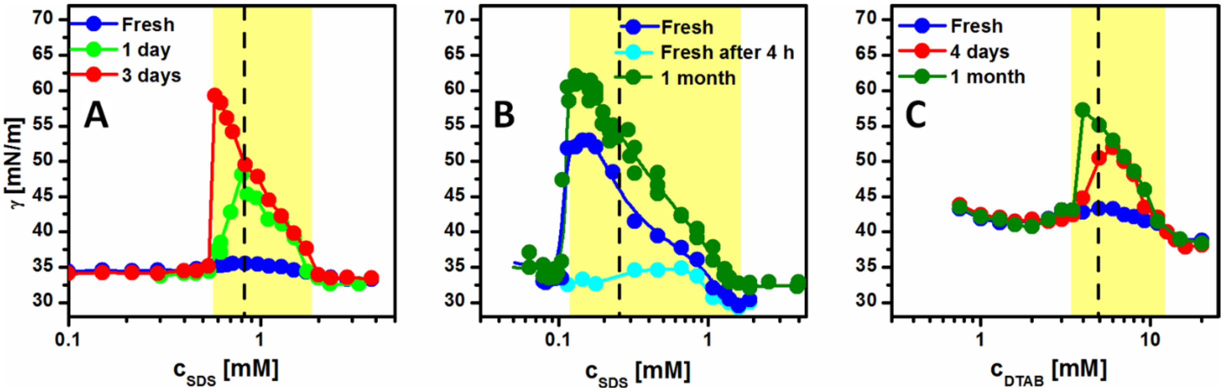

Figure 1.11. Variation of the surface tension with respect to the total concentration of surfactant and the sample age: (A) 100 and (B) 10 ppm Pdadmac/SDS in 0.1 mM NaCl and (C) 100 ppm NaPSS/ DTAB in pure water. Two-phases regions are indicated with shaded areas. Figure reproduced from Varga and Campbell, 2017.[49]

1.3.3.3 Impact of aggregate interactions on the interfacial properties

All the knowledge about the bulk and interfacial properties of P/S mixtures has been applied to the development of different mechanisms for the formation of P/S films at fluid interfaces. Pdadmac/SDS[82,83,136,138] and PEI/SDS[106,139,140] have been two of the most studied systems in this context. In addition to the depletion of material from interfaces as a result of bulk aggregation discussed in the previous section, attention was drawn to how interactions of the formed aggregates with interfaces affect the interfacial properties. Campbell, Varga and co-workers made an important contribution by demonstrating the formation of P/S films at the air/water interface via different mechanisms involving aggregate interactions. To avoid the previously described effects of mixing methodology on the system, freshly prepared P/S mixtures were used in the articles referred to in the following text. The formation of interfacial P/S multilayers through transport under gravity of aggregates self-assembled in the bulk rather than through their direct self-assembly at the surface was demonstrated in Pdadmac/SDS mixtures.[136]

This work was followed by the study of the effects of bulk aggregation at different pH in the phase separation region on PEI/SDS monolayers at the dynamic air/water interface created by an overflowing cylinder.[140] At high pH, i.e., low charge density of PEI chains, depletion of monomers and small complexes occurs. At low pH, i.e., high charge density of PEI chains, the amount of PEI/SDS present at the air/water interface can be dominated by the dissociation and Marangoni spreading (i.e., the spreading of a liquid over another one with higher interfacial tension) from aggregates rather than the conventionally assumed adsorption of complexes. Ellipsometry measurements using fast data acquisition rates were essential to show that the signal fluctuated between the typical values of pure water and patches of monolayer delivered by aggregate dissociation as shown in Figure 1.12. Furthermore, this study demonstrated that the behaviour of P/S mixtures at dynamic interfaces cannot be directly related to their static properties.

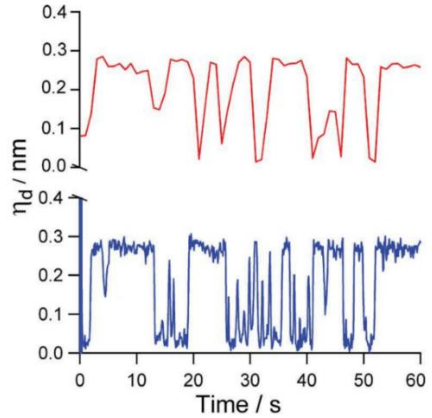

Figure 1.12. Ellipsometry thickness (η_d) measured for PEI/SDS at pH 4 as a function of time using a 1 s (red line) and 0.1 s (blue line) data acquisition rate. Both sets of data exhibit fluctuations of the signal between typical values for the pure water and a surface P/S monolayer. Figure reproduced from Angus-Smyth et al., 2013.[140]

Finally, the impact of non-equilibrium aggregates on the structure and morphology of Pdadmac/SDS mixtures was studied using different preparation protocols.[83] In this work, three different mechanisms of aggregate interactions were defined for the first time: (1) spontaneous association related to the charge/structure of the aggregates in relation to that of the surfactant headgroups in the surface monolayer, (2) unspecific interactions that can be removed by aspiration, and (3) unspecific transport under gravity related to the relative densities of the aggregates and solution with respect to the location of the interface.

1.3.4 Spread films

For nearly a century, non-equilibrium effects have been used to create loaded films of macromolecules, with the earliest studies focusing on spread protein films.[141,142] When the amphiphilic material self-assembles at the air/water interface, the free energy of the system is lowered, making the spreading process thermodynamically favourable. Various methodologies have been used to achieve this, such as the use of organic solvents, aqueous solutions, and protein crystals,[143] and a plethora of studies have validated the efficiency of the spreading methodology in forming kinetically-trapped protein films.[144–147]

Building on the spreading methodology used to create loaded films of proteins and the non-equilibrium features of P/S systems presented in the previous section, Campbell, Varga and co-workers exploited the aggregate interactions in the development of a new methodology to create P/S films at the air/water interface spread from neutral aggregates.[53] The spreading of a small aliquot of NaPSS/DTAB neutral aggregates on pure water resulted in their dissociation remaining the material kinetically trapped in the spread film due to the entropy associated with counterion release to the macroscopic bulk. This method resulted in a significantly higher amount of interfacial material delivered to the interface compared to the equivalent film formed by adsorption of P/S complexes. The same effect was observed for Pdadmac/SDS layers.[49] This methodology has two important advantages: i) the presence of a high amount of material at the interface compared to the adsorption method, and ii) it is fully aqueous and thereby may have economic and environmental advantages due to reducing toxicity over other spreading methods.

Two years later, Tummino et al. studied the influence of aggregates charge and ionic strength of the subphase on the properties and composition of NaPSS/DTAB films spread from aggregates.[50] Figures 1.13A/B and C/D shows the surface excess of NaPSS and DTAB during five consecutive compression/expansion cycles together with the surface pressure – area isotherms of films spread from undercharged and overcharged aggregates, respectively. In the case of undercharged aggregates, the first compression results in squeezing out of excess material, as revealed by the plateau in surface pressure and surface excess. Compression is followed by large hysteresis in surface pressure data. After the first cycle, the film behaved like a perfectly soluble membrane similar to what has been observed in films spread from neutral aggregates.[53] In the case of overcharged aggregates, the surface excess of both components continued to increase after surface pressure data reached the plateau (Figure 1.13D). Further compression/expansion cycles of these films exhibited a limiting behaviour in their surface response, characterised by the retention of hysteresis and a kink in the hysteresis loop at the beginning of the expansion (as marked by a green arrow in Figure 1.13C). This behavior was attributed to the formation of ESs or reservoirs that are reincorporated during the expansion, after a comprehensive study utilizing techniques such as ellipsometry, Brewster angle microscopy (BAM) and NR.

Since the surface composition of films spread from undercharged and overcharged aggregates was similar, the formation of ESs was attributed to nucleation by the presence of some aggregates embedded in the film, and an analogy to the behaviour of lung surfactant where surfactant protein-B has a similar role was made.[148,149] The application of BAM allowed imaging of different lateral morphologies for the ESs formed from successive spreading and surface area compression. However, these ESs were not stable enough over time to allow direct resolution of their detailed structure. Additionally, while the ESs were found to consist of both polyelectrolyte and surfactant for samples on pure water and overcharged P/S aggregates, the authors observed that loops of material composed solely of polyelectrolyte were formed on a subphase with elevated ionic strength regardless the charge of P/S aggregates. Thus, control over the morphology and composition of the extended structures in three dimensions was demonstrated for the first time.

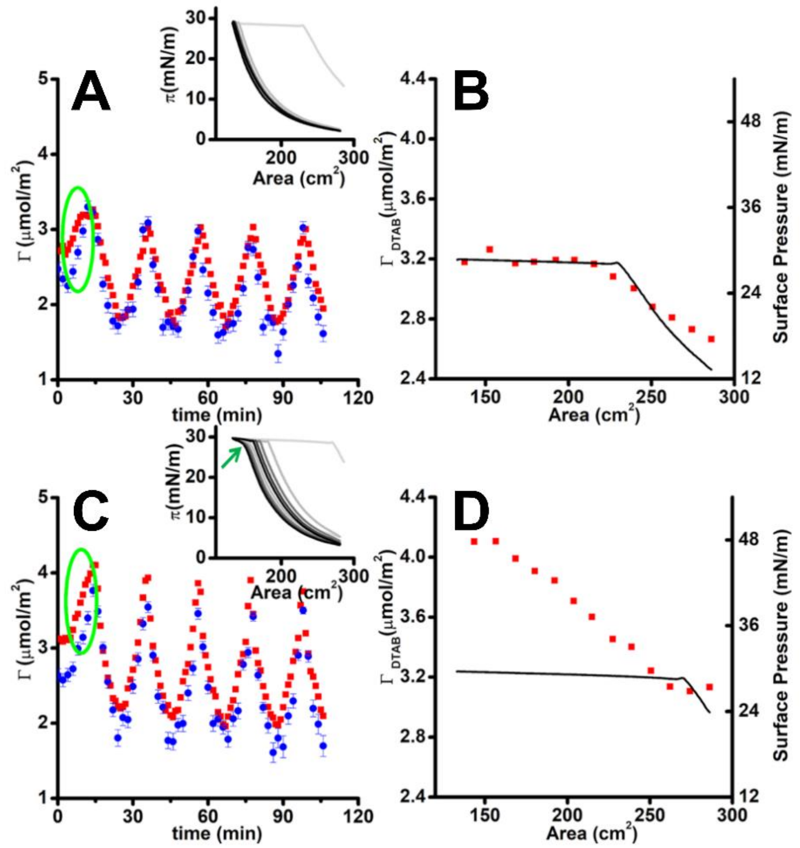

Figure 1.13. Time-resolved surface excess values of DTAB (red squares) and NaPSS (blue circles) obtained by NR during five consecutive compression/expansion cycles of films spread from (A) undercharged and (C) overcharged NaPSS/DTAB aggregates. The surface pressure was recorded at the same time and is shown in the insets. The dependence of the surfactant surface excess with the area during the first compression marked by the green circle in panels A and C is shown for (B) undercharged aggregates and (D) overcharged aggregates. Figure reproduced from Tummino et al., 2018.[50]

The group of Von Klitzing et al. have recently made significant advances in understanding the phenomenon of ES formation in P/S films at the air/water interface. First, they found that the formation of ESs below the surface monolayer composed of surfactant bilayers and an additional mixed layer resulted in foam films that are highly unstable and rapidly collapse.[86] Secondly, they conducted a systematic comparison of the properties and structure of monosulfonated poly(phenylene sulfone) and NaPSS mixtures with CTAB, which are rigid and flexible polyelectrolytes.[87] They showed that compensation of all interfacial charges, specifically, P/S ratios close to 1, is the main driving force for the formation of ESs. Furthermore, they demonstrated that ES formation can be eliminated by using flexible polymers such as NaPSS, which can effectively compensate the charges of the surfactant monolayer. This finding is in contrast to those of other authors. Tummino et al.[50] observed ES formation in NaPSS/DTAB films spread from overcharged aggregates, but the flexibility of NaPSS could explain why they were not stable over time. Penfold et al. observed the formation of multilayers in adsorbed films of NaPSS and decyl, dodecyl and tetradecyltrimethylammonium bromide at high surfactant concentrations.[56,150] As a result, the discrepancies in the overall physical picture indicate that more work on these systems is required to gain a complete understanding. The spreading method has only been tested on the NaPSS/DTAB system exploiting the effect of the charge of the aggregates and the ionic strength of the medium. Expanding the methodology by using other polyelectrolyte architectures, such as hyperbranched or dendrimers, and varying the secondary structure of polypeptides would enhance the methodology and lead to more comprehensive results and a general understanding of the methodology. Additionally, considering the effect of polyelectrolyte stiffness on the dynamic properties and structure of P/S films, using polyelectrolytes of varying rigidity could provide further insights into these systems. Finally, in addition to the ionic strength, the influence of other external parameters on the properties of spread P/S films could be investigated. It is well known, for example, that the charge density of weak polyelectrolytes varies significantly with pH. Therefore, it would be interesting to study the effect of the subphase pH on the spreading of P/S aggregates involving weak polyelectrolytes and the properties of the P/S films they form. Another parameter that could be explored is the compression ratio, defined as A_0/A, where A_0 is the initial surface area. In principle, the variation of the compression ratio could control the coverage of ESs in the collapse region, and it could influence the structure and morphology of the films,[151–153] as well as their rheological properties.[154]

1.4 References

(1) Berti, D.; Palazzo, G. *Colloidal Foundations of Nanoscience*; Berti, D., Palazzo, G., Eds.; Elsevier: Amsterdam, 2014.

(2) Israelachvili, J. N. *Intermolecular and Surface Forces*, 3rd ed.; Elsevier/Academic Press: Amsterdam, 2011.

(3) Tadros, T. F. *An Introduction to Surfactants*; De Gruyter, 2014.

(4) *Handbook of Surface and Colloid Chemistry*, Third.; Birdi, K., Ed.; CRC Press: Boca Raton, 2009.

(5) Tanford, C. *The Hydrophobic Effect: Formation of Micelles and Biological Membranes*; Wiley-Interscience: New York, 1973.

(6) Israelachvili, J. N.; Mitchell, D. J.; Ninham, B. W. Theory of Self-Assembly of Hydrocarbon Amphiphiles into Micelles and Bilayers. *J. Chem. Soc. Faraday Trans. 2 Mol. Chem. Phys.* **1976**, *72*, 1525–1568.

(7) Tanford, C. Micelle Shape and Size. *J. Phys. Chem.* **1972**, *76*, 3020–3024.

(8) Ramanathan, M.; Shrestha, L. K.; Mori, T.; Ji, Q.; Hill, J. P.; Ariga, K. Amphiphile Nanoarchitectonics: From Basic Physical Chemistry to Advanced Applications. *Phys. Chem. Chem. Phys.* **2013**, *15*, 10580–10611.

(9) Llamas, S.; Guzmán, E.; Ortega, F.; Baghdadli, N.; Cazeneuve, C.; Rubio, R. G.; Luengo, G. S. Adsorption of Polyelectrolytes and Polyelectrolytes-Surfactant Mixtures at Surfaces: A Physico-Chemical Approach to a Cosmetic Challenge. *Adv. Colloid Interface Sci.* **2015**, *222*, 461–487.

(10) Radoiu, M. T.; Martin, D. I.; Calinescu, I.; Iovu, H. Preparation of Polyelectrolytes for Wastewater Treatment. *J. Hazard. Mater.* **2004**, *106*, 27–37.

(11) Mortimer, D. A. Synthetic Polyelectrolytes—A Review. *Polym. Int.* **1991**, *25*, 29–41.

(12) Mura, S.; Nicolas, J.; Couvreur, P. Stimuli-Responsive Nanocarriers for Drug Delivery. *Nat. Mater.* **2013**, *12*, 991–1003.

(13) Torchilin, V. P. Structure and Design of Polymeric Surfactant-Based Drug Delivery Systems. *J. Control. Release* **2001**, *73*, 137–172.

(14) Shenoy, D. B.; Antipov, A. A.; Sukhorukov, G. B.; Möhwald, H. Layer-by-Layer Engineering of Biocompatible, Decomposable Core-Shell Structures. *Biomacromolecules* **2003**, *4*, 265–272.

(15) Lankalapalli, S.; Kolapalli, V. R. M. Polyelectrolyte Complexes: A Review of Their Applicability in Drug Delivery Technology. *Indian J. Pharm. Sci.* **2009**, *71*, 481–487.

(16) Wu, L.; Tuo, X.; Cheng, H.; Chen, Z.; Wang, X. Synthesis, Photoresponsive Behavior, and Self-Assembly of Poly(Acrylic Acid)-Based Azo Polyelectrolytes. *Macromolecules* **2001**, *34*, 8005–8013.

(17) Plamper, F. A.; Ruppel, M.; Schmalz, A.; Borisov, O.; Ballauff, M.; Müller, A. H. E. Tuning the Thermoresponsive Properties of Weak Polyelectrolytes: Aqueous Solutions of Star-Shaped and Linear Poly(N,N-Dimethylaminoethyl Methacrylate). *Macromolecules* **2007**, *40*, 8361–8366.

(18) Liu, Z.; Zhang, Z.; Zhou, C.; Jiao, Y. Hydrophobic Modifications of Cationic Polymers for Gene Delivery. *Prog. Polym. Sci.* **2010**, *35*, 1144–1162.

(19) Stuart, M. C.; de Vries, R.; Lyklema, H. Chapter 2 - Polyelectrolytes. In *Fundamentals of Interface and Colloid Science*; Lyklema, J., Ed.; Elsevier Ltd, 2005; Vol. 5, pp 2.1-2.84.

(20) Meka, V. S.; Sing, M. K. G.; Pichika, M. R.; Nali, S. R.; Kolapalli, V. R. M.; Kesharwani, P. A Comprehensive Review on Polyelectrolyte Complexes. *Drug Discov. Today* **2017**, *22*, 1697–

1706.

(21) Hassan, P. A.; Verma, G.; Ganguly, R. Soft Materials-Properties and Applications. In *Functional Materials*; Elsevier Inc., 2012; pp 1–59.

(22) Szilagyi, I.; Trefalt, G.; Tiraferri, A.; Maroni, P.; Borkovec, M. Polyelectrolyte Adsorption, Interparticle Forces, and Colloidal Aggregation. *Soft Matter* **2014**, *10*, 2479–2502.

(23) Manning, G. S. Limiting Laws and Counterion Condensation in Polyelectrolyte Solutions I. Colligative Properties. *J. Chem. Phys.* **1969**, *51*, 924–933.

(24) Manning, G. S. Limiting Laws and Counterion Condensation in Polyelectrolyte Solutions. III. An Analysis Based on the Mayer Ionic Solution Theory. *Small Ions J. Chem. Phys.* **1969**, *51*, 9343.

(25) Manning, G. S. Counterion Condensation Theory Constructed from Different Models. *Phys. A Stat. Mech. its Appl.* **1996**, *231*, 236–253.

(26) Manning, G. S.; Ray, J. Counterion Condensation Revisited. *J. Biomol. Struct. Dyn.* **1998**, *16*, 461–476.

(27) Odijk, T. Polyelectrolytes near the Rod Limit. *J. Polym. Sci.* **1977**, *15*, 477–483.

(28) Netz, R. R.; Joanny, J. F. Adsorption of Semiflexible Polyelectrolytes on Charged Planar Surfaces: Charge Compensation, Charge Reversal, and Multilayer Formation. *Macromolecules* **1999**, *32*, 9013–9025.

(29) Kayitmazer, A. B.; Seyrek, E.; Dubin, P. L.; Staggemeier, B. A. Influence of Chain Stiffness on the Interaction of Polyelectrolytes with Oppositely Charged Micelles and Proteins. *J. Phys. Chem. B* **2003**, *107*, 8158–8165.

(30) Huang, S. C. J.; Artyukhin, A. B.; Wang, Y.; Ju, J. W.; Stroeve, P.; Noy, A. Persistence Length Control of the Polyelectrolyte Layer-by-Layer Self-Assembly on Carbon Nanotubes. *J. Am. Chem. Soc.* **2005**, *127*, 14176–14177.

(31) Shi, L.; Carn, F.; Boué, F.; Buhler, E. Role of the Ratio of Biopolyelectrolyte Persistence Length to Nanoparticle Size in the Structural Tuning of Electrostatic Complexes. *Phys. Rev. E* **2016**, *94*, 032504.

(32) Lu, Y.; Weers, B.; Stellwagen, N. C. DNA Persistence Length Revisited. *Biopolymers* **2002**, *61*, 261–275.

(33) Sato, T.; Norisuye, T.; Fujita, H. Double-Stranded Helix of Xanthan in Dilute Solution: Evidence from Light Scattering. *Polym. J.* **1984**, *16*, 341–350.

(34) Dobrynin, A. V.; Colby, R. H.; Rubinstein, M. Scaling Theory of Polyelectrolyte Solutions. *Macromolecules* **1995**, *28*, 1859–1871.

(35) Sedlák, M. The Ionic Strength Dependence of the Structure and Dynamics of Polyelectrolyte Solutions as Seen by Light Scattering: The Slow Mode Dilemma. *J. Chem. Phys.* **1996**, *105*, 10123–10133.

(36) Srivastava, S.; Nykypanchuk, D.; Fukuto, M.; Halverson, J. D.; Tkachenko, A. V; Yager, K. G.;

Gang, O. Two-Dimensional DNA-Programmable Assembly of Nanoparticles at Liquid Interfaces. *J. Am. Chem. Soc* **2014**, *136*, 1.

(37) Dobrynin, A. V.; Rubinstein, M. Theory of Polyelectrolytes in Solutions and at Surfaces. *Prog. Polym. Sci.* **2005**, *30*, 1049–1118.

(38) Minko, S.; Kiriy, A.; Gorodyska, G.; Stamm, M. Single Flexible Hydrophobic Polyelectrolyte Molecules Adsorbed on Solid Substrate: Transition between a Stretched Chain, Necklace-like Conformation and a Globule. *J. Am. Chem. Soc.* **2002**, *124*, 3218–3219.

(39) Mei, Y.; Lauterbach, K.; Hoffmann, M.; Borisov, O. V.; Ballauff, M.; Jusufi, A. Collapse of Spherical Polyelectrolyte Brushes in the Presence of Multivalent Counterion. *Phys. Rev. Lett.* **2006**, *97*, 158301.

(40) Kamiyama, Y.; Israelachvili, J. Effect of pH and Salt on the Adsorption and Interactions of an Amphoteric Polyelectrolyte. *Macromolecules* **1992**, *25*, 5081–5088.

(41) Shiratori, S. S.; Rubner, M. F. pH-Dependent Thickness Behavior of Sequentially Adsorbed Layers of Weak Polyelectrolytes. *Macromolecules* **2000**, *33*, 4213–4219.

(42) Netz, R. R.; Andelman, D. Neutral and Charged Polymers at Interfaces. *Physics Reports*. **2003**, *380*, 1-95.

(43) Kötz, J.; Kosmella, S.; Beitz, T. Self-Assembled Polyelectrolyte Systems. *Prog. Polym. Sci.* **2001**, *26*, 1199–1232.

(44) Holm, C.; Joanny, J. F.; Kremer, K.; Netz, R. R.; Reineker, P.; Seidel, C.; Vilgis, T. A.; Winkler, R. G. Polyelectrolyte Theory. In *Polyelectrolytes with Defined Molecular Architecture II*; Schmidt, M., Ed.; Springer Berlin Heidelberg: Berlin, Heidelberg, 2004; pp 67–111.

(45) Lindman, B.; Thalberg, K. Polymer-Surfactant Interactions - Recent Developments. In *Interaction of Surfactants with Polymers and Proteins*; Goddard, E. D., Ananthapadmanabhan, K. P., Eds.; CRC Press: Boca Raton, 1993.

(46) Penfold, J.; Thomas, R. K.; Taylor, D. J. F. Polyelectrolyte/Surfactant Mixtures at the Air-Solution Interface. *Curr. Opin. Colloid Interface Sci.* **2006**, *11* (6), 337–344.

(47) Chiappisi, L.; Gradzielski, M. Co-Assembly in Chitosan-Surfactant Mixtures: Thermodynamics, Structures, Interfacial Properties and Applications. *Adv. Colloid Interface Sci.* **2015**, *220*, 92–107.

(48) Bain, C. D.; Claesson, P. M.; Langevin, D.; Mészáros, R.; Nylander, T.; Stubenrauch, C.; Titmuss, S.; von Klitzing, R. Complexes of Surfactants with Oppositely Charged Polymers at Surfaces and in Bulk. *Adv. Colloid Interface Sci.* **2010**, *155*, 32–49.

(49) Varga, I.; Campbell, R. A. General Physical Description of The Behavior of Oppositely Charged Polyelectrolyte/Surfactant Mixtures at the Air/Water Interface. *Langmuir* **2017**, *33*, 5915–5924.

(50) Tummino, A.; Toscano, J.; Sebastiani, F.; Noskov, B. A.; Varga, I.; Campbell, R. A. Effects of Aggregate Charge and Subphase Ionic Strength on the Properties of Spread Polyelectrolyte/Surfactant Films at the Air/Water Interface under Static and Dynamic

Conditions. *Langmuir* **2018**, *34*, 2312–2323.

(51) Campbell, R. A. Recent Advances in Resolving Kinetic and Dynamic Processes at the Air/Water Interface Using Specular Neutron Reflectometry. *Curr. Opin. Colloid Interface Sci.* **2018**, *37*, 49–60.

(52) Guzmán, E.; Llamas, S.; Maestro, A.; Fernández-Peña, L.; Akanno, A.; Miller, R.; Ortega, F.; Rubio, R. G. Polymer-Surfactant Systems in Bulk and at Fluid Interfaces. *Adv. Colloid Interface Sci.* **2016**, *233*, 38–64.

(53) Campbell, R. A.; Tummino, A.; Noskov, B. A.; Varga, I. Polyelectrolyte/Surfactant Films Spread from Neutral Aggregates. *Soft Matter* **2016**, *12*, 5304–5312.

(54) Kayitmazer, A. B.; Seeman, D.; Minsky, B. B.; Dubin, P. L.; Xu, Y. Protein-Polyelectrolyte Interactions. *Soft Matter* **2013**, *9*, 2553–2583.

(55) Langevin, D. Complexation of Oppositely Charged Polyelectrolytes and Surfactants in Aqueous Solutions. A Review. *Adv. Colloid Interface Sci.* **2009**, *147–148*, 170–177.

(56) Taylor, D. J. F.; Thomas, R. K.; Hines, J. D.; Humphreys, K.; Penfold, J. The Adsorption of Oppositely Charged Polyelectrolyte/Surfactant Mixtures at the Air/Water Interface: Neutron Reflection from Dodecyl Trimethylammonium Bromide/Sodium Poly(Styrene Sulfonate) and Sodium Dodecyl Sulfate/Poly(Vinyl Pyridinium Chloride). *Langmuir* **2002**, *18*, 9783–9791.

(57) Naderi, A.; Claesson, P. M.; Bergström, M.; Dedinaite, A. Trapped Non-Equilibrium States in Aqueous Solutions of Oppositely Charged Polyelectrolytes and Surfactants: Effects of Mixing Protocol and Salt Concentration. *Colloids Surfaces A Physicochem. Eng. Asp.* **2005**, *253*, 83–93.

(58) Brunning, A. A Brief Guide to the Twenty Common Amino Acids https://www.compoundchem.com/2014/09/16/aminoacids/ (accessed Jan 25, 2023).

(59) Structure–Function Relationships in Proteins https://basicmedicalkey.com/structure-function-relationships-in-proteins/ (accessed Jan 25, 2023).

(60) Song, Z.; Fu, H.; Wang, R.; Pacheco, L. A.; Wang, X.; Lin, Y.; Cheng, J. Secondary Structures in Synthetic Polypeptides from N-Carboxyanhydrides: Design, Modulation, Association, and Material Applications. *Chem. Soc. Rev.* **2018**, *47*, 7401–7425.

(61) Bonduelle, C. Secondary Structures of Synthetic Polypeptide Polymers. *Polym. Chem.* **2018**, *9*, 1517–1529.

(62) Mondal, S.; Adler-Abramovich, L.; Lampel, A.; Bram, Y.; Lipstman, S.; Gazit, E. Formation of Functional Super-Helical Assemblies by Constrained Single Heptad Repeat. *Nat. Commun.* **2015**, *6*, 1–8.

(63) Nowick, J. S. Exploring β-Sheet Structure and Interactions with Chemical Model Systems. *Acc. Chem. Res.* **2008**, *41*, 1319–1330.

(64) Cheng, P.-N.; Pham, J. D.; Nowick, J. S. The Supramolecular Chemistry of β-Sheets. *J. Am. Chem. Soc.* **2013**, *135*, 5477–5492.

(65) Gao, X.; Matsui, H. Peptide-Based Nanotubes and Their Applications in Bionanotechnology. *Adv. Mater.* **2005**, *17*, 2037–2050.

(66) Kholkin, A.; Amdursky, N.; Bdikin, I.; Gazit, E.; Rosenman, G. Strong Piezoelectricity in Bioinspired Peptide Nanotubes. *ACS Nano* **2010**, *4*, 610–614.

(67) Song, Q.; Goia, S.; Yang, J.; Hall, S. C. L.; Staniforth, M.; Stavros, V. G.; Perrier, S. Efficient Artificial Light-Harvesting System Based on Supramolecular Peptide Nanotubes in Water. *J. Am. Chem. Soc.* **2021**, *143*, 382–389.

(68) Sunde, M.; Serpell, L. C.; Bartlam, M.; Fraser, P. E.; Pepys, M. B.; Blake, C. C. F. Common Core Structure of Amyloid Fibrils by Synchrotron X-Ray Diffraction. *J. Mol. Biol.* **1997**, *273*, 729–739.

(69) Alsalahat, I.; Al-Majdoub, Z. M.; Taha, M. O.; Barber, J.; Aojula, H.; Hodson, N.; Freeman, S. Inhibition of Aggregation of Amyloid-β Through Covalent Modification with Benzylpenicillin; Potential Relevance to Alzheimer's Disease. *Biochem. Biophys. Reports* **2021**, *26*, 100943.

(70) Xiong, M.; Lee, M. W.; Mansbach, R. A.; Song, Z.; Bao, Y.; Peek, R. M.; Yao, C.; Chen, L. F.; Ferguson, A. L.; Wong, G. C. L.; Cheng, J. Helical Antimicrobial Polypeptides with Radial Amphiphilicity. *Proc. Natl. Acad. Sci. U. S. A.* **2015**, *112*, 13155–13160.

(71) Oelker, A. M.; Morey, S. M.; Griffith, L. G.; Hammond, P. T. Helix versus Coil Polypeptide Macromers: Gel Networks with Decoupled Stiffness and Permeability. *Soft Matter* **2012**, *8*, 10887–10895.

(72) Gebhardt, K. E.; Ahn, S.; Venkatachalam, G.; Savin, D. A. Role of Secondary Structure Changes on the Morphology of Polypeptide-Based Block Copolymer Vesicles. *J. Colloid Interface Sci.* **2008**, *317*, 70–76.

(73) Perticaroli, S.; Nickels, J. D.; Ehlers, G.; O'Neill, H.; Zhang, Q.; Sokolov, A. P. Secondary Structure and Rigidity in Model Proteins. *Soft Matter* **2013**, *9*, 9548–9556.

(74) Tang, Z.; Wang, Y.; Podsiadlo, P.; Kotov, N. A. Biomedical Applications of Layer-by-Layer Assembly: From Biomimetics to Tissue Engineering. *Adv. Mater.* **2006**, *18*, 3203–3224.

(75) Hammond, P. T. Building Biomedical Materials Layer-by-Layer. *Mater. Today* **2012**, *15*, 196–206.

(76) Nettles, D. L.; Chilkoti, A.; Setton, L. A. Applications of Elastin-Like Polypeptides in Tissue Engineering. *Adv. Drug Deliv. Rev.* **2010**, *62*, 1479–1485.

(77) Stuart, M. A. C.; Huck, W. T. S.; Genzer, J.; Müller, M.; Ober, C.; Stamm, M.; Sukhorukov, G. B.; Szleifer, I.; Tsukruk, V. V.; Urban, M.; Winnik, F.; Zauscher, S.; Luzinov, I.; Minko, S. Emerging Applications of Stimuli-Responsive Polymer Materials. *Nat. Mater.* **2010**, *9*, 101–113.

(78) Zarrintaj, P.; Ghorbani, S.; Barani, M.; Pal Singh Chauhan, N.; Khodadadi Yazdi, M.; Reza Saeb, M.; Ramsey, J. D.; Hamblin, M. R.; Mozafari, M.; Mostafavi, E. Polylysine for Skin Regeneration: A Review of Recent Advances and Future Perspectives. *Bioeng. Transl. Med.*

2021, e10261.

(79) Alkekhia, D.; Hammond, P. T.; Shukla, A. Layer-by-Layer Biomaterials for Drug Delivery. *Annu. Rev. Biomed. Eng.* **2020**, *22*, 1–24.

(80) Shi, B.; Zheng, M.; Tao, W.; Chung, R.; Jin, D.; Ghaffari, D.; Farokhzad, O. C. Challenges in DNA Delivery and Recent Advances in Multifunctional Polymeric DNA Delivery Systems. *Biomacromolecules* **2017**, *18*, 2231–2246.

(81) Li, N.; Zhao, L.; Qi, L.; Li, Z.; Luan, Y. Polymer Assembly: Promising Carriers as Co-Delivery Systems for Cancer Therapy. *Prog. Polym. Sci.* **2016**, *58*, 1–26.

(82) Campbell, R. A.; Angus-Smyth, A.; Yanez Arteta, M.; Tonigold, K.; Nylander, T.; Varga, I. New Perspective on the Cliff Edge Peak in the Surface Tension of Oppositely Charged Polyelectrolyte/Surfactant Mixtures. *J. Phys. Chem. Lett.* **2010**, *1*, 3021–3026.

(83) Campbell, R. A.; Yanez Arteta, M.; Angus-Smyth, A.; Nylander, T.; Noskov, B. A.; Varga, I. Direct Impact of Nonequilibrium Aggregates on the Structure and Morphology of Pdadmac/SDS Layers at the Air/Water Interface. *Langmuir* **2014**, *30*, 8664–8674.

(84) Braun, L.; Uhlig, M.; von Klitzing, R.; Campbell, R. A. Polymers and Surfactants at Fluid Interfaces Studied with Specular Neutron Reflectometry. *Adv. Colloid Interface Sci.* **2017**, *247*, 130–148.

(85) Uhlig, M.; Miller, R.; von Klitzing, R. Surface Adsorption of Sulfonated Poly(Phenylene Sulfone)/C_{14}TAB Mixtures and Its Correlation with Foam Film Stability. *Phys. Chem. Chem. Phys.* **2016**, *18*, 18414–18423.

(86) Uhlig, M.; Löhmann, O.; Vargas Ruiz, S.; Varga, I.; von Klitzing, R.; Campbell, R. A. New Structural Approach to Rationalize the Foam Film Stability of Oppositely Charged Polyelectrolyte/Surfactant Mixtures. *Chem. Commun.* **2020**, *56*, 952–955.

(87) Braun, L.; Uhlig, M.; Löhmann, O.; Campbell, R. A.; Schneck, E.; von Klitzing, R. Insights into Extended Structures and Their Driving Force: Influence of Salt on Polyelectrolyte/Surfactant Mixtures at the Air/Water Interface. *ACS Appl. Mater. Interfaces* **2022**, *14*, 27347–27359.

(88) Schulze-Zachau, F.; Braunschweig, B. Structure of Polystyrenesulfonate/Surfactant Mixtures at Air–Water Interfaces and Their Role as Building Blocks for Macroscopic Foam. *Langmuir* **2017**, *33*, 3499–3508.

(89) Schulze-Zachau, F.; Braunschweig, B. C_nTAB/Polystyrene Sulfonate Mixtures at Air–Water Interfaces: Effects of Alkyl Chain Length on Surface Activity and Charging State. *Phys. Chem. Chem. Phys.* **2019**, *21*, 7847–7856.

(90) Schnurbus, M.; Hardt, M.; Steinforth, P.; Carrascosa-Tejedor, J.; Winnall, S.; Gutfreund, P.; Schönhoff, M.; Campbell, R. A.; Braunschweig, B. Responsive Material and Interfacial Properties through Remote Control of Polyelectrolyte–Surfactant Mixtures. *ACS Appl. Mater. Interfaces* **2022**, *14*, 4656–4667.

(91) Llamas, S.; Guzmán, E.; Baghdadli, N.; Ortega, F.; Cazeneuve, C.; Rubio, R. G.; Luengo, G. S.

Adsorption of Poly(Diallyldimethylammonium Chloride)—Sodium Methyl-Cocoyl-Taurate Complexes onto Solid Surfaces. *Colloids Surfaces A Physicochem. Eng. Asp.* **2016**, *505*, 150–157.

(92) Llamas, S.; Fernández-Penã, L.; Akanno, A.; Guzmán, E.; Ortega, V.; Ortega, F.; Csaky, A. G.; Campbell, R. A.; Rubio, R. G. Towards Understanding the Behavior of Polyelectrolyte-Surfactant Mixtures at the Water/Vapor Interface Closer to Technologically-Relevant Conditions. *Phys. Chem. Chem. Phys.* **2018**, *20*, 1395–1407.

(93) Guzmán, E.; Fernández-Peña, L.; Ortega, F.; Rubio, R. G. Equilibrium and Kinetically Trapped Aggregates in Polyelectrolyte–Oppositely Charged Surfactant Mixtures. *Curr. Opin. Colloid Interface Sci.* **2020**, *48*, 91–108.

(94) Fernández-Peña, L.; Guzmán, E.; Leonforte, F.; Serrano-Pueyo, A.; Regulski, K.; Tournier-Couturier, L.; Ortega, F.; Rubio, R. G.; Luengo, G. S. Effect of Molecular Structure of Eco-Friendly Glycolipid Biosurfactants on the Adsorption of Hair-Care Conditioning Polymers. *Colloids Surfaces B Biointerfaces* **2020**, *185*, 110578.

(95) Schabes, B. K.; Altman, R. M.; Richmond, G. L. Come Together: Molecular Details into the Synergistic Effects of Polymer-Surfactant Adsorption at the Oil/Water Interface. *J. Phys. Chem. B* **2018**, *122*, 8582–8590.

(96) Schabes, B. K.; Richmond, G. L. Helping Strands: Polyelectrolyte Assists in Surfactant Assembly below Critical Micelle Concentration. *J. Phys. Chem. B* **2020**, *124*, 234–239.

(97) Tran, E.; Carpenter, A. P.; Richmond, G. L. Probing the Molecular Structure of Coadsorbed Polyethylenimine and Charged Surfactants at the Nanoemulsion Droplet Surface. *Langmuir* **2020**, *36*, 9081–9089.

(98) Goddard, E. D.; Gruber, J. V. *Principles of Polymer Science and Technology in Cosmetics and Personal Care*; Marcel Dekker, Inc.: Basel, Switzerland, 1999.

(99) Goddard, E. D. Polymer/Surfactant Interaction-Its Relevance to Detergent Systems. *J. Am. Oil Chem. Soc.* **1994**, *71*, 1–16.

(100) Green, A. J.; Littlejohn, K. A.; Hooley, P.; Cox, P. W. Formation and Stability of Food Foams and Aerated Emulsions: Hydrophobins as Novel Functional Ingredients. *Curr. Opin. Colloid Interface Sci.* **2013**, *18*, 292–301.

(101) Bureiko, A.; Trybala, A.; Kovalchuk, N.; Starov, V. Current Applications of Foams Formed from Mixed Surfactant-Polymer Solutions. *Adv. Colloid Interface Sci.* **2015**, *222*, 670–677.

(102) Szczepanowicz, K.; Bazylińska, U.; Pietkiewicz, J.; Szyk-Warszyńska, L.; Wilk, K. A.; Warszyński, P. Biocompatible Long-Sustained Release Oil-Core Polyelectrolyte Nanocarriers: From Controlling Physical State and Stability to Biological Impact. *Adv. Colloid Interface Sci.* **2015**, *222*, 678–691.

(103) Tiwari, S.; Bahadur, P. Modified Hyaluronic Acid Based Materials for Biomedical Applications. *Int. J. Biol. Macromol.* **2019**, *121*, 556–571.

(104) Taylor, D. J. F.; Thomas, R. K.; Penfold, J. Polymer/Surfactant Interactions at the Air/Water

Interface. *Adv. Colloid Interface Sci.* **2007**, *132*, 69–110.

(105) Piculell, L. Understanding and Exploiting the Phase Behavior of Mixtures of Oppositely Charged Polymers and Surfactants in Water. *Langmuir* **2013**, *29*, 10313–10329.

(106) Tonigold, K.; Varga, I.; Nylander, T.; Campbell, R. A. Effects of Aggregates on Mixed Adsorption Layers of Poly(Ethylene Imine) and Sodium Dodecyl Sulfate at the Air/Liquid Interface. *Langmuir* **2009**, *25*, 4036–4046.

(107) Lee, Y.-L.; Dudek, A.; Ke, T.-N.; Hsiao, F.-W.; Chang, C.-H. Mixed Polyelectrolyte−Surfactant Langmuir Monolayers at the Air/Water Interface. *Macromolecules* **2008**, *41*, 5845–5853.

(108) Goddard, E. D. Polymer-Surfactant Interaction Part I. Uncharged Water-Soluble Polymers and Charged Surfactants. *Colloids and Surfaces* **1986**, *19*, 255–300.

(109) Hunter, R. J. *Foundations of Colloid Science*, 2nd ed.; Oxford University Press: New York, 2001.

(110) Ritacco, H.; Kurlat, D. H. Critical Aggregation Concentration in the PAMPS (10%)/DTAB System. *Colloids Surfaces A Physicochem. Eng. Asp.* **2003**, *218*, 27–45.

(111) Jain, N.; Trabelsi, S.; Guillot, S.; McLoughlin, D.; Langevin, D.; Letellier, P.; Turmine, M. Critical Aggregation Concentration in Mixed Solutions of Anionic Polyelectrolytes and Cationic Surfactants. *Langmuir* **2004**, *20*, 8496–8503.

(112) Shirahama, K.; Tsujii, K.; Takagi, T. Free-Boundary Electrophoresis of Sodium Dodecyl Sulfate-Protein Polypeptide Complexes with Special Reference to SDS-Polyacrylamide Gel Electrophoresis. *J. Biochem.* **1974**, *75*, 309–319.

(113) Miyake, M. Recent Progress of the Characterization of Oppositely Charged Polymer/Surfactant Complex in Dilution Deposition System. *Advances in Colloid and Interface Science*. Elsevier B.V. January 1, 2017, pp 146–157.

(114) Lindman, B.; Antunes, F.; Aidarova, S.; Miguel, M.; Nylander, T. Polyelectrolyte-Surfactant Association—from Fundamentals to Applications. *Colloid J.* **2014**, *76*, 585–594.

(115) Mezei, A.; Mészáros, R.; Varga, I.; Gilányi, T. Effect of Mixing on the Formation of Complexes of Hyperbranched Cationic Polyelectrolytes and Anionic Surfactants. *Langmuir* **2007**, *23*, 4237–4247.

(116) Mészáros, R.; Thompson, L.; Bos, M.; Varga, I.; Gilányi, T. Interaction of Sodium Dodecyl Sulfate with Polyethyleneimine: Surfactant-Induced Polymer Solution Colloid Dispersion Transition. *Langmuir* **2003**, *19*, 609–615.

(117) Bodnár, K.; Fegyver, E.; Nagy, M.; Mészáros, R. Impact of Polyelectrolyte Chemistry on the Thermodynamic Stability of Oppositely Charged Macromolecule/Surfactant Mixtures. *Langmuir* **2016**, *32*, 1259–1268.

(118) Mezei, A.; Pojják, K.; Mészáros, R. Nonequilibrium Features of the Association between Poly(Vinylamine) and Sodium Dodecyl Sulfate: The Validity of the Colloid Dispersion Concept. *J. Phys. Chem. B* **2008**, *112*, 9693–9699.

(119) Bali, K.; Varga, Z.; Kardos, A.; Mészáros, R. Impact of Local Inhomogeneities on the

Complexation between Poly(Diallyldimethylammoniumchloride) and Sodium Dodecyl Sulfate. *Colloids Surfaces A Physicochem. Eng. Asp.* **2019**, *574*, 21–28.

(120) Bali, K.; Varga, Z.; Kardos, A.; Varga, I.; Gilányi, T.; Domján, A.; Wacha, A.; Bóta, A.; Mihály, J.; Mészáros, R. Effect of Dilution on the Nonequilibrium Polyelectrolyte/Surfactant Association. *Langmuir* **2018**, *34*, 14652–14660.

(121) Bodnár, K.; Szarka, K.; Nagy, M.; Mészáros, R. Effect of the Charge Regulation Behavior of Polyelectrolytes on Their Nonequilibrium Complexation with Oppositely Charged Surfactants. *J. Phys. Chem. B* **2016**, *120*, 12720–12729.

(122) Pojják, K.; Bertalanits, E.; Mészáros, R. Effect of Salt on the Equilibrium and Nonequilibrium Features of Polyelectrolyte/Surfactant Association. *Langmuir* **2011**, *27*, 9139–9147.

(123) Goddard, E. D.; Phillips, T. S.; Hannan, R. B. Water Soluble Polymer-Surfactant Interaction - Part I. *J. Soc. Cosmet. Chem.* **1975**, *26*, 461–475.

(124) Goddard, E. D.; Hannan, R. B. Cationic Polymer/Anionic Surfactant Interactions. *J. Colloid Interface Sci.* **1976**, *55*, 73–79.

(125) Goddard, E. D. Polymer/Surfactant Interaction: Interfacial Aspects. *J. Colloid Interface Sci.* **2002**, *256*, 228–235.

(126) Skoda, M. W. A. Recent Developments in the Application of X-Ray and Neutron Reflectivity to Soft-Matter Systems. *Curr. Opin. Colloid Interface Sci.* **2019**, *42*, 41–54.

(127) Maestro, A.; Gutfreund, P. In Situ Determination of the Structure and Composition of Langmuir Monolayers at the Air/Water Interface by Neutron and X-Ray Reflectivity and Ellipsometry. *Adv. Colloid Interface Sci.* **2021**, *293*, 102434.

(128) Staples, E.; Tucker, I.; Penfold, J.; Warren, N.; Thomas, R. K. Organization of Polymer−Surfactant Mixtures at the Air−Water Interface: Poly(Dimethyldiallylammonium Chloride), Sodium Dodecyl Sulfate, and Hexaethylene Glycol Monododecyl Ether. *Langmuir* **2002**, *18*, 5139–5146.

(129) Staples, E.; Tucker, I.; Penfold, J.; Warren, N.; Thomas, R. K.; Taylor, D. J. F. Organization of Polymer−Surfactant Mixtures at the Air−Water Interface: Sodium Dodecyl Sulfate and Poly(Dimethyldiallylammonium Chloride). *Langmuir* **2002**, *18*, 5147–5153.

(130) Taylor, D. J. F.; Thomas, R. K.; Penfold, J. The Adsorption of Oppositely Charged Polyelectrolyte/Surfactant Mixtures: Neutron Reflection from Dodecyl Trimethylammonium Bromide and Sodium Poly(Styrene Sulfonate) at the Air/Water Interface. *Langmuir* **2002**, *18*, 4748–4757.

(131) Bell, C. G.; Breward, C. J. W.; Howell, P. D.; Penfold, J.; Thomas, R. K. Macroscopic Modeling of the Surface Tension of Polymer−Surfactant Systems. *Langmuir* **2007**, *23*, 6042–6052.

(132) Bahramian, A.; Thomas, R. K.; Penfold, J. The Adsorption Behavior of Ionic Surfactants and Their Mixtures with Nonionic Polymers and with Polyelectrolytes of Opposite Charge at the Air-Water Interface. *J. Phys. Chem. B* **2014**, *118*, 2769–2783.

(133) Campbell, R. A.; Yanez Arteta, M.; Angus-Smyth, A.; Nylander, T.; Varga, I. Effects of Bulk

Colloidal Stability on Adsorption Layers of Poly(Diallyldimethylammonium Chloride)/Sodium Dodecyl Sulfate at the Air–Water Interface Studied by Neutron Reflectometry. *J. Phys. Chem. B* **2011**, *115*, 15202–15213.

(134) Ábrahám, Á.; Kardos, A.; Mezei, A.; Campbell, R. A.; Varga, I. Effects of Ionic Strength on the Surface Tension and Nonequilibrium Interfacial Characteristics of Poly(Sodium Styrenesulfonate)/Dodecyltrimethylammonium Bromide Mixtures. *Langmuir* **2014**, *30*, 4970–4979.

(135) Guzmán, E.; Fernández-Peña, L.; Akanno, A.; Llamas, S.; Ortega, F.; G. Rubio, R. Two Different Scenarios for the Equilibration of Polycation—Anionic Solutions at Water–Vapor Interfaces. *Coatings* **2019**, *9*, 438.

(136) Campbell, R. A.; Yanez Arteta, M.; Angus-Smyth, A.; Nylander, T.; Varga, I. Multilayers at Interfaces of an Oppositely Charged Polyelectrolyte/Surfactant System Resulting from the Transport of Bulk Aggregates under Gravity. *J. Phys. Chem. B* **2012**, *116*, 7981–7990.

(137) Ábraham, Á.; Campbell, R. A.; Varga, I. New Method to Predict the Surface Tension of Complex Synthetic and Biological Polyelectrolyte/Surfactant Mixtures. *Langmuir* **2013**, *29*, 11554–11559.

(138) Noskov, B. A.; Grigoriev, D. O.; Lin, S. Y.; Loglio, G.; Miller, R. Dynamic Surface Properties of Polyelectrolyte/Surfactant Adsorption Films at the Air/Water Interface: Poly(Diallyldimethylammonium Chloride) and Sodium Dodecyl sulfate. *Langmuir* **2007**, *23*, 9641–9651.

(139) Gao, Y.; Duc, L. T.; Ali, A.; Liang, B.; Liang, J. T.; Dhar, P. Interface-Induced Disassembly of a Self-Assembled Two-Component Nanoparticle System. *Langmuir* **2013**, *29*, 3654–3661.

(140) Angus-Smyth, A.; Bain, C. D.; Varga, I.; Campbell, R. A. Effects of Bulk Aggregation on PEI-SDS Monolayers at the Dynamic Air-Liquid Interface: Depletion Due to Precipitation versus Enrichment by a Convection/Spreading Mechanism. *Soft Matter* **2013**, *9*, 6103–6117.

(141) Gorter, E.; Grendel, F. On the Spreading of Proteins. *Trans. Faraday Soc.* **1926**, *22*, 477–483.

(142) Ughes, A. H.; Rideal, E. K. On Protein Monolayers. *Proc. R. Soc. London. Ser. A, Contain. Pap. a Math. Phys. Character* **1932**, *137*, 62–77.

(143) MacRitchie, F. Spread Monolayers of Proteins. *Adv. Colloid Interface Sci.* **1986**, *25*, 341–385.

(144) Muramatsu, M.; Sobotka, H. Studies on Unimolecular Layers of Modified Proteins. I. Bovine Serum Albumin and Its Acetyl Derivatives. *J. Colloid Sci.* **1963**, *18*, 625–635.

(145) Eaglesham, A.; Herrington, T. M.; Penfold, J. A Neutron Reflectivity Study of a Spread Monolayer of Bovine Serum Albumin. *Colloids and Surfaces* **1992**, *65*, 9–16.

(146) Miñones Conde, M.; Conde, O.; Trillo, J. M.; Miñones, J. How to Obtain a Well-Spread Monolayer of Lysozyme at the Air/Water Interfaces. *J. Colloid Interface Sci.* **2011**, *361*, 351–360.

(147) Campbell, R. A.; Ang, J. C.; Sebastiani, F.; Tummino, A.; White, J. W. Spread Films of Human Serum Albumin at the Air-Water Interface: Optimization, Morphology, and Durability. *Langmuir* **2015**, *31*, 13535–13542.

(148) López-Rodríguez, E.; Pérez-Gil, J. Structure-Function Relationships in Pulmonary Surfactant Membranes: From Biophysics to Therapy. *Biochim. Biophys. Acta - Biomembr.* **2014**, *1838*, 1568–1585.

(149) Castillo-Sánchez, J. C.; Cruz, A.; Pérez-Gil, J. Structural Hallmarks of Lung Surfactant: Lipid-Protein Interactions, Membrane Structure and Future Challenges. *Arch. Biochem. Biophys.* **2021**, *703*, 108850.

(150) Taylor, D. J. F.; Thomas, R. K.; Li, P. X.; Penfold, J. Adsorption of Oppositely Charged Polyelectrolyte/Surfactant Mixtures. Neutron Reflection from Alkyl Trimethylammonium Bromides and Sodium Poly(Styrenesulfonate) at the Air/Water Interface: The Effect of Surfactant Chain Length. *Langmuir* **2003**, *19*, 3712–3719.

(151) Fang, J.; Dennin, M.; Knobler, C. M.; Godovsky, Y. K.; Makarova, N. N.; Yokoyama, H. Structures of Collapsed Polysiloxane Monolayers Investigated by Scanning Force Microscopy. *J. Phys. Chem. B* **1997**, *101*, 3147–3154.

(152) Lipp, M. M.; Lee, K. Y. C.; Waring, A.; Zasadzinski, J. A. Fluorescence, Polarized Fluorescence, and Brewster Angle Microscopy of Palmitic Acid and Lung Surfactant Protein B Monolayers. *Biophys. J.* **1997**, *72*, 2783–2804.

(153) Alonso, C.; Alig, T.; Yoon, J.; Bringezu, F.; Warriner, H.; Zasadzinski, J. A. More Than a Monolayer: Relating Lung Surfactant Structure and Mechanics to Composition. *Biophys. J.* **2004**, *87*, 4188–4202.

(154) Hilles, H.; Monroy, F.; Bonales, L. J.; Ortega, F.; Rubio, R. G. Fourier-Transform Rheology of Polymer Langmuir Monolayers: Analysis of the Non-Linear and Plastic Behaviors. *Adv. Colloid Interface Sci.* **2006**, *122*, 67–77.

2 Project design

2.1 Aims and objectives

The aim of this PhD project is to gain precise control of the structures self-assembled in spread polyelectrolyte/surfactant films at the air/water interface prepared from the dissociation of aggregates under static and dynamic conditions with the ambition of tuning the film properties in three dimensions and with a focus on biocompatible systems.

PLL/SDS, PLA/SDS, PEI/SDS and NaPSS/DTAB systems were studied using the spreading methodology and various interfacial tools were used to characterise the dynamics, morphology, and structure of the films. The Langmuir technique is crucial in studying the dynamics of systems during compression/expansion cycles and the structure of films at specific compression ratios or pressures. Reflection techniques such as NR, ellipsometry, and BAM are also used to obtain information about the structure, composition, and morphology of the P/S films. NR is particularly helpful in understanding the dynamics of the systems and determining the structure of the films, while ellipsometry and BAM provides information about the homogeneity/heterogeneity and lateral morphology of the films.

There are three specific objectives of this project:

(1) Stepping towards biocompatible systems with a view to potential applications.
(2) Gaining three-dimensional control over film structures.
(3) Tuning the film properties according to the system and various external variables.

The first objective is to extend the spreading methodology to biocompatible systems for potential use in biomedical applications. For this reason, it was first decided to avoid the use of cationic surfactants, as they are highly cytotoxic because they disrupt the negatively charged membrane of cells.[1–3] Therefore, it is convenient to use cationic polyelectrolytes. Different cationic polyelectrolytes with interesting applications were identified such as chitosan,[4] tanfloc,[5,6] or polypeptides such as poly(L-histidine), PLL and PLA. The latter were chosen because of their numerous biomedical applications such as tissue engineering,[7–11] drug and gene delivery,[12–16] and cancer therapy.[17]

The second objective, which applies to all the systems studied, is to control the nucleation of ESs in P/S films, their stability and the ability of these systems to respread during expansion the excess of material expelled during compression. For this purpose, the behaviour of P/S films was studied during consecutive compression/expansion cycles to determine if there is ES formation, if the material is reincorporated during expansion, and if there is material loss from one cycle to the next. This will provide information on the ability of each system to regenerate the monolayer and provide a reproducible response to successive lateral compression/expansion. In addition, the stability of the ESs and their structure will be assessed in experiments at constant compression ratios or pressures. Any links to the structural dynamic properties of lung surfactant will be discussed.

The third objective is to evaluate the impact of three variables on the Marangoni spreading and dissociation of P/S aggregates and the properties of P/S films that have not been exploited before. First, tuning the PP/S interactions in the film and exploring links to any differences in the secondary structure created in bulk. Second, tuning the film morphology and mechanical properties of the films as a function of the maximum compression ratio reached. Third, tuning the P/S interactions in the film by controlling specific characteristics of the polyelectrolyte such as charge density, stiffness, or architecture. Fourth, tuning the aggregate charge, which has been demonstrated to have a significant influence on the properties of NaPSS/DTAB films.[18] This physicochemical insight will furnish the scientific community with a set of tools for tuning the structure and properties of P/S films.

Lastly, it is hoped that, through addressing the objectives described above, the project's insights into the ES formation and dynamics of P/S films, as well as the developed methodologies, may lead to a better understanding of the physicochemical processes that occur during the formation of lipid reservoirs in lung surfactant during respiration. The use of polypeptides is particularly interesting because the surfactant proteins SP-B, which is 30–45% α-helical, and SP-C, which is primarily α-helical, are essential for stabilising the formation of lipid reservoirs, minimising surface tension during exhalation and respreading the material back to the monolayer during expiration.[19]

2.2 Scope of the different studies

Study 1 (chapter 4) focuses on the dynamic behavior and structure of biocompatible spread PLL/SDS films aiming to precisely control the film structures. This work was published in August 2022 in letter format in Chemical Communications (current impact factor ~6).[20] For that reason, the materials and methods section is included in the supplementary information.

Study 2 (chapter 5) constitutes a comparative study of the properties of PLL/SDS and PLA/SDS films aiming to determine the impact of specific PP/S interactions and the secondary structure on the properties, structure, and morphology of the films. Different compression ratios were also applied to evaluate the possibility of tuning the mechanical behaviour and morphology of the films. This study was submitted in December to *Nanoscale* (current impact factor ~8) and at the time of the thesis submission is in peer review.[21]

Study 3 (chapter 6) focuses on effects of the pH subphase on the Marangoni spreading and dissociation of hyperbranched PEI/SDS aggregates, as well as on the properties of the resulting films. This work will be submitted to a physical chemistry journal such as *Langmuir* or *Colloids and Interfaces* (current impact factor ~4) shortly following some further refinement.

Finally, prior to this project, there were three published research articles that contained data on the new P/S films spread methodology involving the dissociation of aggregates.[18,22,23] Chapters 4, 5 and 6 provide the next stages of this development in article form.[20,21,24] As a result of this progress, and following publication of all three new papers, the intention of the co-authors is to publish the basis of the study 4 (chapter 7) as a review article with the intended platform being *Advances in Colloid and Interface Science* (current impact factor ~13). Editorial approval for the submission of this work to the journal has been secured. The following remarks provide context to the intentions of the co-authors and the inclusion of this fourth results chapter as part of this thesis, even though some of the figures comprise previously published data. The scope is that data from a range of techniques involving both undercharged and overcharged aggregates from

4 systems - NaPSS/DTAB, PLL/SDS, PEI/SDS at pH 4 and PEI/SDS at pH 10 - will be systematically compared and reviewed. It may be noted that, at the present time, the neutron data in figure 7.4C need to be re-recorded and those in 7.5A and 7.6A are missing; these data acquisitions are planned in 'easy access' time on the Fluid Interfaces Grazing Angles ReflectOmeter (FIGARO) gifted to us on 30th March 2023. The introduction to the review will be based on that of this thesis, so it is omitted in chapter 7 to avoid repetition, and as a review article there will be no Materials and Methods section. The main figures of results are presented with brief interpretations in the results section. Short summaries of the general behaviour of each system depending on the charge of the aggregates used help place the significance of the results into perspective. This chapter will form the basis of the intended comprehensive review planned for submission in the summer of 2023.

2.3 Contributions

The co-authors have made valuable contributions to the project by providing assistance with experiments, research design, proofreading the papers, and offering advice. For transparency, the contributions to the planning and execution, data acquisition, analysis and writing the manuscript of each chapter are outlined in this section. The following abbreviations will be used to refer to the person who have made specific contributions: Javier Carrascosa-Tejedor (JCT), Richard A. Campbell (RAC), Marina Efstratiou (ME), Laura M. Miñarro (LMM), Imre Varga (IV) Andrea Tummino (AT). In addition to the contributions to each chapter detailed below, JCT has written the proposals submitted to the Institut Laue-Langevin and ISIS for the neutron reflectometry beamtimes.

Chapter 4 is based on the study of PLL/SDS spread films carried out during this PhD. The main contributions to chapter 4 are detailed below:

- Planning and execution: JCT and RAC.
- Data acquisition: JCT except for Figure 4.1A acquired by ME.
- Analysis: JCT.
- Writing the manuscript: JCT (first draft) and all co-authors (revisions)

Chapter 5 is based on the results from the PLL/SDS system obtained by JCT in this PhD, and those obtained from the PLA/SDS system by LMM during her master's degree studies under the supervision of JCT. The main contributions to chapter 5 are detailed below:

- Planning and execution: JCT and RAC.
- Data acquisition: JCT and LMM (see Table 2.1 for more details).
- Analysis: JCT and LMM (see Table 2.1 for more details).
- Writing the manuscript: JCT (first draft) and all co-authors (revisions).

Table 2.1. Contributions to the acquisition and processing/analysis of the data used in the figures presented in chapter 5.

Figure	Panel	Acquisition	Processing/Analysis
5.1	*N/A*	JCT/LMM	JCT/LMM
5.2	*N/A*	*N/A*	*N/A*
5.3	A	JCT	JCT
	B	LMM	LMM
5.4	A, B and C	JCT	JCT
5.5	A, C and E	JCT	JCT
	B, D and F	LMM	LMM
5.6	A, C and E	JCT	JCT
	B, D and F	LMM	LMM
5.7	A, C and E	JCT	JCT
	B, D and F	LMM	LMM
Figures in the supplementary information	*N/A*	JCT	JCT

Chapter 6 is a continuation of the work done by AT on the PEI/SDS system from his PhD thesis (Eötvös-Lorànd University, Budapest, 2018). Although during his thesis AT studied the dynamics of these films using the Langmuir trough and applying the low-Q_Z approach, the data have been reanalysed in this thesis and the study has been completed applying electrophoretic mobility, ellipsometry, BAM and NR full-Q_Z measurements. The main contributions to chapter 6 are detailed below:

- Planning and execution: JCT, IV and RAC.
- Data acquisition: JCT and AT (see Table 2.2 for more details).
- Analysis: JCT and AT (see Table 2.2 for more details).

- Writing the manuscript: JCT and RAC (first draft) and all co-authors (revisions).

Table 2.2. Contributions to the acquisition and processing/analysis of the data used in the figures presented in chapter 6.

Figure	Panel	Acquisition	Processing/Analysis
6.1	A and B	IV	IV
6.2	A and B	AT	AT
6.3	A and B	AT	AT/JCT
6.4	A, and B	JCT	JCT
6.5	A, and B	JCT	JCT
6.6	A, B, C and D	AT/JCT	JCT
6.7	A, B, C and D	AT/JCT	JCT

Chapter 7 presents results obtained in the study of NaPSS/DTAB, PLL/SDS, PEI/SDS at pH 4 and PEI/SDS at pH 10 systems. The main contributions to chapter 7 are detailed below:

- Planning and execution: JCT and RAC.
- Data acquisition: JCT and AT.
- Analysis: JCT and AT.
- Writing the manuscript: JCT (first draft) and all co-authors (revisions).

Table 2.3. Contributions to the acquisition and processing/analysis of the data used in the figures presented in chapter 7.

Figure	Panel	Acquisition	Processing/Analysis
7.1	A	JCT	JCT
	B	JCT	JCT
	C	AT	AT
	D	AT	AT
7.2	A, B, C and D	JCT	JCT
7.3	A, B, C and D	JCT	JCT
7.4	A	AT	AT
	B	JCT	JCT
	C	AT	AT/JCT
	D	AT	AT/JCT
7.5	A	*N/A*	*N/A*
	B	JCT	JCT
	C	AT/JCT	AT/JCT
	D	AT/JCT	JCT

Figure	Panel	Acquisition	Processing/Analysis
7.6	A	*N/A*	*N/A*
	B	JCT	JCT
	C	AT/JCT	AT/JCT
	D	AT/JCT	JCT
7.7	A and B	JCT	JCT
	C and D	AT	AT
7.8	A, B, C and D	JCT	JCT
7.9	A, B, C and D	JCT	JCT
7.10	A	AT	AT
	B	JCT	JCT
	C	AT	AT/JCT
	D	AT	AT/JCT
7.11	A	JCT	JCT
	B	JCT	JCT
	C	AT/JCT	JCT
	D	AT/JCT	JCT
7.12	A	JCT	JCT
	B	JCT	JCT
	C	AT/JCT	AT/JCT
	D	AT/JCT	JCT

2.4 Experiments at large scale facilities

The use of large scale facilities has been essential in achieving the objectives of this thesis. The project made use of two neutron reflectometers: FIGARO at the Institut Laue-Langevin (Grenoble, France) and INTER at the ISIS Rutherford Appleton Laboratory (Didcot, United Kingdom). These experiments are very expensive and heavily labour-intensive, requiring the collaboration of several researchers. All contributors including local contacts are/will be credited as co-authors on resulting publications.

The following is a list of the NR experiments in which the data presented in this thesis were collected. Details include the instrument used, systems under study, dates of the experiment and working team.

- #9-12-461 on FIGARO at the ILL, NaPSS/DTAB and PEI/SDS films, 5 days in 2016 and 2017
  https://doi.ill.fr/10.5291/ILL-DATA.9-12-461
  Richard Campbell, Bence Feher, Andrea Tummino & Imre Varga
- #9-10-1433 on FIGARO at the ILL, NaPSS/DTAB films, 8 days in 2017 and 2018

https://doi.ill.fr/10.5291/ILL-DATA.9-10-1433

Richard Campbell, Bence Feher, Attila Kardos, Federica Sebastiani, Jutta Toscano, Andrea Tummino & Imre Varga

- RB1820556 on INTER at ISIS, PEI/SDS films, 2 days in 2018

  https://doi.org/10.5286/ISIS.E.99690519

  Richard Campbell, Andrea Tummino, Maximilian Skoda & Imre Varga
- #9-12-614 on FIGARO at the ILL, PLL/SDS films, 3 days in 2020

  https://doi.ill.fr/10.5291/ILL-DATA.9-12-614

  Armando Maestro, Andrea Tummino & Javier Carrascosa-Tejedor
- #9-12-631 on FIGARO at the ILL, PLL/SDS films, 2 days in 2021

  https://doi.ill.fr/10.5291/ILL-DATA.9-12-631

  Armando Maestro, Andreas Santamaria, & Javier Carrascosa-Tejedor
- #9-10-1656 on FIGARO at the ILL, PLL/SDS films, 2 days in 2021

  https://doi.ill.fr/10.5291/ILL-DATA.9-10-1656

  Armando Maestro, Andreas Santamaria & Javier Carrascosa-Tejedor
- RB2210138 on INTER at ISIS, PLL/SDS films, 3 days in 2022

  https://doi.org/10.5286/ISIS.E.RB2210138

  Richard Campbell, Marina Efstratiou, Maximilian Skoda & Javier Carrascosa-Tejedor
- RB2200007 on INTER at ISIS, PEI/SDS films, 1 day in 2022

  https://doi.org/10.5286/ISIS.E.RB2210138

  Richard Campbell, Marina Efstratiou, Maximilian Skoda & Javier Carrascosa-Tejedor

2.5 References

(1) Vlachy, N.; Touraud, D.; Heilmann, J.; Kunz, W. Determining the Cytotoxicity of Catanionic Surfactant Mixtures on HeLa Cells. *Colloids Surfaces B Biointerfaces* **2009**, *70*, 278–280.

(2) Manaargadoo-Catin, M.; Ali-Cherif, A.; Pougnas, J. L.; Perrin, C. Hemolysis by Surfactants — A Review. *Adv. Colloid Interface Sci.* **2016**, *228*, 1–16.

(3) Zhou, C.; Wang, Y. Structure–Activity Relationship of Cationic Surfactants as Antimicrobial Agents. *Curr. Opin. Colloid Interface Sci.* **2020**, *45*, 28–43.

(4) Rinaudo, M. Chitin and Chitosan: Properties and Applications. *Prog. Polym. Sci.* **2006**, *31*, 603–632.

(5) Sánchez-Martín, J.; Beltrán-Heredia, J.; Solera-Hernández, C. Surface Water and Wastewater Treatment Using a New Tannin-Based Coagulant. Pilot Plant Trials. *J. Environ. Manage.* **2010**, *91*, 2051–2058.

(6) Sabino, R. M.; Mondini, G.; Kipper, M. J.; Martins, A. F.; Popat, K. C. Tanfloc/Heparin Polyelectrolyte Multilayers Improve Osteogenic Differentiation of Adipose-Derived Stem Cells on Titania Nanotube Surfaces. *Carbohydr. Polym.* **2021**, *251*, 117079.

(7) Tang, Z.; Wang, Y.; Podsiadlo, P.; Kotov, N. A. Biomedical Applications of Layer-by-Layer Assembly: From Biomimetics to Tissue Engineering. *Adv. Mater.* **2006**, *18*, 3203–3224.

(8) Hammond, P. T. Building Biomedical Materials Layer-by-Layer. *Mater. Today* **2012**, *15*, 196–206.

(9) Nettles, D. L.; Chilkoti, A.; Setton, L. A. Applications of Elastin-Like Polypeptides in Tissue Engineering. *Adv. Drug Deliv. Rev.* **2010**, *62*, 1479–1485.

(10) Stuart, M. A. C.; Huck, W. T. S.; Genzer, J.; Müller, M.; Ober, C.; Stamm, M.; Sukhorukov, G. B.; Szleifer, I.; Tsukruk, V. V.; Urban, M.; Winnik, F.; Zauscher, S.; Luzinov, I.; Minko, S. Emerging Applications of Stimuli-Responsive Polymer Materials. *Nat. Mater.* **2010**, *9*, 101–113.

(11) Zarrintaj, P.; Ghorbani, S.; Barani, M.; Pal Singh Chauhan, N.; Khodadadi Yazdi, M.; Reza Saeb, M.; Ramsey, J. D.; Hamblin, M. R.; Mozafari, M.; Mostafavi, E. Polylysine for Skin Regeneration: A Review of Recent Advances and Future Perspectives. *Bioeng. Transl. Med.* **2021**, e10261.

(12) Shi, B.; Zheng, M.; Tao, W.; Chung, R.; Jin, D.; Ghaffari, D.; Farokhzad, O. C. Challenges in DNA Delivery and Recent Advances in Multifunctional Polymeric DNA Delivery Systems. *Biomacromolecules* **2017**, *18*, 2231–2246.

(13) Alkekhia, D.; Hammond, P. T.; Shukla, A. Layer-by-Layer Biomaterials for Drug Delivery. *Annu. Rev. Biomed. Eng.* **2020**, *22*, 1–24.

(14) Manouchehri, S.; Zarrintaj, P.; Saeb, M. R.; Ramsey, J. D. Advanced Delivery Systems Based on Lysine or Lysine Polymers. *Mol. Pharm.* **2021**, *18*, 3652–3670.

(15) Pack, D. W.; Hoffman, A. S.; Pun, S.; Stayton, P. S. Design and Development of Polymers for Gene Delivery. *Nat. Rev. Drug Discov.* **2005**, *4*, 581–593.

(16) González-Aramundiz, J. V.; Lozano, M. V.; Sousa-Herves, A.; Fernandez-Megia, E.; Csaba, N. Polypeptides and Polyaminoacids in Drug Delivery. *Expert Opin. Drug Deliv.* **2012**, *9*, 183–201.

(17) Li, N.; Zhao, L.; Qi, L.; Li, Z.; Luan, Y. Polymer Assembly: Promising Carriers as Co-Delivery Systems for Cancer Therapy. *Prog. Polym. Sci.* **2016**, *58*, 1–26.

(18) Tummino, A.; Toscano, J.; Sebastiani, F.; Noskov, B. A.; Varga, I.; Campbell, R. A. Effects of Aggregate Charge and Subphase Ionic Strength on the Properties of Spread Polyelectrolyte/Surfactant Films at the Air/ Water Interface under Static and Dynamic Conditions. *Langmuir* **2018**, *34*, 2312–2323.

(19) López-Rodríguez, E.; Pérez-Gil, J. Structure-Function Relationships in Pulmonary Surfactant Membranes: From Biophysics to Therapy. *Biochim. Biophys. Acta - Biomembr.* **2014**, *1838*, 1568–1585.

(20) Carrascosa-Tejedor, J.; Santamaria, A.; Tummino, A.; Varga, I.; Efstratiou, M.; Lawrence, M. J.; Maestro, A.; Campbell, R. A. Polyelectrolyte/Surfactant Films: From 2D to 3D Structural Control. *Chem. Commun.* **2022**, *58*, 10687–10690.

(21) Carrascosa-Tejedor, J.; Miñarro, L. M.; Efstratiou, M.; Varga, I.; Skoda, M. W. A.; Gutfreund, P.; Maestro, A.; Lawrence, M. J.; Campbell, R. A. Design of Biocompatible Films with Controllable Properties and Morphology through Specific Polypeptide/Surfactant Interactions. *Nanoscale,* in peer review.

(22) Campbell, R. A.; Tummino, A.; Noskov, B. A.; Varga, I. Polyelectrolyte/Surfactant Films Spread from Neutral Aggregates. *Soft Matter* **2016**, *12*, 5304–5312.

(23) Varga, I.; Campbell, R. A. General Physical Description of The Behavior of Oppositely Charged Polyelectrolyte/Surfactant Mixtures at the Air/Water Interface. *Langmuir* **2017**, *33*, 5915–5924.

(24) Carrascosa-Tejedor, J.; Tummino, A.; Feher, B.; Kardos, A.; Efstratiou, M.; Skoda, M. W. A.; Gutfreund, P.; Maestro, A.; Lawrence, M. J.; Campbell, R. A.; Varga, I. Effects of Macromolecular Charge Density on the Properties of Spread Hyperbranched Polyelectrolyte/Surfactant Films at the Air/Water Interface. Manuscript in progress.

3 Materials and methods

3.1 Materials

15–30 kDa PLL hydrobromide powder, 5–15 kDa PLA hydrochloride powder, 17 kDa NaPSS, 750 kDa hyperbranched PEI solution (50% in water), SDS, sodium dodecyl-d25 sulfate (d-SDS), DTAB, ethanol (≥99.8%), acetone (≥99.5%), D_2O (99.9% D), NaOH and HCl were purchased from Sigma Aldrich. Dodecyl-d25-trimethylammonium bromide (d-DTAB) was purchased from CDN Isotopes. PLL, NaPSS, PEI, d-SDS, d-DTAB and all solvents were used as received. SDS and DTAB were recrystallised twice in ethanol and 4:1 acetone:ethanol mixture, respectively, followed by drying under vacuum. Ultra-pure water was generated by passing deionised water through a Milli-Q unit (total organic content ≤ 4 ppb, resistivity = 18 MΩ·cm).

3.2 Sample preparation

Stocks of 200 ppm by mass PLL, PLA and NaPSS solutions were prepared by dissolving the powder or solution in water and rotating the vial for a few hours. A stock solution of 2000 ppm PEI was prepared by diluting the original PEI solution in water and rotating the vial for a few hours. This solution was further diluted in water to a concentration of 200 ppm. Stock solutions of SDS 10 mM and DTAB 20 mM were prepared in H_2O and diluted to the required concentration for each experiment.

Fresh mixtures of P/S aggregates were always prepared by mixing the same volume of the polyelectrolyte and surfactant solutions at double their final concentrations. The mixtures were immediately used use to limit the growth of large aggregates prior to the experiment. NaPSS/DTAB and PEI/SDS mixtures were prepared by rapidly mixing the solutions under continuous stirring for 3–5 s. PLL/SDS mixtures were prepared by rapidly adding an aliquot of SDS to a vessel containing the aliquot of PLL while magnetic stirring was maintained for 3–5 s.

3.3 Techniques

3.3.1 Electrophoretic mobility/ζ-potential

When particles present in a colloidal dispersion adsorb charged species or ionisation of their surface groups occurs, they acquire a net surface charge that strongly affects the physicochemical properties of the system.[1] Knowing the charge of P/S aggregates in solution is an important tool for understanding these systems because it can determine whether the aggregates form a one-phase or two-phase region.[2]

The application of an electric field to a solution of charged particles causes an acceleration of these towards the oppositely charged electrode. At the same time, they experience an opposite viscous force that increases linearly with the velocity of the particles. Once the equilibrium between these two forces is reached, particles move at a constant velocity. Then, the electrophoretic mobility, μ, can be defined as the velocity of the particle, v, per unit of the applied electric field, E, which depends on the charge of the particles, Q, their radius, a, and the viscosity of the medium, η.

$$\mu = \frac{v}{E} = \frac{Q}{6\pi\eta a} \tag{3.1}$$

The zeta potential, ζ, is generally used to characterise the charge of particles in solution. It cannot be directly measured and it is deduced from μ:[3]

$$\mu = \frac{\varepsilon_0 \varepsilon_m \zeta}{\eta} \tag{3.2}$$

where ε_0 and ε_m are the electric permittivity of vacuum and the solvent, respectively.

In this study, the electrophoretic mobility and zeta-potential of freshly-prepared P/S solutions were determined using a Zetasizer Nano ZS90 (Malvern Instruments Ltd., U.K.) on the basis of laser doppler velocimetry and phase analysis light scattering techniques (M3-PALS). Measurements were performed with a constant concentration of P 100 ppm by varying the S concentration in a range where the transition from undercharged to overcharged aggregates through charge neutrality was observed.

3.3.2 Surface tension measurements

Surface tension is a thermodynamic property defined as the energy required to increase the area of an interface divided by its area (equation 1.1 and 1.2). Its reduction is caused by lowering of the interfacial free energy through the presence of surface-active species. There are different techniques that can be used to characterise the behaviour of amphiphilic molecules at interfaces and determine surface tension.[4–8] Among the different measurement techniques are: i) force methods that use a microbalance, and ii) shape methods that use a droplet or bubble.[8]

The two main techniques based on measurements with a microbalance used are Wilhelmy plate and Noüy Ring methods. In this project, the Wilhelmy method has been used. Figure 3.1A shows a schematic representation of this method. A plate made of filter paper (or platinum) with a well-defined geometry is partially immersed at the air/water interface. Consequently, this plate experiences different forces: surface tension (the force exerted by the liquid meniscus on the plate), gravity and the Archimedes pull. The total force (*F*) can be defined as:

$$F = 2(w + t)\,\gamma\,cos\Phi + \left(\rho_p wlt\right)g - (\rho_l wht)g \tag{3.3}$$

where ρ_P and ρ_l are the density of the plate and the liquid, respectively, *g* is the gravitational force, ϕ is the contact angle and *w*, *l*, *t* and *h* are the width, the length, the thickness and the immersed depth of the plate, respectively. When the plate is maintained at a constant immersion during the whole experiment, the contribution of gravity and the Archimedes pull will also be constant and therefore equation 3.3 can be reduced to:

$$F = 2(w + t)\,\gamma\,cos\Phi \tag{3.4}$$

If the plate is completely wetted $\phi = 0$, which in turn makes the term $\cos\phi = 1$. The complete wetting of the plate is important to ensure a near-zero contact angle.

The Langmuir technique allows one to study the phase and mechanical behaviour of thin films at the air/water interface when applying increasing lateral pressure, and has been used extensively to characterise Langmuir films formed by highly insoluble molecules such as lipids.[6,9] The method uses a Wilhelmy plate to measure surface pressure (Π), which is defined as the difference between the surface tension of pure water (γ_0) and that of the film (γ).

$$\Pi = \gamma_0 - \gamma \tag{3.5}$$

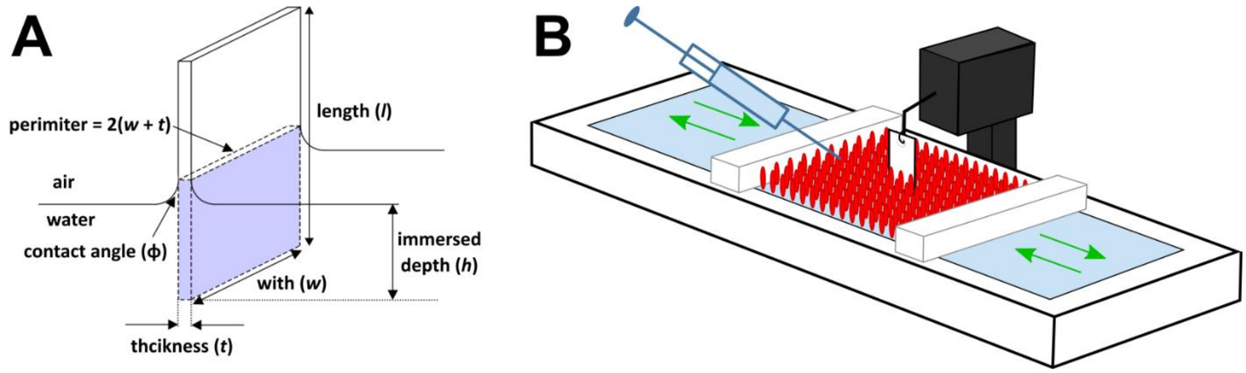

Figure 3.1. (A) Schematic representation of the Wilhelmy plate method adapted from Martin and Szablewski, 2001.[10] (B) Schematic representation (not to scale) of a Langmuir trough. The green arrows indicate the direction of barriers movement during compression or expansion. Adapted from Larsen, 2014.[11]

The determination of the surface pressure as a function of surface area (*A*) at constant temperature provides a Π–*A* isotherm, which provides information about the phase behaviour of the film. Π–*A* isotherms can also be used to determine the phase diagram of binary mixtures at the interface. Typically for insoluble films, the Π–*A* isotherm shows different regions: i) when no external pressure is applied , the film is in a so-called two-dimensional gas state; ii) compression of the film (i.e., area reduction) causes interactions between molecules, resulting in an increase in Π and a series of two-dimensional transformations as a consequence of the increasing interactions between molecules; iii) eventually, at very low areas, the monolayer can collapse into three-dimensional structures causing a sharp decrease in Π. The collapse is related to the maximum Π of the monolayer, and different mechanisms exist depending on the nature and structure of the film.[12] It can be reversible or irreversible depending on whether the excess material expelled from the surface monolayer after the collapse is reincorporated upon expansion or not. Finally, surface compression/expansion isotherms are generated by repeatedly compressing then expanding the same film, and hysteresis is the term used to refer to any deviation in data recorded during compression and expansion. In this context, lung surfactant films have received a lot of attention due to their reproducible dynamics over successive cycles, collapse mechanism and hysteresis, which, along with the ability to reach high Π, is considered a good marker of lung surfactant activity.[12–16] Isotherms are typically plotted as a function of the area per molecule. This is only possible, however, if the molecules are highly insoluble, such as lipids, and the number of molecules spread across the interface is known. Since two-component mixtures are used in this project and not all of the spreading material remains at the interface, the isotherms are presented as a function of the total *A*, i.e., the area of the trough in cm^2.

The Langmuir trough was used in this work to investigate the dynamic response of P/S films at the air/water interface during compression/expansion cycles, as well as to assess the stability of the P/S films when they are compressed at a given compression ratio or when Π control is used to keep the film at a given Π. All the troughs were equipped with two barriers that move symmetrically while Π is recorded as a function of *A* or time. Before filling them with water, they were thoroughly cleaned with soap, ethanol, and Milli-Q water. Subsequently, the P/S solution was spread dropwise across all the air/water interface. After the stabilisation of the signal (typically less than 10 min), the variation of Π was recorded during successive compression/expansion cycles or compression and stabilisation at a given *A* or Π.

This technique was coupled to the various reflection techniques described in the following sections. Langmuir troughs of different sizes were used for this purpose according to the specific requirements of each instrument and experiment. Troughs with a large maximum *A* were required for studies at high compression ratios to avoid barriers blocking the laser. The spread volume of the P/S aggregate solution was chosen so that the experiment would start with a surface monolayer to study the possible surface monolayer/ESs transitions. The spread volume, as well as the speed of the barriers, were scaled from one experiment to the other considering the dimensions of the different troughs used. To compare the results obtained in those studies in which different troughs were used, the Π–*A* isotherms are plotted as a function of A/A_0.

Table 3.1. Troughs used in this work indicating the maximum area and the techniques coupled to them.

Trough	Maximum *A* (cm^2)	Coupled techniques
Kibron G1	166.4	Ellipsometry and BAM
Kibron G2	280	Ellipsometry and BAM using high compression ratios
Nima FIGARO	265	NR
Nima 721BAM	710	Ellipsometry and BAM using high compression ratios

3.3.3 Ellipsometry

Ellipsometry is a non-destructive optical technique based on the polarisation changes that light undergoes upon reflection at an interface.[17] When light interacts with an interface between two media that have different refractive indices, one part is refracted and the other reflected. The polarisation changes of the incident and reflected beams are defined by the parallel (*p*) and perpendicular (*s*) components of the electric field. These changes are characterised by the reflection coefficients r_p and r_s, which are defined by the following equation:

$$r_p = |r_p|e^{i\delta_p} \tag{3.6}$$

$$r_s = |r_s|e^{i\delta_s} \tag{3.7}$$

where $|r_p|$ and $|r_s|$ are the amplitudes of the reflection coefficients, and δ_p and δ_s the phase difference between the reflected and incident waves of *p*- and *s*-polarisation, respectively. The ellipsometric angles Δ and Ψ can be directly obtained in experimental measurements of ellipsometry. Δ is defined by the phase shift, $\Delta = \delta_p - \delta_s$, and Ψ is defined by the ratio of amplitudes, $\tan \Psi = |r_p|/|r_s|$. Thus, the ellipticity (ρ) can be defined as:

$$\rho = \frac{r_p}{r_s} = tan\Psi e^{i\Delta} \tag{3.8}$$

The main components of an ellipsometer are shown in Figure 3.2. A well collimated beam is generated by a monochromatic light source, usually a laser. Next, there are a series of optical elements that are indispensable for determining the polarisation changes. First, the incident beam passes through a polariser that generates linearly polarised light and then it passes through a compensator that introduces a phase difference between the *p* and *s* components producing elliptically polarised light. The interaction of light with the optical system under study causes a polarisation change which is measured by a variable polarisation analyser followed by a detector.

Ellipsometry is widely used in the study of surfaces and thin films, both at fluid and solid interfaces.[18–25] When ellipsometry is used with solid interfaces, the ellipsometric angles can be modelled to determine the thickness and refractive index of the film under study.[26–28] If the variation of the refractive index with the concentration (*dn/dc*) of the system is also known, de

Feijter's equation can be used to calculate the surface excess.[21] For non-absorbing thin films, i.e. thickness ≤ $2\pi/\lambda$ according to the 1st order approximation of Drude,[29] at the air/water interface only Δ is highly sensitive to the presence of material at the interface as the changes in Ψ are relatively small. For this reason, many studies at the air/water interface do not include the values of Ψ in the data analysis. In this case, the surface excess can be calculated from the increment of Δ considering de Feijter's equation[21] and a suitable model: an "oil-like model" assuming that there are changes in the thickness of the film at constant density (i.e., at a constant refractive index), or a "particle like model" assuming that there are changes in the layer density at constant thickness (more information can be found in the supporting information of Campbell et al.[30]). Although this technique can be used to obtain quantitative information, it lacks accuracy due to dependence of Δ on anisotropy.[31,32] However, the high sensitivity of this technique allows one to monitor the kinetics of adsorption processes[21,33,34] and changes in the amount of material present at an interface with high precision.[23,30,35] Indeed, calibrating ellipsometry data against NR allows for effective modelling and ellipsometry can act as one contrast to model with NR data.[36,37]

In this project, the variation of $d\Delta = \Delta_{P/S}$ (for the P/S film) – Δ_{water} (for pure water which approximately accounts for the contribution of surface roughness) are reported as an approximately proportional measure of the surface excess. All the experiments were performed at a fixed angle of incidence (50 or 51°) close to the Brewster angle of water (53.1°, see section 3.3.4 for more information about the Brewster angle) where the changes in delta caused by the presence of a film at the interface are maximised. The variation of $d\Delta$ is used as a qualitative indication for the evolution of P/S films during dynamics to motivate and complement data from NR experiments. Nevertheless, Because of the relatively small probed area (~1 mm^2) and fast acquisition time (~5 s), inhomogeneities in the interface on the micrometer scale manifest themselves as temporal fluctuations when they pass through the area illuminated by the laser spot.[23,38–40] This makes ellipsometry an ideal technique to do time/spatial resolved experiments. This information would typically not be resolved by techniques like NR that are space-averaged over the centimetre length scale.[24]

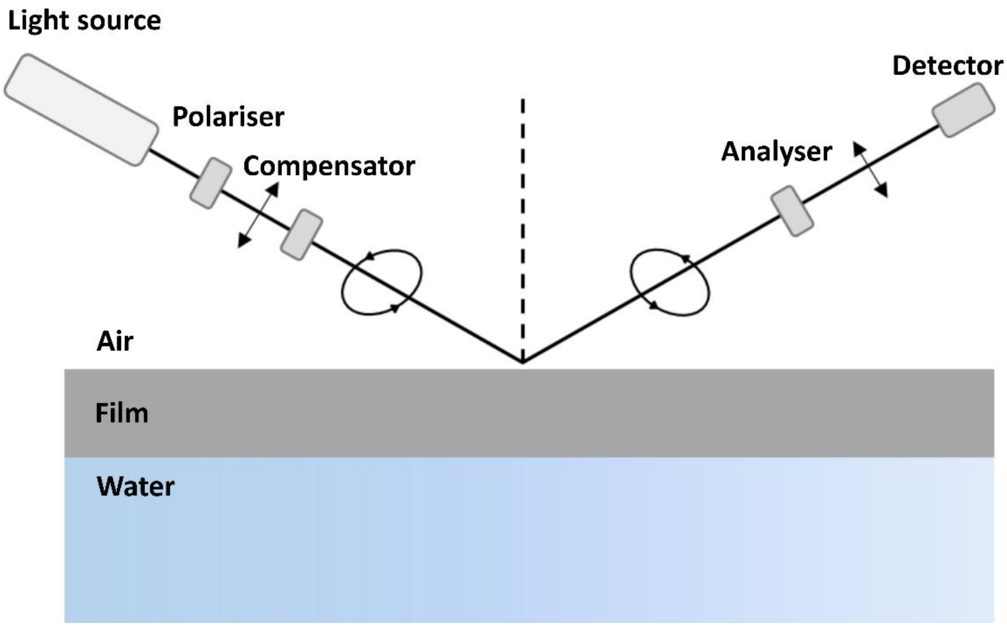

Figure 3.2. Schematic representation of the main components of an ellipsometer and the principles of an ellipsometry measurement at the air/water interface: Elliptically polarised light is reflected at the interface and undergoes a polarisation change that is measured by the analyser followed by a detector.

Ellipsometry experiments were performed using two different ellipsometers coupled to the Langmuir trough technique. A black plate was placed at the bottom of the trough to adsorb the refracted light and prevent it from reaching the detector. A Picometer Light ellipsometer (Beaglehole Instruments, New Zealand) was used in the laboratories of the Partnership for Soft Condensed Matter, at the Institut Laue-Langevin. An angle of incidence of 51° and a data acquisition rate of 0.2 Hz were used. An EP4 ellipsometer (Accurion, Germany) equipped with a blue diode laser with a wavelength of λ = 489.2 nm was used at the Pharmacy and Optometry Department of the University of Manchester. An angle of incidence of 50° and a data acquisition rate of 0.1 Hz were used.

3.3.4 Brewster angle microscopy

BAM is a direct and non-destructive imaging technique based on the principles of light reflection explained in section 3.3.3. BAM was first proposed in 1991 as a direct observation method of first-order phase transitions and two-dimensional domains in monolayers without relying on fluorescent probes.[41,42] The latter is one of the main advantages of using BAM over fluorescence microscopy, as fluorescent probes can modify the properties of the system and can be rejected by highly ordered phases.[43] As a result, the use of BAM in conjunction with a Langmuir trough to facilitate the measurement at the air/water interface has become a widely used technique to characterise fluid monolayers at the air/water interface. The shape of the condensed phase domains in lipid monolayers, their inner texture and the lateral inhomogeneity can be visualised.[41,42,44–46] BAM has shown the importance of the headgroups in lipid monolayer structure[47] and can provide quantitative structural information.[48] It has been used in the study of the interaction of Langmuir monolayers with peptides,[49,50] proteins[51–53] or nanoparticles.[54,55] Specifically, this technique has also proven useful in the study of P/S mixtures at the air/water interface,[56–58] and two-dimensional into three-dimensional transitions in different systems.[23,59,60]

Although the measurement principles and setup are very similar to those of ellipsometry, there are several notable differences. This technique is based on the principle that when *p*-polarised light is directed at an ideal interface (with no surface roughness) at a specific angle known as the Brewster angle, θ_B, the reflected light is negligible. The following equation defines θ_B:

$$\theta_B = tan^{-1}\left(\frac{n_2}{n_1}\right) \tag{3.9}$$

where n_1 is the refractive index of the medium through which the incident beam propagates and n_2 is the refractive index of the substrate. Thus, for the air/water interface, $\theta_B = \tan^{-1}(1.33/1) = 53.1^o$. According to equation 3.9, if there is a film at the interface with a refractive index different from that of either medium, the Brewster angle conditions are not satisfied, resulting in the reflection of some of the *p*-polarised light.

BAM was used in this work to characterise the lateral organisation and the homogeneity/inhomogeneity of P/S films on the micrometre scale. It should be noted that, due to its micrometric resolution, BAM enables the detection of micrometric domains, but not individual nanometric P/S aggregates. An Accurion Nanofilm EP3 Brewster angle microscope (Germany) equipped with a Nd:YAG laser (λ = 532 nm), a 10x objective and a charge coupled device (CCD) detector was used in this project. A laser and a polariser are used to generate the *p*-polarised incident beam. As in ellipsometry, a black plate was placed at the bottom of the trough to prevent refracted light from reaching the detector. Because only a small portion of the illuminated area has the correct focal distance, a microscopic lens that moves toward and away from the interface is used to correct the focal distance of the entire detected area. BAM images are recorded using a CCD camera. In addition, the use of an anti-vibration table is required because otherwise, the image intensity would fluctuate significantly, making adjusting the focal distance difficult. The spreading of the P/S aggregates and subsequent formation of a surface monolayer causes a change in the refractive index at the interface, resulting in light reflection. Images from the same experiment were recorded using the same laser intensity and gain with no background subtraction. As a result, a homogeneous surface monolayer can be visualised as a grey image and any additional material that thickens the film will contribute to the reflected light. Compression in the surface monolayer region is typically characterised by a continuous increase in intensity as the compression proceeds. When the surface monolayer collapses, material expulsion from the monolayer can result in the formation of ESs, which cause light reflection at another interface, such that they will be observed as brighter regions in the image. Depending on the system, ESs may appear as discrete bright patches on the µm-scale distributed across the interface or as bright linear regions that may be related to film folding.

3.3.5 Neutron reflectometry

To understand the principles of this technique, how to use it, the information it provides and how to analyse the data obtained, it is necessary to understand how neutrons interact with matter. For this reason, the basic principles of neutron scattering are covered in section 3.3.5.1 before moving on to the most widely used application of neutron reflectometry, specular NR. Next, the two approaches used in this project to study P/S films at the air/water interface will be explained. Finally, a brief description of the neutron reflectometers used in this work is included in section 3.3.5.5.

3.3.5.1 Neutron scattering

Neutrons are subatomic particles with specific properties that make them effective probes for studying materials and their properties. As their name implies, they are neutral particles that, unlike X-rays, interact with the nuclei of atoms rather than with the electronic cloud. This property is responsible for some of the most important advantages of this type of radiation.

Neutrons can penetrate deep into matter because for most materials the neutron capture probability (absorption) is very small, allowing the study of materials that are opaque to other types of radiation, the determination of the internal structure or the study of samples buried in complex sample environments. Neutrons are non-destructive, allowing the samples to be studied multiple times or using long exposure times without altering their structure or composition.

The strength of the coherent interaction of neutrons with nuclei is determined by the coherent scattering cross section, which can be defined as the probability of a neutron being scattered by nuclei without losing its phase. It can be calculated as follows:

$$\sigma = 4\pi s^2 \tag{3.10}$$

where s is the coherent scattering length of the nucleus. This magnitude, which has been experimentally determined for the majority of elements, does not vary monotonically across the periodic table and can take either positive or negative values, with negative values accounting for a 180° phase shift after the scattering event. Moreover, the scattering length can vary strongly among different isotopes of the same element. The latter is particularly important when studying hydrogen-containing materials because hydrogen/deuterium substitution allows one to vary the scattering contrast of a sample (or part of a sample).[61] This is possible thanks to the very different scattering lengths of hydrogen, -3.74×10^{-5} Å, and deuterium, 6.67×10^{-5} Å. In addition, this can also be exploited to tune the scattering contrast of the solvent by mixing H_2O and D_2O which, in conjunction with hydrogen/deuterium substitution in molecules, allows highlighting or hiding specific parts of the structure, obtaining information of a region or phenomenon of interest. We will return to this point later.

The interaction of neutrons with nuclei can be inelastic, when there is an exchange of energy during the scattering process, or elastic, when the energy of the incident and the scattered neutrons is the same and only their direction changes. Since NR has been used in this project, the following description of neutron scattering considers only elastic scattering events.

The particle-wave duality is a fundamental principle of quantum mechanics that describes the behaviour of subatomic particles as both particles with a definite position and momentum, p, and waves that propagate and interfere with other waves. As a result, using the de Broglie equation one can relate the wavelength of a particle to its mass, m, (1.6749×10^{-27} kg for a neutron at rest) and velocity, v, through the de Broglie equation:

$$\lambda = \frac{h}{p} = \frac{h}{m \cdot v} \tag{3.11}$$

where h is the Planck's constant. The time independent Schrödinger equation can be used to describe the neutron-matter interaction as follows:

$$-\frac{h^2}{8\pi^2 m}\nabla^2\Psi + V\Psi = E\Psi \tag{3.12}$$

where the first operator is related to the kinetic energy, V is the neutron-matter interaction potential, Ψ is the neutron wave fucntion and E the energy of the system. In neutron scattering, the interactions between neutrons and nuclei present in the medium through which they move is approximated using the Fermi pseudopotential density, defined as:

$$V = \frac{h^2}{2\pi m}\rho \tag{3.13}$$

where ρ is the scattering length density (SLD) related to the ability of the material to scatter neutrons which in turn depends on the coherent scattering length of the nucleus and the number of nuclei per unit of volume, n_j.

$$\rho = \sum_j s_j n_j \tag{3.14}$$

By approximately solving the Schrödinger equation with the Fermi pseudopotential as the interaction potential, the neutron scattering cross section can be calculated and compared with experimental data.

3.3.5.2 Specular reflection of neutrons

NR has become a widely used technique to study films and surfaces with applications from materials science to chemistry and soft matter to biology.[25,61–67] In particular, this technique has been widely used to study soft matter at interfaces, as it presents three main advantages: neutrons have wavelengths on the nanometer scale (similar to the thickness of many fluid molecular films), their penetration through many materials is high, and they interact with the nuclei of the atoms and are sensitive to their isotopic form.

When a neutron beam or any radiation is directed to an interface, reflection and refraction occurs depending on the refractive index of the molecules. In general, the refractive index for neutrons can be written as:

$$n \approx 1 - \frac{\lambda^2}{2\pi}\rho \tag{3.15}$$

where λ is the wavelength and ρ the scattering length density given by

$$\rho = \frac{b}{M_v} \tag{3.16}$$

where M_v is the molecular volume and b the scattering length of the molecule, which itself is the sum of the coherent scattering lengths of each of its constituent atoms.

As it was mentioned in the previous section, the possibility of using isotopic contrast variation methods is one of the main advantages of neutron scattering techniques. In the study of surfactant and lipid monolayers at the air/water interface, the deuteration of the head or tails provides high contrast between both parts of the layered structure.[63,66,68] Moreover, a mixture of 8.1% v/v D_2O in H_2O, known as air contrast matched water (ACMW), has an SLD of zero (the same as air), which makes the subphase practically invisible to neutrons. Thus, the interfacial material will be mainly responsible for the neutron scattering, even though there is always some background scattering as well. One can also use mixtures of H_2O and D_2O to tune the SLD of the subphase in order to match the SLD of any molecule or part of a molecule.

Specular NR is the most common application of NR. In a typical reflectivity experiment, the neutron beam is directed at the interface at a grazing (small) incident angle θ_i (defined as the angle between the surface and the beam). The specular reflection occurs when θ_i and the reflection angle, θ_r, of the neutrons with respect to surface are equal. The specular reflectivity, *R*, is defined as the number of neutrons in the specular reflection divided by that in the incident beam. Moreover, total external reflection occurs when the neutron beam imping the interface at an angle below to the critical angle, θ_c, defined as:

$$\theta_c = \sqrt{\frac{\Delta\rho\lambda^2}{\pi}} \tag{3.17}$$

where $\Delta\rho$ is the difference of SLD between the two media separated by the interface.

In NR experiments, reflection of neutrons causes a change in the momentum transfer normal to the interface, Q_z, that is defined by the difference of the modulus of the wave vectors of the incoming ($\overrightarrow{k_\iota}$) and the reflected ($\overrightarrow{k_r}$) beams.

$$Q_z = \left|\overrightarrow{k_\iota} - \overrightarrow{k_r}\right| = \frac{4\pi}{\lambda} sin\theta \tag{3.18}$$

Since Q_z is related to θ (and is proportional at the low-angle limit), total external reflection occurs when Q_z is below a critical value. Above the critical Q_z, the reflectivity falls as a function of Q_z^4 at a perfect interface.

P/S films at the air/water interface are an example of a multilayer system. Even in the case of a surface monolayer, three layers each of them separated by an interface can be distinguished: the aliphatic chains of the surfactant, the surfactant headgroups which may contain a fraction of polyelectrolyte, and the polyelectrolyte. When neutrons arrived at the first interface, some will be reflected, and some will be transmitted. Those that have been transmitted will reach the second interface, where the same process occurs, and so on at each of the interfaces present in the system. The interference of the waves reflected at each of the interfaces produces Kiessig fringes in the reflectivity profile. The resulting fringe pattern, i.e., the position and intensity of the fringes, depends on the thickness of the film (or the different layers that can be distinguished in the film), the roughness and the refractive index, and thus the composition.

It is worth noting that there are two ways to perform NR measurements. Basically, they consist of measuring the reflectivity as a function of Q_z, which is determined by λ and θ (equation 3.18). Therefore, NR measurements can be recorded by varying either or both λ and θ. In the first method, a monochromatic beam is used and θ is varied, so that each reflectivity data point corresponds to one value of θ. On the other hand, it is also possible to use a polychromatic neutron beam containing a wide range of λ and a few incident angles to obtain the reflectivity profile. In spallation sources, a pulsed neutron beam is obtained by bombarding a heavy target material with high-energy protons accelerated in a synchrotron.[69] In reactor sources, where neutrons are produced from fission, usually ^{235}U nuclei, choppers are used to modulate the neutron beam and produce well-defined pulses of neutrons.[70,71] In both cases, the time it takes a neutron to travel a known distance, *L*, until it arrives to the detector is determined using the following equation:

$$t = \frac{m_n}{h} L\lambda \tag{3.19}$$

Where t is the time-of-flight (TOF), which gives its name to this technique, and m_n is the mass of the neutron. Thus, the use of equation 3.19 allows determining the wavelength of the neutron detected. Since this method allows data to be obtained over a wide range of Q_z simultaneously, it is the method of choice for kinetic studies.[67] A good example of this is the low-Q_z approach explained in section 3.3.5.4.

The raw data obtained from NR experiments cannot be used directly in the analysis. To provide the absolute values of reflectivity as a function of Q_z, the data must be reduced or normalised to the incident beam spectrum. The TOF technique allows to determine the wavelength of a detected neutron using equation 3.19, which can then be converted to Q_z using equation 3.18. Data reduction involves normalising the raw data using a direct beam measurement (without the sample) to determine the transmission of the sample cell, measuring e.g. a clean D_2O interface to correct the intensity with a scaling factor if attenuators were used and subtracting the background. Furthermore, this process takes into account any potential instrument related corrections, such as angle-dependent detector distance and calculates the instrumental resolution. Once the data reduction process is completed, a set of data independent of the instrument or facility is obtained.

The following two sections described the classical full-Q_z approach and the recently developed low-Q_z approach.

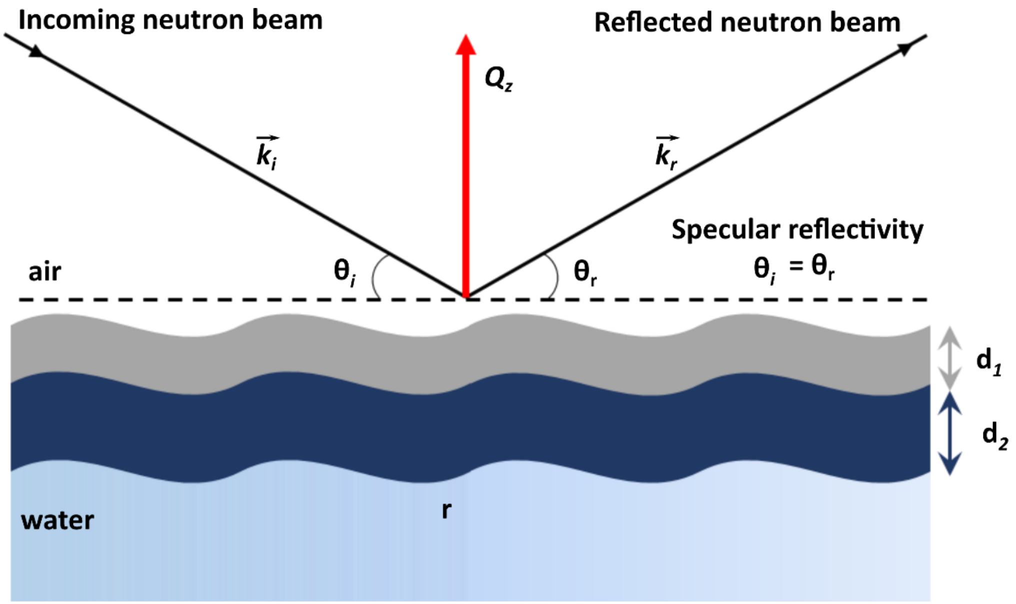

Figure 3.3. Schematic representation of specular neutron reflection ($\theta_i = \theta_r$) at the air/water interface in the presence of a film with two layers with different SLD represented by different colors. NR provides the determination of the SLD profile normal to the interface and the thickness (d_1 and d_2), water content and roughness (r) of the different layers.

3.3.5.3 Full-Q_z approach: structural analysis

Traditionally, specular NR has been widely used for the characterisation of the structure and composition of thin films at the air/water interface.[61,66,72,73] The accurate determination of the structure of the interfacial film requires lengthy measurements over all the range of Q_z (typically up to ~0.25–0.30 $Å^{-1}$), in multiple isotopic contrasts.

Full-Q_z measurements have been used in this project to determine the structure of P/S films by measuring generally three different isotopic contrasts: (1) deuterated surfactant in ACMW, in which the scattering is dominated by the surfactant and is essential to determine the thickness of the monolayer and the surfactant ESs; (2) deuterated surfactant in D_2O, which is essential to determine the amount of polymer, since the SLD of deuterated surfactant (6.69×10^{-6} $Å^{-2}$ for d-SDS and 5.13×10^{-6} $Å^{-2}$ for d-DTAB) and D_2O (6.36×10^{-6} $Å^{-2}$) are similar; and (3) hydrogenous surfactant in D_2O in which the scattering is dominated by the subphase and therefore is very sensitive to the penetration of the surfactant in the bulk when they form ESs, being essential to determine the coverage of ESs.

Data modelling is carried out most usually by calculating the reflectivity for a model system, physically representative of the system under study, using, for example, the Parratt's recursive formalism.[25,65,66,74,75] The structural model consists of stratified layers characterised by their thickness, *d*, scattering length density, ρ, and roughness, *r*. The application of the Fresnel equations to the model system provides the theoretical reflectivity. In addition, the numerical values of *d*, ρ and *r* are obtained by varying various parameters of the layers in the fitting process and minimising the difference between the theoretical and measured reflectivity curves.[75,76] In this project, the data were analysed using the Motofit package and the different contrasts were co-refined.[76] The model used for a P/S monolayer consists of three layers: (1) surfactant tails, (2) surfactant headgroups with electrostatically bound polyelectrolyte and solvent, and (3) a hydrated polyelectrolyte layer. The ESs, whose structure in spread P/S films has been resolved for the first time in this project, were included in the model as (4) an additional layer formed by a surfactant bilayer and, in some cases, it has been possible to resolve the presence of (5) polyelectrolyte in another layer, implying that the surfactant bilayers are wrapped by polyelectrolyte. A general procedure of fitting the data with different isotopic contrasts using a structural model with the minimum number of layers required has been followed. The feasibility of using different contrasts and various constraints in the fit gives additional accuracy to the analysis. The surface excess, Γ, in moles per unit area is expressed as:

$$\Gamma = \frac{\rho d v_f}{b N_A} \tag{3.20}$$

where v_f is the volume fraction and N_A the Avogadro's number. One example of a fitting constraint is that used in the study of surfactant or lipid monolayers. The value of Γ in one layer of tails is forced to be equal to that in an adjacent layer of solvated heads. Without the introduction of this constraint the fit will be physically meaningless.[50,66,75] Furthermore, a roughness consistent with the presence of capillary waves considering the surface tension was applied to all interfaces.[66,77,78]

3.3.5.4 Low-Q_z approach: compositional dynamics

Specular NR is as very useful tool to solve the interfacial composition and the structure of mixtures at the air/water interface. However, the time required to acquire the data over the full-

Q_z range can be longer than many time scales related to kinetic or dynamic processes of interest,[67] which has limited application of the technique to date. Recently, a new low-Q_z analysis of the interfacial composition that overcomes this limitation has been developed.[58,79,80] While equation 3.19 gives access to the surface excess of a single component, in binary mixtures, such as P/S mixtures, the so-called "scattering excess" (ρ*d*) for both components in a model of data recorded at low-Q_z is additive and can be expressed using the following equation:

$$\rho d = N_A\left(\Gamma_x b_x + \Gamma_y b_y\right) \tag{3.21}$$

where x and y are the two different components. A protocol has been established to use in the reduction only data at low-Q_z values (0.01–0.03 Å^{-2}) on ACMW and using two isotopic contrasts of one of the components. Only data at low-Q_z are used so that the measurement is insensitive to the structure but very sensitive to the surface excess. The surface excess of both species can be determined solving the linear equations 3.21 and 3.22.

$$(\rho d)_1 = N_A(\Gamma_{h-x} b_{h-x} + \Gamma_{h-y} b_{h-y}) \tag{3.22}$$

$$(\rho d)_2 = N_A\left(\Gamma_{h-x} b_{h-x} + \Gamma_{d-y} b_{d-y}\right) \tag{3.23}$$

In the case of experiment 1 (equation 3.21), it is possible to express the additive scattering contributions of the hydrogenous component $h - x$ and hydrogenous component $h - y$, whereas in the case of experiment 2 (equation 3.22), it is possible to express the additive scattering contributions of $h - x$ and deuterated component $d - y$. In the former case, accurate determination of the background scattering is necessary in order to attribute the additional scattering to that of the weakly-scattering interfacial components. Here the strong scattering of the deuterated molecules dominates the scattering excess of experiment 2, and simultaneous solving of equations 3.21 and 3.22 allows one to determine the surface excesses of component x and y. One of the great advantages of this application is the significant reduction of time (approximately a factor of 60) required to solve binary systems interfacial composition. In this work, data were reduced over a range of 4.5–12 Å to get Q_z = 0.01–0.03 Å^{-1} without background subtraction. The background was instead determined as the average value from a series of measurements of the air/ACMW interface. This is essential to determine the surface excess of a hydrogenous component that cannot be obtained or is very expensive in its deuterated form, which is the case for the polyelectrolytes used in this project.

This implementation of NR, was developed through work on dynamic compression/expansion cycles of P/S films on a Langmuir trough by Campbell et al. in 2016,[58] and was first applied to kinetic measurements involving the interaction of a short, designed peptide with lipid monolayers by Ciumac et al.[50] The technique provided the definitive data in resolving the nucleated ES formation mechanism in spread P/S films by Tummino et al. in 2018.[23] It has also been used to determine the kinetics of photoswitching of designed surfactants to reveal an unusual monolayer-bilayer transition[81] and to quantify for the first time the adsorption of a fluorocarbon gas on phospholipid monolayers.[37] A detailed description of this powerful, recent approach as well as the important factors that should be considered when applying it have been reported in different articles and reviews.[23,58,62,67]

3.3.5.5 Instruments

Two different TOF reflectometers have been used in this project: the FIGARO at the Institut Laue-Langevin (Grenoble, France) and INTER at ISIS, Rutherford Appleton Laboratory (Didcot, UK).

FIGARO is an horizontal high-flux TOF reflectometer placed at a reactor source optimised for liquid/liquid and air/liquid interfaces.[70] There are several characteristics which makes FIGARO very well suited to study kinetic processes at the air/water interface. The first one is the stability of the reactor source which ensures a constant neutron flux. The second one is the low natural incident angle (0.62°) and the possibility to use the chopper pairs to select the flux option and resolution. Different reviews reported a detailed description of FIGARO, as well as the principal advantages and some outstanding studies carried on the instrument.[67,70] The low-Q_z data were recorded using a wavelength range λ = 2–16 Å, a 7% resolution in dλ/λ and an angle of incidence θ = 0.62°. For the new mid-Q_z approach presented in chapter 4, an incident angle of 1.97° was used and data were reduced over 3.6–20 Å to get Q_z = 0.02–0.12 Å^{-1}.

INTER is a TOF reflectometer at ISIS located at the Target Station 2 that was optimised for the study of chemical interfaces.[82] Data were recorded using a wavelength range λ = 1.5–16 Å, a 5.5% resolution in $d\,Q_z/Q_z$ and two angles of incidence (θ_1 = 0.8° and θ_2 = 2.3°).

Table 3.2 summarises the techniques used in this project indicating the main information provided by each one.

Table 3.2. Summary of the techniques used in this project indicating the main information that can be obtained from them.

Technique	Information
ζ-potential measurements	Measurement of the charge of the aggregates
Langmuir technique	Resolution of the static and dynamic behaviour in response to lateral compression
Ellipsometry	Estimation of the total amount of interfacial material + insight into lateral inhomogeneities
Brewster angle microscopy	Homogeneity/inhomogeneity of the film and interfacial organisation of the material
Neutron Reflectometry	Determination of the interfacial structure and real-time composition analysis

3.4 References

(1) Hunter, R. J. *Zeta Potential in Colloidal Science: Principles and Applications*, 1st ed.; Ottewill, R. H., Rowell, R. L., Eds.; Academic Press, 1981.

(2) Varga, I.; Campbell, R. A. General Physical Description of The Behavior of Oppositely Charged Polyelectrolyte/Surfactant Mixtures at the Air/Water Interface. *Langmuir* **2017**, *33*, 5915–5924.

(3) Bhattacharjee, S. DLS and Zeta Potential – What They Are and What They Are Not? *J. Control. Release* **2016**, *235*, 337–351.

(4) Ebnesajjad, S.; Landrock, A. H. Surface Tension and its Measurement. In *Adhesives Technology Handbook*; Elsevier, 2015; pp 19–34.

(5) Stauffer, C. E. The Measurement of Surface Tension by the Pendant Drop Technique. *J. Phys. Chem.* **1965**, *69*.

(6) Kaganer, V. M.; Möhwald, H.; Dutta, P. Structure and Phase Transitions in Langmuir Monolayers. *Rev. Mod. Phys.* **1999**, *71*, 779–819.

(7) Drelich, J.; White, C. L.; Fang, C. Measurement of Interfacial Tension in Fluid-Fluid Systems. *Encyclopedia of Surface and Colloid Science*; Marcel Dekker, Inc., 2002; pp 3152–3166.

(8) Berry, J. D.; Neeson, M. J.; Dagastine, R. R.; Chan, D. Y. C.; Tabor, R. F. Measurement of Surface and Interfacial Tension Using Pendant Drop Tensiometry. *J. Colloid Interface Sci.* **2015**, *454*, 226–237.

(9) Brown, A. T.; Cicuta, P. Biological Fluid Interfaces and Membranes. *Oxford Handb. Soft*

Condens. Matter **2017**, 535–588.

(10) Martin, P.; Szablewski, M. *Langmuir-Blodgett Troughs - Operating Manual*, 6th ed.; Grunfeld, F., Ed.; Nima Technology Ltd: Milton Keynes, England, 2001.

(11) Larsen, M. C. Binary Phase Diagrams At the Air-Water Interface: An Experiment for Undergraduate Physical Chemistry Students. *J. Chem. Educ.* **2014**, *91*, 597–601.

(12) Lee, K. Y. C. Collapse Mechanisms of Langmuir Monolayers. *Annu. Rev. Phys. Chem.* **2008**, *59*, 771–791.

(13) Notter, R. H.; Taubold, R.; Mavis, R. D. Hysteresis in Saturated Phospholipid Films and Its Potential Relevance for Lung Surfactant Function in Vivo. *Exp. Lung Res.* **1982**, *3*, 109–127.

(14) Veldhuizen, R.; Nag, K.; Orgeig, S.; Possmayer, F. The Role of Lipids in Pulmonary Surfactant. *Biochim. Biophys. Acta* **1998**, *1408*, 90–108.

(15) Lopez-Rodriguez, E.; Pérez-Gil, J. Structure-Function Relationships in Pulmonary Surfactant Membranes: From Biophysics to Therapy. *Biochim. Biophys. Acta - Biomembr.* **2014**, *1838*, 1568–1585.

(16) Sosnowski, T. R.; Kubski, P.; Wojciechowski, K. New Experimental Model of Pulmonary Surfactant for Biophysical Studies. *Colloids Surfaces A Physicochem. Eng. Asp.* **2017**, *519*, 27–33.

(17) Azzam, R. M. A.; Bashara, N. M. *Ellipsometry and Polarized Light*; North-Holland Publishing Company: Amsterdam, 1977.

(18) Benjamins, J.; Thuresson, K.; Nylander, T. Ellipsometry Studies of Nonionic Surfactant Adsorption at the Oil - Water Interface. *Langmuir* **2005**, *21* , 149–159..

(19) Thoma, M.; Schwendler, M.; Baltes, H.; Helm, C. A.; Pfohl, T.; Riegler, H.; Mo, H. Ellipsometry and X-Ray Reflectivity Studies on Monolayers of Phosphatidylethanolamine and Phosphatidylcholine in Contact with n-Dodecane, n-Hexadecane, and Bicyclohexyl. *Langmuir* **1996**, *12*, 1722–1728.

(20) Motschmann, H.; Teppner, R. Ellipsometry in Interface Science. *Stud. Interface Sci.* **2001**, *11*, 1–42.

(21) De Feijter, J. A.; Benjamins, J.; Veer, F. A. Ellipsometry as a Tool to Study the Adsorption Behavior of Synthetic and Biopolymers at the Air-Water Interface. *Biopolymers* **1978**, *17*, 1759–1772.

(22) Kamble, S.; Patil, S.; Kulkarni, M. Spectroscopic Ellipsometry of Fluid and Gel Phase Lipid Bilayers in Hydrated Conditions. *Colloids Surfaces B Biointerfaces* **2019**, *176*, 55–61.

(23) Tummino, A.; Toscano, J.; Sebastiani, F.; Noskov, B. A.; Varga, I.; Campbell, R. A. Effects of Aggregate Charge and Subphase Ionic Strength on the Properties of Spread Polyelectrolyte/Surfactant Films at the Air/Water Interface under Static and Dynamic Conditions. *Langmuir* **2018**, *34*, 2312–2323.

(24) Clifton, L. A.; Campbell, R. A.; Sebastiani, F.; Campos-Terán, J.; Gonzalez-Martinez, J. F.; Björklund, S.; Sotres, J.; Cárdenas, M. Design and Use of Model Membranes to Study

Biomolecular Interactions Using Complementary Surface-Sensitive Techniques. *Adv. Colloid Interface Sci.* **2020**, *277*, 102118.

(25) Maestro, A.; Gutfreund, P. In Situ Determination of the Structure and Composition of Langmuir Monolayers at the Air/Water Interface by Neutron and X-Ray Reflectivity and Ellipsometry. *Adv. Colloid Interface Sci.* **2021**, *293*, 102434.

(26) Landgren, M.; Jönsson, B. Determination of the Optical Properties of Si/SiO_2 Surfaces by Means of Ellipsometry, Using Different Ambient Media. *J. Phys. Chem.* **1993**, *97*, 1656–1660.

(27) Tiberg, F.; Landgren, M. Characterization of Thin Nonionic Surfactant Films at the Silica/Water Interface by Means of Ellipsometry. *Langmuir* **1993**, *9*, 927–932.

(28) Ainalem, M. L.; Campbell, R. A.; Nylander, T. Interactions between DNA and Poly(Amido Amine) Dendrimers on Silica Surfaces. *Langmuir* **2010**, *26*, 8625–8635.

(29) Drude, P. *The Theory of Optics*; Longmans, Green, and Co.: New York, 1902.

(30) Campbell, R. A.; Ang, J. C.; Sebastiani, F.; Tummino, A.; White, J. W. Spread Films of Human Serum Albumin at the Air-Water Interface: Optimization, Morphology, and Durability. *Langmuir* **2015**, *31*, 13535–13542.

(31) Casson, B. D.; Braun, R.; Bain, C. D. Phase Transitions in Monolayers of Medium-Chain Alcohols on Water Studied by Sum-Frequency Spectroscopy and Ellipsometry. *Faraday Discuss.* **1996**, *104*, 209–229.

(32) Ducharme, D.; Max, J. J.; Salesse, C.; Leblanc, R. M. Ellipsometric Study of the Physical States of Phosphatidylcholines at the Air-Water Interface. *J. Phys. Chem.* **1990**, *94*, 1925–1932.

(33) Reiter, R.; Motschmann, H.; Knoll, W. Ellipsometric Characterization of Streptavidin Binding to Biotin-Functionalized Lipid Monolayers at the Water/Air Interface. *Langmuir* **1993**, *9*, 2430–2435.

(34) Campbell, R. A.; Tummino, A.; Varga, I.; Milyaeva, O. Y.; Krycki, M. M.; Lin, S. Y.; Laux, V.; Haertlein, M.; Forsyth, V. T.; Noskov, B. A. Adsorption of Denaturated Lysozyme at the Air-Water Interface: Structure and Morphology. *Langmuir* **2018**, *34*, 5020–5029.

(35) Angus-Smyth, A.; Bain, C. D.; Varga, I.; Campbell, R. A. Effects of Bulk Aggregation on PEI-SDS Monolayers at the Dynamic Air-Liquid Interface: Depletion Due to Precipitation versus Enrichment by a Convection/Spreading Mechanism. *Soft Matter* **2013**, *9*, 6103–6117..

(36) Angus-Smyth, A.; Campbell, R. A.; Bain, C. D. Dynamic Adsorption of Weakly Interacting Polymer/Surfactant Mixtures at the Air/Water Interface. *Langmuir* **2012**, *28*, 12479–12492.

(37) Liu, X.; Counil, C.; Shi, D.; Mendoza-Ortega, E. E.; Vela-Gonzalez, A. V.; Maestro, A.; Campbell, R. A.; Krafft, M. P. First Quantitative Assessment of the Adsorption of a Fluorocarbon Gas on Phospholipid Monolayers at the Air/Water Interface. *J. Colloid Interface Sci.* **2021**, *593*, 1–10.

(38) Motschmann, H.; Reiter, R.; Lawall, R.; Duda, G.; Stamm, M.; Wegner, G.; Knoll, W. Ellipsometric Characterization of Langmuir Monolayers of “Hairy-Rod” Polymers at the Air-Water Interface. *Langmuir* **1991**, *7*, 2743–2747.

(39) Tonigold, K.; Varga, I.; Nylander, T.; Campbell, R. A. Effects of Aggregates on Mixed Adsorption Layers of Poly(Ethylene Imine) and Sodium Dodecyl Sulfate at the Air/Liquid Interface. *Langmuir* **2009**, *25*, 4036–4046.

(40) Campbell, R. A.; Yanez Arteta, M.; Angus-Smyth, A.; Nylander, T.; Noskov, B. A.; Varga, I. Direct Impact of Nonequilibrium Aggregates on the Structure and Morphology of Pdadmac/SDS Layers at the Air/Water Interface. *Langmuir* **2014**, *30*, 8664–8674..

(41) Hénon, S.; Meunier, J. Microscope at the Brewster Angle: Direct Observation of First-Order Phase Transitions in Monolayers. *Rev. Sci. Instrum.* **1991**, *62*, 936–939.

(42) Hoenig, D.; Moebius, D. Direct Visualization of Monolayers at the Air-Water Interface by Brewster Angle Microscopy. *J. Phys. Chem.* **1991**, *95*, 4590–4592.

(43) Meunier, J. Why a Brewster Angle Microscope? *Colloids Surfaces A Physicochem. Eng. Asp.* **2000**, *171*, 33–40.

(44) Rodríguez Patino, J. M.; Carrera Sánchez, C.; Rodríguez Niño, M. R. Morphological and Structural Characteristics of Monoglyceride Monolayers at the Air-Water Interface Observed by Brewster Angle Microscopy. *Langmuir* **1999**, *15*, 2484–2492.

(45) Vollhardt, D. Brewster Angle Microscopy: A Preferential Method for Mesoscopic Characterization of Monolayers at the Air/Water Interface. *Curr. Opin. Colloid Interface Sci.* **2014**, *19*, 183–197.

(46) Vollhardt, D.; Fainerman, V. B. Characterisation of Phase Transition in Adsorbed Monolayers at the Air/Water Interface. *Adv. Colloid Interface Sci.* **2010**, *154*, 1–19.

(47) Miones, J.; Rodríguez Patino, J. M.; Conde, O.; Carrera, C.; Seoane, R. The Effect of Polar Groups on Structural Characteristics of Phospholipid Monolayers Spread at the Air–Water Interface. *Colloids Surfaces A Physicochem. Eng. Asp.* **2002**, *203*, 273–286.

(48) Roldán-Carmona, C.; Giner-Casares, J. J.; Pérez-Morales, M.; Martín-Romero, M. T.; Camacho, L. Revisiting the Brewster Angle Microscopy: The Relevance of the Polar Headgroup. *Adv. Colloid Interface Sci.* **2012**, *173*, 12–22.

(49) Castano, S.; Desbat, B. Structure and Orientation Study of Fusion Peptide FP23 of Gp41 from HIV-1 Alone or Inserted into Various Lipid Membrane Models (Mono-, Bi- and Multibi-Layers) by FT-IR Spectroscopies and Brewster Angle Microscopy. *Biochim. Biophys. Acta - Biomembr.* **2005**, *1715*, 81–95.

(50) Ciumac, D.; Campbell, R. A.; Xu, H.; Clifton, L. A.; Hughes, A. V.; Webster, J. R. P.; Lu, J. R. Implications of Lipid Monolayer Charge Characteristics on Their Selective Interactions with a Short Antimicrobial Peptide. *Colloids Surfaces B Biointerfaces* **2017**, *150*, 308–316.

(51) Winsel, K.; Hönig, D.; Lunkenheimer, K.; Geggel, K.; Witt, C. Quantitative Brewster Angle Microscopy of the Surface Film of Human Broncho-Alveolar Lavage Fluid. *Eur. Biophys. J.*

2003, *32*, 544–552.

(52) Alonso, C.; Alig, T.; Yoon, J.; Bringezu, F.; Warriner, H.; Zasadzinski, J. A. More Than a Monolayer: Relating Lung Surfactant Structure and Mechanics to Composition. *Biophys. J.* **2004**, *87*.

(53) Daear, W.; Mahadeo, M.; Prenner, E. J. Applications of Brewster Angle Microscopy from Biological Materials to Biological Systems. *Biochim. Biophys. Acta* **2017**, *1859*, 1749–1766.

(54) Guzmán, E.; Liggieri, L.; Santini, E.; Ferrari, M.; Ravera, F. Influence of Silica Nanoparticles on Phase Behavior and Structural Properties of DPPC—Palmitic Acid Langmuir Monolayers. *Colloids Surfaces A Physicochem. Eng. Asp.* **2012**, *413*, 280–287.

(55) Sheridan, A. J.; Slater, J. M.; Arnold, T.; Campbell, R. A.; Thompson, K. C. Changes to DPPC Domain Structure in the Presence of Carbon Nanoparticles. *Langmuir* **2017**, *33*, 10374–10384.

(56) Jain, N. J.; Albouy, P.-A.; Langevin, D. Study of Adsorbed Monolayers of a Cationic Surfactant and an Anionic Polyelectrolyte at the Air−Water Interface. *Langmuir* **2003**, *19*, 5680–5690.

(57) Llamas, S.; Fernández-Penã, L.; Akanno, A.; Guzmán, E.; Ortega, V.; Ortega, F.; Csaky, A. G.; Campbell, R. A.; Rubio, R. G. Towards Understanding the Behavior of Polyelectrolyte-Surfactant Mixtures at the Water/Vapor Interface Closer to Technologically-Relevant Conditions. *Phys. Chem. Chem. Phys.* **2018**, *20*, 1395–1407.

(58) Campbell, R. A.; Tummino, A.; Noskov, B. A.; Varga, I. Polyelectrolyte/Surfactant Films Spread from Neutral Aggregates. *Soft Matter* **2016**, *12*, 5304–5312.

(59) Lipp, M. M.; Lee, K. Y. C.; Waring, A.; Zasadzinski, J. A. Fluorescence, Polarized Fluorescence, and Brewster Angle Microscopy of Palmitic Acid and Lung Surfactant Protein B Monolayers. *Biophys. J.* **1997**, *72*, 2783–2804.

(60) González-Delgado, A. M.; Pérez-Morales, M.; Giner-Casares, J. J.; Muñoz, E.; Martín-Romero, M. T.; Camacho, L. Reversible Collapse of Insoluble Monolayers: New Insights on the Influence of the Anisotropic Line Tension of the Domain. *J. Phys. Chem. B* **2009**, *113*, 13249–13256.

(61) Narayanan, T.; Wacklin, H.; Konovalov, O.; Lund, R. Recent Applications of Synchrotron Radiation and Neutrons in the Study of Soft Matter. *Crystallogr. Rev.* **2017**, *23*, 160–226..

(62) Braun, L.; Uhlig, M.; von Klitzing, R.; Campbell, R. A. Polymers and Surfactants at Fluid Interfaces Studied with Specular Neutron Reflectometry. *Adv. Colloid Interface Sci.* **2017**, *247*, 130–148.

(63) Fragneto-Cusani, G. Neutron Reflectivity at the Solid/Liquid Interface: Examples of Applications in Biophysics. *J. Phys. Condens. Matter* **2001**, *13*, 4973–4989.

(64) Lu, J. R.; Zhao, X.; Yaseen, M. Protein Adsorption Studied by Neutron Reflection. *Curr. Opin. Colloid Interface Sci.* **2007**, *12*, 9–16.

(65) Skoda, M. W. A. Recent Developments in the Application of X-Ray and Neutron Reflectivity

to Soft-Matter Systems. *Curr. Opin. Colloid Interface Sci.* **2019**, *42*, 41–54.

(66) Campbell, R. A.; Saaka, Y.; Shao, Y.; Gerelli, Y.; Cubitt, R.; Nazaruk, E.; Matyszewska, D.; Lawrence, M. J. Structure of Surfactant and Phospholipid Monolayers at the Air/Water Interface Modeled from Neutron Reflectivity Data. *J. Colloid Interface Sci.* **2018**, *531*, 98–108.

(67) Campbell, R. A. Recent Advances in Resolving Kinetic and Dynamic Processes at the Air/Water Interface Using Specular Neutron Reflectometry. *Curr. Opin. Colloid Interface Sci.* **2018**, *37*, 49–60.

(68) Nagle, J. F.; Tristram-Nagle, S. Structure of Lipid Bilayers. *Biochim. Biophys. Acta - Rev. Biomembr.* **2000**, *1469*, 159–195.

(69) Bauer, G. S. Physics and Technology of Spallation Neutron Sources. *Nucl. Instruments Methods Phys. Res. Sect. A Accel. Spectrometers, Detect. Assoc. Equip.* **2001**, *463*, 505–543.

(70) Campbell, R. A.; Wacklin, H. P.; Sutton, I.; Cubitt, R.; Fragneto, G. FIGARO: The New Horizontal Neutron Reflectometer at the ILL. *Eur. Phys. J. Plus* **2011**, *126*, 1–22.

(71) Dewhurst, C. D.; Grillo, I.; Honecker, D.; Bonnaud, M.; Jacques, M.; Amrouni, C.; Perillo-Marcone, A.; Manzin, G.; Cubitt, R. The Small-Angle Neutron Scattering Instrument D33 at the Institut Laue–Langevin. *Appl. Cryst.* **2016**, *49*, 1–14.

(72) Penfold, J.; Thomas, R. K.; Taylor, D. J. F. Polyelectrolyte/Surfactant Mixtures at the Air-Solution Interface. *Curr. Opin. Colloid Interface Sci.* **2006**, *11*, 337–344.

(73) Taylor, D. J. F.; Thomas, R. K.; Hines, J. D.; Humphreys, K.; Penfold, J. The Adsorption of Oppositely Charged Polyelectrolyte/Surfactant Mixtures at the Air/Water Interface: Neutron Reflection from Dodecyl Trimethylammonium Bromide/Sodium Poly(Styrene Sulfonate) and Sodium Dodecyl Sulfate/Poly(Vinyl Pyridinium Chloride). *Langmuir* **2002**, *18*, 9783–9791.

(74) Parratt, L. G. Surface Studies of Solids by Total Reflection of X-Rays. *Phys. Rev.* **1954**, *95*, 369.

(75) Gerelli, Y. Aurore: New Software for Neutron Reflectivity Data Analysis. *J. Appl. Crystallogr.* **2016**, *49*, 330–339.

(76) Nelson, A. Co-Refinement of Multiple-Contrast Neutron/X-Ray Reflectivity Data Using MOTOFIT. *J. Appl. Crystallogr.* **2006**, *39*, 273–276.

(77) Braslau, A.; Deutsch, M.; Pershan, P. S.; Weiss, A. H.; Als-Nielsen, J.; Bohr, J. Surface Roughness of Water Measured by X-Ray Reflectivity. *Phys. Rev. Lett.* **1985**, *54*, 114–117.

(78) Tikhonov, A. M.; Mitrinovic, D. M.; Li, M.; Huang, Z.; Schlossman, M. L. An X-Ray Reflectivity Study of the Water-Docosane Interface. *J. Phys. Chem. B* **2000**, *104*, 6336–6339.

(79) Ábraham, Á.; Campbell, R. A.; Varga, I. New Method to Predict the Surface Tension of Complex Synthetic and Biological Polyelectrolyte/Surfactant Mixtures. *Langmuir* **2013**, *29*.

(80) Fauser, H.; Von Klitzing, R.; Campbell, R. A. Surface Adsorption of Oppositely Charged C_{14}TAB-PAMPS Mixtures at the Air/Water Interface and the Impact on Foam Film Stability.

J. Phys. Chem. B **2015**, *119*, 348–358.

(81) Honnigfort, C.; Campbell, R. A.; Droste, J.; Gutfreund, P.; Hansen, M. R.; Ravoo, B. J.; Braunschweig, B. Unexpected Monolayer-to-Bilayer Transition of Arylazopyrazole Surfactants Facilitates Superior Photo-Control of Fluid Interfaces and Colloids. *Chem. Sci.* **2020**, *11*, 2085–2092.

(82) Webster, J.; Holt, S.; Dalgliesh, R. INTER the Chemical Interfaces Reflectometer on Target Station 2 at ISIS. *Phys. B Condens. Matter* **2006**, *385–386*, 1164–1166.

4 Study 1: Polyelectrolyte/surfactant films: from 2D to 3D structural control

Javier Carrascosa-Tejedor,[1,2] Andreas Santamaria,[1,3] Andrea Tummino,[1] Imre Varga,[4] Marina Efstratiou,[2] M. Jayne Lawrence,[2] Armando Maestro,[5,6*] and Richard A. Campbell[2*]

1. Institut Laue-Langevin, 71 Avenue des Martyrs, CS20156, 38042 Grenoble, France
2. Division of Pharmacy and Optometry, Faculty of Biology, Medicine and Health, University of Manchester, Oxford Road, Manchester M13 9PT, UK
3. Departamento de Química Física, Facultad de Ciencias, Universidad Complutense de Madrid, Ciudad Universitaria s/n, 28040 Madrid, Spain
4. Institute of Chemistry, Eötvös Loránd University, 112, Budapest H-1518, Hungary
5. Centro de Física de Materiales (CSIC, UPV/EHU) - Materials Physics Center MPC, Paseo Manuel de Lardizabal 5, E-20018 San Sebastián, Spain
6. Basque Foundation for Science, Plaza Euskadi 5, Bilbao, 48009, Spain

*corresponding authors: Armando Maestro and Richard A. Campbell

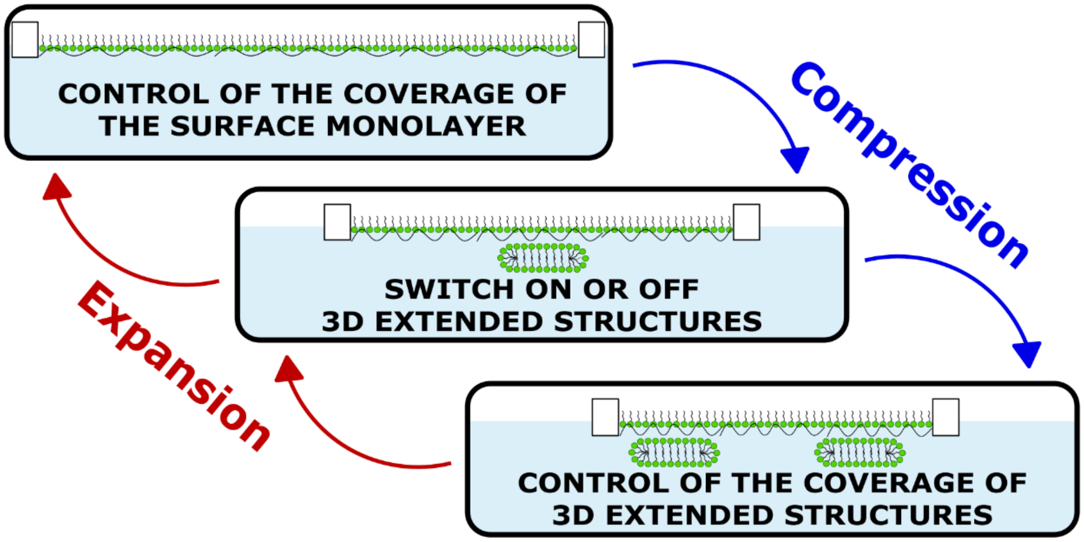

Figure 4.1. Table of contents illustrating control of the coverage of the surface monolayer, switching on or off 3D ESs, and control of the coverage of 3D ESs. Compression and expansion arrows are depicted to emphasise the reversible dynamics.

4.1 Abstract

Reversible control of the 3D structure of polyelectrolyte/surfactant films at the air/water interface is showcased. A recently discovered mechanism is exploited to form highly efficient, stable and biocompatible films by spreading aggregates composed of poly-L-lysine and sodium dodecyl sulfate on the surface of water. Reversible control of: (1) the surface monolayer coverage, (2) the switching on or off discrete ESs, and (3) the extended structure coverage is demonstrated for the first time. The intricacy by which the film structures can be controlled is unprecedented and opens exciting potential to optimise film properties by chemical design for novel biomedical transfer applications.

4.2 Introduction

The design of polymer-based nanofilms with controllable architecture attracts strong attention due to applications in areas such as biosensing,[1] tissue engineering[2] and drug delivery.[3] Preparation approaches include Langmuir-Blodgett (LB) and Langmuir-Schaeffer (LS) deposition onto solids from monolayers at the air/water interface,[4] the formation of layer-by-layer (LbL) films on solids,[5] and the formation of multilayer structures at both fluid and solid interfaces.[6] LB and LS deposition methods benefit from use of a Langmuir trough as the density, morphology and in-plane structures of films can be tuned prior to transfer.[7] While a transition from 2D to 3D structures has been reported in surfactant mixtures,[8] such an observation has not been made on polymer-based nanofilms to the knowledge of the authors. The development of new film formation methods is therefore of utmost importance.

A new approach to form P/S films at the air/water interface was established a few years ago.[9] The approach involves dropping fresh aqueous dispersions of P/S aggregates onto the surface of water, which dissociate and spread material at the surface that remains kinetically-trapped in a film due to the entropy associated with counterion release. The aggregates are pre-formed in P/S solutions at a molar ratio where complexes associate due to lack of colloidal stability,[10] initially with a size on the order of 100 nm.[9] Advantages of the approach include use of water as the spreading solvent and fast creation of films with a high amount of material compared with adsorbed layers, which offer both environmental and economic advantages in potential applications. Recent work showed that NaPSS/DTAB aggregates can nucleate ESs of different morphologies upon successive spreading or compression of the surface area.[11] The charge/structure of the aggregates determine if ESs form, hence an interfacial mechanism where aggregates nucleate self-assembly of ESs was inferred, conceptually analogous to the function of lung surfactant protein B during respiration.[12] Even so, a study limitation was that the ESs were inferred from a surface excess of surfactant exceeding its monolayer coverage, as a direct structural characterisation was precluded due to their transient nature.

The aim of this work is to control 2D versus 3D structures in P/S spread films of relevance to biomedical transfer applications. The investigated mixture is PLL/SDS. Both are biocompatible with PLL used in many biomedical applications such as complexing agents with DNA/siRNA for gene delivery,[13] and in cancer therapy,[14] while SDS is used in oral pharmaceutical formulations up to 1 wt%.[15] Also, they are used in film transfer applications such as PLL in a dual-responsive nanofluidic device,[16] to promote cellular adhesion,[17] and for skin regeneration,[18] and SDS in self-healing hydrogels.[19] An important pre-requisite of studying this system was that ESs formed upon film compression are stable with time, allowing them to be characterised directly, and making them robust in potential applications. PLL was chosen over other polypeptides because in the bulk SDS can induce rigid in-plane interactions in a β-sheet conformation.[20] This pre-requisite was met, as ellipsometry data comparing compressed spread films of the NaPSS/DTAB and PLL/SDS systems show that only the latter type of film is stable (Figure 4.2A).

4.3 Results and discussion

Our methodology is to form a film by dispensing aqueous droplets containing PLL/SDS aggregates onto the water surface of a Langmuir trough and use barriers to control its surface area. The spreading solutions comprise 100 ppm PLL and 0.80 mM SDS, which self-assemble to form negatively charged aggregates as characterised by zeta potential (section 4.6.1), chosen simply because aggregates charged with excess surfactant are effective in forming ESs for the NaPSS/DTAB system.[11] Several reflectometry techniques are applied to complement in situ measurements of the surface pressure. Ellipsometry is used to measure the phase shift from the presence of the film, $d\Delta$, which is related to the total amount of interfacial material per unit area.[21] BAM is used to image the lateral morphology on the µm-scale.[22] Three implementations of NR are applied to resolve the film composition and structure. First is the recently-developed low-Q_z analysis (0.01–0.03 Å^{-1}), where Q_z is the momentum transfer normal to the interface, to resolve the surface excesses of PLL and SDS during three compression/expansion cycles.[23] Second is the full-Q_z analysis (0.01–0.25 Å^{-1}) to resolve the interfacial structure at a high film compression state.[24] Third is a novel mid-Q_z analysis (0.02–0.12 Å^{-1}) to resolve the structural dynamics during one cycle. Full details about the materials and methods used are provided in section 4.6.2.

The dynamics of PLL/SDS spread films were first examined by combining measurements of Π with the low-Q_z analysis of NR, ellipsometry and BAM. First, the Π–A film response over three cycles is shown in Figure 4.2B. Film compression initially results in a continuous increase in Π, attributed to enhanced molecular interactions with an increasing number of surfactant molecules per unit area in what we term the 'surface monolayer', i.e., a layer of surfactant in contact with air (hydrophobic driving force) with hydrated polyelectrolyte bound to the headgroups (electrostatic driving force).[25] Upon further compression, beyond state iii, Π remains constant at ~28 mN/m, which is attributed to collapse of the surface monolayer, i.e. expulsion of material either to bound ESs or the bulk. Expansion of the film is characterised by a large hysteresis in Π, the presence of a pseudo-plateau and a final value of Π close to the initial one, consistent with reincorporation of material back into the surface monolayer yet with a kinetic barrier.

The low-Q_z analysis of NR was applied to provide the surface excesses of PLL and SDS and the results are shown in Figure 4.2C. An explanation of the fitting procedure is provided in section 4.6.3. In comparison with the value Γ_{SDS} = 4.0 ± 0.1 µmol/m^2 at the collapse, upon further compression Γ_{SDS} continually rises to exceed this value. This observation demonstrates that the material expelled from the surface monolayer beyond the collapse remains bound in the form of ESs rather than being lost to the bulk. From Γ_{SDS} = 5.5 ± 0.1 µmol/m^2 at the maximum compression state measured, and with the assumption that Γ_{SDS} in the surface monolayer does not increase by further compression of the film after the collapse, it may be noted that 27 ± 1% of the SDS would be in the ESs; we will return to this point later. Moreover, despite the large hysteresis in Π, there is no hysteresis in Γ, indicating that there are equivalent amounts of material in the film at corresponding surface areas during compression or expansion, which suggests that the hysteresis is attributed to a kinetic barrier for the transfer of material from the ESs to the surface monolayer. These results are supported qualitatively in values of *d*Δ recorded over successive cycles using ellipsometry (section 4.6.4). Lastly, the film composition over successive cycles is generally similar, hinting at their robustness to potential applications.

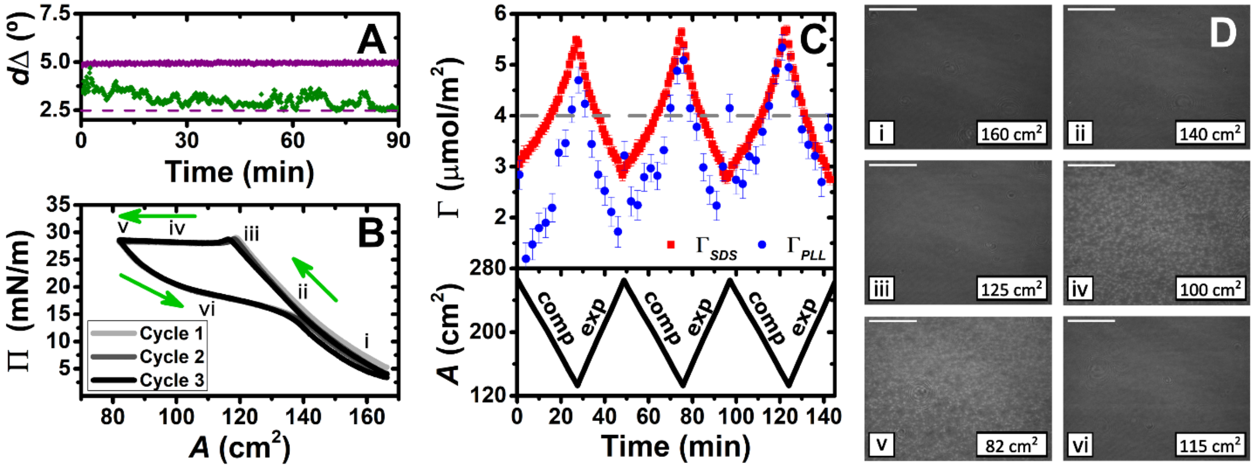

Figure 4.2. (A) Variation of *d*Δ as a function of time for NaPSS/DTAB (green) and PLL/SDS (purple) films compressed by a factor of 2; purple dashed line indicates the *d*Δ value corresponding to a full monolayer of PLL/SDS and NaPSS/DTAB. (B) Variation of Π as a function of *A*; green arrows indicate the direction of the compression/expansion and i-vi indicate different compression/expansion states. (C) Variation of the surface excess of PLL (blue circles) and SDS (red squares) from the NR low-Q_z analysis during three cycles, and for reference the area (black lines), versus time; grey dashed line indicates Γ_{SDS} at the collapse. (D) BAM images of a PLL/SDS film corresponding to states i–v during compression and state vi during expansion as indicated in panel A; scale bars are 100 µm.

Next, we applied BAM to visualise the films (Figure 4.2D). While prior to the collapse, images i, ii and iii are uniform with increasing brightness, images iv and v after exhibit discrete regions on the µm-scale that grow in number during compression, which we have reproduced in higher resolution combined with analysis of their coverage in section 4.6.5. The regions are attributed to discrete ESs in contact with the surface monolayer and disappear in image vi upon expansion due to transfer of material back to the surface monolayer resulting in a homogeneous film once again.

A second implementation of NR exploiting the full Q_z-range allows us to resolve the ESs of PLL/SDS films at maximum compression state v (Figure 4.2B). Neutron reflectivity profiles in 4 isotopic contrasts with fits to a common interfacial model in stratified layers, and volume fraction

(v_f) profiles are shown in Figure 4.3A and B, respectively. An explanation of the fitting procedure and a table of structural parameters is provided (section 4.6.6). A Kiessig fringe observed in data in the two isotopic contrasts that have the greatest scattering contrast between the surfactant chains and solvent, i.e., PLL with deuterated SDS in ACMW (ACMW, 8.1% v/v D_2O in H_2O) and PLL with SDS in D_2O (purple arrow), reveal the presence of ESs with surfactant present below the surface monolayer. The extended structure layer has a thickness of 21.8 ± 0.8 Å (almost twice that of the SDS monolayer), and a model also involving PLL in the layer did not improve the fit. We infer that the structures are either discrete patches of SDS bilayer wrapped by unresolved PLL or bound SDS hemimicelles. The amount of SDS present in the extended structure is 29 ± 1%, consistent with the 27 ± 1% calculated above on the assumption that the surface monolayer does not change in coverage beyond the collapse.

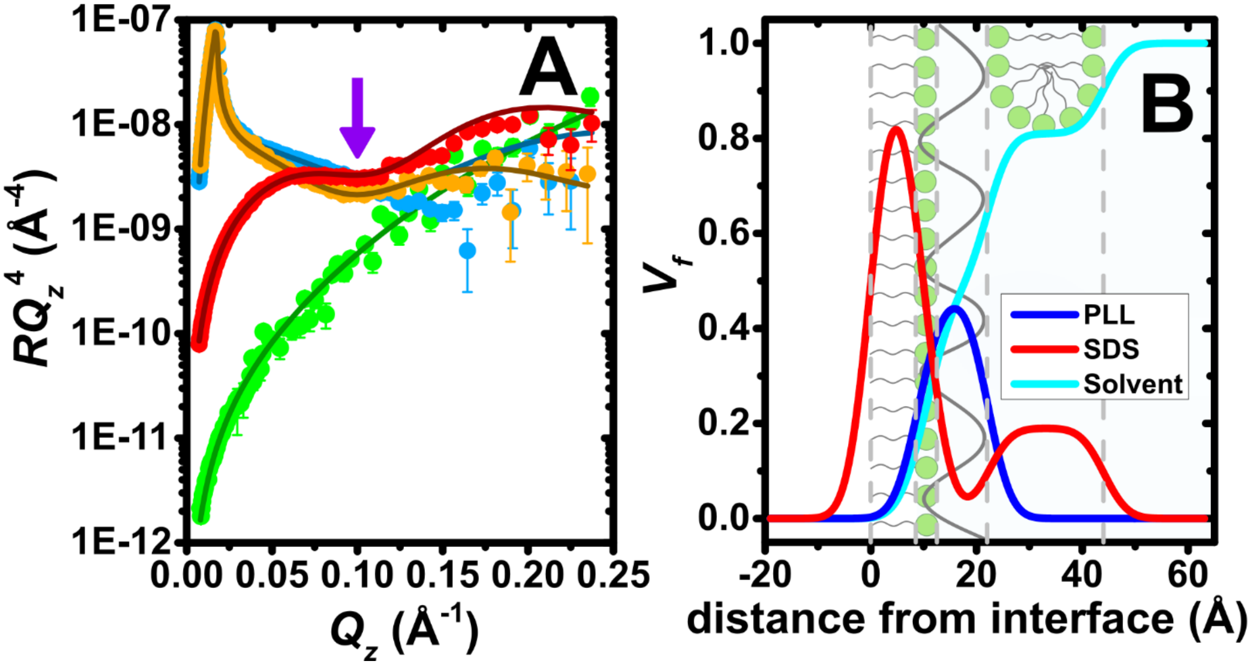

Figure 4.3. (A) Neutron reflectivity profiles of a PLL/SDS spread film with deuterated SDS in D_2O (blue), SDS in D_2O (orange), deuterated SDS in ACMW (red), and SDS in ACMW (green); continuous lines show the model fits; purple arrow at Q_z = 0.1 Å^{-1} indicates a Kiessig fringe symptomatic of the ES. (B) Corresponding V_f profiles of PLL (blue), SDS (red) and solvent (cyan).

Although ESs in adsorbed P/S layers have been recently the focus of an experimental study,[26] here we have resolved for the first time the ESs of a P/S film formed by the aggregate spreading approach.

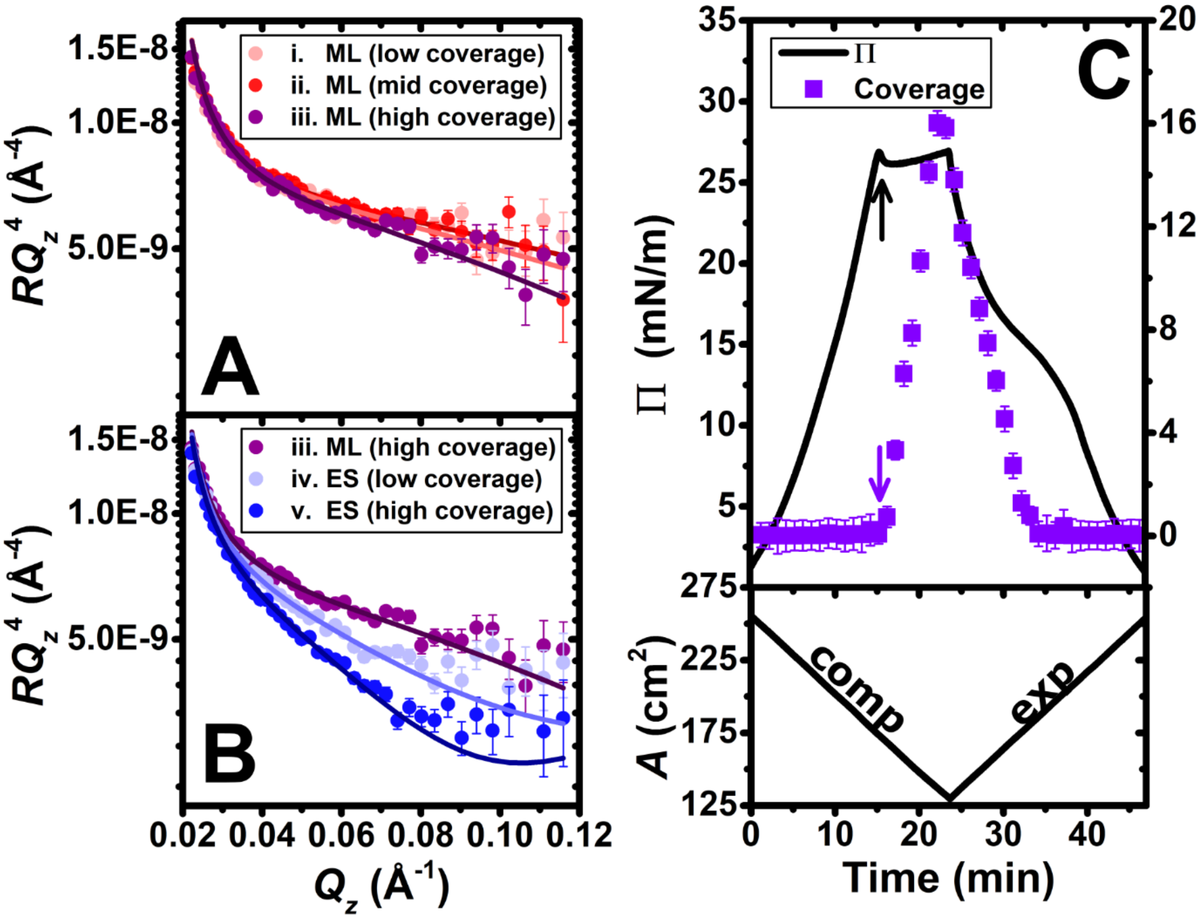

Figure 4.4. Neutron reflectivity profiles of a PLL/SDS spread film in D_2O at different compression states: (A) monolayer (ML) region and (B) extended structure (ES) region; indices i-v are defined in Figure 4.2B; solid lines show the simulated ML models and fitted ES models. (C) Variation of Π (black line) and fitted ES coverage (violet squares) with respect to the time; black and violet arrows indicate film collapse and the onset of ESs, respectively; variation of area versus time is also shown.

Lastly, we performed a third implementation of NR involving a novel mid-Q_z analysis to follow the structural dynamics of PLL/SDS films during one cycle. A single contrast of PLL with SDS in D_2O was chosen for maximum sensitivity to the surfactant in the ES (strong difference in scattering between the chains and solvent) compared with in the surface monolayer (weak difference in scattering between the chains and air). The scope is to resolve the change in thickness or coverage of the ESs with respect to film compression. Data until the collapse (states i, ii and iii in Figure 4.2B), combined with simulations of the reflectivity profiles based on the coverage of the surface monolayer from Figure 4.2C, show that changing monolayer coverage indeed has a small effect on the data (Figure 4.4A). However, data from the collapse (states iii, iv and v), combined with fits of the volume fraction at a constant ES thickness of 21.8 Å reveal the higher sensitivity of the measurements to the coverage of the extended structure (Figure 4.4B). By comparison, fits of the data after the collapse to a model where the thickness of the ES changes at a constant volume fraction exhibited significantly worse agreement, as revealed by an increase of up to 30% in the global χ^2 parameter (section 4.6.7). It can be concluded that after collapse of the surface monolayer, the coverage of discrete patches of the wrapped bilayer or hemimicelles can now be controlled.

The coverage of ESs, in comparison with the variation of Π, as a function of time is displayed in Figure 4.4C. The ESs start to form (violet arrow) at the collapse (black arrow). The coverage increases with film compression beyond the collapse and decreases back down to 0% during the Π pseudo-plateau upon expansion, indicating that the surfactant in the ESs has been fully resupplied to the monolayer. While the increase in coverage of ESs takes ~7 min, the reduction takes ~10 min, consistent with the kinetic barrier to resupply of material to the surface monolayer. Although NR has been used previously to resolve changes in film composition under surface area dynamic,[9,11] this is the first time to the knowledge of the authors that it has been used to resolve changes in the ESs of a dynamic air/water interface, and critically it highlights the unprecedented control gained over 2D versus 3D structures in P/S films, schematically illustrated in Figure 4.5.

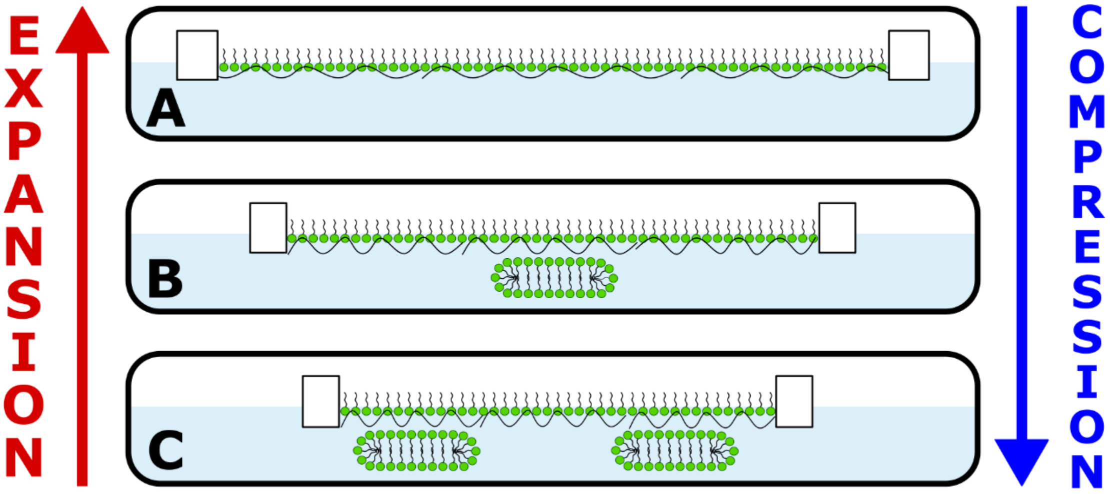

Figure 4.5. Schematic illustration of (A) control of the coverage of the surface monolayer, (B) switching on or off 3D ESs, and (C) control of the coverage of 3D ESs.

4.4 Conclusions

The spread PLL/SDS films studied in the present work are stable and reversible in their dynamics, which make them robust and amenable to transfer applications.[27] The combination of the new film spreading approach with established deposition techniques may offer economic and environmental advantages as the amount of materials used and waste generated are low compared to other methods.[28] As a result, 3D structures could be designed with controllable architecture and deposited onto solids for biomedical applications such as wound dressings, antimicrobial coatings or drug delivery applications.[29]

Coupling of reflectometry techniques to a Langmuir trough has allowed us to elucidate the compositional and structural dynamics and directly characterise the ESs in spread P/S films for the first time. This approach must now be urgently applied to other systems to understand in greater depth the physicochemical film properties, such as by tuning specific amino acid interactions with reference to different polypeptide conformations adopted in the bulk (e.g. α-helices by polyarginine/SDS versus β-sheets by PLL/SDS).[20]

The mid-Q_z structural dynamic application of NR showcased in this study opens the possibility to understand a wide variety of synthetic and biological systems that adopt 3D morphologies. Further applications of the method include, for example, particle–laden interfaces that present buckling or jamming phenomena,[30] and lung surfactant models where the transfer of lipid between the surface monolayer and ESs during respiration is vital for the stabilisation of alveoli.[12]

4.5 Acknowledgements

We thank the Institut Laue-Langevin for beam time on FIGARO (DOIs: https://doi.org/10.5291/ILL-DATA.9-12-614 and https://doi.org/10.5291/ILL-DATA.9-12-631), Simon Wood for technical assistance and the Partnership for Soft Condensed Matter (PSCM) for lab support. IV acknowledges the financial support from the Hungarian National Research, Development and Innovation Office (NKFIH K116629). AM acknowledges the financial support from MICINN under grant PID2021-129054NA-I00 and the IKUR Strategy of the Basque Government.

4.6 Supplementary information

4.6.1 ζ-potential measurements of PLL/SDS aggregates

100 ppm PLL mixed with an SDS concentration varying from 0.4 mM to 1 mM results in a transition from positively to negatively charged PLL/SDS aggregates. Figure 4.6 shows the variation of the ζ-potential of PLL/SDS aggregates with respect to the SDS concentration. While stoichiometric charge mixing of the components would require 0.48 mM SDS, excess surfactant is needed to produce neutral aggregates: 0.63 mM in total. Since the excess of SDS needed for the neutralisation of aggregates is low, a high binding efficiency of SDS to PLL chains is evident.

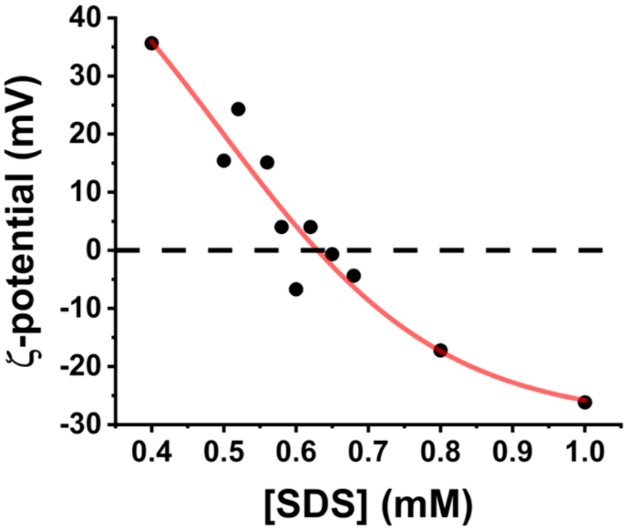

Figure 4.6. Variation of the ζ-potential of freshly prepared PLL/SDS mixtures at a constant concentration of 100 ppm PLL varying the concentration of SDS between 0.4–1.0 mM. Experimental data points are shown (black circles) together with a sigmoidal fit (red line). The black dashed line indicates neutral charge. The data points displayed are the average of three measurements of each sample. From the scatter in the data, the uncertainty of each measurement is around ± 5 mV.

4.6.2 Materials and methods

4.6.2.1 Materials

15–30 kDa poly-(L-lysine) hydrobromide powder, poly(sodium styrenesulfonate), sodium dodecyl sulfate, sodium dodecyl-d25 sulfate, dodecyltrimethylammonium bromide, acetone (≥99.5%), ethanol (≥99.8%) and D_2O were purchased from Sigma Aldrich. PLL, NaPSS and D_2O were used as received. SDS and DTAB were recrystallised twice in ethanol and 4:1 acetone:ethanol mixtures, respectively, followed by drying under vacuum. Ultra-pure water was generated by passing deionised water through a Milli-Q unit (total organic content ≤ 4 ppb, resistivity = 18 MΩ·cm).

4.6.2.2 Sample preparation

PLL/SDS mixtures were prepared pouring an aliquot of PLL 200 ppm solution into a clean vessel containing a magnetic stirrer. An aliquot of the same volume of SDS 1.6 mM was then rapidly added to the vessel with stirring maintained for 3–5 s. PLL/SDS mixtures were always prepared immediately before use (maximum of 1 min) to limit the growth of any aggregates prior to the experiment. NaPSS/DTAB mixtures were prepared by pouring solutions of NaPSS 200 ppm and DTAB 20 mM at the same time into the vessel.

4.6.2.3 ζ-potential

A Zetasizer Nano ZS90 (Malvern Instruments Ltd., U.K.) using laser doppler velocimetry and phase analysis light scattering techniques (M3-PALS) was used in this work to determine the ζ-potential of PLL/SDS freshly-prepared solutions. Measurements were performed with a constant concentration of PLL 100 ppm by varying the SDS concentration between 0.4–1.0 mM.

4.6.2.4 Langmuir trough

The Langmuir trough technique has been used to study the behaviour of spread PLL/SDS films during consecutive compression/expansion cycles by using two movable barriers. Π, which is the difference between the surface tension of pure water and that of the film, was recorded using a Wilhelmy plate. In the present work, we have used this technique to characterise the dynamic behaviour of the films during compression/expansion cycles, as well as the stability of the ESs over time at a constant area. The Langmuir trough has also been coupled to different reflectometry techniques.

In the present work, three different Langmuir troughs were used, namely a Kibron G1 (Finland) with dimensions of 260 × 80 mm (this trough was coupled to the Brewster angle microscope and the Beaglehole ellipsometer, using a maximum and minimum surface area of 166 and 88 cm^2, respectively; the speed of the barriers during the compression/expansion cycles was 3.16 cm^2/min, i.e., 49 min/cycle); a Kibron G2 (Finland) with dimensions of 405 × 80 mm (this trough was coupled to the Accurion ellipsometer, using a maximum and minimum surface area of 280 and 140 cm^2, respectively; the speed of the barriers during the compression/expansion cycles was 5.4 cm^2/min, i.e., 49 min/cycle); and a Nima (UK) with dimensions of 300 × 100 mm (this trough was coupled to the neutron reflectometer, using a maximum and minimum surface area of 265 and 130 cm^2, respectively; the speed of the barriers during the compression/expansion cycles was 5.5 cm^2/min, i.e., 49 min/cycle). The trough and barriers were carefully cleaned with detergent, ethanol and water before filling them with Milli-Q water. Subsequently, a freshly prepared solution of PLL/SDS aggregates was spread dropwise across the entire air/water interface (1130, 1900 and 1800 µL for the respective three troughs mentioned above). 530 µL of NaPSS/DTAB aggregates were spread in the experiment performed using the Kibron G2 trough. After 20 min of equilibration, the variation of the surface pressure as a function of the area was recorded.

4.6.2.5 Ellipsometry

Ellipsometry is a non-destructive optical technique based on determination of changes in the polarisation of light upon reflection at an interface. From these polarisation changes, it is possible to obtain information about the phase difference between the parallel and perpendicular components of the incident and the reflected beam, Δ, and the ratio of amplitudes of the parallel and perpendicular components defined as $\tan\Psi = |r_p|/|r_s|$. The ellipsometric angles are related to the total reflection coefficients by the ellipticity, ρ, defined as $\rho = r_p/r_s = \tan(\Psi)e^{i\Delta}$, that depends on the angle of incidence, the wavelength and both the thickness and the dielectric properties of the material. At the air/water interface, Δ is much more sensitive than Ψ to changes in coverage of thin films.[21,31] Often only changes in Δ are analysed, which is the approach taken in the present work, where $d\Delta = \Delta_{P/S}$ (for the P/S film) – Δ_{water} (for pure water). Values of $d\Delta$ are presented to remove the contribution of surface roughness leading to the response of $d\Delta$ being sensitive to the surface excess of fluid thin films, and temporal fluctuations being related to lateral heterogeneity on the micrometer length scale.[32]

Ellipsometry experiments were performed using two different ellipsometers. An Accurion EP4 ellipsometer (Germany) equipped with a blue diode laser with a wavelength of λ = 489.2 nm was used to record the stability measurements presented in Figure 4.2A at an angle of incidence of 50° and a data acquisition rate of 0.1 Hz. A Beaglehole Picometer Light ellipsometer (New

Zealand) equipped with a He-Ne laser with a wavelength of λ = 632.8 nm was used to record the dynamics presented in Figure 4.7 at an angle of incidence of 51° and a data acquisition rate of 0.2 Hz.

4.6.2.6 Brewster angle microscopy

Brewster angle microscopy is an optical technique that allows characterising the homogeneity/inhomogeneity of the film as well as the interfacial organisation of the material on the micrometre scale.[22] An Accurion Nanofilm EP3 Brewster angle microscope (Germany) equipped with a Nd:YAG laser (λ = 532 nm) was used. Images of the PLL/SDS film at the air/water interface were taken at an angle of incidence equal to the Brewster angle, 53.1° for the air/water interface, without background subtraction and using a 10× objective and a CCD detector. The polariser and analyser were adjusted so that *p*-polarised light was reflected at the interface. Thus, the air/water interface appears as a black image, the presence of a homogeneous fluid film with a different refractive index appears as a gray image and the additional layer of ESs appears as brighter regions.

4.6.2.7 Neutron reflectometry

NR has been used as a powerful tool to elucidate the structure and dynamic behaviour of a wide variety of systems at interfaces.[23,24,33] Specular reflectivity, *R*, defined as the number of neutrons scattered from the interface divided by that in the incident beam, is recorded at grazing incident angles as a function of the momentum transfer normal to the interface, Q_z, defined as:

$$Q_z = \frac{4\pi sin\theta}{\lambda} \qquad (3.18)$$

where λ is the wavelength and θ the incident angle. Neutron scattering from a molecule depends on SLD, ρ, which is defined as the ratio of the sum of the coherent scattering lengths, *b*, of its constituent atoms and its molecular volume, V_m. The use of isotopic contrast variation allows one to resolve the structure and composition of the interface by the substitution of hydrogen for deuterium, which maximises the differences between the molecules present at the interface and/or the subphase. Indeed, a mixture of 8.1% v/v D_2O in H_2O presents particular interest because its SLD, like that of air, is zero, which is why it is known as ACMW making the subphase practically invisible to neutrons.

Neutron reflectivity measurements were performed on the TOF neutron reflectometer FIGARO at the Institut Laue-Langevin (Grenoble, France).[34] A chopper pair was used to generate neutron pulses with a wavelength resolution of 7% dλ/λ. Three different incident angles θ = 0.63°, 1.97° and 3.78° were used to record the low-Q_z, mid-Q_z and high-Q_z range, respectively. The data were reduced using COSMOS[35] and analysed with Motofit.[36] The three different implementations of NR used in this work are explained in detail in sections 4.6.3, 4.6.6 and 4.6.7.

4.6.3 Low-Q_z compositional analysis: fitting

The use of FIGARO with its low natural incident angle allows a high-flux configuration at a stable reactor source that makes it a unique instrument to study dynamics at the air/water interface.[23,34]

The recently developed low-Q_z analysis was used to follow the variations of the surface excess of PLL and SDS during the compression/expansion of the film.[9] The NR data were reduced over 4.5–12 Å to get Q_z = 0.01–0.03 Å^{-1} where the reflectivity profile is insensitive to the structure of the film but very sensitive to the surface excess, which for a single component is defined as:

$$\Gamma = \frac{\rho d v_f}{b N_A} \tag{3.20}$$

where d is the thickness of the layer and N_A is Avogadro's number. Background was not subtracted from the data and two isotopic contrasts were used: (1) PLL with d-SDS in ACMW and (2) PLL with SDS in ACMW. Then, two different data sets can be used to resolve Γ_{PLL} and Γ_{SDS} by solving the linear equations:

$$\rho_d \cdot d_d = N_A \cdot (\Gamma_{PLL} \cdot b_{PLL} + \Gamma_{SDS} \cdot b_{d-SDS}); \tag{4.1}$$

$$\rho_h \cdot d_h = N_A \cdot (\Gamma_{PLL} \cdot b_{PLL} + \Gamma_{SDS} \cdot b_{h-SDS}); \tag{4.2}$$

where $\rho_d = 1 \times 10^{-6}$ Å^{-2} and $\rho_h = 4 \times 10^{-6}$ Å^{-2} are the values of SLD fixed for contrast 1 and 2, respectively, d_d and d_h are the thickness values fitted for contrast 1 and 2, respectively. While the strong scattering in contrast 1 allows resolving Γ_{SDS} in 1 min slices, the low scattering in contrast 2 makes it necessary to accurately determine the background and resolve 3 min slices to have better statistics, less noisy data and resolve accurately Γ_{PLL}. For that reason, the background was determined as the average value from a series of measurements of the air/ACMW interface using 1 min slices (3.74×10^{-5}) and 3 min slices (3.76×10^{-5}). The parameters d_d and d_h were fitted using the fit batch data option of Motofit,[36] a single layer model and a roughness of 3.5 Å and the results were then used to solve equations 4.1 and 4.2. Table 4.1 shows the values of scattering length, molecular volume and scattering length density used for each component studied in this work.

Table 4.1. Scattering length (*b*), molecular volume (V_m) and scattering length density (ρ) used in this work for the different components studied.

Component	***b* (fm)**	**V_m (Å^3)**	**ρ (x 10^{-6} Å^{-2})**
SS Headgroups	29.71	61	4.87
$C_{12}H_{25}$-Chains	–13.76	352	–0.39
$C_{12}D_{25}$-Chains	246.53	352	7.00
SDS Molecules	15.95	413	0.39
d_{25}-SDS Molecules	276.24	413	6.69
PLL (in ACMW)	18.85	173	1.09
PLL (in D_2O)	53.35	173	3.09

4.6.4 Ellipsometry data on spread PLL/SDS film dynamics

In order to verify if the surface pressure dynamics and the variation of interfacial material in the film was reproducible, 6 consecutive compression/expansion cycles of a PLL/SDS film were performed. In addition to the data shown in Figure 4.2C, where Γ_{SDS} and Γ_{PLL} are reproducible over three cycles, Figure 4.7 shows that the response of the film in terms of Π and $d\Delta$ is very similar over 6 consecutive cycles. These results indicate that the material expelled from the monolayer to ESs in each compression is efficiently reincorporated during each expansion, proving the high reproducibility of spread PLL/SDS film dynamics, which may be particularly important for transfer applications.

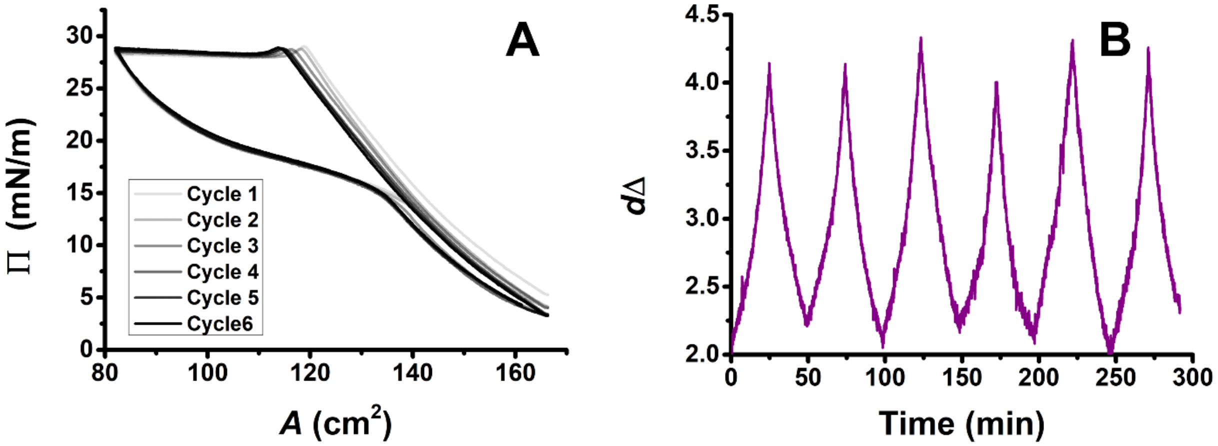

Figure 4.7. Variation of (A) Π as a function of *A* and (B) *d*Δ as a function of time during 6 consecutive compression/expansion cycles for spread PLL/SDS films.

4.6.5 Brewster angle microscopy images

The BAM images shown in the Figure 4.2D of the manuscript are shown in Figure 4.8 at a higher resolution. Before collapse, it is possible to clearly observe the presence of a homogeneous surface monolayer with a refractive index different from that of water, the intensity of which increases with the compression of the film. After the collapse, the presence of ESs below the surface monolayer causes another refractive index change such that discrete regions start to become visible on the µm-scale.

Next, a quantitative analysis of the BAM image in the compressed state v has been carried out. For this purpose, ImageJ software has been used to clean the image and calculate the fraction of the area occupied by the ESs. Although the result of the fraction of area occupied by the ESs variying considerably on changing the threshold used for the analysis, the value obtained was around 30 %. In this system, this calculation is difficult because the instrument is not focused on the ESs but on the surface monolayer, making it difficult to obtain accurate values of the area occupied by the ESs. However, this technique shows that the ESs are formed after the collapse and their number increase with the compression, which is in agreement with the increasing coverage obtained from the mid-Q_z analysis.

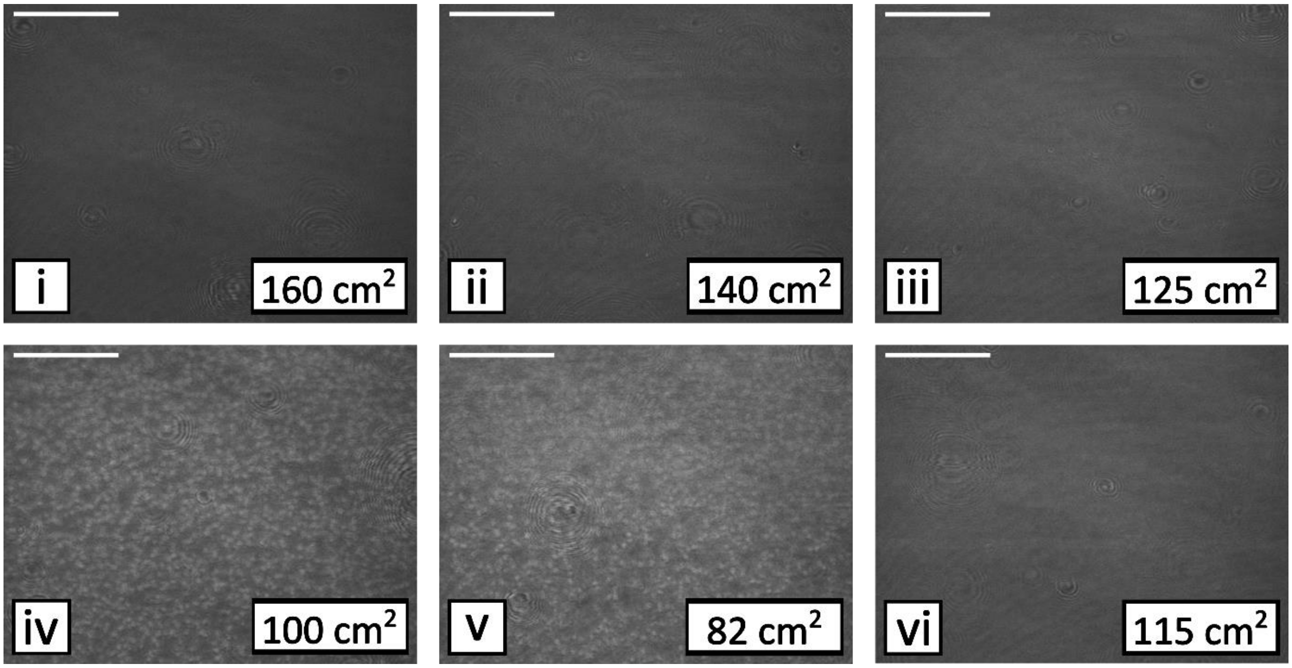

Figure 4.8. BAM images of PLL/SDS films at different compression states. The states i-vi correspond to the states indicated in Figure 4.2D.

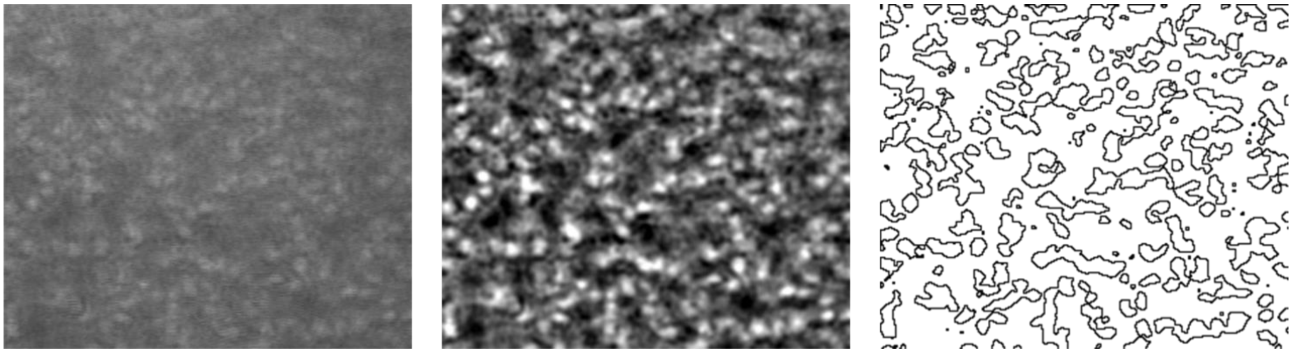

Figure 4.9. Zoom of a region of the image in the compression state v (left) together with the image cleaning treatment (centre) and the calculation of the area occupied by the ESs (right).

4.6.6 Full-Q_z structural analysis: fitting and parameters

The full-Q_z range Q_z = 0.01–0.25 Å^{-1} was recorded to resolve the structure of PLL/SDS films at high compression ratio in 4 isotopic contrasts: PLL with d-SDS in ACMW, PLL with d-SDS in D_2O, PLL with h-SDS in D_2O and PLL with h-SDS in ACMW. The background was subtracted from the data using the area detector.

The global fit of the full-Q_z data has been performed considering a model comprising four stratified layers as it was the smallest number of layers to result in a satisfactory fit of the data: 1) surfactant tails, 2) surfactant headgroups with PLL electrostatically bound and solvent, 3) PLL layer and solvent, and 4) the ESs formed by the surfactant molecules expelled from the interface and solvent. Each layer, *i*, is characterised by four parameters: the SLD, the thickness (d_i), the roughness and the solvent volume fraction (v_f). Firstly, a roughness of 3.5 Å consistent with the presence of capillary waves was applied to all interfaces.[37] Secondly, we considered that the SDS monolayer (i.e. the surfactant layer in contact with air with hydrated polyelectrolyte bound to the headgroups) surface excess is equal to 4.0 ± 0.1 μmol/m^2 as obtained from the low-Q_z analysis when the film collapses. Thus, the thickness of the surfactant tails layer was fixed to 8.5 Å. In addition, the surface excess of surfactant tails must be equal to the surface excess of headgroups to ensure physical reality. Besides, here the interfacial film is composed of surfactant and polyelectrolyte that interact electrostatically, making the headgroups layer more condensed due to the presence of PLL. Since PLL present labile protons in the amine groups that can exchange with the solution, we have considered a 90% of proton/deuterium exchange as generally considered for proteins. Therefore, another constraint is introduced as the SLD of the headgroups layer must be consistent between the contrasts in ACMW, where the SLD of PLL is equal to 1.09 $\times 10^{-6}$ Å^{-2}, and the contrast in D_2O, where the SLD of PLL is equal to 3.09 $\times 10^{-6}$ Å^{-2}. Finally, the parameters that have been fitted are *d* and v_f of layers 3 (PLL) and 4 (ESs). The amount of PLL in the headgroups has been fixed but iteratively modified until the difference between the model and the experimental data (χ^2) is minimised, thus obtaining the model that best represents the structure of the P/S film. Residual background values were used as follows: 1×10^{-7} for d-SDS in ACMW, 3×10^{-7} for d-SDS and h-SDS in D_2O, and 4×10^{-6} for h-SDS in ACMW. Table 4.2 shows the parameters used and fitted in the full-Q_z structural analysis. The uncertainties of the fitting parameters have been calculated as the difference between the optimised parameter and the variation of the optimised parameter that gives rise to an increase of the χ^2 of the fit by 10%. Finally, the uncertainties of the surface excess values of SDS and PLL derived from the full-Q_z fit can be determined from the uncertainties in layer 2 and 3 for PLL, and layers 1, 2 and 4 for SDS.

Thus, the uncertainties of the surface excess have been calculated as the square-root of the linear sum of squared standard uncertainties.

The surface excess of SDS obtained from the full-Q_z fit (5.7 ± 0.3 μmol/cm^2) is in agreement with the one obtained from the low-Q_z at maximum compression (5.6 ± 0.1 μmol/cm^2). However, a significant lower surface excess of PLL is obtained from the low-Q_z (4.7 ± 0.3 μmol/cm^2) respect to the full-Q_z (6.3 ± 0.5 μmol/cm^2), which could be related to the fact that the low-Q_z present high sensitivity to the surface excess but not to the interfacial structure, while the full-Q_z is very sensitive to the structure but less to the surface excess.

Table 4.2. Thickness (d_i), scattering length density (ρ_i), solvent volume fraction (v_{fi}) and composition obtained from the correspondent fit for each layer of the PLL/SDS films spread from overcharged aggregates, where i is the layer number. The parameters fitted are d_3, v_{f3}, d_4 and v_{f4}.

Layer	Parameter	d-SDS/ACMW	d-SDS/D₂O	h-SDS/D₂O	h-SDS/ACMW
1	d_1 (Å)	8.5 ± 0.2	8.5 ± 0.2	8.5 ± 0.2	8.5 ± 0.2
	ρ_1 (x 10^{-6} Å^{-2})	7	7	-0.39	-0.39
	v_{f1}	0	0	0	0
	Composition	100% SDS chains	100% SDS chains	100% SDS chains	100% SDS chains
2	d_2 (Å)	4	4	4	4
	ρ_2 (x 10^{-6} Å^{-2})	2.90	3.94	3.94	2.90
	v_{f2}	23 ± 1	23 ± 1	23 ± 1	23 ± 1
	Composition	37% SDS heads 40% PLL 23 % solvent	37% SDS heads 40% PLL 23 % solvent	37% SDS heads 40% PLL 23 % solvent	37% SDS heads 40% PLL 23 % solvent
3	d_3 (Å)	9.6 ± 0.7	9.6 ± 0.7	9.6 ± 0.7	9.6 ± 0.7
	ρ_3 (x 10^{-6} Å^{-2})	1.09	3.09	3.09	1.09
	v_{f3}	48 ± 4	48 ± 4	48 ± 4	48 ± 4
	Composition	52% PLL 48% solvent	52% PLL 48% solvent	52% PLL 48% solvent	52% PLL 48% solvent
4	d_4 (Å)	21.8 ± 0.8	21.8 ± 0.8	21.8 ± 0.8	21.8 ± 0.8
	ρ_4 (x 10^{-6} Å^{-2})	6.69	6.69	0.39	0.39
	v_{f4}	81.2 ± 0.7	81.2 ± 0.7	81.2 ± 0.7	81.2 ± 0.7
	Composition	19% SDS 81% solvent	19% SDS 81% solvent	19% SDS 81% solvent	19% SDS 81% solvent

Indeed, the variation of the thickness and the solvent content of the PLL layer provides fits with similar χ^2 but a surface excess varying from 5.8 ± 0.5 to 6.7 ± 0.7 μmol/cm^2 (green square and circle in Table 4.3 and Figure 4.10, respectively), showing that the sensitivity to the surface excess of this layer in the full-Q_z is lower. Table 4.3 and Figure 4.10 shows the results obtained from the fits varying the thickness and the solvent of the PLL layer.

Table 4.3. χ^2 and Γ_{PLL} values of different fits varying the amount of solvent of the PLL layer. The first three columns show the results of the fits fixing the thickness of the film and varying the amount of solvent. The last three columns show the results of the fits changing the solvent and fitting the thickness of the PLL layer. The green box indicates the fits with similar and low χ^2 values shown in Figure 4.10 with a green circle.

$d_{4,fixed}$ = 9.6 Å			$d_{4,fitted}$		
$v_{f,4}$ (%)	χ^2	Γ_{PLL}	*d* (Å)	χ^2	Γ_{PLL}
20	31.7741	8.99	7.00	12.8575	6.91
25	23.2029	8.52	7.41	10.8608	6.87
30	16.2872	8.05	7.85	9.00087	6.81
35	11.0186	7.59	8.32	7.35884	6.73
40	7.39466	7.12	8.82	6.04526	6.62
45	5.41828	6.66	9.35	5.21099	6.47
50	5.09806	6.19	9.91	5.06135	6.29
55	6.44817	5.73	10.47	5.87218	6.06
60	9.48864	5.26	10.99	8.0018	5.76
65	14.2441	4.80	11.41	11.8823	5.37
70	20.7463	4.33	11.65	17.9588	4.89

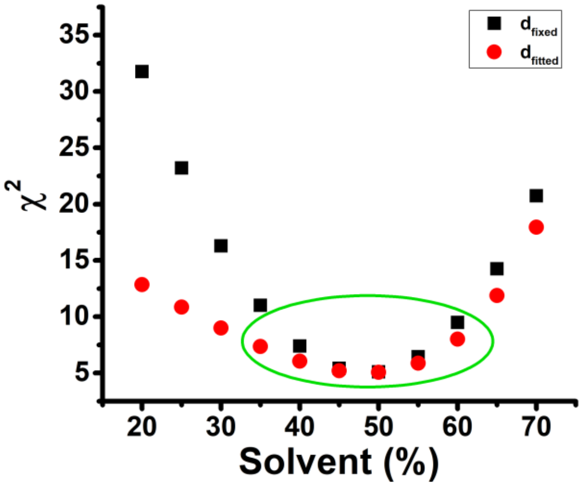

Figure 4.10. Variation of the χ^2 of different fits varying the amount of solvent in the PLL layer and fixing (black squares) or fitting (red circles) its thickness. The green circle indicates the region where the amount of solvent can vary from 35 to 60 % yielding fits with similar χ^2.

4.6.7 Mid-Q_z structural dynamics: fitting

A novel time-resolved method was used to follow variations of the reflectivity in the mid-Q_z range allowing the characterisation of structural changes during film dynamics. Data were recorded using an incident angle of 1.97° and reduced over 3.6–20 Å to get Q_z = 0.02–0.12 Å^{-1}. The reason why we chose the mid-Q_z region to follow the structural dynamics is because the Kiessig fringe that reveals the presence of the ESs appears in this region. In addition, the peak of the neutron flux is at Q_z = 0.1 Å^{-1} where the Kiessig fringe appears. We chose the contrast of PLL with h-SDS in D_2O because it is very sensitive to the presence of the surfactant ES as the difference in scattering between the surfactant chains and the solvent is very high, while it is less sensitive to the monolayer as the difference in scattering between air and surfactant chains is low. Thus, the formation of an extended structure of hydrogenous material in D_2O and the incident angle used offer the optimal conditions to follow the structural changes taking place during the collapse of the film.

We have fitted the mid-Q_z data with two different approaches showing that the decrease in reflectivity when we compress beyond the collapse of the film is due to the increase in the coverage of the ESs and not its thickness. In both cases the model that best fits the full-Q_z data reported in Table 4.2 has been used, varying only the coverage and/or thickness of the fourth layer. The first approach consists of a batch fit of the coverage fixing the thickness to the one obtained in the full-Q_z model (d_4 = 21.8 Å). The second approach consists of a batch data fit of the coverage fixing the thickness to d_4 = 21.8 × (Cov./Cov.max) Å, where Cov. is the coverage obtained in the previous fit and Cov.$_{\text{max}}$ is the one obtained at full compression, i.e., 16 %. In this way, we can keep constant the volume fraction and verify if the changes in reflectivity results from changes in the coverage (approach 1) or thickness (approach 2) looking at the χ^2 obtained in each case. Table 4.4 shows the values of coverage and χ^2 derived from the fits and Figure 4.11 shows the comparison between the χ^2 values obtained for each slice using both approaches. The 17- and 22-min slices correspond to the first and the last slice recorded in the Π plateau region, respectively. The results show that a lower χ^2 is obtained for all slices using the approach 1, with a maximum difference of 30% in the slice 19. Therefore, we demonstrate that the structural changes taking place during the collapse of the film are due to an increase of the coverage and not the thickness.

Table 4.4. Values of coverage and χ^2 obtained from the fits of 1-min slices in the Π plateau region using approaches 1 and 2 described in the text.

	Approach 1 d_4 = 22 Å			**Approach 2** d_4 = 22 · (Cov./Cov.$_{max}$) Å		
Slice (min)	**d_4 (Å)**	**Coverage (%)**	**χ^2**	**d_4 (Å)**	**Coverage (%)**	**χ^2**
17	22	3	1.316	4	24	1.463
18	22	6	2.126	9	19	2.880
19	22	8	2.318	11	18	3.263
20	22	11	1.533	15	17	2.153
21	22	14	1.427	19	17	1.788
22	22	16	1.830	22	--	--

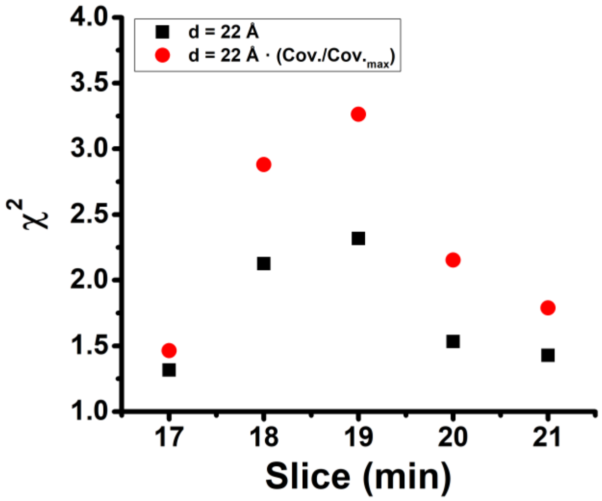

Figure 4.11. Variation of the χ^2 of each 1-min slice in the Π plateau region using approaches 1 (black squares) and 2 (red circles) for the ESs of spread PLL/SDS films.

4.7 References

(1) Guan, W.; Zhou, W.; Lu, J.; Lu, C. Luminescent Films for Chemo- and Biosensing. *Chem. Soc. Rev.* **2015**, *44*, 6981–7009.

(2) Hammond, P. T. Building Biomedical Materials Layer-by-Layer. *Mater. Today* **2012**, *15*, 196–206.

(3) Zelikin, A. N. Drug Releasing Polymer Thin Films: New Era of Surface-Mediated Drug Delivery. *ACS Nano* **2010**, *4*, 2494–2509.

(4) Oliveira, O. N.; Caseli, L.; Ariga, K. The Past and the Future of Langmuir and Langmuir–Blodgett Films. *Chem. Rev.* **2022**, *122*, 6459–6513.

(5) Richardson, J. J.; Cui, J.; Björnmalm, M.; Braunger, J. A.; Ejima, H.; Caruso, F. Innovation in Layer-by-Layer Assembly. *Chem. Rev.* **2016**, *116*, 14828–14867.

(6) Campbell, R. A.; Yanez Arteta, M.; Angus-Smyth, A.; Nylander, T.; Varga, I. Multilayers at Interfaces of an Oppositely Charged Polyelectrolyte/Surfactant System Resulting from the Transport of Bulk Aggregates under Gravity. *J. Phys. Chem. B* **2012**, *116*, 7981–7990.

(7) Ariga, K. Don't Forget Langmuir–Blodgett Films 2020: Interfacial Nanoarchitectonics with Molecules, Materials, and Living Objects. *Langmuir* **2020**, *36*, 7158–7180.

(8) Rubia-Payá, C.; Jimenez-Millán, E.; Giner-Casares, J. J.; Brezesinski, G.; Martín-Romero, M. T.; Camacho, L. From Two-Dimensional to Three-Dimensional at the Air/Water Interface: The Self-Aggregation of the Acridine Dye in Mixed Monolayers. *Langmuir* **2013**, *29*, 4796–4805.

(9) Campbell, R. A.; Tummino, A.; Noskov, B. A.; Varga, I. Polyelectrolyte/Surfactant Films Spread from Neutral Aggregates. *Soft Matter* **2016**, *12*, 5304–5312.

(10) Mészáros, R.; Thompson, L.; Bos, M.; Varga, I.; Gilányi, T. Interaction of Sodium Dodecyl Sulfate with Polyethyleneimine: Surfactant-Induced Polymer Solution Colloid Dispersion Transition. *Langmuir* **2003**, *19*, 609–615.

(11) Tummino, A.; Toscano, J.; Sebastiani, F.; Noskov, B. A.; Varga, I.; Campbell, R. A. Effects of Aggregate Charge and Subphase Ionic Strength on the Properties of Spread Polyelectrolyte/Surfactant Films at the Air/Water Interface under Static and Dynamic Conditions. *Langmuir* **2018**, *34*, 2312–2323.

(12) Castillo-Sánchez, J. C.; Cruz, A.; Pérez-Gil, J. Structural Hallmarks of Lung Surfactant: Lipid-Protein Interactions, Membrane Structure and Future Challenges. *Arch. Biochem. Biophys.* **2021**, *703*, 108850.

(13) Shi, B.; Zheng, M.; Tao, W.; Chung, R.; Jin, D.; Ghaffari, D.; Farokhzad, O. C. Challenges in DNA Delivery and Recent Advances in Multifunctional Polymeric DNA Delivery Systems. *Biomacromolecules* **2017**, *18*, 2231–2246.

(14) Li, N.; Zhao, L.; Qi, L.; Li, Z.; Luan, Y. Polymer Assembly: Promising Carriers as Co-Delivery Systems for Cancer Therapy. *Prog. Polym. Sci.* **2016**, *58*, 1–26.

(15) Lin, P. Y.; Chuang, E. Y.; Chiu, Y. H.; Chen, H. L.; Lin, K. J.; Juang, J. H.; Chiang, C. H.; Mi, F. L.; Sung, H. W. Safety and Efficacy of Self-Assembling Bubble Carriers Stabilized with Sodium Dodecyl Sulfate for Oral Delivery of Therapeutic Proteins. *J. Control. Release* **2017**, *259*, 168–175.

(16) Li, J.; An, P.; Qin, C.; Sun, C. L.; Sun, M.; Ji, Z.; Wang, C.; Du, G.; Liu, J.; Xie, Y. Bioinspired Dual-Responsive Nanofluidic Diodes by Poly-L-Lysine Modification. *ACS Omega* **2020**, *5*, 4501–4506.

(17) Pokharna, P. P.; Ghantasala, M. K.; Rozhkova, E. A. 3D Printed Polylactic Acid and Acrylonitrile Butadiene Styrene Fluidic Structures for Biological Applications: Tailoring Bio-Material Interface via Surface Modification. *Mater. Today Commun.* **2021**, *27*, 102348.

(18) Lam, J.; Clark, E. C.; Fong, E. L. S.; Lee, E. J.; Lu, S.; Tabata, Y.; Mikos, A. G. Evaluation of Cell-Laden Polyelectrolyte Hydrogels Incorporating Poly(L-Lysine) for Applications in Cartilage Tissue Engineering. *Biomaterials* **2016**, *83*, 332–346.

(19) Tuncaboylu, D. C.; Sari, M.; Oppermann, W.; Okay, O. Tough and Self-Healing Hydrogels Formed via Hydrophobic Interactions. *Macromolecules* **2011**, *4*, 4997–5005.

(20) Novotná, P.; Urbanová, M. Vibrational Circular Dichroism Study of Polypeptide Model–Membrane Systems. *Anal. Biochem.* **2012**, *427*, 211–218.

(21) De Feijter, J. A.; Benjamins, J.; Veer, F. A. Ellipsometry as a Tool to Study the Adsorption Behavior of Synthetic and Biopolymers at the Air-Water Interface. *Biopolymers* **1978**, *17*, 1759–1772.

(22) Daear, W.; Mahadeo, M.; Prenner, E. J. Applications of Brewster Angle Microscopy from Biological Materials to Biological Systems. *Biochim. Biophys. Acta* **2017**, *1859*, 1749–1766.

(23) Campbell, R. A. Recent Advances in Resolving Kinetic and Dynamic Processes at the Air/Water Interface Using Specular Neutron Reflectometry. *Curr. Opin. Colloid Interface Sci.* **2018**, *37*, 49–60.

(24) Skoda, M. W. A. Recent Developments in the Application of X-Ray and Neutron Reflectivity to Soft-Matter Systems. *Curr. Opin. Colloid Interface Sci.* **2019**, *42*, 41–54.

(25) Uhlig, M.; Löhmann, O.; Vargas Ruiz, S.; Varga, I.; Von Klitzing, R.; Campbell, R. A. New Structural Approach to Rationalize the Foam Film Stability of Oppositely Charged Polyelectrolyte/Surfactant Mixtures. *Chem. Commun.* **2020**, *56*, 952–955.

(26) Braun, L.; Uhlig, M.; Löhmann, O.; Campbell, R. A.; Schneck, E.; von Klitzing, R. Insights into Extended Structures and Their Driving Force: Influence of Salt on Polyelectrolyte/Surfactant Mixtures at the Air/Water Interface. *ACS Appl. Mater. Interfaces* **2022**, *14*, 27347–27359.

(27) Lee, Y.-L.; Dudek, A.; Ke, T.-N.; Hsiao, F.-W.; Chang, C.-H. Mixed Polyelectrolyte−Surfactant Langmuir Monolayers at the Air/Water Interface. *Macromolecules* **2008**, *41*, 5845–5853.

(28) Lipton, J.; Weng, G. M.; Röhr, J. A.; Wang, H.; Taylor, A. D. Layer-by-Layer Assembly of Two-Dimensional Materials: Meticulous Control on the Nanoscale. *Matter* **2020**, *2*, 1148–1165.

(29) Stuart, M. A. C.; Huck, W. T. S.; Genzer, J.; Müller, M.; Ober, C.; Stamm, M.; Sukhorukov, G. B.; Szleifer, I.; Tsukruk, V. V.; Urban, M.; Winnik, F.; Zauscher, S.; Luzinov, I.; Minko, S. Emerging Applications of Stimuli-Responsive Polymer Materials. *Nat. Mater.* **2010**, *9*, 101–113.

(30) Leahy, B. D.; Pocivavsek, L.; Meron, M.; Lam, K. L.; Salas, D.; Viccaro, P. J.; Lee, K. Y. C.; Lin, B. Geometric Stability and Elastic Response of a Supported Nanoparticle Film. *Phys. Rev. Lett.* **2010**, *105*, 058301.

(31) Clifton, L. A.; Campbell, R. A.; Sebastiani, F.; Campos-Terán, J.; Gonzalez-Martinez, J. F.; Björklund, S.; Sotres, J.; Cárdenas, M. Design and Use of Model Membranes to Study Biomolecular Interactions Using Complementary Surface-Sensitive Techniques. *Adv. Colloid Interface Sci.* **2020**, *277*, 102118.

(32) Tonigold, K.; Varga, I.; Nylander, T.; Campbell, R. A. Effects of Aggregates on Mixed Adsorption Layers of Poly(Ethylene Imine) and Sodium Dodecyl Sulfate at the Air/Liquid Interface. *Langmuir* **2009**, *25*, 4036–4046.

(33) Braun, L.; Uhlig, M.; von Klitzing, R.; Campbell, R. A. Polymers and Surfactants at Fluid Interfaces Studied with Specular Neutron Reflectometry. *Adv. Colloid Interface Sci.* **2017**, *247*, 130–148.

(34) Campbell, R. A.; Wacklin, H. P.; Sutton, I.; Cubitt, R.; Fragneto, G. FIGARO: The New Horizontal Neutron Reflectometer at the ILL. *Eur. Phys. J. Plus* **2011**, *126*, 1–22.

(35) Gutfreund, P.; Saerbeck, T.; Gonzalez, M. A.; Pellegrini, E.; Laver, M.; Dewhurst, C.; Cubitt, R. Towards Generalized Data Reduction on a Chopper-Based Time-of-Flight Neutron Reflectometer. *J. Appl. Crystallogr.* **2018**, *51*, 606–615.

(36) Nelson, A. Co-Refinement of Multiple-Contrast Neutron/X-Ray Reflectivity Data Using MOTOFIT. *J. Appl. Crystallogr.* **2006**, *39*, 273–276.

(37) Campbell, R. A.; Saaka, Y.; Shao, Y.; Gerelli, Y.; Cubitt, R.; Nazaruk, E.; Matyszewska, D.; Lawrence, M. J. Structure of Surfactant and Phospholipid Monolayers at the Air/Water Interface Modeled from Neutron Reflectivity Data. *J. Colloid Interface Sci.* **2018**, *531*, 98–108.

5 Study 2: Design of biocompatible films with controllable properties and morphology through specific polypeptide/surfactant interactions

Javier Carrascosa-Tejedor,[1,2*] Laura M. Miñarro,[1] Marina Efstratiou,[2] Imre Varga,[3] Maximilian W. A. Skoda,[4] Philipp Gutfreund,[1] Armando Maestro,[5,6] M. Jayne Lawrence[2*] and Richard A. Campbell[2*]

1. Institut Laue-Langevin, 71 Avenue des Martyrs, CS20156, 38042 Grenoble, France
2. Division of Pharmacy and Optometry, Faculty of Biology, Medicine and Health, University of Manchester, Oxford Road, Manchester M13 9PT, UK
3. Institute of Chemistry, Eötvös Loránd University, 112, Budapest H-1518, Hungary
4. ISIS Neutron and Muon Source, Rutherford Appleton Laboratory, Harwell Campus, Didcot OX11 0QX, UK
5. Basque Foundation for Science, Plaza Euskadi 5, Bilbao, 48009, Spain
6. Centro de Física de Materiales (CSIC, UPV/EHU) - Materials Physics Center MPC, Paseo Manuel de Lardizabal 5, E-20018 San Sebastián, Spain.

*corresponding authors: Javier Carrascosa-Tejedor, M. Jayne Lawrence and Richard A. Campbell

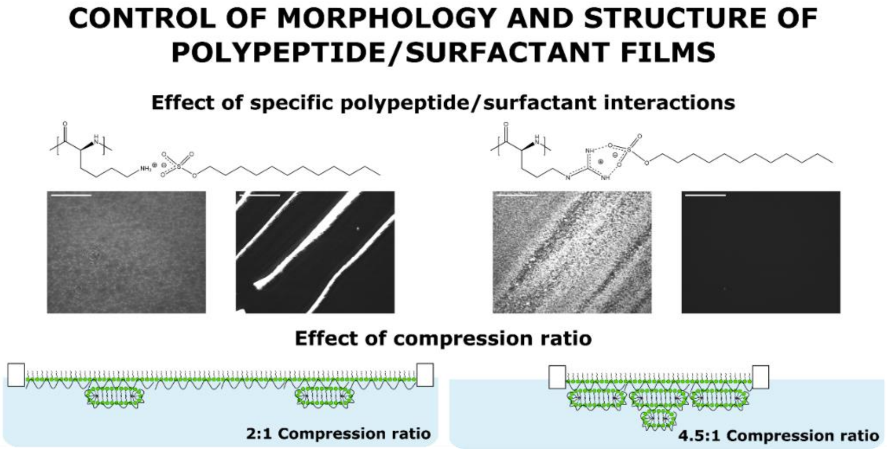

Figure 5.1. Table of contents illustrating the effect of specific PP/S interactions on the morphology of spread PLL/SDS and PLA/SDS films, and the effect of compression ratio on the structure of PLL/SDS films.

5.1 Abstract

We show for the first time the possibility to tune the structural and mechanical properties and morphology of biocompatible spread polypeptide/surfactant films at the air/water interface of a Langmuir trough as a function of the maximum compression ratio of the surface area. The systems studied are PLL or PLA with SDS, chosen because SDS (i) interacts more strongly with PLA due to formation of hydrogen bonds between the guanidinium group and its oxygen atoms, and (ii) induces β-sheet and α-helix conformations of PLL and PLA in the bulk, respectively, which hints that different interactions may be used to tune the properties of films containing ESs. NR reveals that application of a high compression ratio (4.5:1) to compact PLL/SDS monolayers results in the nanoscale self-assembly of ESs containing up to two PLL-wrapped SDS bilayers. Brewster angle microscopy images the ESs in PLL/SDS films as discrete regions on the micrometre scale while additional linear regions in PLA/SDS films are related to macroscopic folding of the film. The collapse mechanism of PLL/SDS films compressed to a very high ratio (10:1) is irreversible due to the formation of solid domains that remain embedded in the film upon expansion while that of PLA/SDS films is reversible. Ellipsometry demonstrates high stability of the different film morphologies resolved, making them amenable to potential transfer applications. These findings demonstrate that even subtle differences in the side group of a polypeptide can have a major influence on the film response, opening the possibility to design new biocompatible or biodegradable films with tailored properties for applications such as in tissue engineering, biosensors and antimicrobial coatings.

5.2 Introduction

Polypeptides are biocompatible and biodegradable polymers composed of a repeating sequence of amino acids linked by peptide bonds. They have attracted attention as promising biomaterials in numerous studies since they exhibit unique properties such as designability, biocompatibility, susceptibility to proteolysis, tuned hydrophilicity/hydrophobicity, inherent chirality and the ability to self-assemble in secondary structures (α-helices or β-sheets).[1] The latter property influences their size, stiffness, and function and facilitates the formation of well-defined supramolecular assemblies.[2,3] Indeed, the secondary structure of polypeptides can determine their antibacterial activity,[4] the stiffness of a gel,[5] or the morphology of self-assembled vesicles.[6] This is a unique property of polypeptides that many widely studied synthetic polymers such as NaPSS[7,8] PEI[9,10] or Pdadmac[11,12] do not present. There are 20 different natural amino acids and a wide variety of non-natural ones that offer the possibility to build polypeptides with a rich chemical diversity using the facile ring-opening polymerisation method.[13] The possibility to modify polypeptides including functional groups such as sugar moieties, reactive handles, charged species or surface active groups allows one to design a large number of different biomaterials.[14] In addition, they are versatile as they can be designed to respond to various stimuli (temperature, pH, ionic strength, light, enzymatic/biological or magnetic), allowing control of their properties and structure.[13]

Polypeptides have been widely used for the creation of multilayers in applications such as tissue engineering[15] or drug delivery,[16] both consisting exclusively of polypeptides[17] and in conjunction with other polyelectrolytes.[18] They have also been used to form polyplexes with nucleic acids in gene delivery,[19] and PP/S complexes.[20] However, despite significant advances made during the last decades in the field of P/S mixtures at the air/water interface, examples of work to tune and develop PP/S film properties are scarce.[21,22] Furthermore, the properties of P/S films cannot be directly extrapolated to PP/S films since, in addition to the electrostatic interactions, polypeptides can adopt secondary structures and form multiple hydrogen bonds. Previously, the equilibrium[23] and dynamic[24] properties of PLL/SDS mixtures were studied at the air/water interface. It was suggested that PLL adopts a β-sheet conformation at the interface, although this was inferred only from surface tension measurements. The application of NR later allowed direct quantification of the amounts of PLL and SDS at different pH values.[25] Differences between the results obtained by surface tensiometry and NR were rationalised in terms of different polypeptide conformations that affected only the surface tension values.

Recently, we have demonstrated precise control over the formation of ESs in PLL/SDS films at the air/water interface using a Langmuir trough with respect to compression or expansion of *A*.[26] The structures of these films consist of a surfactant monolayer, a layer of polypeptide bound to the surfactant headgroups (together, hereon in, referred to as the ‘surface monolayer’) as well as discrete patches either of surfactant bilayer wrapped by polypeptide or bound surfactant hemimicelles; the two possibilities were not distinguished from the experimental data. Reversible control of the quantity of a single additional layer of ESs using the Langmuir trough barriers was demonstrated up to a coverage of 18.8 ± 0.7%. In this work, PLL/SDS films were created using a film formation methodology,[27] which was recently developed using P/S mixtures by exploiting the dissociation and interfacial spreading of material from aggregates that had self-assembled in solution due to lack of colloidal stability of formed complexes.[28] The spreading of these aggregates at the air/water interface results in their dissociation and the material remains kinetically trapped due to the entropy associated with counterion release. Possibilities to trigger the formation of ESs through changing the charge and/or structure of the aggregates, and tune the resulting interfacial morphology through successive spreading of aggregates or compression of the surface area, were also demonstrated.[29] Recently, it has also been demonstrated that the stiffness of the polyelectrolyte plays an important role in the formation of ESs.[30] To the best of the authors' knowledge, these are the only examples of investigations in the literature on adsorbed layers or trapped films of oppositely charged PP/S mixtures at the air/water interface. Thus, this work provides a basis for the future development of PP/S films at the air/water interface, which has not been broadly exploited to date.

Given the multiple applications and all the above-mentioned characteristics that make polypeptides unique from other polyelectrolytes, the study of PP/S films at the air/water interface is of great interest, especially for applications where biocompatibility and biodegradability are essential. The present work involves a comparison of films involving different PP/S systems: PLL/SDS and PLA/SDS. The molecular structures of PLL, PLA and SDS are shown in Figure 5.2. Both polypeptides have positively charged groups in their side chains at physiological pH due to their high pK_a. Consequently, they exhibit strong electrostatic interactions with oppositely charged molecules or surfaces. Although they present a similar chemical structure, the interaction of the ammonium group of PLL with SDS is purely electrostatic, yet the guanidinium group can form additional hydrogen bonds that make the PLA/SDS interaction stronger.[31] Thus, specific PP/S headgroup interactions influence the resulting properties of the mixtures. Indeed, it has been shown that SDS induces the β-sheet conformation of PLL[23,25,32–35] and the α-helix conformation of PLA[34–37] in solution. Furthermore, it was shown that the secondary structure of polypeptides when forming complexes in solution is maintained when deposited as multilayers on solids,[38] which suggests that these differences may mean that PP/S films containing ESs may exhibit distinct physicochemical properties.

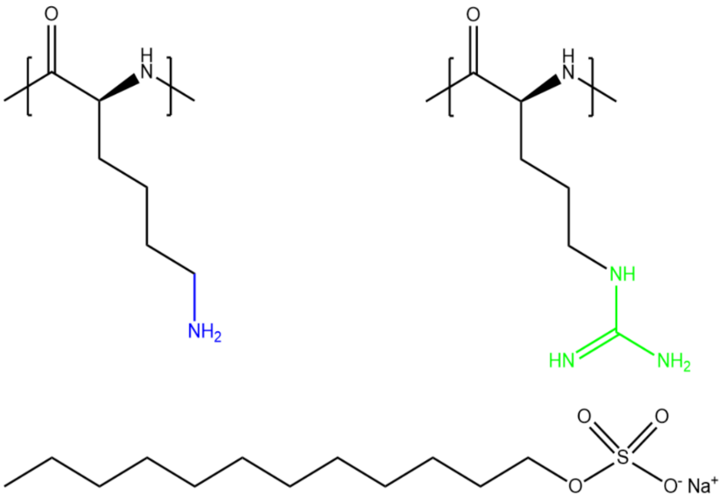

Figure 5.2. Chemical structures of PLL (left), PLA (right) and SDS (bottom). The ammonium group of PLL and the guanidinium group of PLA are indicated in blue and green, respectively.

The aim of this work is to resolve differences in the structural and mechanical properties and resulting morphologies between PLL/SDS and PLA/SDS films spread at the air/water interface with respect to the maximum compression ratio, defined as A_0/A, where A_0 is the initial surface area, and hence the amount of ESs present. The scope is to understand how specific PP/S interactions may be tuned for the development of new biocompatible or biodegradable films for a range of applications. An approach is used to manipulate films to different maximum compression ratios to determine if higher coverage of ESs than previously observed can be obtained, and if their increased coverage affects the mechanical properties of the films. The underlying hypothesis is that as these two PP/S systems adopt distinct secondary structures in the bulk, there may be distinct physicochemical properties of their spread films when compressed to produce ESs. It is hoped that this work will help us to understand better the influence on spread film properties of the polyelectrolyte stiffness,[30] where the hierarchy is β-sheet > α-helix > random coil. The application of a powerful combination of reflectometry techniques –NR, ellipsometry and BAM – allows us to resolve key processes that determine the dynamic behaviour of these PP/S films with respect to different lengths on the micrometre- and nanoscale.

5.3 Materials and Methods

5.3.1 Materials

15–30 kDa (~176 amino acids/molecule) poly-(L-lysine) hydrobromide and 5-15 kDa (~64 amino acids/molecule) poly-L-arginine hydrochloride powders, sodium dodecyl sulfate, sodium dodecyl-d25 sulfate, ethanol (≥99.8%) and D_2O were purchased from Sigma Aldrich. PLL, PLA, d-SDS and D_2O were used as received. SDS was recrystallised twice in ethanol followed by drying under vacuum. Ultra-pure water was generated by passing deionised water through a Milli-Q unit (total organic content ≤ 4 ppb, resistivity = 18 MΩ·cm).

5.3.2 Sample preparation

PLL and PLA stock solutions were prepared by dissolving the powder in H_2O and rotating the vial for a few hours. A stock solution of SDS 10 mM was prepared in H_2O and diluted to the required concentration for each experiment.

Fresh mixtures of PP/S aggregates were always prepared immediately before use to limit the growth of large aggregates prior to the experiment. First, an aliquot of 200 ppm PLL or PLA solution was poured into a clean vial containing a magnetic stirrer. Then, an aliquot of the same volume of SDS was rapidly added to the vial with stirring maintained for 3–5 s. Thus, the concentrations of polypeptide and surfactant in the final solution were half of those in the aliquots.

5.3.3 ζ-potential

ζ-potential measurements of PP/S aggregates were carried out using a Zetasizer Nano ZS90 and the M3-PLAS technique (Malvern Instruments Ltd., U.K.) to estimate the charge of the aggregates. The charge of the aggregates was determined at a constant concentration of P (100 ppm) as a function of the SDS concentration using a range of 0.4–1.0 mM and 0.2–1.0 mM for PLL and PLA, respectively.

5.3.4 Langmuir technique

Use of a Langmuir trough allows the study of the dynamic behaviour of the spread PP/S films during changes of *A*. The troughs used have two barriers that move symmetrically to record Π–*A* isotherms during consecutive compression/expansion cycles and stability measurements of the films over time at a constant area. Troughs of different sizes were used according to the requirements of the different setups of the applied techniques (NR, ellipsometry or BAM). The isotherms are presented as a function of A/A_0 (the inverse of the compression ratio) in order to compare the data obtained using different troughs. The Wilhelmy plate method has been used to record the variation of Π defined as the difference between the surface tension of pure water and that of the film using a filter paper plate.

The different troughs used in the present work are Kibron G1 and G2 (Finland) and Nima 721BAM (UK). A volume of 1130 µl of PLL/SDS and 1500 µl of PLA/SDS mixtures was used to create the initial films when using the Kibron G1 trough. The amount spread was chosen to obtain a surface monolayer at Π = 5–10 mN/m, which allows to study the surface monolayer/ESs transitions during successive cycles. The volume spread as well as the speed of the barriers was scaled to be consistent between the different troughs used. The trough and barriers were carefully cleaned with detergent Decon 90, ethanol and water before filling them with Milli-Q water.

5.3.5 Neutron reflectometry

NR is a widely used technique in the study of interfaces that allows the composition and structure perpendicular to the interface on the nanoscale to be determined accurately.[39–41] In an NR experiment, a neutron beam is incident onto the interface under study at grazing incident angles. Specular reflectometry occurs when the angle of incidence, θ, and the angle of reflection are equal. The reflectivity, *R*, is defined as the ratio between the reflected and the incident intensity and is recorded as a function of the momentum transfer normal to the interface, Q_z, defined as

$$Q_z = \frac{4\pi sin\theta}{\lambda} \tag{3.18}$$

where λ is the wavelength. The SLD is a measure of the scattering power of a material, and it is defined as the sum of the scattering lengths, *b*, of each nucleus in the molecule over its molecular volume (V_m). The surface excess of surfactant or polyelectrolyte in each layer, Γ_i, can be obtained as follows:

$$\Gamma_i = \frac{\rho d v_f}{b N_A} \tag{3.20}$$

Where v_f is the volume fraction, *d* is the thickness of the film and N_A the Avogadro's number.

Specular NR measurements were performed on the time-of-flight reflectometer INTER at the ISIS Pulsed Neutron and Muon Source (Didcot, UK) to resolve the structure of PLL/SDS films at a high compression ratio. Two different grazing incident angles of 0.8° and 2.3° and a wavelength range of λ = 1.5–16 Å were used. The absolute reflectivity was calibrated using a pure D_2O subphase. Three different isotopic contrasts were recorded: (1) d-SDS/ACMW (a mixture of 8.1% v/v D_2O in H_2O, SLD = 0 Å^{-2}), in which the scattering is dominated by the surfactant and is essential for determining the coverage of the surfactant monolayer and the ESs; (2) d-SDS/D_2O, which allows to determine the amount of PLL in the system as the SLDs of d-SDS (6.69×10^{-6} Å^{-2}) and D_2O (6.36×10^{-6} Å^{-2}) are close in value; and (3) h-SDS/D_2O, in which the scattering is dominated by the subphase and therefore it is very sensitive to the penetration of h-SDS in the bulk when they form ESs. The values of *b*, SLD and V_m of each of the components, information about the model applied to fit the data and details of the fitting procedure can be found in section 5.7.1. The data were analysed using the Motofit package and the different contrasts were co-refined.[42] The general procedure of fitting the data with different isotopic contrasts using a structural model with the minimum number of layers required has been followed.

5.3.6 Ellipsometry

Ellipsometry is an optical technique based on the polarisation changes that light undergoes when it is reflected at an interface. These changes are defined by the ratio of the overall Fresnel reflectivity coefficients of the parallel (r_P) and the perpendicular (r_S) components of the electric field, whose relative amplitude and phase change by different amounts. In experimental measurements of ellipsometry, the ellipsometric angles Δ, defined as the phase shift between the two components, and Ψ, where tan Ψ is the amplitude ratio, can be directly obtained.

$$\frac{r_P}{r_S} = tan\,\Psi\, e^{i\Delta} \tag{3.8}$$

In contrast to studies at solid/liquid interfaces that can be tuned to provide sensitivity of Ψ and Δ to the density and thickness of interfacial material,[43] the application of ellipsometry in the study of thin transparent films at the air/water interface offers poor sensitivity of Ψ to the film properties and often only values of Δ are interpreted.[27,44,45] The values of $d\Delta = \Delta_{PP/S}$ (for the PP/S film) – Δ_{water} (for pure water which approximately accounts for the contribution of surface roughness) are reported as an approximately proportional measure of the total surface amount of the PP/S films. The relatively small probed area (~1 mm^2) and the fast acquisition time (~5 s) makes ellipsometry an ideal technique to do time/spatial resolved experiments as temporal fluctuations in the signal can reveal the presence of inhomogeneities in the interface on the micrometer scale.[27,44,46]

The ellipsometry data were recorded using two different ellipsometers coupled to a Langmuir trough. A Beaglehole Picometer Light ellipsometer (New Zealand) equipped with a He-Ne laser with a wavelength of λ = 632.8 nm was used to record the variation of $d\Delta$ during compression/expansion cycles at an angle of incidence of 51° and a data acquisition rate of 0.2 Hz. An Accurion EP4 ellipsometer (Germany) equipped with a blue diode laser with a wavelength of λ = 489.2 nm was used to record the stability measurements presented in section 5.7.3 at an angle of incidence of 50° and a data acquisition rate of 0.1 Hz.

5.3.7 Brewster angle microscopy

BAM is a direct and non-invasive imaging technique used to characterise the in-plane organisation of fluid films at the air/water interface and the presence of inhomogeneities.[47] When *p*-polarised light is directed at the Brewster angle (~53.1°) onto the air/water interface, the reflectivity is almost zero. The presence of a thin film at the air/water interface whose refractive index is different from that of water causes the reflection of the incident light allowing visualisation and imaging of the film under study. Any additional material that thickens the film will contribute to the reflected light. Thus, a dark image is observed when light is directed onto the air/water interface or a homogenous layer, yet the presence of inhomogeneous patches of ESs will be observed as brighter regions. An Accurion Nanofilm EP3 Brewster angle microscope (Germany) equipped with a Nd:YAG laser (λ = 532 nm), a 10x objective and a CCD detector was used at an angle of incidence θ = 53.1°. Background was not subtracted.

5.4 Results and discussion

A characterisation of the charge of the complexes was carried out first with a fixed polypeptide concentration of 100 ppm as a function of the SDS concentration. Figure 5.3 shows the results obtained for the PLL/SDS and the PLA/SDS systems. The variation of the ζ-potential as function of the bulk surfactant concentration follows a similar trend as that of other P/S systems.[27,28,48] The increase of the concentration of SDS results in a transition from positive to negative surface charge density. The concentration of surfactant needed to produce neutral PLL/SDS or PLA/SDS aggregates is 0.63 and 0.57 mM, respectively. The experimental values are close to the equivalent monomer concentration of 100 ppm of the polypeptides of 0.48 and 0.52 mM, respectively, evidencing a strong binding between the components at the point of charge neutrality. Nevertheless, the lower excess of SDS required to neutralise PLA/SDS aggregates (0.05 mM) compared to PLL/SDS aggregates (0.15 mM) suggests that the interaction of SDS with PLA is stronger than with PLL. The PP/S interaction strength depends on the electrostatic interactions between the charged groups and the hydrophobic interactions between surfactant chains. Since the same surfactant is used, the differences observed might arise from different specific PP/S interactions.

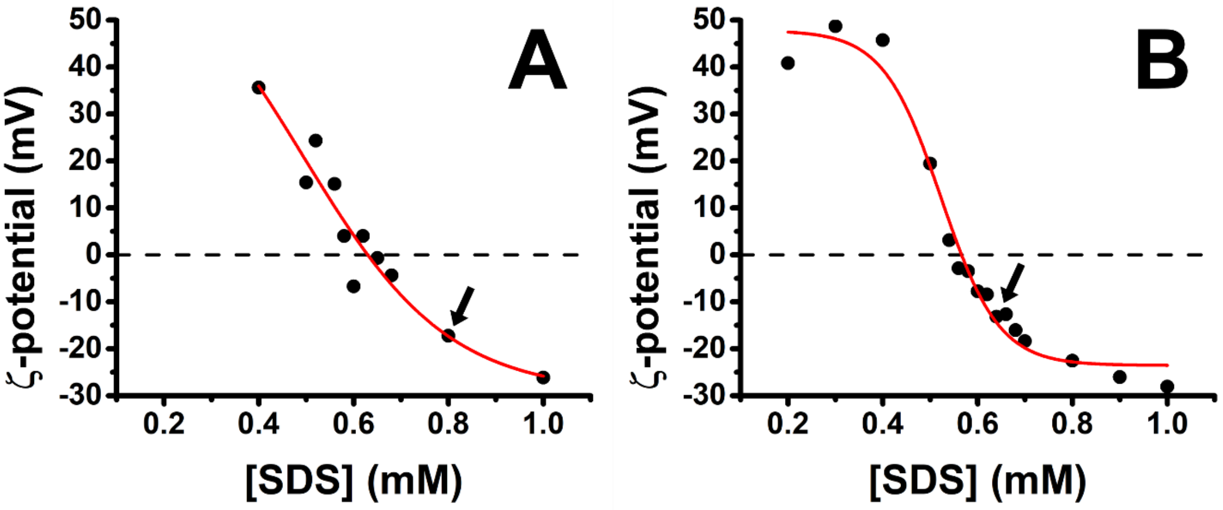

Figure 5.3. Variation of the ζ-potential of (A) PLL/SDS (reproduced from Carrascosa-Tejedor et al., 2022)[26] and (B) PLA/SDS aggregates as a function of the concentration of SDS and at a constant concentration of 100 ppm polypeptide. The black circles represent the experimental data points and the red line a sigmoidal fit. The black dashed lines indicate neutral charge. The standard error in the ζ-potential values was found to be around 10%, smaller than the symbol size. Black arrows indicate the concentrations used to create the films.

The stronger affinity of SDS to PLA found in this work is in agreement with isothermal titration calorimetry results where it was observed that the enthalpy upon SDS binding to PLA and PLL was –15.4 ± 1 and –6.9 ± 1 kJ/mol, respectively.[49] In addition, it has also been demonstrated that the electrophoretic mobility of arginine in sodium sulfate solutions was lower than that of lysine.[31] These results are also in agreement with the molecular dynamics simulations, where a greater affinity of sulfate to the guanidinium group was predicted and was attributed to the planar geometry of the group allowing hydrogen bonding with the two sulfate oxygen atoms. It may be noted that the strong binding at the point of charge neutrality observed in both systems is in agreement with other systems previously reported such as Pdadmac/SDS[48] or PEI/SDS,[50] but contrasts sharply with that of NaPSS/DTAB,[27] where for a bulk polyelectrolyte concentration of 100 ppm, the excess of surfactant needed to neutralise the aggregates is 5.5 mM. These differences may be related to the ability of the polyelectrolyte to wrap surfactant aggregates, which would be significantly influenced by its stiffness,[51–53] and it has also been found that more rigid polyelectrolytes form denser films.[7] Thus, the experimental charge neutrality may be an important parameter when assessing the stability of formed ESs in P/S or PP/S films, given that they were shown to be stable over time for PLL/SDS films with strong bulk binding[26] and unstable for NaPSS/DTAB films with weaker bulk binding.[29] Furthermore, it has been recently demonstrated that the stiffness of the polymer plays an important role in the stabilisation of ESs in adsorbed P/S layers.[30] Although the compensation of interfacial charges was identified as the main driving force for the formation of ESs, the possibility to control the 2D to 3D nature of the film by increasing the polyelectrolyte stiffness was demonstrated. The low binding efficiency of DTAB to NaPSS at the point of charge neutrality could be related also with its low persistence length (~1 nm), which may explain the difficulty to form stable ESs when this system is used.[29]

Concentrations of 0.80 and 0.62 mM were chosen to create the spread PLL/SDS and PLA/SDS films, respectively, because aggregates overcharged with an excess of surfactant have been shown to be efficient in forming ESs in previous studies.[26,29]

We reported previously the structure of PLL/SDS films at a 2:1 compression ratio using NR and a coverage of 19% of ESs was shown.[26] Nevertheless, it was not clear whether there was an additional PLL layer underneath the ESs as the inclusion of a low coverage of it in the model resulted in equivalent model fits to the experimental data. The structure of PLL/SDS films at a 4.5:1 compression ratio was studied using NR in the hope that increased coverage of any PLL layer that may be present in the ESs would allow it to be clearly resolved. If we assume that all of the surfactant expelled from the surface monolayer is incorporated in the surfactant bilayer structure, resolved for PLL/SDS films in our recent work,[29] coverage of the ESs should in principle reach 100% at a 4:1 compression ratio. Therefore, we could test the hypothesis that if all the material remains bound to the film upon further compression, a second layer of ESs would form beyond this compression ratio.

Figure 5.4A shows the reflectivity profiles measured and the model fits obtained from the analysis. The sharp and clear Kiessig fringes in the reflectivity profiles indicate the presence of a multilayered structure. Further evidence for the lateral domains of ESs on the micrometre scale includes a slight indication of off-specular neutron scattering and attenuation of the total reflection of D_2O by 4%. From the position of the minimum in the d-SDS/ACMW contrast (Q_z = 0.1 $Å^{-1}$), the presence of ESs with a length scale around 60 Å can be deduced. An optimised model of 6 stratified layers was found to be necessary to fit the data: (1) SDS tails, (2) SDS headgroups with PLL and solvent, (3) PLL, (4) PLL/SDS ESs with solvent, (5) PLL and (6) PLL/SDS ESs with solvent. More details about the model together with a table of optimised fitting parameters can be found in section 5.7.1. The analysis confirms our hypothesis that the compression of the film beyond a ratio of 4:1 leads to the formation of a second layer of ESs. Furthermore, compatible with a physical picture where polyelectrolyte screens the oppositely charged headgroups in adjacent surfactant bilayers, a PLL layer was required between the two layers of ESs, as described in section 5.7.2. An additional layer of PLL beneath the second layer of ESs did not, however, improve the quality of the fit, most likely due to its low coverage.

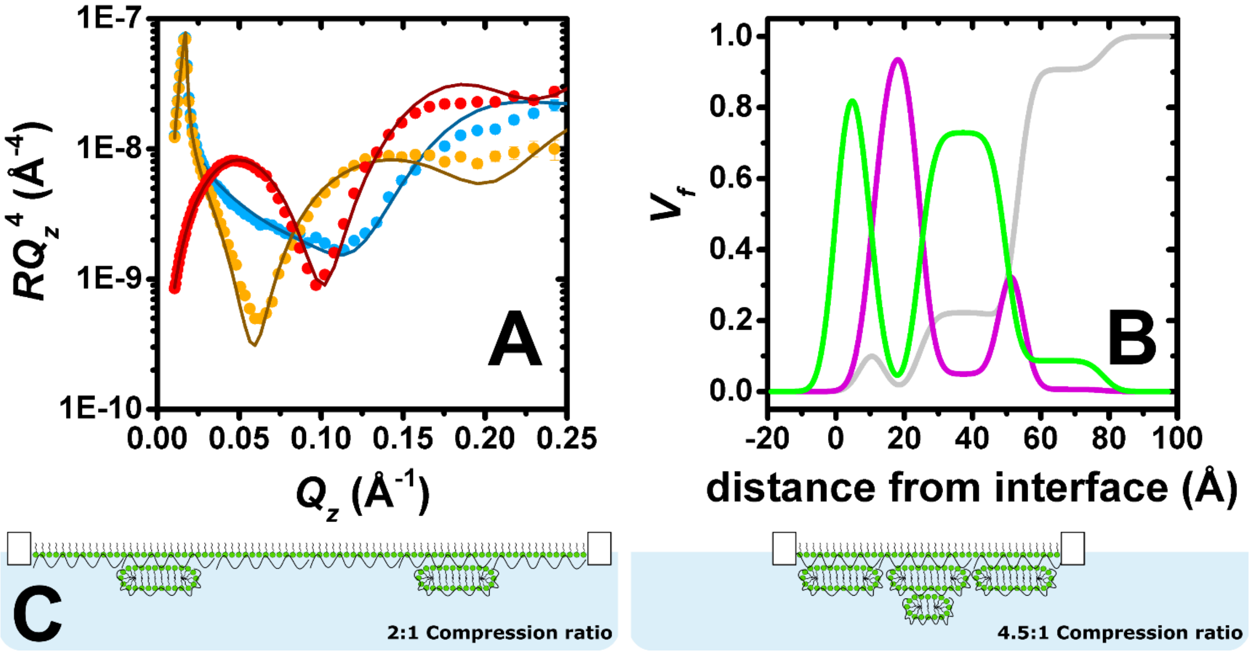

Figure 5.4. (A) Neutron reflectivity profiles of a PLL/SDS film compressed by a 4.5:1 compression ratio using d-SDS/ACMW (red circles), d-SDS/D_2O (blue circles) and h-SDS/D_2O (orange circles) contrasts. The continuous lines show the model fits. (B) Corresponding volume fraction profiles of SDS (green) solvent (grey) and PLL (purple). (C) Schematic illustrations of the structures of PLL/SDS films using 2:1 and 4.5:1 compression ratios.

Figure 5.4B shows the volume fraction profiles corresponding to the analysis. The high volume-fraction of PLL and SDS in the surface monolayer as well as in the first layer of ESs evidences the presence of a very compact film at the interface. It should be further noted that absence of a Bragg diffraction peak in any of the reflectivity profiles shows that P/S aggregates with an internal liquid crystalline structure were not resolved to have remained trapped in the spread film.[54] Thus, it can be concluded that the compression of the film allows the formation of a very compact film and the formation of an additional layer of ESs beneath when the first one reaches a high enough coverage. Figure 5.4C shows a two-dimensional schematic illustration of the structure of PLL/SDS films using a 2:1 and 4.5:1 compression ratio; illustrations are merely representative and are not to scale.

Having demonstrated the ability to increase the amount of ESs by increasing the compression ratio, we turn in the following sub-sections to the dynamic behaviour of PLL/SDS and PLA/SDS films during compression/expansion cycles as a function of the maximum compression ratio. First, the results of PLL/SDS films using a 2:1 compression ratio already published[26] are compared with the ones obtained on PLA/SDS films. Subsequently, data from samples involving two different maximum compression ratios of 5:1 and 10:1 are described. Thus, both the influence of (i) specific polypeptide/headgroups interactions and (ii) the formation of compact films on the properties of the films will be considered.

5.4.1 Maximum compression ratio of 2:1

Figure 5.5 shows the results obtained in the study of the dynamic behaviour of PLL/SDS and PLA/SDS films during consecutive compression/expansion cycles using the Langmuir trough, ellipsometry and BAM up to a maximum compression ratio of 2:1. It is worth noting that considering the volume and concentration of SDS in the spreading aliquot and the volume of water in the Langmuir trough, the final SDS concentration in both PP/S systems is less than 7×10^{-3} mM, where SDS alone still presents negligible surface activity,[55] hence, the interfacial properties measured are determined by the spread film. Through application of multiple experimental techniques previously,[26] the Π–A isotherms of PLL/SDS films can be described as follows. The data are characterised by three different regions (Figure 5.5A). First, compression of the film leads to an increase in the number of surfactant molecules per unit area in the surface monolayer, which results in a continuous increase in Π (from state i through state ii to state iii). Second, further compression of the film leads to its collapse as shown by the constant collapse pressure, Π_c, at ~28 mN/m: this is attributed to retention of the most compact state of the surface monolayer and ejection of surplus material to ESs upon further compression of the film (beyond state iii through state iv to state v).[26,29]

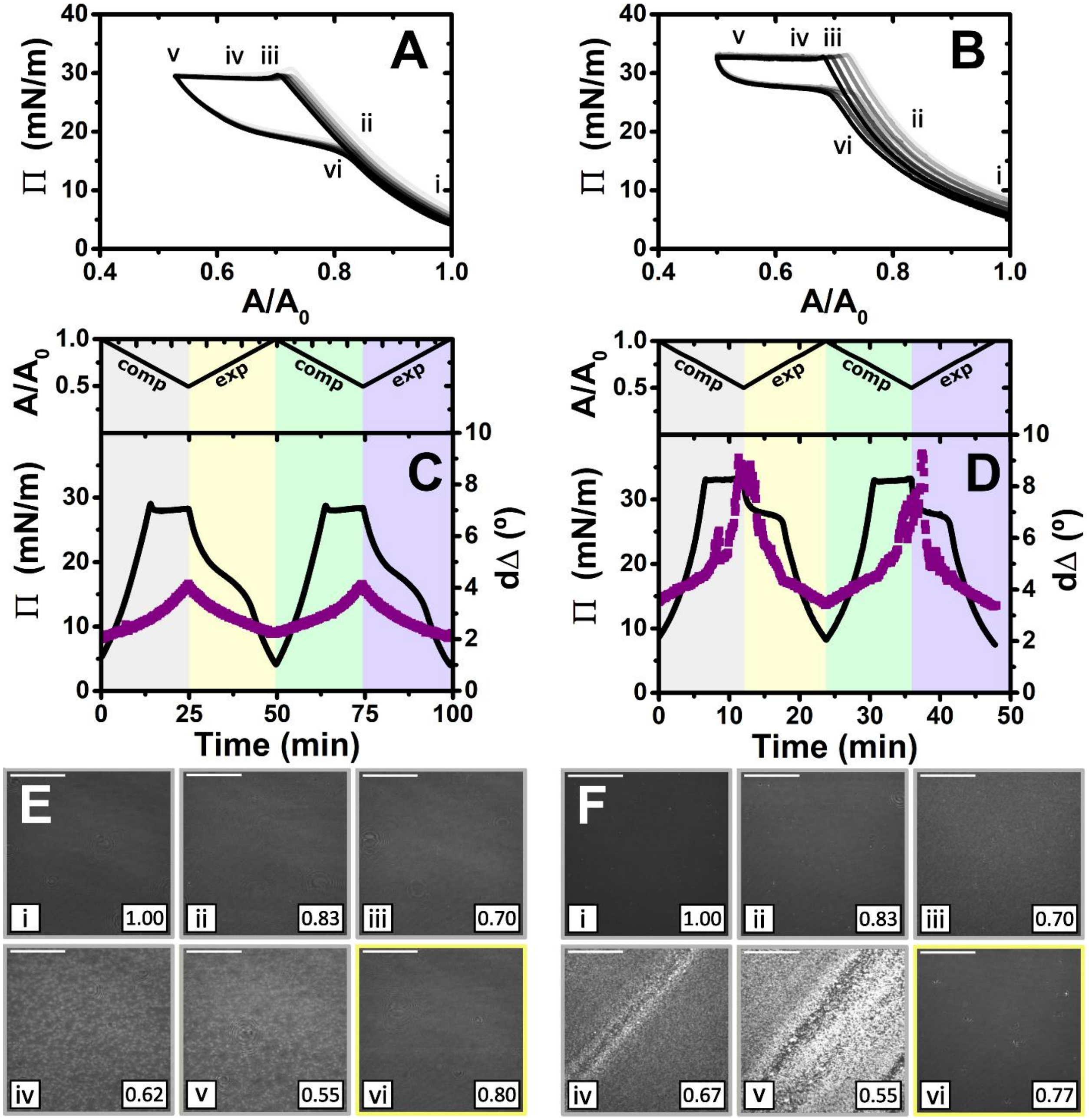

Figure 5.5. Π–*A* isotherms of (A) PLL/SDS and (B) PLA/SDS films using a 2:1 compression ratio during 5 consecutive compression/expansion cycles. The transparency of the data indicates the number of cycle, with cycle 1 being the most transparent and cycle 5 the least and the indices i-vi indicate different compression states. Variation of Π (black line) and *d*Δ (purple squares) as a function of time during two consecutive compression/expansion cycles of (C) PLL/SDS and (D) PLA/SDS films. The variation of *A* versus time is also included at the top of the graph. The different shadowed areas indicate the compression/expansion of the film. BAM images of (E) PLL/SDS (reproduced from Carrascosa-Tejedor et al., 2022)[26] and (F) PLA/SDS films corresponding to states i-vi as indicated in panels A and B and using the colour code of panels C and D. Scale bars are 100 µm.

Third, expansion of the film is characterised by a large hysteresis in Π, the presence of a pseudo-plateau and the merging of the isotherm on expansion into the isotherm on compression at large A/A_0, consistent with the reincorporation of material back into the surface monolayer yet with a kinetic barrier (through state vi). The mechanical properties of the film are reproducible over successive cycles. Consistent with the above description, the values of $d\Delta$ from ellipsometry continue to increase beyond the surface pressure collapse (Figure 5.5C), and it was data from NR that allowed us to confirm not only that Γ_{SDS} exceeds that in an SDS monolayer at ×2 its critical micelle concentration (cmc),[56] but that the coverage of the surface monolayer remains constant and the excess material is ejected into the ESs. BAM images (Figure 5.5E) also support this physical picture as the morphologies shown contain discrete regions on the µm-scale that grow in number with increasing compression only at higher compression ratios than the surface pressure collapse (states iv and v).

The Π–A response of PLA/SDS films (Figure 5.5B) is qualitatively similar to that of PLL/SDS films, exhibiting the three characteristic regions mentioned above. Therefore, we could expect that the dynamic behaviour of these films may be explained with a similar physical picture. The ellipsometry data (Figure 5.5D) show that the amount of material at the interface increases continuously with the compression beyond the surface pressure collapse and there is no evidence of loss of material from one cycle to the other. Thus, formation of ESs in PLA/SDS films is strongly inferred. In addition, the presence of fluctuations in $d\Delta$ is probably related to the presence of film inhomogeneities with a higher density of material.[44,46] Lastly, the BAM images (Figure 5.5F) clearly show the formation of discrete micro-domains after the collapse and the presence of areas with high intensity that are consistent with the $d\Delta$ fluctuations (states iv and v), even though they appear to have a distinct morphology from the ESs observed for PLL/SDS. Therefore, we can conclude that the PLA/SDS system exhibits the formation of ESs and that we can control their formation with the compression/expansion of the film, as has been previously reported for the PLL/SDS system.[26] Furthermore, it is shown that the properties of the films and the morphology of the ESs can be tuned by using polypeptides with different side chains that interact differently with the surfactant.

Although the mechanical responses of both systems to the compression/expansion cycles are similar, there are significant differences worth noting. The first one is the Π_C, ~28 mN/m and ~34 mN/m for the PLL and PLA/SDS films, respectively, while Π of an SDS monolayer at its cmc is 31 mN/m.[55] It has been shown that the interaction of SDS with other polyelectrolytes gives rise to very different interfacial properties, varying significantly the minimum surface tension, i.e., the higher Π reached.[25,44] Hence, the polyelectrolyte properties influence significantly the maximum compression state of the SDS molecules that can be reached before the film collapses.[55] This is also supported by the ellipsometry data, as the amount of interfacial material is significantly higher for PLA. One could expect that the differences in Π_C may be related to the ability of the polypeptide to interact with surfactant headgroups with a contribution in the plane of the headgroups layer (see Figure 5.5). However, the molecular volumes of lysine and arginine amino acids are 177 and 181 Å^3,[57] respectively, which are very similar. While the interaction between lysine monomers and the sulfate headgroup is purely electrostatic, the guanidinium group presents additional interactions due to the formation of hydrogen bonds with the oxygen atoms from the sulfate.[31] This difference gives rise to lateral interactions between the different chemical groups that may explain the formation of a layer with a higher coverage of surfactant in the surface monolayer. This interpretation is also in agreement with the discussion of the ζ-potential results presented above, where a smaller excess bulk surfactant concentration was required to neutralise PLA than PLL complexes. Another significant difference is the slope of the pseudo-plateau during the expansion, which is significantly lower for the PLA/SDS system. This could be related to the rate at which the material from the ESs is reincorporated into the surface monolayer upon film expansion. This would imply that PLA/SDS material recovery occurs much faster with a slope close to zero during a plateau on film expansion, while the higher slope in the case of PLL suggests that the reincorporation of the material from the ESs into the surface monolayer is slower than their formation, as has been demonstrated using NR.[26] Nevertheless, NR of PLA/SDS films (beyond the scope of the present work) would be necessary to confirm this inference, since ellipsometry cannot distinguish between the surface monolayer and the ESs. The collapse mechanism of both systems when compressed by 2:1 is reversible, reflecting the high efficiency of respreading of material upon expansion.

Having demonstrated the formation of ESs for both PP/S systems during dynamic compression/expansion cycles, Π and $d\Delta$ were recorded at a constant compression ratio of 2:1 to study the stability of the films. The results, presented in section 5.7.3, show that both films are stable for more than 1 h, making them robust and amenable for possible transfer applications.

5.4.2 Maximum compression ratio of 5:1

Higher compression ratios have also been applied to resolve if the mechanical film behaviour and the resulting morphologies can be tuned with respect to PP/S interactions in the films that contain a second layer of ESs. For this purpose, a maximum compression ratio of 5:1 (Figure 5.6) from the same spread volume and speed of the barriers were used as in the experiments described above. Compression of the films beyond a ratio of 2:1 results in the appearance of a new region during the compression where Π starts to increase again (Figure 5.6A and B). This result is surprising since the maximum Π of the system is broadly related to the most compact state of the surfactant in the surface monolayer. This new region would imply that the surface coverage of the surface monolayer is further increased, giving rise to an increase in the number of SDS molecules per unit area and a decrease in the amount of solvent in the headgroups layer. Although this is possible, in principle, considering that there is 23% of water in the headgroups layer when the film is compressed by a ratio of 2:1,[26] it was observed that the Wilhelmy plate is pulled sideways in the high-Π region, suggesting the formation of a solid film that exerts an additional force on the sensor, consistent with very low water content in PLL/SDS films resolved using NR above. An experiment reported in section 5.7.4 demonstrates that indeed the measured values of Π are affected below A/A_0 = 0.33, hence hereon in we will refer to values of Π that exceed Π_c as values of an 'apparent Π'. Another significant difference with respect to the 2:1 compression is the appearance of a second collapse in the PLA/SDS system, which could be related to a change in the film structure after full coverage of the first layer of ESs is reached.

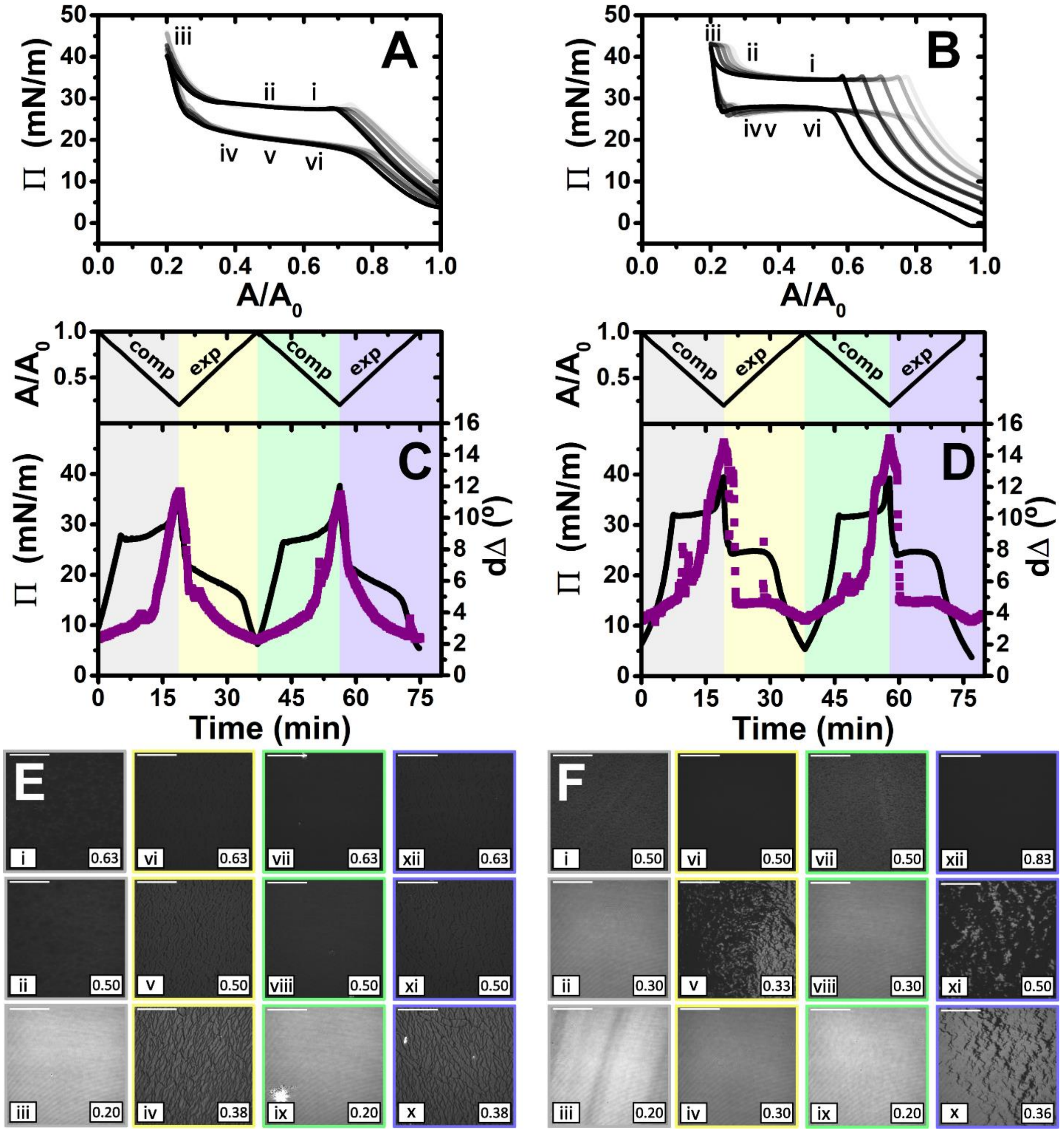

Figure 5.6. Π–*A* isotherms of (A) PLL/SDS and (B) PLA/SDS films using a 5:1 compression ratio during 5 consecutive compression/expansion cycles. The transparency of the data indicates the number of cycle, with cycle 1 being the most transparent and cycle 5 the least and the indices i-vi indicate different compression states. Variation of Π (black line) and *d*Δ (purple squares) as a function of time during two consecutive compression/expansion cycles of (C) PLL/SDS and (D) PLA/SDS films. The variation of *A* versus time is also included at the top of the graph. The different shadowed areas indicate the compression/expansion of the film. BAM images of (E) PLL/SDS and (F) PLA/SDS films corresponding to states i-vi as indicated in panels A and B and using the colour code of panels C and D. Note that only the indices i-vi have been included in panels A and B for the sake of clarity. Scale bars are 100 μm.

The ellipsometry data (Figures 5.6C and D) show that the approximate amount of material at the interface increased further beyond film compression of a 2:1 ratio. The $d\Delta$ values increase by factors of 2.9 and 1.7 with respect to the 2:1 compression ratio for PLL and PLA, respectively. It is worth noting that in going from a compression ratio of 2:1 to 5:1, assuming that no material is lost from the interface, the amount of material should increase by a factor of 2.5, so the higher value obtained here for PLL/SDS films, in combination with the steeper slope in the ellipsometry data upon increasing compression ratio, suggest that there is a contribution of the anisotropy of ESs to the ellipticity.

BAM images of PLL/SDS and PLA/SDS films (Figures 5.6E and F) show a continuous increase in the number of ESs until a homogeneous, high-intensity image is observed, suggesting a very high coverage of ESs. The PLA/SDS system presents additional linear regions with higher intensity that could be related to the folding of the film when the ESs layer is fully coated, which is consistent with the second plateau observed in the Π–A isotherm. During expansion, fracture and reincorporation of the material can be observed gradually in the PLL/SDS system, whereas for the PLA/SDS system the solid film disappears abruptly shortly after the start of decompression. The $d\Delta$ values during expansion are in good agreement with the morphologies observed using BAM. The gradual disappearance of the solid film in the PLL/SDS system is translated into a continuous decrease of $d\Delta$ during expansion. However, the PLA/SDS system shows a dramatic drop in the values during expansion followed by a plateau, attributed to whether or not the solid domains are in the region of the interface illuminated by the laser. Then, the value of $d\Delta$ in the plateau coincides with the value at the collapse during compression. This confirms that the material is reincorporated by efficiently filling the surface area created upon expansion at a very similar rate to the barriers movement during expansion, i.e., with minimal kinetic barrier. The stability of the films compressed to a maximum ratio of 5:1 was also studied by Π and ellipsometry (Figure 5.11) showing stable $d\Delta$ values for more than 1 h.

5.4.3 Maximum compression ratio of 10:1

Lastly, films were compressed to a maximum ratio of 10:1, and the results obtained are shown in Figure 5.7. The isotherms show qualitatively similar behaviour to that described above for the maximum compression ratio of 5:1. However, there are a number of differences that give us additional information about the systems, especially in the case of PLL/SDS. A second kink in the apparent Π of the PLL/SDS film and a large shift of the isotherm from the first to the second cycle, as well as from the second to the third is observed (Figure 5.7A). These features may suggest that loss of material to the bulk occurs during the second kink. However, the apparent Π values reached in the minimum area are constant during the successive cycles, which precludes irreversible loss.

Similarly to the data on films with a maximum compression ratio of 5:1, the ellipsometry data show a continuous increase in *d*Δ during compression. However, the expansion is characterised by an initial region with a continuous decrease in *d*Δ followed by large temporal fluctuations that are present also in the subsequent full compression/expansion cycle. In addition, although the *d*Δ values at the beginning of the second cycle are lower, the ones at the maximum compression ratio are similar, suggesting that there is no irreversible loss of material from the spread film.

We consider now the morphology of the spread films from the two systems in turn. BAM images presented in Figure 5.7E show the fracture of the solid PLL/SDS film during the first compression (state iii) and the presence of solid domains throughout the rest of the experiment (states v, viii, ix, x, xi, and xii). The characteristic behaviour of PLL/SDS films compressed to a maximum ratio of 10:1 can be explained by combining the information obtained from the different techniques. The application of high compression ratios results in the formation of a solid film that is fractured when a 10:1 compression ratio is reached. The expansion of the film is characterised by the presence of solid domains observed in the BAM images that contain a much larger amount of material and explain the large *d*Δ fluctuations. A similar behaviour has been reported for other polymers at the air/water interface.[46,58] Thus, we can conclude that the application of a 10:1 compression ratio gives rise to the irreversible formation of solid domains whose excess of material is not respread and remain trapped at the interface coexisting with the surface monolayer. Finally, the apparent Π–*A* isotherms can now be explained by the fact that after the formation of these solid domains, the excess of material trapped in them does not contribute to the apparent Π until the solid film forms again. Thus, the surface monolayer region is displaced considerably but the same apparent Π and *d*Δ values are always reached at the minimum area.

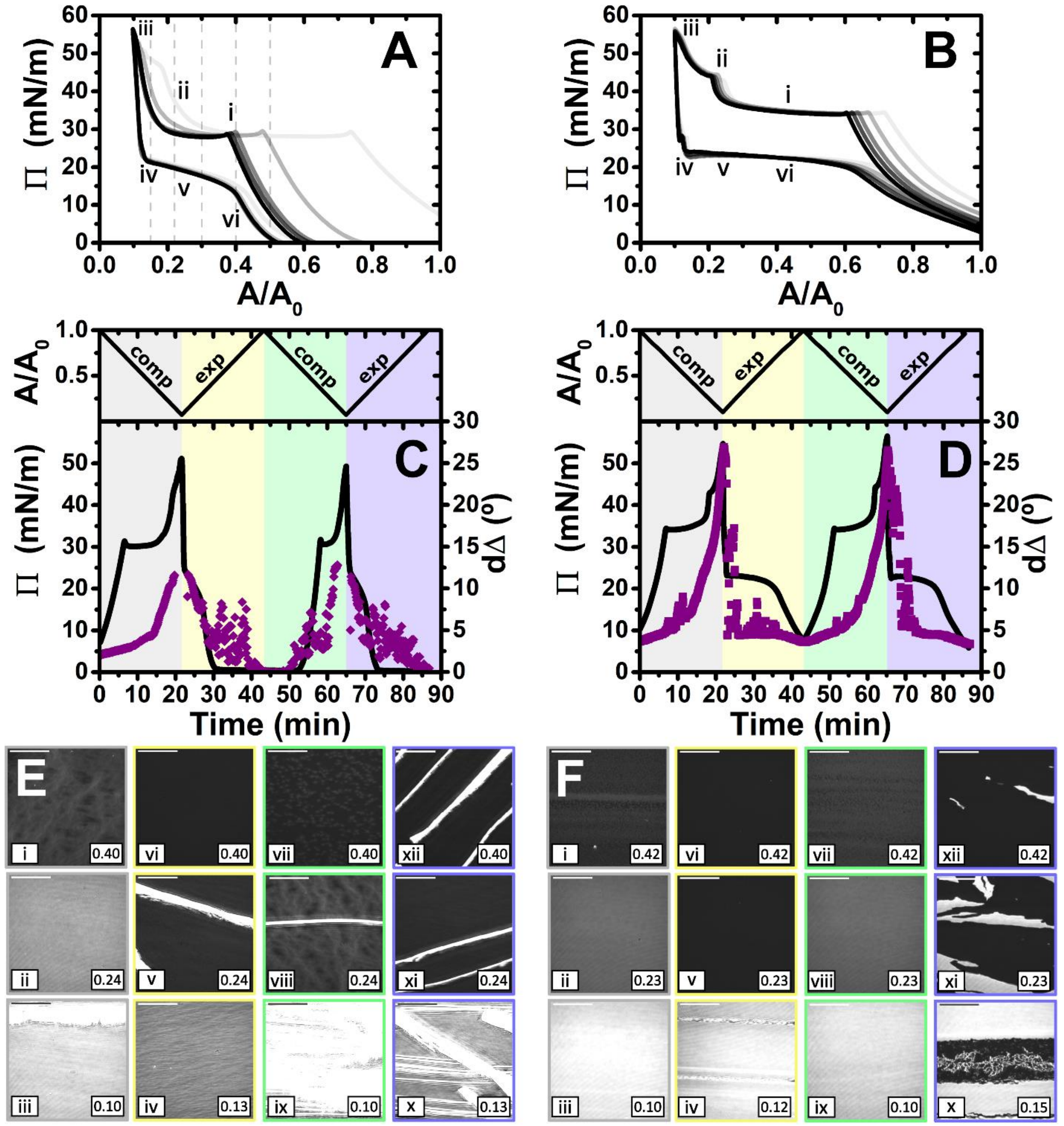

Figure 5.7. Π–*A* isotherms of (A) PLL/SDS and (B) PLA/SDS films using a 10:1 compression ratio during 5 consecutive compression/expansion cycles. The transparency of the data indicates the number of cycle, with cycle 1 being the most transparent and cycle 5 the least and the indices i-vi indicate different compression states. Variation of Π (black line) and *d*Δ (purple squares) as a function of time during two consecutive compression/expansion cycles of (C) PLL/SDS and (D) PLA/SDS films. The variation of *A* versus time is also included at the top of the graph. The different shadowed areas indicate the compression/expansion of the film. BAM images of (E) PLL/SDS and (F) PLA/SDS films corresponding to states i-vi as indicated in panels A and B and using the colour code of panels C and D. Note that only the indices i-vi have been included in panels A and B for the sake of clarity. Scale bars are 100 µm.

The behaviour of PLA/SDS films compressed to maximum ratio of 10:1 shown in Figure 5.7F is very similar to that presented above for the maximum compression ratio of 5:1, but interestingly in this case, the second kink in the apparent Π results in a small shift of the isotherm in the successive cycles, yet the behaviour is reproducible. The ellipsometry data show a very high amount of material in the film (approximately double), and a very similar trend when a 10:1 compression ratio is reached. Temporal fluctuations can be observed related to the presence of film folding and the characteristic plateau during expansion. The values of $d\Delta$ at the minimum and maximum area remain stable from the first to the second cycle, showing once again the great capacity of these systems to stabilise the formation of ESs and to respread their material back to the surface monolayer during film expansion. BAM images show the formation of the solid film during the first cycle without fracturing the film (state iii). Instead, the images at high compression ratios suggest that the PLA/SDS film folds during the second collapse (states ii and iv). Thus, while the PLL/SDS film exhibits an irreversible collapse mechanism at high Π leading to the formation of solid domains that are trapped at the interface, the PLA/SDS system exhibits a reversible collapse mechanism in which the film folds and excess material is respread in the surface monolayer during expansion.

These results suggest that PLL/SDS films can form solid aggregates that redisperse with greater difficulty than PLA/SDS aggregates. The significant differences observed in the behaviour of these systems may be related to the interaction between the polypeptide molecules, which are the ones that confer the mechanical properties to the film. Although we do not have direct evidence about the secondary structure of the polypeptides at the interface, previous studies suggest that the secondary structure is maintained when the polypeptides are deposited on solid surfaces.[38] While the α-helices formed by PLA present side chains facing outward and thus decreasing the interactions between them, it is understood that beta-sheets present edges free to form hydrogen bonds with other beta-sheet edges belonging to different molecules.[59,60] This could give rise to the formation of an extensive hydrogen bond network throughout the film that would confer a more rigid structure and stability to the aggregates formed by PLL/SDS. These observations are in agreement with the formation of solid precipitates due to inter-chain hydrogen bonding between β-sheets and the formation of coacervates when random-coiled or α-helical polypeptides interact between them.[2] Indeed, amyloid fibrils are used in numerous biomedical applications because they are made up of β-sheets which give them a rigid and cohesive nature and excellent mechanical properties such as large persistence length.[2] Finally, it is worth noting that the properties of individual polypeptide chains have a great influence on the properties of the aggregates they form. Thus, the results obtained here also agree with the greater stifness of β-sheets with respect to the α-helices. The behaviour using a 10:1 compression ratio represents additional evidence of the above explanation. The β-sheet conformation that PLL adopts when interacting with SDS in bulk is characterised by an extensive network of hydrogen bonds and is stiffer than the α-helix structure adopted by PLA.[34,61] Additional hydrogen bonding between PLL chains at high compression ratios and edge-to-edge interactions between different beta-sheets could give rise to aggregation and formation of the solid domains observed that remain trapped at the air/water interface. Although the results are consistent with a β-sheet conformation for PLL and an α-helix conformation for PLA, the application of circular dichroism and Fourier transform infrared spectroscopy in the future will be essential to understand better the role of the secondary structure of different polypeptides in spread PP/S films.

5.5 Conclusions

We have shown for the first time in the present work that specific PP/S interactions in spread films compressed to different maximum ratios of the surface area can be used to tune their mechanical and structural properties as well as their resulting morphologies. PLL/SDS films show the presence of discrete ESs after the collapse until a solid film is formed. In contrast, PLA/SDS films show linear regions as well with a higher amount of material related to film folding. In addition, the application of the highest compression ratios studied (up to 10:1) shows that PLL/SDS films form more stable solid aggregates that redisperse with greater difficulty upon expansion and even become trapped at the interface. Different morphologies of the ESs are evident depending on the compression ratio applied. PLA/SDS films show reversible collapse regardless of the compression ratio used, whereas PLL/SDS films show irreversible collapse at the highest compression ratio applied.

NR data recorded over the full Q_z-range showed the ability of PLL/SDS films to nucleate a high coverage of ESs when a sufficiently high compression ratio is applied. The low amount of water in these films and the presence of two distinct layers of ESs present a consistent physical picture with the solid films observed using BAM. Future application of the low-Q_Z[27] and mid-Q_Z[26] approaches of NR will be essential to deeply understand the dynamic behaviour of the films.

Although there is no direct evidence of retention of the secondary structure of PLL and PLA in the ESs of the spread films, the work was based on the hypothesis that different secondary structures formed in bulk complexes of the two systems may result in distinct film properties where ESs are present, and this turned out to be correct. The results indicate that the films obtained in this work are more rigid than the ones obtained before using a flexible random-coil polyelectrolyte,[29] which is consistent with the higher stiffness of the β-sheet and α-helix conformations with respect to the random coil and with previous studies showing the important role that polyelectrolyte stiffness plays in ESs formation.[30] Therefore, we may approach the possibility of designing with high precision PP/S films that form ESs.

In summary, high potential of using polypeptides in combination with oppositely charged surfactants in spread films at the air/water interface has been demonstrated. The richness of these molecules in terms of chemical diversity, biodegradability, biocompatibility, biomimicry, and the possibility of controlling their primary and secondary structure and, therefore, their function, in film applications opens up a wide field of research. Here, we present only two examples of PP/S films and how their properties can be controlled, yet this work provides the platform for the development of a broad range of PP/S systems. Thus, the continuation of these studies using different polypeptides and surfactants could have an important contribution to the development of new biomaterials with applications in tissue engineering,[62] biosensors[63] or antimicrobial coatings.[64]

5.6 Acknowledgements

We thank ISIS Neutron and Muon Source for allocations of neutron beamtime (DOI: https://doi.org/10.5286/ISIS.E.RB2210138), the Partnership for Soft Condensed Matter (PSCM) for lab support and Benoit Laurent for technical assistance with the ellipsometer. IV acknowledges the financial support from the Hungarian National Research, Development and Innovation Office (NKFIH K116629). AM acknowledges the financial support from MICINN under grant PID2021-129054NA-I00 and the IKUR Strategy of the Basque Government. ME and RC acknowledge the Engineering and Physical Research Council (UK) for support with grant EP/V029495/1.

5.7 Supplementary information

5.7.1 Neutron reflectivity fitting procedure

The NR full-Q_z approach was used to resolve the structure of PLL/SDS films at a 4.5:1 compression ratio in 3 different isotopic contrasts. The three contrasts measured are important to get specific information about the structure of the film. The d-SDS/ACMW contrast is very sensitive to SDS molecules both in the surface monolayer and the ESs. The h-SDS/D_2O contrast provides a sensitive measurement of the amount of ESs, as the difference between the SLD of SDS and the bulk is high. Thus, the penetration of h-SDS molecules into the D_2O subphase causes a strong modulation of the reflectivity profile. Lastly, the d-SDS/D_2O contrast is essential to determine the presence of PLL in the ESs. Here, the SDS molecules and the subphase have a similar SLD but it is very different from that of PLL.

The data analysis has been performed in the Motofit software package of Igor Pro.[42] The analysis followed the general procedure of co-refining fits of the data in different isotopic contrasts using a structural model with a minimum number of layers. The optimised model has 6 stratified layers: (1) SDS tails, (2) SDS headgroups with PLL and solvent, (3) PLL, (4) PLL/SDS ESs and solvent, (5) PLL, and (6) PLL/SDS ESs and solvent. The multilayer structure is shown schematically in Figure 5.8. Each layer, i, is characterised by four parameters: the SLD (ρ_i), the thickness (d_i), the roughness and the solvent volume fraction ($V_{f,solvent}$). Table 5.1 shows the values of scattering length, b, molecular volume, V_m, and scattering length density, ρ, of SDS and PLL.

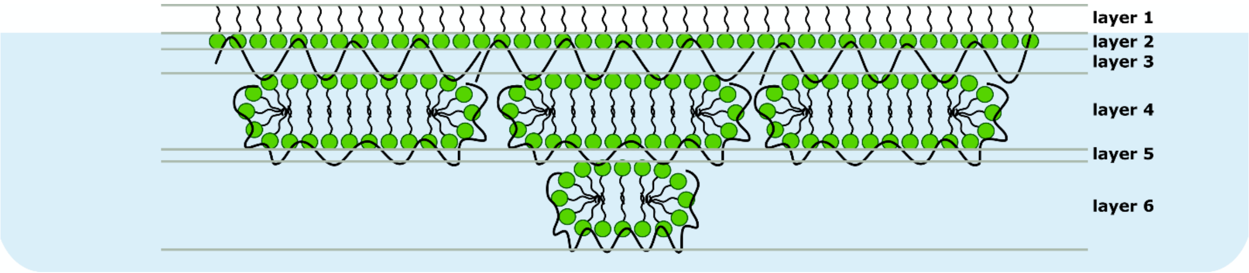

Figure 5.8. Schematic representation of the multilayer structure used in the NR data analysis.

Table 5.1. Scattering length (*b*), molecular volume (V_m) and scattering length density (*ρ*) used in this work for the different components studied.

Component	*b* (fm)	V_m (Å³)	ρ (x 10^{-6} Å^{-2})
SS Headgroups	29.71	61	4.87
$C_{12}H_{25}$-Chains	–13.76	352	–0.39
$C_{12}D_{25}$-Chains	246.53	352	7.00
SDS Molecules	15.95	413	0.39
d_{25}-SDS Molecules	276.24	413	6.69
PLL (in ACMW)	18.85	173	1.09
PLL (in D_2O)	53.35	173	3.09

All interfaces were given a roughness of 3.5 Å, which is consistent with the presence of capillary waves.[56] All 'surface monolayer' (layers 1 and 2) parameters were fixed to those previously obtained with a 2:1 compression ratio,[26] as it was observed that the monolayer composition did not change after collapse, e.g., the thickness of the SDS tails was 8.5 Å as the SDS surface excess in the monolayer (i.e. the surfactant layer in contact with air with hydrated polyelectrolyte bound to the headgroups) equals 4.0 ± 0.1 μmol/m^2.[56] In the case of the headgroups layer (layer 2), there were two important constraints applied. First, the surface excess of tails and headgroups was constrained to be equal to ensure physical reality. Second, the SLD of the headgroups layer depended on the subphase used since PLL has labile protons in the amine groups that can exchange with the solution. We assumed 90% proton/deuterium exchange for PLL,[57] which translates into a headgroups SLD of 1.09×10^{-6} Å^{-2} in ACMW and 3.09×10^{-6} Å^{-2} in D_2O.

To minimise the number of free fitting parameters, a number of further model assumptions were made. First, the two layers of ESs were constrained to have the same thickness, given that they are each dominated by self-assembly of patches of SDS bilayer. Second, the same PLL/SDS stoichiometry as in the surfactant headgroups layer (layer 2) was used in the ESs (layers 4 and 6), i.e. 40% PLL. Third, as the solvent volume fraction of the PLL layers (layers 3 and 5) converged to zero in each preliminary fit, solvent was excluded in the optimised model. Five free fitting parameters remained: *d* of layers 3 (PLL), 5 (PLL) and 4 = 6 (ESs), and the solvent volume fraction, v_f, of layers 4 (ESs) and 6 (ESs). A genetic algorithm used, restricting fitting ranges of parameters to a physically meaningful values: 2–15 Å and 20–30 Å for the thicknesses of the PLL and ESs layers, respectively, with 0–1 for the two solvent volume fractions. Residual background values were used as follows: 5 × 10^{-6} for d-SDS in ACMW and 3 × 10^{-6} for d-SDS and h-SDS in D_2O. The parameters used and fitted are shown in Table 5.2. The uncertainties of the fitting parameters have been calculated as the difference between the optimised parameter and the variation of the optimised parameter that gives rise to an increase of the χ^2 of the fit by 10%.

Table 5.2. Thickness (d_i), scattering length density (ρ_i), and composition obtained from the correspondent fit for each layer of the PLL/SDS films spread from overcharged aggregates, where *i* is the layer number.

Layer	Parameter	d-SDS/ACMW	d-SDS/D_2O	h-SDS/D_2O
1	d_1 (Å)	8.5		
	ρ_1 (x 10^{-6} Å^{-2})	7	7	-0.39
	Composition	100% SDS chains		
2	d_2 (Å)	4		
	ρ_2 (x 10^{-6} Å^{-2})	2.90	3.94	3.94
	Composition	37% SDS heads 40% PLL 23% solvent		
3	d_3 (Å)	12.0 ± 0.7		
	ρ_3 (x 10^{-6} Å^{-2})	1.09	3.09	3.09
	Composition	100% PLL		
4	d_4 (Å)	26 ± 2		
	ρ_4 (x 10^{-6} Å^{-2})	6.35	6.47	0.55
	Composition	73% SDS 5% PLL 22% solvent		
5	d_5 (Å)	3 ± 1		
	ρ_5 (x 10^{-6} Å^{-2})	1.09	3.09	3.09
	Composition	100% PLL		
6	d_5 (Å)	26 ± 7		
	ρ_5 (x 10^{-6} Å^{-2})	6.35	6.47	0.55
	Composition	9% SDS 1% PLL 90% solvent		

5.7.2 Neutron reflectivity fitting demonstration of PLL between the extended structures

Figure 5.9 shows the reflectivity profiles and fits using the optimised model (A) with and an alternative model (B) without PLL (layer 5) located between the two layers of ESs (layers 4 and 6). A fit of the data using the optimised model where the PLL layer is included between the ESs results in a χ^2 value of 18 (panel A), while the absence of this layer leads to a χ^2 of 25 (panel B), i.e. an increase of > 40% where the relative increase in number of free fitting parameters is 25%. In the case where the PLL layer is omitted, the model fit of the d-SDS/D_2O contrast (i.e. the data most sensitive to the penetration of PLL beneath the surface monolayer) deviates strongly from the experimental data around the Kiessig fringe, emphasising the need for PLL to be included between the ESs. This result is also supported by the physical nature of oppositely charged polypeptide electrostatically screening the charges of the surfactant headgroups in the ESs.

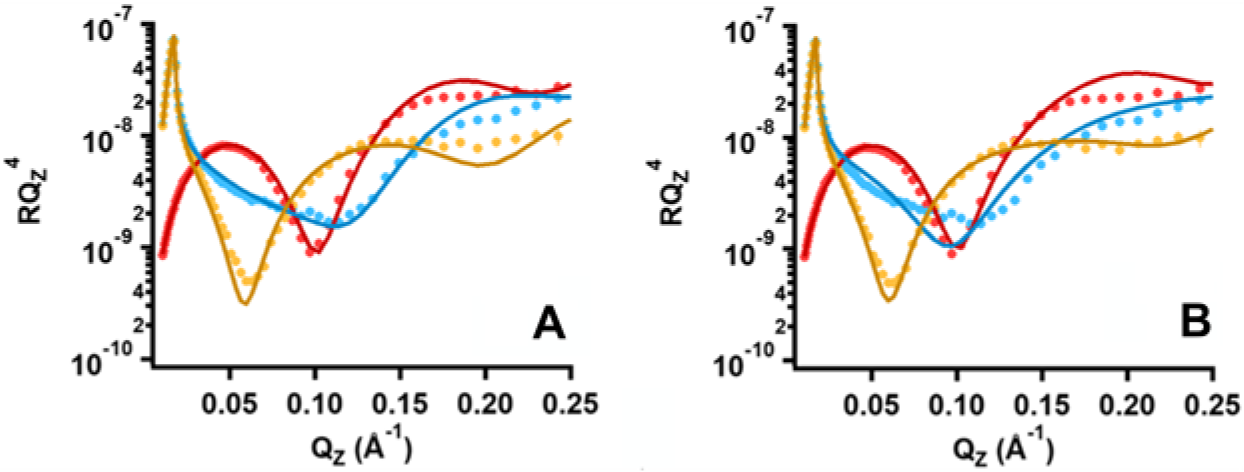

Figure 5.9. Neutron reflectivity profiles of a PLL/SDS film compressed to a 4.5:1 ratio using d-SDS/ACMW (red circles), d-SDS/D_2O (blue circles) and h-SDS/D_2O (orange circles) contrasts. The continuous lines show the fits using a model (A) with PLL between the ESs layers and (B) without PLL layer between the ESs layers.

5.7.3 Surface pressure and ellipsometry stability measurements

Ellipsometry was used to probe the stability of PLL/SDS and PLA/SDS films compressed to ratios of 2:1 and 5:1. These two compression ratios were chosen as the first is representative of the states of the films during the surface pressure collapse, and the second is representative of the states after the second kink in the isotherms where the apparent Π increases above Π_c. These experiments are considered insightful for assessing whether the films could be transferred to solids for future applications. The use of a technique such as Langmuir Blodgett/Schaeffer would require films with the ESs to be stable for a period under optimal transfer conditions.

The experiments were performed by compressing the films at a constant speed until the maximum compression ratio was reached and the barriers were stopped. Both Π and *d*Δ were recorded during compression and for at least 1 h at maximum compression. Figures 5.10 and 5.11 shows the results obtained using a maximum compression ratio of 2:1 and 5:1, respectively. In all cases, Π relaxes after the barriers are stopped but *d*Δ values remain stable indicating that the films presenting ESs that retain the excess of material are stable over long periods of time.

The high stability of the films makes it possible to determine their structure using NR. Such structural measurements usually last between 40 min and 1 h. Therefore, ellipsometry confirms that the amount of material present at the interface does not change during the NR measurement. Furthermore, the stability and the solid character of the films at high compression ratios indicates that they are suitable candidates for transfer to solid supports.

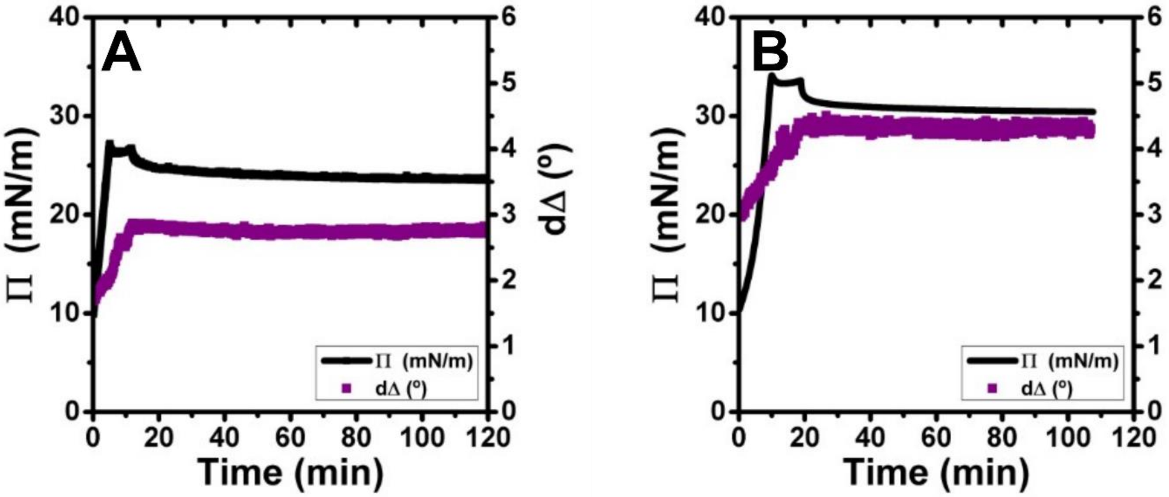

Figure 5.10. Variation of Π (black line) and *d*Δ (purple diamonds) as a function of time of (A) PLL/SDS and (B) PLA/SDS spread films at a 2:1 compression ratio.

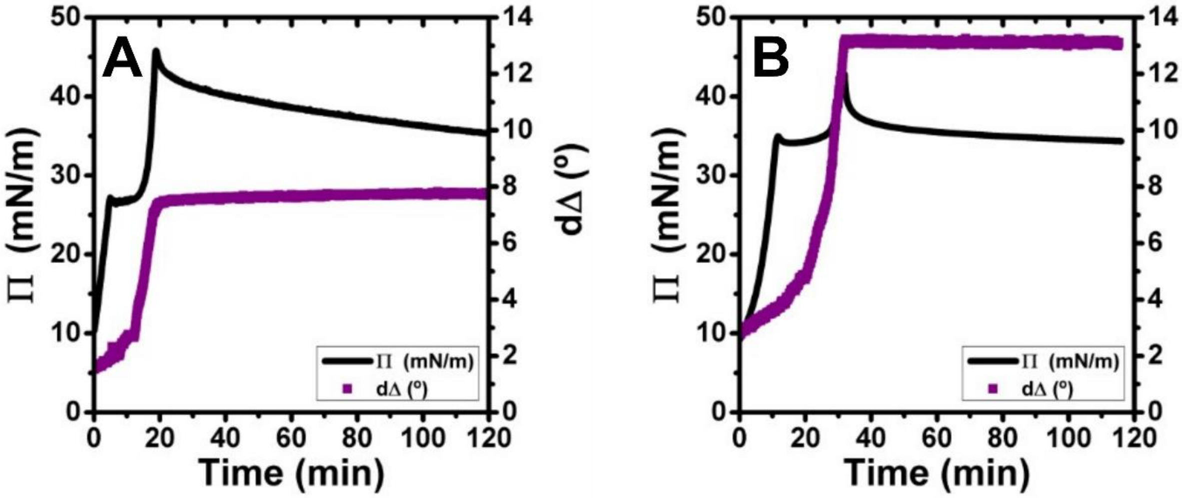

Figure 5.11. Variation of Π (black line) and *d*Δ (purple diamonds) as a function of time of (A) PLL/SDS and (B) PLA/SDS spread films at a 5:1 compression ratio.

5.7.4 Verification of surface pressure values at high compression ratios

Figure 5.12 shows data obtained in an experiment performed using 2 surface pressure sensors on PLL/SDS films with respect to compression of the surface area to a ratio of 10:1. The experiments were performed because of doubts over possible artefacts in measurements of Π that exceeded Π_c in case a phase transition of the film to a solid nature meant that the plate experienced an additional force from being pulled sideways during the compression process, and hence the values of Π no longer represented true surface pressure. Sensor 1 with a single plate was placed in contact with the film at the air/water interface and kept at the same position during the compression, while sensor 2 was repeatedly made to contact the film with a fresh plate each time while the barriers has briefly stopped the compression process. It was assumed that sensor 2 could not be affected by the possible artefact of the plate being pulled sideways. The approximately constant values obtained with sensor 2 after the collapse point indicates that the increase in surface pressure above Π_c is related to the additional force exerted by the solid film.

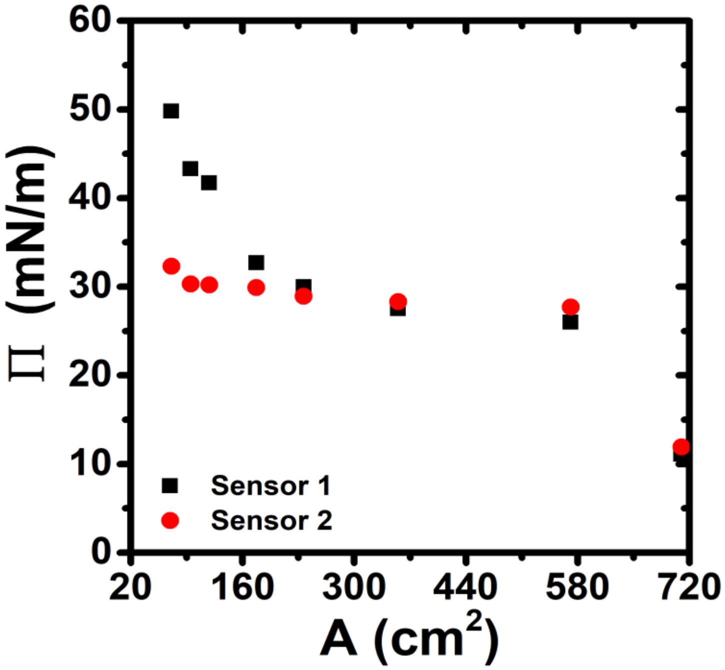

Figure 5.12. Variation of Π as a function of *A* using two different pressure sensors according to the methodology described in the text above.

5.8 References

(1) Song, Z.; Han, Z.; Lv, S.; Chen, C.; Chen, L.; Yin, L.; Cheng, J. Synthetic Polypeptides: From Polymer Design to Supramolecular Assembly and Biomedical Application. *Chem. Soc. Rev.* **2017**, *46* (21), 6570–6599.

(2) Song, Z.; Fu, H.; Wang, R.; Pacheco, L. A.; Wang, X.; Lin, Y.; Cheng, J. Secondary Structures in Synthetic Polypeptides from N-Carboxyanhydrides: Design, Modulation, Association, and Material Applications. *Chem. Soc. Rev.* **2018**, *47* (19), 7401–7425.

(3) Bonduelle, C. Secondary Structures of Synthetic Polypeptide Polymers. *Polym. Chem.* **2018**, *9* (13), 1517–1529.

(4) Xiong, M.; Lee, M. W.; Mansbach, R. A.; Song, Z.; Bao, Y.; Peek, R. M.; Yao, C.; Chen, L. F.; Ferguson, A. L.; Wong, G. C. L.; Cheng, J. Helical Antimicrobial Polypeptides with Radial Amphiphilicity. *Proc. Natl. Acad. Sci. U. S. A.* **2015**, *112* (43), 13155–13160.

(5) Oelker, A. M.; Morey, S. M.; Griffith, L. G.; Hammond, P. T. Helix versus Coil Polypeptide Macromers: Gel Networks with Decoupled Stiffness and Permeability. *Soft Matter* **2012**, *8* (42), 10887–10895.

(6) Gebhardt, K. E.; Ahn, S.; Venkatachalam, G.; Savin, D. A. Role of Secondary Structure Changes on the Morphology of Polypeptide-Based Block Copolymer Vesicles. *J. Colloid Interface Sci.* **2008**, *317* (1), 70–76.

(7) Stubenrauch, C.; Albouy, P. A.; von Klitzing, R.; Langevin, D. Polymer/Surfactant Complexes

at the Water/Air Interface: A Surface Tension and X-Ray Reflectivity Study. *Langmuir* **2000**, *16* (7), 3206–3213.

(8) Schulze-Zachau, F.; Braunschweig, B. C_nTAB/Polystyrene Sulfonate Mixtures at Air–Water Interfaces: Effects of Alkyl Chain Length on Surface Activity and Charging State. *Phys. Chem. Chem. Phys.* **2019**, *21* (15), 7847–7856.

(9) Tran, E.; Mapile, A. N.; Richmond, G. L. Peeling Back the Layers: Investigating the Effects of Polyelectrolyte Layering on Surface Structure and Stability of Oil-in-Water Nanoemulsions. *J. Colloid Interface Sci.* **2021**, *599*, 706–716.

(10) Ciunel, K.; Armélin, M.; Findenegg, G. H.; von Klitzing, R. Evidence of Surface Charge at the Air/Water Interface from Thin-Film Studies on Polyelectrolyte-Coated Substrates. *Langmuir* **2005**, *21* (11), 4790–4793.

(11) Guzmán, E.; Ritacco, H.; Rubio, J. E. F.; Rubio, R. G.; Ortega, F. Salt-Induced Changes in the Growth of Polyelectrolyte Layers of Poly(Diallyl-Dimethylammonium Chloride) and Poly(4-Styrene Sulfonate of Sodium). *Soft Matter* **2009**, *5*, 2130–2142.

(12) Akanno, A.; Guzmán, E.; Fernández-Peña, L.; Llamas, S.; Ortega, F.; Rubio, R. G. Equilibration of a Polycation-Anionic Surfactant Mixture at the Water/Vapor Interface. *Langmuir* **2018**, *34* (25), 7455–7464.

(13) Shen, Y.; Fu, X.; Fu, W.; Li, Z. Biodegradable Stimuli-Responsive Polypeptide Materials Prepared by Ring Opening Polymerization. *Chem. Soc. Rev.* **2015**, *44* (3), 612–622.

(14) Deming, T. J. Synthesis of Side-Chain Modified Polypeptides. *Chem. Rev.* **2016**, *116* (3), 786–808.

(15) Tang, Z.; Wang, Y.; Podsiadlo, P.; Kotov, N. A. Biomedical Applications of Layer-by-Layer Assembly: From Biomimetics to Tissue Engineering. *Adv. Mater.* **2006**, *18* (24), 3203–3224.

(16) Alkekhia, D.; Hammond, P. T.; Shukla, A. Layer-by-Layer Biomaterials for Drug Delivery. *Annu. Rev. Biomed. Eng.* **2020**, *22*, 1–24.

(17) Haynie, D. T.; Zhang, L.; Rudra, J. S.; Zhao, W.; Zhong, Y.; Palath, N. Polypeptide Multilayer Films. *Biomacromolecules* **2005**, *6* (6), 2895–2913.

(18) Richardson, J. J.; Cui, J.; Björnmalm, M.; Braunger, J. A.; Ejima, H.; Caruso, F. Innovation in Layer-by-Layer Assembly. *Chem. Rev.* **2016**, *116* (23), 14828–14867.

(19) Pack, D. W.; Hoffman, A. S.; Pun, S.; Stayton, P. S. Design and Development of Polymers for Gene Delivery. *Nat. Rev. Drug Discov.* **2005**, *4* (7), 581–593.

(20) Ponomarenko, E. A.; Waddon, A. J.; Bakeev, K. N.; Tirrell, D. A.; MacKnight, W. J. Self-Assembled Complexes of Synthetic Polypeptides and Oppositely Charged Low Molecular Weight Surfactants. Solid-State Properties. *Macromolecules* **1996**, *29* (12), 4340–4345.

(21) Guzmán, E.; Llamas, S.; Maestro, A.; Fernández-Peña, L.; Akanno, A.; Miller, R.; Ortega, F.; Rubio, R. G. Polymer-Surfactant Systems in Bulk and at Fluid Interfaces. *Adv. Colloid Interface Sci.* **2016**, *233*, 38–64.

(22) Guzmán, E.; Fernández-Peña, L.; Ortega, F.; Rubio, R. G. Equilibrium and Kinetically

Trapped Aggregates in Polyelectrolyte–Oppositely Charged Surfactant Mixtures. *Curr. Opin. Colloid Interface Sci.* **2020**, *48*, 91–108.

(23) Buckingham, J. H.; Lucassen, J.; Hollway, F. Surface Properties of Mixed Solutions of Poly-L-Lysine and Sodium Dodecyl Sulfate. I. Equilibrium Surface Properties. *J. Colloid Interface Sci.* **1978**, *67* (3), 423–431.

(24) Lucassen, J.; Hollway, F.; Buckingham, J. H. Surface Properties of Mixed Solutions of Poly-L-Lysine and Sodium Dodecyl Sulfate. II. Dynamic Surface Properties. *J. Colloid Interface Sci.* **1978**, *67* (3), 432–440.

(25) Penfold, J.; Tucker, I.; Thomas, R. K.; Taylor, D. J. F.; Zhang, X. L. PH Sensitive Adsorption of Polypeptide/Sodium Dodecyl Sulfate Mixtures. *Langmuir* **2006**, *22* (18), 7617–7621.

(26) Carrascosa-Tejedor, J.; Santamaria, A.; Tummino, A.; Varga, I.; Efstratiou, M.; Lawrence, M. J.; Maestro, A.; Campbell, R. A. Polyelectrolyte/Surfactant Films: From 2D to 3D Structural Control. *Chem. Commun.* **2022**, *58* (76), 10687–10690.

(27) Campbell, R. A.; Tummino, A.; Noskov, B. A.; Varga, I. Polyelectrolyte/Surfactant Films Spread from Neutral Aggregates. *Soft Matter* **2016**, *12* (24), 5304–5312.

(28) Mészáros, R.; Thompson, L.; Bos, M.; Varga, I.; Gilányi, T. Interaction of Sodium Dodecyl Sulfate with Polyethyleneimine: Surfactant-Induced Polymer Solution Colloid Dispersion Transition. *Langmuir* **2003**, *19* (3), 609–615.

(29) Tummino, A.; Toscano, J.; Sebastiani, F.; Noskov, B. A.; Varga, I.; Campbell, R. A. Effects of Aggregate Charge and Subphase Ionic Strength on the Properties of Spread Polyelectrolyte/Surfactant Films at the Air/Water Interface under Static and Dynamic Conditions. *Langmuir* **2018**, *34* (6), 2312–2323.

(30) Braun, L.; Uhlig, M.; Löhmann, O.; Campbell, R. A.; Schneck, E.; von Klitzing, R.. Insights into Extended Structures and Their Driving Force: Influence of Salt on Polyelectrolyte/Surfactant Mixtures at the Air/Water Interface. *ACS Appl. Mater. Interfaces* **2022**, *14* (23), 27347–27359.

(31) Wernersson, E.; Heyda, J.; Kubíčková, A.; Křížek, T.; Coufal, P.; Jungwirth, P. Effect of Association with Sulfate on the Electrophoretic Mobility of Polyarginine and Polylysine. *J. Phys. Chem. B* **2010**, *114* (36), 11934–11941.

(32) Satake, I.; Yang, J. T. Interaction of Sodium Decyl Sulfate with Poly(L-ornithine) and Poly(L-lysine) in Aqueous Solution. *Biopolymers* **1976**, *15* (11), 2263–2275.

(33) Takeda, K.; Iba, A.; Shirahama, K. Kinetic Study on Conformational Changes of Poly(L-Lysine) in Sodium Alkyl Sulfate Solutions. Effects of Surfactant Chain Length and Added NaCl. *Bull. Chem. Soc. Jpn.* **1982**, *55* (4), 985–989.

(34) Novotná, P.; Urbanová, M. Vibrational Circular Dichroism Study of Polypeptide Model–Membrane Systems. *Anal. Biochem.* **2012**, *427* (2), 211–218.

(35) Novotná, P.; Urbanová, M. A Solid Phase Vibrational Circular Dichroism Study of Polypeptide-Surfactant Interaction. *Chirality* **2015**, *27* (12), 965–972.

(36) McCord, R. W.; Blakeney, E. W.; Mattice, W. L. Conformational Changes Induced in Ionized Poly(L-Arginine) and Poly(L-Histidine) by Sodium Dodecyl Sulfate. *Biopolymers* **1977**, *16* (6), 1319–1329.

(37) Ichimura, S.; Mita, K.; Zama, M. Conformation of Poly(L-Arginine). I. Effects of Anions. *Biopolymers* **1978**, *17* (12), 2769–2782.

(38) Boulmedais, F.; Bozonnet, M.; Schwinté, P.; Voegel, J. C.; Schaaf, P. Multilayered Polypeptide Films: Secondary Structures and Effect of Various Stresses. *Langmuir* **2003**, *19* (23), 9873–9882.

(39) Campbell, R. A. Recent Advances in Resolving Kinetic and Dynamic Processes at the Air/Water Interface Using Specular Neutron Reflectometry. *Curr. Opin. Colloid Interface Sci.* **2018**, *37*, 49–60.

(40) Skoda, M. W. A. Recent Developments in the Application of X-Ray and Neutron Reflectivity to Soft-Matter Systems. *Curr. Opin. Colloid Interface Sci.* **2019**, *42*, 41–54.

(41) Maestro, A.; Gutfreund, P. In Situ Determination of the Structure and Composition of Langmuir Monolayers at the Air/Water Interface by Neutron and X-Ray Reflectivity and Ellipsometry. *Adv. Colloid Interface Sci.* **2021**, *293*, 102434.

(42) Nelson, A. Co-Refinement of Multiple-Contrast Neutron/X-Ray Reflectivity Data Using MOTOFIT. *J. Appl. Crystallogr.* **2006**, *39*, 273–276.

(43) Ainalem, M. L.; Campbell, R. A.; Nylander, T. Interactions between DNA and Poly(Amido Amine) Dendrimers on Silica Surfaces. *Langmuir* **2010**, *26* (11), 8625–8635.

(44) Tonigold, K.; Varga, I.; Nylander, T.; Campbell, R. A. Effects of Aggregates on Mixed Adsorption Layers of Poly(Ethylene Imine) and Sodium Dodecyl Sulfate at the Air/Liquid Interface. *Langmuir* **2009**, *25* (7), 4036–4046.

(45) Milyaeva, O. Y.; Gochev, G.; Loglio, G.; Miller, R.; Noskov, B. A. Influence of Polyelectrolytes on Dynamic Surface Properties of Fibrinogen Solutions. *Colloids Surfaces A Physicochem. Eng. Asp.* **2017**, *532*, 108–115.

(46) Motschmann, H.; Reiter, R.; Lawall, R.; Duda, G.; Stamm, M.; Wegner, G.; Knoll, W. Ellipsometric Characterization of Langmuir Monolayers of “Hairy-Rod” Polymers at the Air-Water Interface. *Langmuir* **1991**, *7*, 2743–2747.

(47) Daear, W.; Mahadeo, M.; Prenner, E. J. Applications of Brewster Angle Microscopy from Biological Materials to Biological Systems. *Biochim. Biophys. Acta* **2017**, *1859* (10), 1749–1766.

(48) Varga, I.; Campbell, R. A. General Physical Description of The Behavior of Oppositely Charged Polyelectrolyte/Surfactant Mixtures at the Air/Water Interface. *Langmuir* **2017**, *33* (23), 5915–5924.

(49) Skvarnavičius, G.; Dvareckas, D.; Matulis, D.; Petrauskas, V. Thermodynamics of Interactions Between Charged Surfactants and Ionic Poly(Amino Acids) by Isothermal Titration Calorimetry. *ACS Omega* **2019**, *4* (17), 17527–17535.

(50) Mezei, A.; Mészáros, R. Novel Method for the Estimation of the Binding Isotherms of Ionic Surfactants on Oppositely Charged Polyelectrolytes. *Langmuir* **2006**, *22* (17), 7148–7151.

(51) Wallin, T.; Linse, P. Monte Carlo Simulations of Polyelectrolytes at Charged Micelles. 1. Effects of Chain Flexibility. *Langmuir* **1996**, *12* (2), 305–314.

(52) Hansson, P. Self-Assembly of Ionic Surfactants in Polyelectrolyte Solutions: A Model for Mixtures of Opposite Charge. *Langmuir* **2001**, *17* (14), 4167–4180.

(53) Akinchina, A.; Linse, P. Monte Carlo Simulations of Polyion-Macroion Complexes. 2. Polyion Length and Charge Density Dependence. *J. Phys. Chem. B* **2003**, *107* (32), 8011–8021.

(54) Campbell, R. A.; Yanez Arteta, M.; Angus-Smyth, A.; Nylander, T.; Varga, I. Multilayers at Interfaces of an Oppositely Charged Polyelectrolyte/Surfactant System Resulting from the Transport of Bulk Aggregates under Gravity. *J. Phys. Chem. B* **2012**, *116* (27), 7981–7990.

(55) Lu, J. R.; Marrocco, A.; Su, T. J.; Thomas, R. K.; Penfold, J. Adsorption of Dodecyl Sulfate Surfactants with Monovalent Metal Counterions at the Air-Water Interface Studied by Neutron Reflection and Surface Tension. *J. Colloid Interface Sci.* **1993**, *158* (2), 303–316.

(56) Campbell, R. A.; Saaka, Y.; Shao, Y.; Gerelli, Y.; Cubitt, R.; Nazaruk, E.; Matyszewska, D.; Lawrence, M. J. Structure of Surfactant and Phospholipid Monolayers at the Air/Water Interface Modeled from Neutron Reflectivity Data. *J. Colloid Interface Sci.* **2018**, *531*, 98–108.

(57) Jacrot, B. The Study of Biological Structures by Neutron Scattering from Solution. *Reports Prog. Phys.* **1976**, *39* (10), 953.

(58) Reda, T.; Hermel, H.; Höltje, H.-D. Compression/Expansion Hysteresis of Poly(l-Glutamic Acid) Monolayers Spread at the Air/Water Interface. *Langmuir* **1996**, *12* (26), 6452–6458.

(59) Richardson, J. S.; Richardson, D. C. Natural β-Sheet Proteins Use Negative Design to Avoid Edge-to-Edge Aggregation. *Proc. Natl. Acad. Sci. U.S.A.* **2002**, *99* (5), 2754–2759.

(60) Cheng, P.-N.; Pham, J. D.; Nowick, J. S. The Supramolecular Chemistry of β-Sheets. *J. Am. Chem. Soc.* **2013**, *135* (15), 5477–5492.

(61) Perticaroli, S.; Nickels, J. D.; Ehlers, G.; O'Neill, H.; Zhang, Q.; Sokolov, A. P. Secondary Structure and Rigidity in Model Proteins. *Soft Matter* **2013**, *9* (40), 9548–9556.

(62) Nettles, D. L.; Chilkoti, A.; Setton, L. A. Applications of Elastin-Like Polypeptides in Tissue Engineering. *Adv. Drug Deliv. Rev.* **2010**, *62* (15), 1479–1485.

(63) Puiu, M.; Bala, C. Peptide-Based Biosensors: From Self-Assembled Interfaces to Molecular Probes in Electrochemical Assays. *Bioelectrochemistry* **2018**, *120*, 66–75.

(64) Salwiczek, M.; Qu, Y.; Gardiner, J.; Strugnell, R. A.; Lithgow, T.; McLean, K. M.; Thissen, H. Emerging Rules for Effective Antimicrobial Coatings. *Trends Biotechnol.* **2014**, *32* (2), 82–90.

6 Study 3: Effects of macromolecular charge density on the properties of spread hyperbranched polyelectrolyte/surfactant films at the air/water interface

Javier Carrascosa-Tejedor,[1,2†] Andrea Tummino,[2,3†] Bence Feher,[4] Attila Kardos,[4] Marina Efstratiou,[1] Maximilian W. A. Skoda,[5] Philipp Gutfreund,[2] Armando Maestro,[6,7] M. Jayne Lawrence,[1] Richard A. Campbell[1*] and Imre Varga[4*]

1. Division of Pharmacy and Optometry, Faculty of Biology, Medicine and Health, University of Manchester, Oxford Road, Manchester M13 9PT, UK
2. Institut Laue-Langevin, 71 Avenue des Martyrs, CS20156, 38042 Grenoble, France
3. CEA Commissariat à l'Energie Atomique et aux Energies Alternatives, 17 Rue des Martyrs, 38054 Grenoble Cedex 9, France
4. Institute of Chemistry, Eötvös Loránd University, 112, Budapest H-1518, Hungary
5. ISIS Neutron and Muon Source, Rutherford Appleton Laboratory, Harwell Campus, Didcot OX11 0QX, UK
6. Basque Foundation for Science, Plaza Euskadi 5, Bilbao, 48009, Spain
7. Centro de Física de Materiales (CSIC, UPV/EHU) - Materials Physics Center MPC, Paseo Manuel de Lardizabal 5, E-20018 San Sebastián, Spain.

† joint first authors with equal contributions

*corresponding authors: Richard A. Campbell and Imre Varga

6.1 Abstract

The influence of the subphase pH on the interfacial properties and structure of films spread from hyperbranched PEI/SDS overcharged aggregates at the air/water interface has been investigated. For this purpose, we used a range of interfacial techniques that exploit different time and length

scales, namely ellipsometry, NR and BAM The spreading of PEI/SDS aggregates on a pure water subphase adjusted to pH 4 or pH 10 (close to the natural pH of the PEI solution used) resulted in the formation of films characterised by the presence of extended surfactant bilayers structures wrapped by PEI bound to a surface monolayer of both components. NR, BAM and ellipsometry studies reveal the formation of a more compact and rigid film at pH 4 and the presence of embedded aggregates at pH 10. These results can be explained by the greater dissociation of the aggregates at pH 4 due to the higher charge density of PEI, and at pH 10 the presence of aggregates with a low surface charge density that remain trapped at the interface. It can be therefore concluded that the pH of the subphase can have important effects on the spreading of P/S aggregates involving a weak polyelectrolyte as well as the dynamic and structural properties of resulting films.

6.2 Introduction

P/S mixtures have been studied for decades both in the bulk[1–4] and at supported[5–7] and fluid[8–12] interfaces. The interest in the understanding and development of these materials lies in their wide spread use in everyday products such as detergents,[1] cosmetics,[13] pharmaceuticals[14] and lubricants.[15] However, the inherent non-equilibrium nature of the aggregates formed by P/S mixtures has presented a significant challenge when attempting to understand their behavior, although significant progress in this matter has been made over the last two decades. A key non-equilibrium aspect is related to their phase behavior, as during mixing complexes form that have low charge density, lack colloidal stability and as a result aggregate. When the formed aggregates lack colloid stability even in the homogenised P/S mixture their slow aggregation occurs resulting in the phase separation of a concentrated P/S phase in equilibrium with a dilute surfactant solution. However, this phase separation may take place on several days, weeks or even months timescale depending on the concentration and colloid stability of the formed aggregates.[16,17] However, when the surfactant is present in a sufficiently large excess the P/S aggregates formed during mixing can develop colloid (kinetic) stability due to the excess surfactant adsorption taking place on the surface of these aggregates.[18–20] Yet these aggregates typically do not disperse into individual charged P/S complexes if the bulk composition changes and the ionic strength is low.[16,19,21–23] This effect manifests itself even in the mixing of the components when local concentration gradients result in the instantaneous formation of kinetically trapped aggregates that remain intact even if the sample composition once fully mixed is in the equilibrium one-phase region.[24,25]

There are various facets of the ways in which non-equilibrium effects present in P/S mixtures can influence their resulting interfacial behaviour. The initial focus was to understand the depletion of material from solution as a result of aggregation (a dispersion of a concentrated P/S phase), implying that the concentrations of the components in solution (either free or in the form of complexes) available to form an adsorbed layer is lower, in turn resulting in a higher surface tension.[17] Focus then turned to how the aggregates themselves can influence the interfacial properties, such as through becoming kinetically trapped in the interface, undergoing specific interactions with an adsorbed layer, or being transported under gravity.[26] Work on the mixture PEI/SDS at a dynamic air/water interface using the overflowing cylinder technique showed that there can be even more material delivered to the interface by the dissociation of aggregates and Marangoni spreading of their components than the conventionally-assumed diffusion and adsorption of complexes from the bulk.[27] Strong implications for the use of polyelectrolytes and surfactants under technologically relevant conditions were implied.

A few years ago, using a system composed of NaPSS/DTAB, we developed a new methodology to form highly efficient spread P/S films through dropping onto the surface of pure water a small aliquot of neutral aggregates.[28] The dissociation of the aggregates accompanied by the Marangoni spreading of the surface-active components resulted in the formation of a Langmuir film that exploited a further non-equilibrium effect by remaining trapped at the interface due to the entropy associated with counterion release into solution. It was shown that a higher surface excess resulted than from the adsorption of complexes resulting from the equivalent concentrations of the components from the bulk, and that no organic spreading solvent was required, together hinting at potential cost and environmental improvements in the use of these films for potential transfer applications.[29–31]

We went on to explore effects of aggregate charge and ionic strength of the subphase again using the NaPSS/DTAB system.[32] Here it was shown that overcharged aggregates (with a surfactant excess present on their surface) resulted in spread films which upon either successive spreading or compression of the surface area on a Langmuir trough resulted in ESs of additional material beneath the 'surface monolayer', defined as a layer of surfactant in contact with air and polyelectrolyte bound to the headgroups. Even so, ellipsometry showed that these ESs were not stable enough with time to allow direct resolution of their detailed structure. It was also shown that increased ionic strength of the subphase switched off ES formation.[32,33] Recent work turned to exploiting specific polypeptide/surfactant interactions, where ESs in biocompatible PLL/SDS spread films were shown to be stable with time leading to direct resolution of their structure with respect to the surface area.[33] Three-dimensional control of the film structure through reversible tuning of the coverage not only of the surface monolayer but also of the ESs was demonstrated for the first time.

While the properties of spread P/S films have now been investigated on systems involving several charged linear polyelectrolytes,[17,28,32,33] no work on these films has been published to date involving either hyperbranched polyelectrolytes or polyelectrolytes where the charge density can be tuned. To address these points, the present work focuses on films spread through the dissociation of overcharged aggregates on pure water subphases at pH 4 and pH 10 of the PEI/SDS system, which has been extensively studied in previous works.[20,27,34] Overcharged aggregates were chosen simply because they have been shown to result in the formation of ESs for the NaPSS/DTAB[32] and PLL/SDS[33] systems. Subphase pH values of 4 and 10 were chosen because PEI is highly cationic in the former case and almost neutral in the latter case, and additionally, for ease of data comparisons, these values and the 750 kDa molecular weight of the polyelectrolyte matched those used in previous studies on adsorbed layers under static[35] and dynamic[27] conditions. In the static case, a notable conclusion was that there are aggregates embedded in adsorbed layers of PEI/SDS at pH 10 but not at pH 4.

The aim of the present work is to understand effects of charge density on spread P/S films involving a hyperbranched polyelectrolyte for the first time. The objective is to resolve differences in the behavior of hyperbranched spread PEI/SDS films prepared using overcharged aggregates with the linear spread NaPSS/DTAB and PLL/SDS films studied previously. Following characterisation of the charge of the bulk complexes to select the composition of mixtures used to prepare the aggregates for film preparation, several surface-sensitive techniques are applied to the films including Π–*A* isotherms, ellipsometry, BAM and NR under both dynamic and static conditions. Previous work on NaPSS/DTAB films showed the influence of the ionic strength of the subphase on the dissociation of the aggregates and the dynamic properties of the spread films.[32] In this work, we want to study the influence of the subphase pH on the dissociation of PEI/SDS aggregates and the dynamic properties of the spread films since the number of charges in PEI segments varies with the pH.

6.3 Materials and Methods

6.3.1 Materials

750-kDa hyperbranched PEI solution (50% in water), SDS, d-SDS, ethanol (≥99.8%) and D_2O, NaOH and HCl were purchased from Sigma Aldrich. PEI, d-SDS and all solvents were used as received. SDS was recrystallised twice in ethanol followed by drying under vacuum. Ultra-pure water was generated by passing deionised water through a Milli-Q unit (total organic content ≤ 4 ppb, resistivity = 18 MΩ·cm).

6.3.2 Sample preparation

A stock solution of 2000 ppm by mass PEI was prepared by diluting the original PEI solution (50% in water) in water and rotating the vial for a few hours. This stock was further diluted in water to 200 ppm. Stock solutions of SDS and d-SDS 10 mM were prepared and diluted to the required concentration for each experiment. It is worth noting that the natural pH of 100 ppm PEI solutions is 10.

Fresh mixtures of PEI/SDS aggregates were always prepared by rapidly mixing the same volume of the polyelectrolyte and surfactant solutions at double their final concentrations. The mixtures were extracted within 5 s after mixing the components and spread within the following 30 s to limit the growth of large aggregates prior to film formation. Since this study aims to study the influence of subphase pH on the dissociation of PEI/SDS aggregates and the spread film properties, only the pH of the subphase was adjusted to 10 (low PEI charge density) or 4 (high PEI charge density) using concentrated solutions of NaOH or HCl, respectively.

6.3.3 Electrophoretic mobility

Electrophoretic mobility measurements were recorded using a Zetasizer Nano ZS90 and the M3-PLAS technique (Malvern Instruments Ltd., U.K.) to estimate the surface charge of the aggregates. Measurements were performed at a constant concentration of PEI (100 ppm) as a function of the SDS concentration using a range of 0.4–3.5 mM. Two parallels of electrophoretic mobility measurements were recorded at each pH and the values were averaged.

6.3.4 Langmuir technique

The application of the Langmuir trough allows studying the dynamic response of P/S films at the air/water interface during compression/expansion cycles and evaluating the stability of the films when they are compressed at a given compression ratio. For that purpose, different troughs have were used in this work depending on the specific setup needed to combine this technique with the ones explained below (ellipsometry, BAM and NR). All the troughs were equipped with two barriers that move symmetrically while Π was recorded as a function of *A* or time. The surface pressure, defined as the difference between the surface tension of water and that of the interface under study, was recorded using the Wilhelmy plate method. A Kibron G1 trough (Finland, A_{max} = 166.4 cm^2) was used to record the Π–*A* isotherms of 100 ppm PEI/2.5 mM SDS films during successive compression/expansion cycles. Prior to the experiment, the trough was carefully cleaned with soap, ethanol and Milli-Q water. Then, an aliquot of 290 µL of a fresh mixture of PEI/SDS was spread on the correspondent subphase. This quantity was chosen to start the experiment with a surface monolayer in order to study the possible transition from surface monolayer to ESs during successive cycles. After 10 minutes of equilibration, the films were compressed by a factor of 2:1 using a 4.5 cm^2/min compression/expansion rate.

The Langmuir trough technique was coupled to ellipsometry, BAM and NR. Given the different requirements of each setup, the different Langmuir troughs used, and the details of each experiment are indicated in the description of each technique. The spread volumes and the compression/expansion ratio were scaled from one experiment to the other considering the dimensions of the troughs to be consistent.

6.3.5 Ellipsometry

Ellipsometry is an optical technique highly sensitive and precise to determine changes in the surface excess of material at the air/water interface.[36] It is based on the changes in the polarisation of light when it is reflected at an interface. These changes are defined by the ellipticity, ρ, which is related to the experimentally determined ellipsometric angles Ψ and Δ by the following equation:

$$\rho = \frac{r_P}{r_S} = tan\,\Psi\, e^{i\Delta} \tag{3.8}$$

where r_P and r_S are the reflectivity coefficients of the parallel and perpendicular components of the electric field, respectively. When ellipsometry is applied in the study of thin films at the air/water interface, often only values of Δ are considered because Ψ is practically insensitive to changes in the surface excess.[35,37] For that reason, only Δ values are analysed in this work. The ellipsometry data is presented as $d\Delta = \Delta_{P/S}$ (for the P/S film) – Δ_{water} (for pure water), which provides an estimate of the surface excess of fluid thin films.[38]

Ellipsometry was used to examine the stability of PEI/SDS films. In this case, spread films were prepared, and then the barriers were used to reduce the surface area until a surface pressure of 40 mN/m was achieved, after which the surface pressure was held constant. An aliquot of 2000 µL PEI/SDS aggregates was spread in this case to ensure that Π = 40 mN/m is reached before reaching the minimum area at which the barriers pass through the beam path. We decided to hold the pressure at 40 mN/m to promote a high coverage of ESs. The ellipsometry data were recorded using an Accurion EP4 ellipsometer (Germany) equipped with a blue diode laser with a wavelength of λ = 489.2 nm coupled to a Kibron G2 trough (Finland, A_{max} = 280 cm^2). An angle of incidence of 50° and a data acquisition rate of 0.1 Hz were used. Because of the fast acquisition rate and the relatively small probed area (~1 mm^2), ellipsometry is an ideal technique to detect the presence of inhomogeneities on the micrometre scale as temporal fluctuations in the signal.[35,37,39]

6.3.6 Brewster angle microscopy

BAM experiments were performed to image the PEI/SDS films during the acquisition of the Π–*A* isotherms to get information about the in-plane organisation of the films and the presence of inhomogeneities in the µm scale.[40] A Nanofilm EP3 Accurion Brewster angle microscope (Germany) equipped with a 50 mW Nd:YAG laser (λ = 532 nm), a CCD detector and a 10x magnification objective was used. BAM images were taken at the Brewster angle of water (53.1°) without background subtraction. The setup used emitted *p*-polarised light that is guided towards the air/water interface. Thus, the image of the pure air/water interface appears black. The presence of a PEI/SDS monolayer causes a change in the refractive index of the interface which results in the reflection of light, resulting in a homogenous grey image. Finally, the presence of ESs beneath the surface monolayer appears as regions with high intensity (white bands or discrete regions).

6.3.7 Neutron reflectometry

NR is a powerful technique used to resolve the composition and structure of fluid films at the air/water interface.[41,42] A typical NR experiment consists of shining a neutron beam on the interface under study at grazing incident angles and recording the neutrons reflected using neutron detectors. The ratio between the intensity of the reflected and the incident neutrons known as reflectivity, *R*, is usually recorded as a function of the momentum transfer normal to the interface, Q_z, defined as:

$$Q_z = \frac{4\pi sin\theta}{\lambda} \tag{3.18}$$

where λ is the wavelength of the neutron beam and θ the angle of incidence. In this work, specular NR has been used, i.e., the angle of incidence and reflection are equal. Since neutrons interact with the nuclei of atoms, isotopic contrast variation is exploited to vary the SLD of a material, defined as the sum of the scattering length of each atom, *b*, divided by the molecular volume, V_m.

First, the low-Q_z approach[28] was used to determine the changes in the composition of PEI/SDS films during successive compression/expansion cycles. For that purpose, the Π-*A* isotherm experiment was reproduced using a Nima trough (UK, A_{max} = 265 cm^2). Two independent measurements were recorded generating data in 1 min slices and using deuterated or hydrogenous SDS, and ACMW (air contrast matched water, a mixture of 8.1% v/v D_2O in H_2O, SLD = 0 Å^{-2}) as subphase. The different techniques used in this work allow to study the films at different time and size scales. In addition, ellipsometry and BAM are very sensitive to the presence of inhomogeneities. Therefore, it is important to note that the area illuminated by the neutron beam is in the order of a few cm^2, so the average composition and structure of the different surface regions is measured. Measurements were performed on the FIGARO reflectometer at the Institut Laue-Langevin (Grenoble, France)[43] using a wavelength range λ = 2–16 Å, a 7% resolution in dλ/λ and an angle of incidence θ = 0.62°. The high flux at low-Q_z values, essential for the measurements involving hydrogenous material on ACMW, and low natural incident angle of FIGARO instrument make it possible to resolve the composition of the P/S films, i.e, the PEI and SDS surface excess, Γ, defined as:

$$\Gamma_i = \frac{V_{f,i}}{bN_A} \qquad (3.20)$$

where v_f is the volume fraction of the component, N_A is the Avogadro's number and *d* is the thickness of the film. The two data sets can be used to determine Γ_{PEI} and Γ_{SDS} by solving the following equations:

$$\rho_1 \cdot d_1 = N_A \cdot (\Gamma_{PEI} \cdot b_{PEI} + \Gamma_{SDS} \cdot b_{d-SDS}) \qquad (6.1)$$

$$\rho_2 \cdot d_2 = N_A \cdot (\Gamma_{PEI} \cdot b_{PEI} + \Gamma_{SDS} \cdot b_{h-SDS}) \qquad (6.2)$$

where $\rho_1 = 4 \times 10^{-6}$ Å^{-2} and $\rho_2 = 0.34 \times 10^{-6}$ Å^{-2} are the SLD values used in the model fits and *d* is the thickness fitted. As data using only the low-Q_z values (0.01–0.03 Å^{-1}) was analysed, these measurements are insensitive to the structure and only the amounts of PEI and SDS contribute to the scattering excess. The background (5.57×10^{-6}) was determined as the average value obtained in 10 independent reflectivity measurements of ACMW. Motofit[44] was used to fit the thickness of a single layer model with a roughness of 3.5 Å and the SLD values indicated above. The values of *b*, molecular volume, V_m, and SLD used in this work are listed in Table 6.1. The values of b and SLD of PEI have been calculated considering a 90% proton/deuterium exchange of the amino groups, and a 60% and 25% of protonation in PEI molecules at pH 4 and 10, as previously determined.[2]

Table 6.1. Scattering length (*b*), molecular volume (V_m) and scattering length density (ρ) used in this work for the different components studied.

Component	*b* (fm)	V_m (Å^3)	ρ (x 10^{-6} Å^{-2})
SS Headgroups	29.71	61	4.87
$C_{12}H_{25}$-Chains	–13.76	352	–0.39
$C_{12}D_{25}$-Chains	246.53	352	7.00
SDS Molecules	15.95	413	0.39
d_{25}-SDS Molecules	276.24	413	6.69
PEI (in ACMW) pH 4	3.21	78	0.41
PEI (in D_2O) pH 4	16.7	78	2.15
PEI (in ACMW) pH 10	4.19	78	0.54
PEI (in D_2O) pH 10	14.73	78	1.90

Then, the full-Q_z (0.01–0.25 Å^{-1}) approach was used to determine the structure perpendicular to the interface of PEI/SDS films. For that purpose, the ellipsometry experiment was reproduced using a Nima trough (UK, A_{max} = 700 cm^2). Measurements were performed on the INTER reflectometer at the ISIS Pulsed Neutron and Muon Source (Didcot, UK) using a wavelength range λ = 1.5–16 Å, a 5.5% resolution in $d\lambda/\lambda$ and two angles of incidence ($\theta_1 = 0.8°$ and $\theta_2 = 2.3°$). Three different isotopic contrasts were recorded: d-SDS/ACMW, d-SDS/D_2O, and h-SDS/D_2O. D_2O was used to calibrate the absolute reflectivity. However, only the d-SDS/ACMW and h-SDS/D_2O were considered to determine the structure of the films because the d-SDS/D_2O contrast did not fit the common model. A more detailed explanation about the influence of isotopic effects on the system is discussed in the results and the section 6.7.

Co-refinement of the d-SDS/ACMW and h-SDS/D_2O was carried out using Motofit[44] to provide a model that results in a satisfactory fit of the two contrasts. A model comprising 5 stratified layers was necessary to obtain a satisfactory co-refinement of the data: (1) SDS tails, (2) SDS headgroups with PEI electrostatically bound and solvent, (3) PEI layer and solvent, (4) SDS ESs and solvent, (5) PEI layer and solvent. 4 parameters are used to define each layer, *i*: the thickness (d_i), the SLD (ρ_i), the solvent volume fraction ($V_{f,solvent}$) and the roughness. A roughness of 4.2 Å consistent with the presence of capillary waves considering the surface tension of the system (40 mN/m) was applied to all interfaces.[45,46] Three different constraints were used to fit the surface monolayer. The first one is that the surface excess of tails and heads must be the same. The second one is that, given the dependence of the PEI SLD on the subphase used due to proton/deuterium exchange, the SLD of the headgroups layer in the ACMW and D_2O contrasts must be consistent with the presence of the same amount of PEI. Lastly, to minimise the number of fitting parameters and, given that the most sensitive contrast to the amount of PEI in the headgroups is the d-SDS/D_2O, we considered stoichiometric charge binding. The parameters fixed in the fit are the roughness of all layers, the thickness of layer 2, the SLD of all layers, and the solvent volume fraction of layer 1. Besides, the thickness of layer 1 has been fixed but iteratively modified while the thickness and $V_{f,solvent}$ of layers 3, 4 and 5 have been fitted minimising the χ^2 of the fit. The values of the parameters fitted have been restricted using the genetic algorithm as follows: 2–15 Å and 20–30 Å for the thickness of PEI and ESs layers, respectively, and 0–100% for all $V_{f,solvent}$. Residual background values of 5×10^{-6} and 2×10^{-6} were used for the d-SDS/ACMW, and the h-SDS/D_2O contrasts, respectively. The uncertainty of each parameter has been calculated as the difference between the optimised parameter and the value of that parameter that results in a 10% increase in χ^2.

6.4 Results and discussion

Prior to presentation and discussion of new results on hyperbranched spread PEI/SDS films, a general description of the physical behavior of linear NaPSS/DTAB [28,32]and spread PLL/SDS[33] films when manipulated on a Langmuir trough is given. Upon compression of the surface area, the surface pressure increases until it reaches a critical value for each system of around 28 mN/m. Further compression results in a surface pressure plateau during which the values do not increase. This coincides with the formation of discrete ESs bound to the surface monolayer, which increase in coverage with ongoing compression of the surface area. Reincorporation of material from the ESs back into the surface monolayer occurs upon expansion of the surface area, albeit with a kinetic barrier, shows that cycling of the surface area is reproducible and the structural changes are reversible.

As ESs were produced using overcharged aggregates for the NaPSS/DTAB and PLL/SDS systems, first we characterise the change in surface charge of 100 ppm PEI/SDS complexes with varying bulk surfactant concentration so that the appropriate bulk surfactant concentration value can be selected to produce overcharged aggregates. Figure 6.1 shows electrophoretic mobility data recorded on PEI/SDS mixtures for (A) pH 4 and (B) pH 10. As expected, the results at pH 4 show that complexes exhibit positive charge at low bulk surfactant concentrations, and with increasing values there is charge reversal beyond the bulk composition corresponding to charge neutral complexes. The composition of charge neutrality is 1.56 mM, which is consistent with previous findings.[2] Previous studies have indicated that the binding of SDS to PEI at pH 4 is 60%.[2] At pH 10, charge neutrality is achieved at a lower concentration of 0.57 mM SDS due to the lower charge density of PEI, i.e. fewer SDS molecules are required to neutralise the polyelectrolyte charges. The scattering intensities below charge neutrality were very low, so the data are omitted as they have low significance and are not needed for this objective. The results highlight the impact of pH on PEI/SDS interactions, which can affect the spreading of the PEI/SDS aggregates in water adjusted to either pH 4 or pH 10.

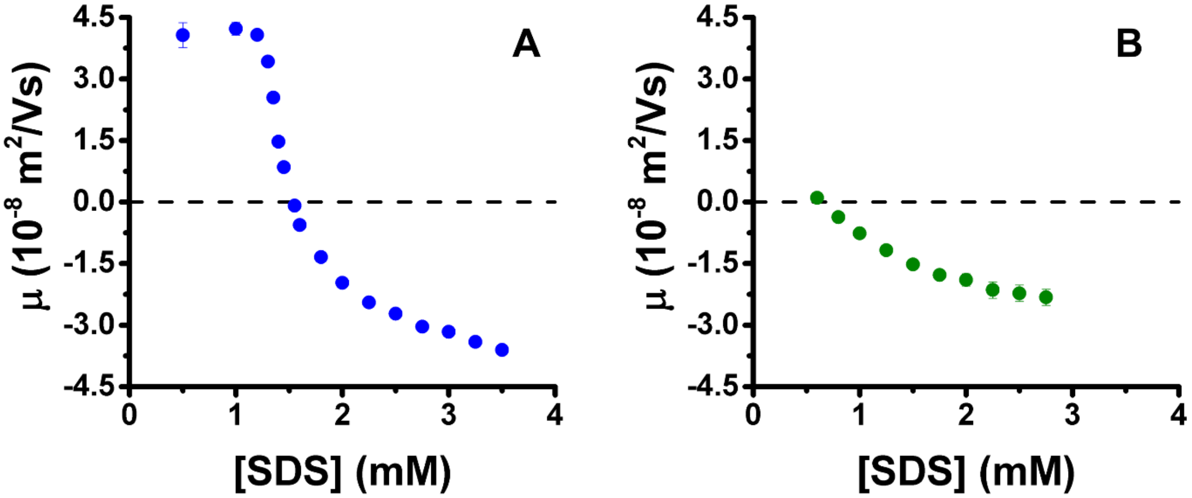

Figure 6.1. Variation of the electrophoretic mobility of PEI/SDS aggregates with the concentration of SDS using a constant concentration of 100 ppm PEI at (A) pH 4 and (B) pH 10. The black dashed lines indicate neutral charge. The error bars in the graph are smaller than the symbols.

A concentration of 2.5 mM SDS was chosen to produce overcharged aggregates for the creation of the spread PEI/SDS films. While the aggregates made to produce the spread films in this work resulted from mixing the components without pH adjustment, i.e. close to pH 10,[20] the choice of this value – where the aggregates are overcharged at both pH 4 and pH 10 – means that if any aggregates were to become embedded in resulting spread films without a change in their composition on a subphase with either pH value, they would remain overcharged with a surfactant corona.[20] Specifically, it may be noted that according to our mixing protocol, equal volumes of 200 ppm PEI and 5.0 mM SDS were mixed to produce turbid dispersions of overcharged aggregates in 100 ppm PEI/2.5 mM SDS mixture.

Figure 6.2 shows three compression/expansion cycles of spread PEI/SDS films on a Langmuir trough. The surface pressure at the maximum compression ratio reached of spread films on a pH 4 subphase (panel A) is around 32 mN/m, while that of films spread on pH 10 subphase (panel B) is 37 mN/m. Additionally, several 'blips' in the data can be observed only upon expansion of films on a pH 10 subphase, which we infer not be experimental artefacts but consistent with the presence of aggregates remaining embedded in the films, as they are for adsorbed layers, resulting in discrete Marangoni spreading events at the surface pressure rises. These differences provide a first indication that the P/S interactions in the spread films can be strongly affected by the degree of protonation of the polyelectrolyte.

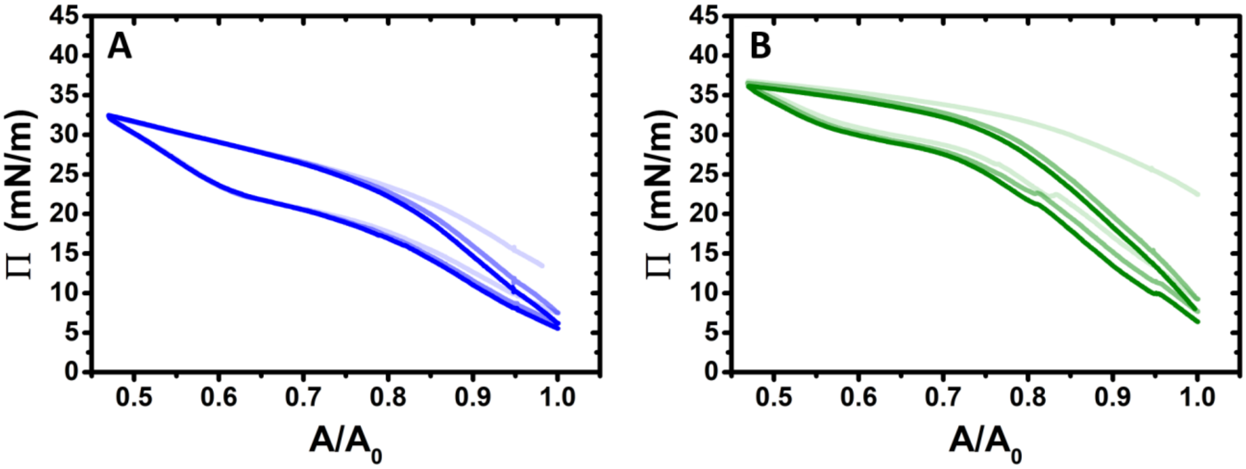

Figure 6.2. Π of PEI/SDS spread films on pure water subphases adjusted to (A) pH 4 and (B) pH 10 during three compression/expansion cycles on a Langmuir trough, where the maximum compression ratio is 2.0 ($A/A_0 = 0.5$), and successive cycles are darker in color.

Commonly with the behavior of the linear NaPSS/DTAB,[28,32] but not PLL/SDS[33] films, the surface pressure during the first compression is higher than in that of subsequent cycles, which is attributed to annealing of the film into a different morphology rather than loss of material during the first compression. Data below from NR will allow us to confirm that the same interpretation is appropriate in this case. However, the general shapes of the isotherms of spread PEI/SDS films are very different to that of NaPSS/DTAB and spread PLL/SDS films, as there is no clear plateau in the surface pressure beyond which it has been shown that ESs form. Indeed, the surface tension of a layer of PEI/SDS complexes is 30 mN/m,[35] which hints that a surface pressure of around 43 mN/m could be required to saturate the chains layer of the surface monolayer of the spread film. As it is known that the surface structures at the air/water interface of linear P/S films are influenced by the stiffness of the polyelectrolyte backbone,[47] the different shapes of the isotherms for spread hyperbranched PEI/SDS films may be related to the different macromolecular architectures rather than simply to the different electrostatic interactions.

We went on to resolve the film composition in terms of the surface excesses of PEI, Γ_{PEI}, and SDS, Γ_{SDS}, also over three compression/expansion cycles on a Langmuir trough, again at subphase pH values of 4 and 10, using the low-Q_z implementation of NR. Figure 6.3 shows the measured values of Γ_{PEI} and Γ_{SDS} over the three cycles. The most striking observation is that Γ_{SDS} reaches 7.4 ± 0.1 μmol/m^2 at pH 4 and 6.1 ± 0.1 μmol/m^2 at pH 10 by the end of the first compression. It may be noted that the uncertainties in these measured values are both very low due to the strong difference in scattering between the deuterated and hydrogenous surfactant in comparison with the weakly-scattering polyelectrolyte on the contrast-matched subphase. These values both far exceed the surface excess of SDS at limiting surface coverage at its critical micelle concentration of 4.20 ± 0.09 μmol/m^2.[48] It may be noted that the onset of formation of ESs for PLL/SDS films occurs upon compression once the surfactant coverage in the surface monolayer reaches 4.0 ± 0.1 μmol/m^2,[33] a value lower than the limiting surface coverage of the surfactant alone, hence these data strongly imply that, similarly to the films spread from overcharged aggregates for NaPSS/DTAB[32] and PLL/SDS,[33] ESs including SDS present beneath the surface monolayer form upon compression of spread PEI/SDS films on subphases of both pH values studied. Concerning the stoichiometry of the films, the results show that the amount of SDS and PEI is approximately the same at pH 4, while there is a large excess of PEI at pH 10. At pH 4, the high charge density of PEI results in the compensation of the charged headgroups in the surfactant monolayer. However, electrophoretic mobility measurements showed that only 60% of SDS binds to PEI molecules at pH 4.[2] Therefore, the extra binding step that leads to the apparent neutralisation of the films at pH 4 must occur during spreading, a process in which the rapid equilibrium of protonation of PEI plays an important role. At pH 10, the low charge density of PEI results in a high excess of PEI molecules needed to neutralise the charges of the headgroups in the surfactant monolayer.

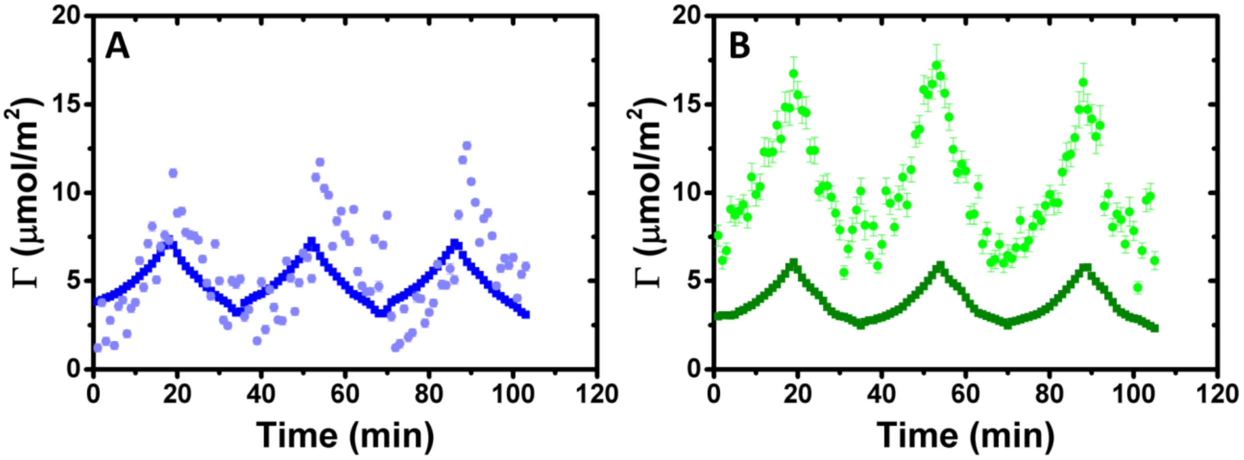

Figure 6.3. Surface excesses of PEI (lighter circles) and SDS (darker squares) of spread PEI/SDS films on pure water subphases adjusted to (A) pH 4 and (B) pH 10 during three compression/expansion cycles on a Langmuir trough, where the maximum compression ratio is 2.0 (A/A_0 = 0.5), resolved using the low-Q_z implementation of NR.

The recorded values of Γ_{PEI} are much more scattered, with higher error bars, as expected due to the lower scattering contrast between the polyelectrolyte in comparison with the measured background from the weakly-scattering hydrogenous surfactant on the contrast-matched subphase. What we can infer, if these measured values are a true representation of the PEI surface excess, is that Γ_{PEI} exceeds Γ_{SDS}, and the values of Γ_{PEI} are higher on a subphase of pH 10 than pH 4. Nevertheless, interpretation of these data must be carried out with a note of caution, as any aggregates embedded in the films may result in excess scattering that could significantly alter the measured values of Γ_{PEI} but not those of Γ_{SDS}. Therefore, judgement on this point should be reserved until full analysis of the film structure upon compression reported below.

Next, we examined the stability of spread PEI/SDS films at a high compression ratio, at which we have inferred above that ESs have formed, with measurements of *d*Δ from ellipsometry and surface pressure on a Langmuir trough.

With a pH 4 subphase, as the barriers compress and the surface pressure increases, so does the values of *d*Δ, showing that the surface excess of material per unit area increases also. Even so, it is notable that there are some small fluctuations in the values of *d*Δ, which we will come back to later in our interpretation of images of the lateral morphology from BAM. Once maximum compression is reached, the surface excess remains virtually constant with a relaxation in the signal of just 3%, suggesting that the ESs formed during compression are very stable with time. There are no temporal fluctuations observed in the data at constant surface pressure, which can be interpreted either in terms of a lack of aggregates embedded in the films or in terms of a large number of small aggregates whose average number is practically constant in the area probed by the laser beam or in terms of a higher stiffness of the films where the signal from any aggregates in the area probed by the laser is constant with time.

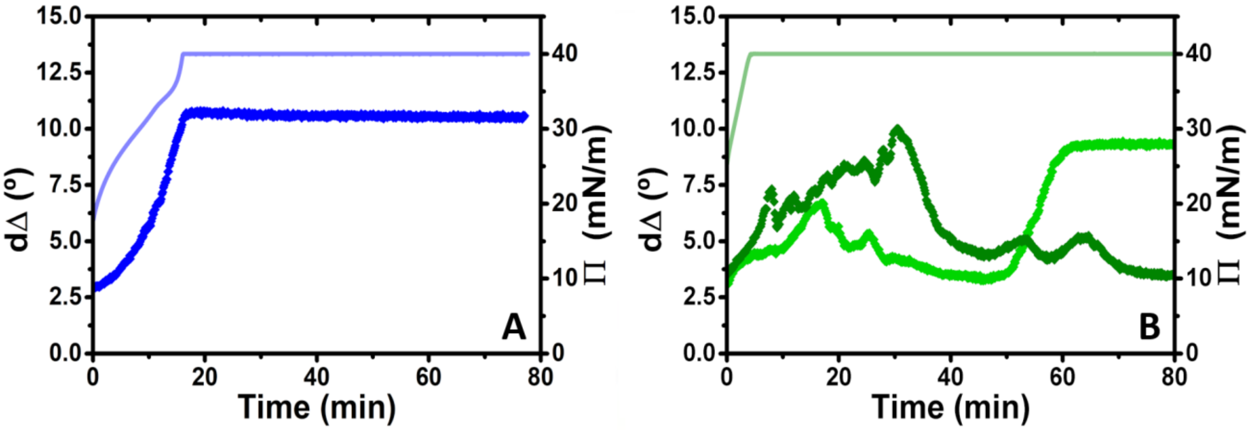

<u>Figure 6.4.</u> Ellipsometry *d*Δ (diamonds) and surface pressure (lines) data of spread PEI/SDS films on pure water subphases adjusted to (A) pH 4 and (B) pH 10 where the films are initially compressed to a surface pressure of 40 mN/m and then held at that surface pressure. In the latter case, ellipsometry data from two experiments are shown to highlight the variable nature of the temporal fluctuations.

With a pH 10 subphase, the maximum surface pressure is achieved with less compression of the surface area by the barriers, consistent with the higher starting surface pressure of the spread films (25 mN/m as opposed to 18 mN/m). A key difference is observed in the ellipsometry data where pronounced temporal fluctuations are observed, and data shown from two equivalent experiments reveal that the fluctuations, within the same bounds of around 3–8°, are seemingly random with time. It follows in this case that the spread films are not rigid and the number of either embedded aggregates or ESs fluctuates significantly as they are being transported in and out of the area probed by the laser beam on the second timescale.

Data from additional techniques are required to distinguish the possibilities raised in the data interpretations for subphases of both pH values. Next, we turned to optical imaging from BAM, and in this case, prior to a description of the results, it is important to highlight what we may hope to infer from the data. The technique has a resolution on the µm-scale while freshly formed P/S aggregates have a size on the hundreds of nm-scale.[28] Therefore, we would not expect to resolve the presence of individual aggregates embedded in the films, yet we may hope to resolve any lateral association of the aggregates or the presence of ESs. Also, while in the absence of BAM imaging, we do not know the dimensions of the ESs for spread PEI/SDS films, it was possible to resolve a network of ESs in spread PLL/SDS films with a morphology on a length scale of hundreds of µm.[33] Finally, the exposure time of the BAM images was typically 1 s. As a result, whether or not the intensity fluctuates for images taken at the same A/A_0 may reveal information about the mobility or rigidity of the film. Figure 6.5 shows images recorded with decreasing A/A_0 (increasing compression ratio) for spread PEI/SDS films during compression on subphases of both pH values.

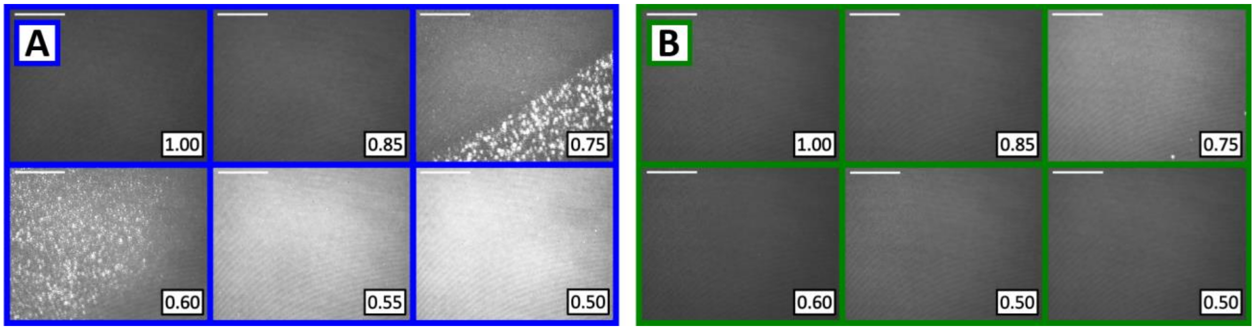

Figure 6.5. BAM images of spread PEI/SDS films on pure water subphases adjusted to (A) pH 4 and (B) pH 10 during compression of the surface area on a Langmuir trough, where the insets show the value of A/A_0 (inverse of the compression ratio), and the scale bars are 100 µm.

With a subphase of pH 4, upon film compression, discrete bright patches on the tens of µm-scale are observed from A/A_0 values from 0.75, yet the longer-range order of their presence is on the hundreds of µm-scale. The small fluctuations upon film compression observed with ellipsometry in Figure 6.4 are therefore explained as domains of ESs or embedded aggregates that pass through the area of the interface probed by the laser beam. Upon further compression of the film, the morphology becomes more homogeneous and rigid, as when an A/A_0 value below 0.55 is reached there is no observed movement in the film. While it would be intuitive to infer that the bright patches observed are the ESs, objectively, these images are not sufficient to distinguish them from embedded aggregates and another technique applied below will be required to do so.

With a subphase of pH 10, the films exhibited increasing intensity with compression from A/A_0 = 1–0.75 homogenous, yet fluctuations are observed thereafter even down to an A/A_0 value of 0.5. Even at constant compression ratios, the images fluctuated in intensity, and of the two images shown at this compression ratio, the latter has a reduction in brightness of 11%. This result explains the key difference in the ellipsometry data of the films on subphases at the two values: the films are rigid at pH 4 yet mobile at pH 10.

Nevertheless, questions remain about the nature of any aggregates embedded in the films, and a direct structural characterisation of films was missing. The structural implementation of NR with data recorded in three isotopic contrasts over the fully accessible Q_z-range was applied. Figure 6.6 shows data recorded for spread PEI/SDS films compressed and held at 40 mN/m for both studied pH values as well as resulting model fits and volume fraction profiles normal to the interface, and Tables 6.2 and 6.3 reports the fitted structural parameters for the films at pH 4 and 10, respectively. It is important to note that, as mentioned in the description of the NR technique, the d-SDS/D_2O contrast does not fit the same model as the other two contrasts. While the d-SDS/ACMW and h-SDS/D_2O contrasts can be co-refined resulting in a satisfactory result, the inclusion of the d-SDS/D_2O contrast results in an increase of more than 100% in the χ^2 of the fit (see section 6.7.1). This issue may be related to isotopic effects that alter intermolecular interactions or interactions of molecules with the solvent.[47] For that reason, only the results of d-SDS/ACMW and h-SDS/D_2O contrasts are discussed here.

First, the reflectivity profiles of both systems show a clear Kiessig fringe that denotes the presence of a multilayer structure, similar to that observed in the PLL/SDS system.[33] In addition, the model used requires the presence of 5 layers in both cases: (1) SDS tails, (2) SDS headgroups with PEI electrostatically bound and solvent, (3) PEI layer and solvent, (4) SDS ESs and solvent, (5) PEI layer and solvent. The extra layer of PEI beneath the surfactant ESs is in agreement with results recently obtained in the study of PLL/SDS films using high compression ratios, in which the presence of polyelectrolyte below the ESs was inferred for the first time, suggesting that the surfactant bilayer is wrapped by polyelectrolyte.

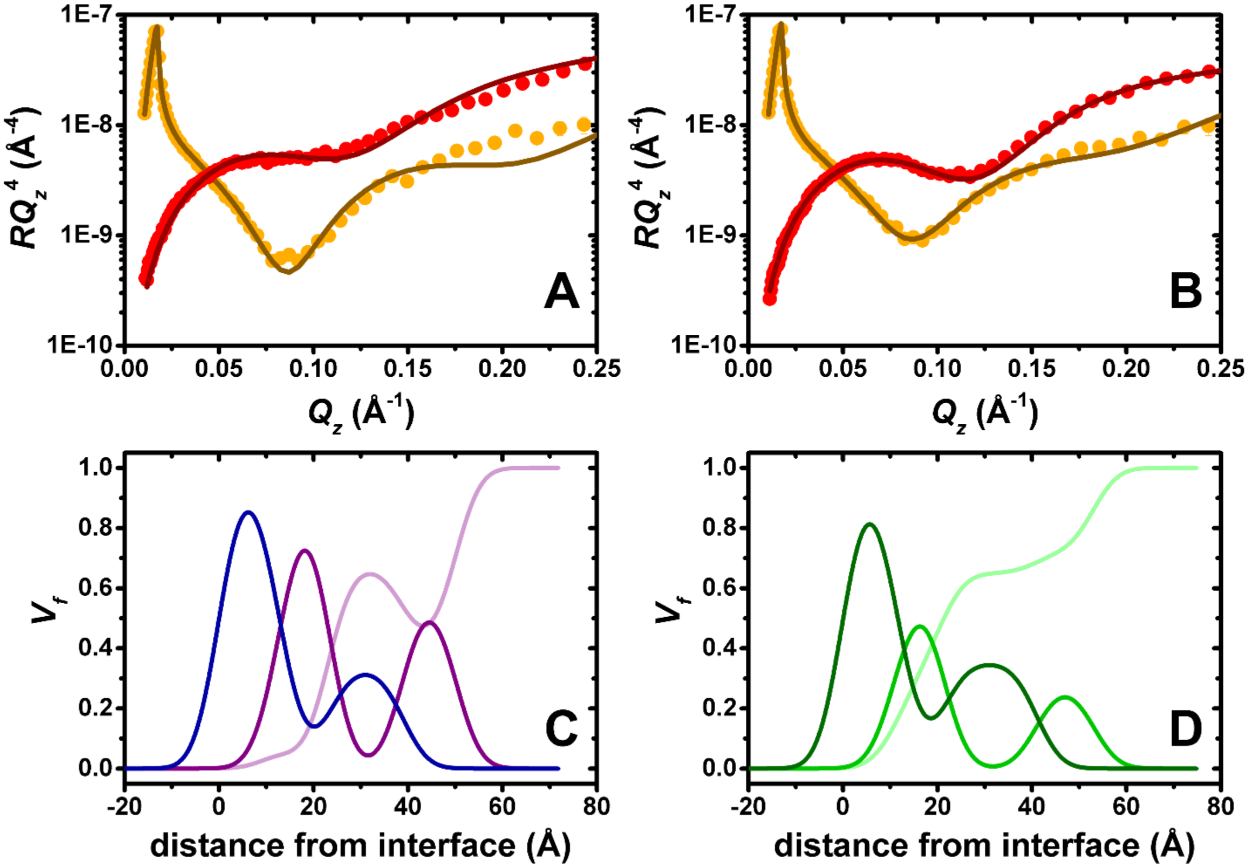

Figure 6.6. Neutron reflectivity (A/B) data (points) and model fits (lines) of spread PEI/SDS films in two isotopic contrasts involving PEI with d-SDS in ACMW (red) and h-SDS in D_2O (orange) on pure water subphases adjusted to (A/C) pH 4 and (B/D) pH 10 and compressed and held at 40 mN/m, resolved using the full-Q_z implementation of NR; (C/D) resulting volume fraction profiles where surfactant is blue/dark green, polyelectrolyte is mauve/green and solvent is pink/light green in the two panels, respectively.

At pH 4, the thickness of the surfactant tails is 11 ± 1 Å, which corresponds to a significantly higher amount of surfactant in the surface monolayer than that of the surfactant alone[48] or when interacting with PLL.[33] This suggests that a very compact surface monolayer is formed, as reflected by the composition of layer 3 of about 100% PEI. This observation is in agreement with the explanation of the ellipsometry and BAM results above concerning presence of a rigid film. The ESs present are composed of a layer of surfactant of 16 ± 1 Å, lower than the one expected for an SDS bilayer, and a PEI layer beneath (layer 5) that is less compact and more extended than above it (layer 3).

At pH 10, the thickness of the surfactant tails is 10 ± 1 Å and there is a 66% of PEI in layer 3 indicating a less compact surface monolayer in this case, which is also in agreement with the ellipsometry and BAM results implying the presence of a mobile film. The ESs present below are composed of a layer of surfactant of 20 ± 1 Å, matching the presence of a bilayer of SDS and, similar to the results obtained at pH 4, a PEI layer beneath (layer 5) that is less compact and more extended than that above it (layer 3).

Table 6.2. Thickness (d_i), scattering length density (ρ_i), and composition obtained from the fit of the PEI/SDS films spread on a subphase adjusted to pH 4, where *i* is the layer number.

Layer	Parameter	d-SDS/ACMW	d-SDS/D₂O
1	d_1 (Å)	11 ± 1	
	ρ_1 (x 10^{-6} Å^{-2})	7	−0.39
	Composition (*V*%)	100% SDS chains	
2	d_2 (Å)	4	
	ρ_2 (x 10^{-6} Å^{-2})	2.76	3.58
	Composition (*V*%)	45% SDS heads 45% PEI 10% solvent	
3	d_3 (Å)	8 ± 1	
	ρ_3 (x 10^{-6} Å^{-2})	0.41	2.15
	Composition (*V*%)	99 ± 10% PEI 1 ± 10% solvent	
4	d_4 (Å)	16 ± 1	
	ρ_4 (x 10^{-6} Å^{-2})	6.69	0.39
	Composition (*V*%)	33 ± 3% SDS 67 ± 3% solvent	
5	d_5 (Å)	11 ± 1	
	ρ_5 (x 10^{-6} Å^{-2})	0.41	2.15
	Composition (*V*%)	60 ± 6% PEI 40 ± 6% solvent	

Table 6.3. Thickness (d_i), scattering length density (ρ_i), and composition obtained from the fit of the PEI/SDS films spread on a subphase adjusted to pH 10, where *i* is the layer number.

Layer	Parameter	d-SDS/ACMW	d-SDS/D_2O
1	d_1 (Å)	10 ± 1	
	ρ_1 (x 10^{-6} Å^{-2})	7	-0.39
	Composition (*V*%)	100% SDS chains	
2	d_2 (Å)	4	
	ρ_2 (x 10^{-6} Å^{-2})	2.71	3.39
	Composition (*V*%)	41% SDS heads 41% PEI 18% solvent	
3	d_3 (Å)	7 ± 1	
	ρ_3 (x 10^{-6} Å^{-2})	0.54	1.9
	Composition (*V*%)	66 ± 17% PEI 34 ± 17% solvent	
4	d_4 (Å)	20 ± 1	
	ρ_4 (x 10^{-6} Å^{-2})	6.69	0.39
	Composition (*V*%)	35 ± 2% SDS 65 ± 2% solvent	
5	d_5 (Å)	12 ± 2	
	ρ_5 (x 10^{-6} Å^{-2})	0.54	1.9
	Composition (*V*%)	28 ± 5% PEI 72 ± 5% solvent	

6.5 Conclusions

The effects of subphase pH on the properties and structure of P/S films spread from aggregates containing a hyperbranched weak polyelectrolyte whose charge density varies significantly with pH were investigated for the first time in this work. The results show that these films behave significantly differently when spread on a water subphase at pH 4 and pH 10. The use of a variety of surface-sensitive techniques that provide information at different time and length scales has been critical for elucidation of the film behavioral properties.

At both pH values, the general physical picture of the structures of spread PEI/SDS films upon compression of the surface area are similar, consisting of a PEI/SDS surface monolayer with bound discrete surfactant ESs wrapped in PEI. However, the subphase pH has a clear influence on the detailed structure. At pH 4, the thickness of the tails in the surface monolayer is greater while beneath the surface monolayer, the next layer is almost entirely composed of PEI, and the thickness of the ESs is significantly lower than at pH 10. BAM images and ellipsometry together have revealed that the films are rigid at pH 4 and mobile at pH 10. Furthermore, ellipsometry has revealed that the films at pH 10 are highly heterogeneous due to a larger quantity of aggregates embedded in them, a physical picture that is similar to that observed on adsorbed layers in previous work. Thus, we can conclude that the increase in PEI charge density when aggregates are spread on a water subphase at pH 4 results in the dissociation of most of the PEI/SDS aggregates and the formation of a homogenous compact film, while embedded aggregates remain intact and trapped at the interface resulting in a heterogenous mobile film at pH 10. These observations can be explained by the lower surface charge density of PEI/SDS aggregates due to the lower charge density of PEI at pH 10, which limits aggregate dissociation and may even favor aggregate fusion, resulting in larger aggregates.[35]

The general structure of PEI/SDS films upon surface area compression is generally similar to that obtained for PLL/SDS films. However, while the PLL/SDS system shows a plateau during compression whose onset coincides with the formation of ESs, in the case of spread PEI/SDS films, the surface pressure continues to increase after the onset of ESs formation. This result is in agreement with the higher coverage of SDS in the surface monolayer.

These findings provide a method for fine-tuning the dynamic properties and structures of spread P/S films at the air/water interface. The results obtained in recent years indicate that we are getting closer to the goal of being able to design P/S films based on dynamic properties or desired structure, controlling parameters such as polyelectrolyte stiffness, charge density of the polyelectrolyte, ionic strength of the subphase, or charge of the aggregates used to create the films. Such films may be highly useful for a range of transfer applications.

6.6 Acknowledgements

We thank ISIS Neutron and Muon Source for allocations of neutron beamtime (DOI: https://doi.org/10.5286/ISIS.E.RB2210138), the Partnership for Soft Condensed Matter (PSCM) for lab support. IV acknowledges the financial support from the Hungarian National Research, Development and Innovation Office (NKFIH K116629). AM acknowledges the financial support from MICINN under grant PID2021-129054NA-I00 and the IKUR Strategy of the Basque

Government. ME and RC acknowledge the Engineering and Physical Research Council (UK) for support with grant EP/V029495/1.

6.7 Supplementary information

6.7.1 Neutron reflectivity fits including d-SDS/D_2O contrast

As mentioned in the manuscript, the d-SDS/D_2O contrast was not included since it does not fit the same model as the other two contrasts but corresponds to a surface PEI/SDS monolayer. Figure 6.7 shows the reflectivity and volume fraction profiles obtained by co-refinement of the three contrasts while Tables 6.4 and 6.5 show the fitting parameters for the measurements at pH 4 and pH 10, respectively. It can be seen that the fits to the d-SDS/ACMW and h-SDS/D_2O contrasts deviate from the reflectivity profiles with respect to those obtained using only those two contrasts, and the model used is not valid for fitting the d-SDS/D_2O contrast. In fact, while the χ^2 of the fits without including this contrast is 8.5 and 6.9 for pH 4 and 10, respectively, these values increase to 19.8 and 21.1 when it is included. It was recently reported that isotopic effects can result in the variation of the coverage of ESs in P/S films at the air/water interface.[47] The isotopic effects were discussed in terms of the SDS contrast or the subphase contrast used. However, the results obtained in this work show that the combination of both contrasts of SDS with both contrasts of solvents fit to the same model. It has been also demonstrated that the charge density of PEI can vary from H_2O to D_2O depending on the pH, but no significant differences were observed in the results of PEI/SDS aggregates at pH 4 and 10.[49] Therefore, although there is a clear isotopic effect that results in a different structure when the d-SDS/ D_2O contrast is used, future work is required to understand its origin.

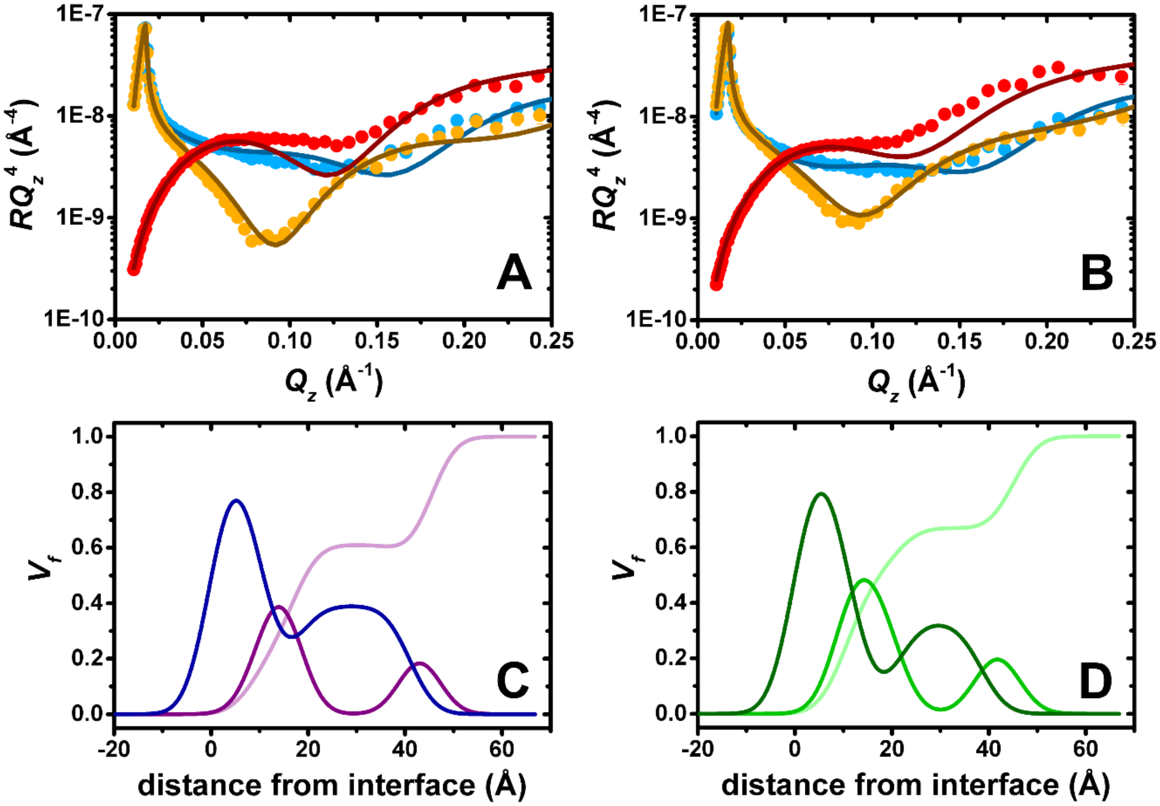

Figure 6.7. Neutron reflectivity (A/B) data (points) and model fits (lines) of spread PEI/SDS films in three isotopic contrasts involving PEI with d-SDS in ACMW (red) and (blue) h-SDS in D_2O (orange) on pure water subphases adjusted to (A/C) pH 4 and (B/D) pH 10 and compressed and held at 40 mN/m, resolved using the full-Q_z implementation of NR; (C/D) resulting volume fraction profiles where surfactant is blue/dark green, polyelectrolyte is mauve/green and solvent is pink/light green in the two panels, respectively

Table 6.4. Thickness (d_i), scattering length density (ρ_i), and composition obtained from the fit of the PEI/SDS films spread on a subphase adjusted to pH 4, where *i* is the layer number.

Layer	Parameter	d-SDS/ACMW	d-SDS/D_2O	h-SDS/D_2O
1	d_1 (Å)	9 ±1		
	ρ_1 (x 10^{-6} Å^{-2})	7	7	−0.39
	Composition	100% SDS chains		
2	d_2 (Å)	4		
	ρ_2 (x 10^{-6} Å^{-2})	3.96	4.31	4.31
	Composition	39% SDS heads 35% PEI 26% solvent		
3	d_3 (Å)	4 ± 1		
	ρ_3 (x 10^{-6} Å^{-2})	0.41	2.15	2.15
	Composition	80% PEI 20% solvent		
4	d_4 (Å)	24 ± 2		
	ρ_4 (x 10^{-6} Å^{-2})	6.69	6.69	0.39
	Composition	39% SDS 61% solvent		
5	d_5 (Å)	4 ± 3		
	ρ_5 (x 10^{-6} Å^{-2})	0.41	2.15	2.15
	Composition	50% PEI 50% solvent		

Table 6.5. Thickness (d_i), scattering length density (ρ_i), and composition obtained from the fit of the PEI/SDS films spread on a subphase adjusted to pH 10, where *i* is the layer number.

Layer	Parameter	d-SDS/ACMW	d-SDS/D_2O	h-SDS/D_2O
1	d_1 (Å)	10 ± 1		
	ρ_1 (x 10^{-6} Å^{-2})	7	7	−0.39
	Composition	100% SDS chains		
2	d_2 (Å)	4		
	ρ_2 (x 10^{-6} Å^{-2})	3.96	4.31	4.31
	Composition	41% SDS heads 25% PEI 34% solvent		
3	d_3 (Å)	7 ± 2		
	ρ_3 (x 10^{-6} Å^{-2})	0.41	2.15	2.15
	Composition	50% PEI 50% solvent		
4	d_4 (Å)	18 ± 1		
	ρ_4 (x 10^{-6} Å^{-2})	6.69	6.69	0.39
	Composition	33% SDS 67% solvent		
5	d_5 (Å)	7 ± 2		
	ρ_5 (x 10^{-6} Å^{-2})	0.41	2.15	2.15
	Composition	34% PEI 66% solvent		

6.8 References

(1) Goddard, E. D. Polymer/Surfactant Interaction-Its Relevance to Detergent Systems. *J. Am. Oil Chem. Soc.* **1994**, *71*, 1–16.

(2) Mezei, A.; Mészáros, R. Novel Method for the Estimation of the Binding Isotherms of Ionic Surfactants on Oppositely Charged Polyelectrolytes. *Langmuir* **2006**, *22*, 7148–7151..

(3) Bain, C. D.; Claesson, P. M.; Langevin, D.; Mészáros, R.; Nylander, T.; Stubenrauch, C.; Titmuss, S.; Klitzing, R. V. Complexes of Surfactants with Oppositely Charged Polymers at Surfaces and in Bulk. *Adv. Colloid Interface Sci.* **2010**, *155*, 32–49.

(4) Hoffmann, I.; Heunemann, P.; Prévost, S.; Schweins, R.; Wagner, N. J.; Gradzielski, M. Self-Aggregation of Mixtures of Oppositely Charged Polyelectrolytes and Surfactants Studied by Rheology, Dynamic Light Scattering and Small-Angle Neutron Scattering. *Langmuir* **2011**, *27*, 4386–4396..

(5) Claesson, P. M.; Dedinaite, A.; Poptoshev, E. Polyelectrolyte-Surfactant Interactions at Solid-Liquid Interfaces Studied with Surface Force Techniques. In *Physical Chemistry of Polyelectrolytes*; Radeva, T., Ed.; CRC Press: New York, 2001; p 447.

(6) Naderi, A.; Claesson, P. M. Adsorption Properties of Polyelectrolyte-Surfactant Complexes on Hydrophobic Surfaces Studied by QCM-D. *Langmuir* **2006**, *22*, 7639–7645.

(7) Fernández-Peña, L.; Abelenda-Nuñez, I.; Hernández-Rivas, M.; Ortega, F.; Rubio, R. G.; Guzmán, E. Impact of the Bulk Aggregation on the Adsorption of Oppositely Charged Polyelectrolyte-Surfactant Mixtures onto Solid Surfaces. *Adv. Colloid Interface Sci.* **2020**, *282*, 102203.

(8) Kristen, N.; Vüllings, A.; Laschewsky, A.; Miller, R.; Klitzing, R. V. Foam Films from Oppositely Charged Polyelectolyte/Surfactant Mixtures: Effect of Polyelectrolyte and Surfactant Hydrophobicity on Film Stability. *Langmuir* **2010**, *26*, 9321–9327.

(9) Bahramian, A.; Thomas, R. K.; Penfold, J. The Adsorption Behavior of Ionic Surfactants and Their Mixtures with Nonionic Polymers and with Polyelectrolytes of Opposite Charge at the Air-Water Interface. *J. Phys. Chem. B* **2014**, *118*, 2769–2783.

(10) Schulze-Zachau, F.; Braunschweig, B. Structure of Polystyrenesulfonate/Surfactant Mixtures at Air–Water Interfaces and Their Role as Building Blocks for Macroscopic Foam. *Langmuir* **2017**, *33*, 3499–3508.

(11) Akanno, A.; Guzmán, E.; Fernández-Peña, L.; Ortega, F.; Rubio, R. G. Surfactant-Like Behavior for the Adsorption of Mixtures of a Polycation and Two Different Zwitterionic Surfactants at the Water/Vapor Interface. *Molecules* **2019**, *24*, 3442.

(12) Campbell, R. A.; Angus-Smyth, A.; Yanez Arteta, M.; Tonigold, K.; Nylander, T.; Varga, I. New Perspective on the Cliff Edge Peak in the Surface Tension of Oppositely Charged Polyelectrolyte/Surfactant Mixtures. *J. Phys. Chem. Lett.* **2010**, *1*, 3021–3026.

(13) Llamas, S.; Guzmán, E.; Ortega, F.; Baghdadli, N.; Cazeneuve, C.; Rubio, R. G.; Luengo, G. S.

Adsorption of Polyelectrolytes and Polyelectrolytes-Surfactant Mixtures at Surfaces: A Physico-Chemical Approach to a Cosmetic Challenge. *Adv. Colloid Interface Sci.* **2015**, *222*, 461–487.

(14) Gradzielski, M. Polyelectrolyte-Surfactant Complexes As a Formulation Tool for Drug Delivery. *Langmuir* **2022**, *38*, 13330–13343.

(15) Dedinaite, A.; Pettersson, T.; Mohanty, B.; Claesson, P. M. Lubrication by Organized Soft Matter. *Soft Matter* **2010**, *6*, 1520–1526.

(16) Naderi, A.; Claesson, P. M.; Bergström, M.; Dedinaite, A. Trapped Non-Equilibrium States in Aqueous Solutions of Oppositely Charged Polyelectrolytes and Surfactants: Effects of Mixing Protocol and Salt Concentration. *Colloids Surfaces A Physicochem. Eng. Asp.* **2005**, *253*, 83–93.

(17) Varga, I.; Campbell, R. A. General Physical Description of The Behavior of Oppositely Charged Polyelectrolyte/Surfactant Mixtures at the Air/Water Interface. *Langmuir* **2017**, *33*, 5915–5924.

(18) Guzmán, E.; Fernández-Peña, L.; Ortega, F.; Rubio, R. G. Equilibrium and Kinetically Trapped Aggregates in Polyelectrolyte–Oppositely Charged Surfactant Mixtures. *Curr. Opin. Colloid Interface Sci.* **2020**, *48*, 91–108.

(19) Mezei, A.; Pojják, K.; Mészáros, R. Nonequilibrium Features of the Association between Poly(Vinylamine) and Sodium Dodecyl Sulfate: The Validity of the Colloid Dispersion Concept. *J. Phys. Chem. B* **2008**, *112*, 9693–9699.

(20) Mészáros, R.; Thompson, L.; Bos, M.; Varga, I.; Gilányi, T. Interaction of Sodium Dodecyl Sulfate with Polyethyleneimine: Surfactant-Induced Polymer Solution Colloid Dispersion Transition. *Langmuir* **2003**, *19*, 609–615.

(21) Ábrahám, Á.; Mezei, A.; Mészáros, R. The Effect of Salt on the Association between Linear Cationic Polyelectrolytes and Sodium Dodecyl Sulfate. *Soft Matter* **2009**, *5*, 3718–3726.

(22) Pojják, K.; Bertalanits, E.; Mészáros, R. Effect of Salt on the Equilibrium and Nonequilibrium Features of Polyelectrolyte/Surfactant Association. *Langmuir* **2011**, *27*, 9139–9147.

(23) Mezei, A.; Mészáros, R.; Varga, I.; Gilányi, T. Effect of Mixing on the Formation of Complexes of Hyperbranched Cationic Polyelectrolytes and Anionic Surfactants. *Langmuir* **2007**, *23*, 4237–4247.

(24) Mészáros, R. The Thermodynamic Stability of the Mixtures of Hyperbranched Poly(Ethyleneimine) and Sodium Dodecyl Sulfate at Low Surfactant-to-Polyelectrolyte Ratios. *J. Colloid Interface Sci.* **2009**, *338*, 444–449.

(25) Bali, K.; Varga, Z.; Kardos, A.; Mészáros, R. Impact of Local Inhomogeneities on the Complexation between Poly(Diallyldimethylammoniumchloride) and Sodium Dodecyl Sulfate. *Colloids Surfaces A Physicochem. Eng. Asp.* **2019**, *574*, 21–28.

(26) Campbell, R. A.; Yanez Arteta, M.; Angus-Smyth, A.; Nylander, T.; Noskov, B. A.; Varga, I. Direct Impact of Nonequilibrium Aggregates on the Structure and Morphology of

Pdadmac/SDS Layers at the Air/Water Interface. *Langmuir* **2014**, *30*, 8664–8674.

(27) Angus-Smyth, A.; Bain, C. D.; Varga, I.; Campbell, R. A. Effects of Bulk Aggregation on PEI-SDS Monolayers at the Dynamic Air-Liquid Interface: Depletion Due to Precipitation versus Enrichment by a Convection/Spreading Mechanism. *Soft Matter* **2013**, *9*, 6103–6117.

(28) Campbell, R. A.; Tummino, A.; Noskov, B. A.; Varga, I. Polyelectrolyte/Surfactant Films Spread from Neutral Aggregates. *Soft Matter* **2016**, *12*, 5304–5312.

(29) Lee, Y.-L.; Dudek, A.; Ke, T.-N.; Hsiao, F.-W.; Chang, C.-H. Mixed Polyelectrolyte−Surfactant Langmuir Monolayers at the Air/Water Interface. *Macromolecules* **2008**, *41*, 5845–5853.

(30) Lipton, J.; Weng, G. M.; Röhr, J. A.; Wang, H.; Taylor, A. D. Layer-by-Layer Assembly of Two-Dimensional Materials: Meticulous Control on the Nanoscale. *Matter* **2020**, *2*, 1148–1165.

(31) Stuart, M. A. C.; Huck, W. T. S.; Genzer, J.; Müller, M.; Ober, C.; Stamm, M.; Sukhorukov, G. B.; Szleifer, I.; Tsukruk, V. V.; Urban, M.; Winnik, F.; Zauscher, S.; Luzinov, I.; Minko, S. Emerging Applications of Stimuli-Responsive Polymer Materials. *Nat. Mater.* **2010**, *9*, 101–113.

(32) Tummino, A.; Toscano, J.; Sebastiani, F.; Noskov, B. A.; Varga, I.; Campbell, R. A. Effects of Aggregate Charge and Subphase Ionic Strength on the Properties of Spread Polyelectrolyte/Surfactant Films at the Air/ Water Interface under Static and Dynamic Conditions. *Langmuir* **2018**, *34*, 2312–2323.

(33) Carrascosa-Tejedor, J.; Santamaria, A.; Tummino, A.; Varga, I.; Efstratiou, M.; Lawrence, M. J.; Maestro, A.; Campbell, R. A. Polyelectrolyte/Surfactant Films: From 2D to 3D Structural Control. *Chem. Commun.* **2022**, *58*, 10687–10690.

(34) Tran, E.; Carpenter, A. P.; Richmond, G. L. Probing the Molecular Structure of Coadsorbed Polyethylenimine and Charged Surfactants at the Nanoemulsion Droplet Surface. *Langmuir* **2020**, *36*, 9081–9089.

(35) Tonigold, K.; Varga, I.; Nylander, T.; Campbell, R. A. Effects of Aggregates on Mixed Adsorption Layers of Poly(Ethylene Imine) and Sodium Dodecyl Sulfate at the Air/Liquid Interface. *Langmuir* **2009**, *25*, 4036–4046.

(36) Azzam, R. M. A.; Bashara, N. M. *Ellipsometry and Polarized Light*; North-Holland Publishing Company: Amsterdam, 1977.

(37) Milyaeva, O. Y.; Gochev, G.; Loglio, G.; Miller, R.; Noskov, B. A. Influence of Polyelectrolytes on Dynamic Surface Properties of Fibrinogen Solutions. *Colloids Surfaces A Physicochem. Eng. Asp.* **2017**, *532*, 108–115.

(38) De Feijter, J. A.; Benjamins, J.; Veer, F. A. Ellipsometry as a Tool to Study the Adsorption Behavior of Synthetic and Biopolymers at the Air-Water Interface. *Biopolymers* **1978**, *17*, 1759–1772.

(39) Motschmann, H.; Reiter, R.; Lawall, R.; Duda, G.; Stamm, M.; Wegner, G.; Knoll, W. Ellipsometric Characterization of Langmuir Monolayers of “Hairy-Rod” Polymers at the Air-Water Interface. *Langmuir* **1991**, *7*, 2743–2747.

(40) Daear, W.; Mahadeo, M.; Prenner, E. J. Applications of Brewster Angle Microscopy from Biological Materials to Biological Systems. *Biochim. Biophys. Acta* **2017**, *1859* , 1749–1766.

(41) Skoda, M. W. A. Recent Developments in the Application of X-Ray and Neutron Reflectivity to Soft-Matter Systems. *Curr. Opin. Colloid Interface Sci.* **2019**, *42*, 41–54.

(42) Narayanan, T.; Wacklin, H.; Konovalov, O.; Lund, R. Recent Applications of Synchrotron Radiation and Neutrons in the Study of Soft Matter. *Crystallogr. Rev.* **2017**, *23*, 160–226.

(43) Campbell, R. A.; Wacklin, H. P.; Sutton, I.; Cubitt, R.; Fragneto, G. FIGARO: The New Horizontal Neutron Reflectometer at the ILL. *Eur. Phys. J. Plus* **2011**, *126*, 1–22.

(44) Nelson, A. Co-Refinement of Multiple-Contrast Neutron/X-Ray Reflectivity Data Using MOTOFIT. *J. Appl. Crystallogr.* **2006**, *39*, 273–276.

(45) Braslau, A.; Deutsch, M.; Pershan, P. S.; Weiss, A. H.; Als-Nielsen, J.; Bohr, J. Surface Roughness of Water Measured by X-Ray Reflectivity. *Phys. Rev. Lett.* **1985**, *54*, 114–117.

(46) Tikhonov, A. M.; Mitrinovic, D. M.; Li, M.; Huang, Z.; Schlossman, M. L. An X-Ray Reflectivity Study of the Water-Docosane Interface. *J. Phys. Chem. B* **2000**, *104*, 6336–6339.

(47) Braun, L.; Uhlig, M.; Löhmann, O.; Campbell, R. A.; Schneck, E.; von Klitzing, R. Insights into Extended Structures and Their Driving Force: Influence of Salt on Polyelectrolyte/Surfactant Mixtures at the Air/Water Interface. *ACS Appl. Mater. Interfaces* **2022**, *14*, 27347–27359.

(48) Campbell, R. A.; Saaka, Y.; Shao, Y.; Gerelli, Y.; Cubitt, R.; Nazaruk, E.; Matyszewska, D.; Lawrence, M. J. Structure of Surfactant and Phospholipid Monolayers at the Air/Water Interface Modeled from Neutron Reflectivity Data. *J. Colloid Interface Sci.* **2018**, *531*, 98–108.

(49) Bastardo, L. A.; Mészaros, R.; Varga, I.; Gilányi, T.; Cleasson, P. M. Deuterium Isotope Effects on the Interaction between Hyperbranched Polyethylene Imine and an Anionic Surfactant. *J. Phys. Chem. B* **2005**, *109*, 16196–16202.

7 Study 4: General physical description of the behaviour of spread oppositely charged polyelectrolyte/surfactant films at the air/water interface

Javier Carrascosa-Tejedor,[1,2] Andrea Tummino,[2,3] Marina Efstratiou,[1] Maximilian W. A. Skoda,[4] Philipp Gutfreund,[2] Armando Maestro,[5,6] M. Jayne Lawrence,[1] Imre Varga[7*] and Richard A. Campbell[1*]

1. Division of Pharmacy and Optometry, Faculty of Biology, Medicine and Health, University of Manchester, Oxford Road, Manchester M13 9PT, UK
2. Institut Laue-Langevin, 71 Avenue des Martyrs, CS20156, 38042 Grenoble, France
3. CEA Commissariat à l'Energie Atomique et aux Energies Alternatives, 17 Rue des Martyrs, 38054 Grenoble Cedex 9, France
4. ISIS Neutron and Muon Source, Rutherford Appleton Laboratory, Harwell Campus, Didcot OX11 0QX, UK
5. Basque Foundation for Science, Plaza Euskadi 5, Bilbao, 48009, Spain
6. Centro de Física de Materiales (CSIC, UPV/EHU) - Materials Physics Center MPC, Paseo Manuel de Lardizabal 5, E-20018 San Sebastián, Spain.
7. Institute of Chemistry, Eötvös Loránd University, 112, Budapest H-1518, Hungary

*corresponding authors: Richard A. Campbell and Imre Varga

7.1 Abstract

A new methodology was invented a few years ago to form efficient spread P/S films by exploiting a mechanism where aggregates of the components dissociate and spread material across a water surface as a result of Marangoni flow, and the resulting films become kinetically trapped as a result of the entropy associated with counterion release. Since initial studies on traditional linear P/S mixtures, work has extended to hyperbranched P/S mixtures and PP/S mixtures as a function of the charge of the aggregate spread and the charge density of the polyelectrolyte/subphase

conditions. This review is based not only on published data but also new data filling in gaps where appropriate to deliver the most comprehensive general physical description to date of the physicochemical properties of spread films in terms of their composition, structures and morphology both under static (fixed surface area) and dynamic (compression/expansion cycles) conditions. The results highlight the complexity of the problem, as changing one variable such as the stiffness or polyelectrolyte charge density, or the ability of bulk PP/S aggregates to exploit differences in secondary structure, can have different implications from changing directly the film properties to a difference in the bulk binding of the aggregates used in the film spreading procedure that in turn changes indirectly the film properties. Key conclusions are that different systems can produce ESs upon surface area compression regardless of the charge of the aggregates used in the spreading process while others require overcharged aggregates, which are inferred to become embedded in the films and nucleate the transfer of material from the surface monolayer to associated reservoirs. Also, the stability of the reservoirs varies according to the system studied as well, with the most stable and tunable reservoirs originating in PP/S spread films, where we infer that interactions linked to secondary structures may be retained in ESs in the films. The results point to the need for more experimental data on different systems studied systematically under varying conditions to develop further understanding the physical picture of these films and work towards their use in biomedical or film transfer applications, which may have certain economic and environmental advantages over film preparation methods that are currently available.

7.2 Results

As indicated in section 2.2, this chapter is the basis for writing a review of the general behaviour of spread P/S films at the air/water interface. Hence, the introduction to the review will be based on that of this thesis, so it is omitted in this chapter to avoid repetition, and as it is a review article there will be no Materials and Methods section, because while much of the data is new, data on all systems will have been published and the Materials and Methods sections will be cited.

7.2.1 Polyelectrolyte/surfactant films spread from undercharged aggregates

The Langmuir technique is a fundamental technique in this study as it allows the study of the dynamic behaviour when P/S films are subjected to lateral compression. In addition, the use of the Wilhelmy plate as a microbalance allows the recording of the Π–*A* isotherm, which is indispensable for interpreting the behaviour of these systems. The combination of this technique with others such as ellipsometry, BAM or NR offers the possibility to study in detail the composition, structure, morphology and presence of heterogeneities in the P/S films. The Π–*A* isotherms of the films spread from undercharged aggregates are shown in Figure 7.1.

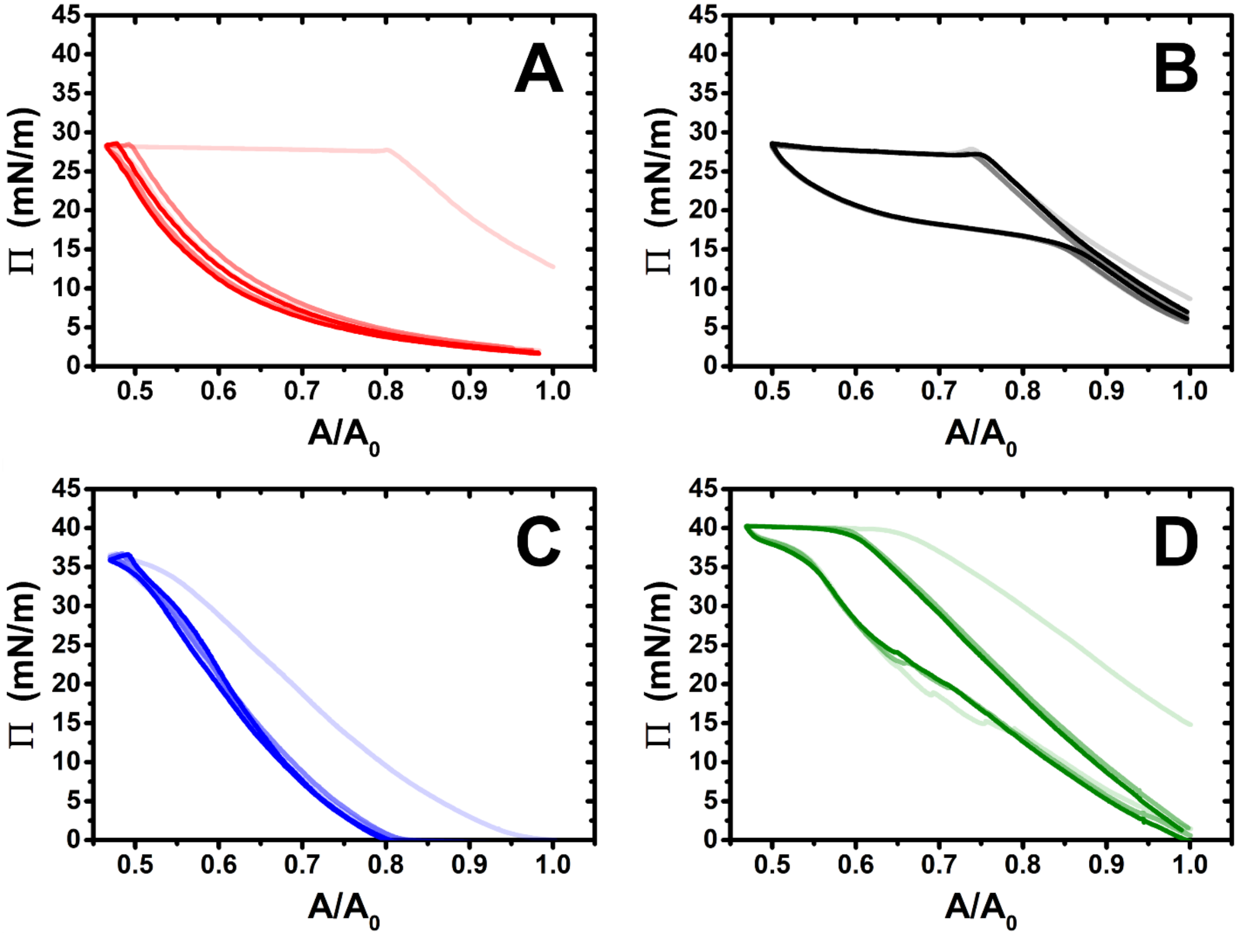

Figure 7.1. Π–*A* isotherms of 3 cycles of (A) NaPSS/DTAB, (B) PLL/SDS, (C) PEI/SDS at pH 4 and (D) PEI/SDS at pH 10 films spread from undercharged aggregates. Cycles are displayed progressively from lighter to darker.

We have already described in a couple of papers the general features that can appear in the isotherms and their relation with the properties of the film.[1,2] In short, the compression of a P/S monolayer results in an increase in Π as a result of the increasing interactions between molecules present at the interface. The point at which the monolayer reaches its most compact state is known as collapse. From this point on, the surface pressure remains constant during compression and depending on the type of collapse mechanism, ejection of material to the bulk or formation of ESs occur. Some systems present the ability to fully reincorporate the material expelled back to the monolayer and others do not. The presence of hysteresis and a kink or pseudo-plateau during the expansion during consecutive cycles constitutes a characteristic feature that suggests the formation of ESs and the reincorporation of material back to the monolayer. Some general remarks on the different systems are noted in the following.

NaPSS/DTAB: the Π–*A* isotherm during the first cycle shows a large plateau at ~27 mN/m during the compression, exhibits hysteresis and there is an abrupt decrease of Π from the first to the second cycle. The isotherm shifts to lower A/A_0 and does not retain hysteresis for the following cycles.

PLL/SDS: the Π–*A* isotherm is characterised by a large plateau at ~28 mN/m during the compression, a pseudo-plateau during expansion and a final Π value close to the initial one. Large hysteresis is observed during the three cycles and the data are reproducible.

PEI/SDS pH 4: the Π–*A* isotherm during the first cycle reaches the collapse at 36 mN/m close to the minimum A/A_0, exhibits some hysteresis and there is a decrease of Π from the first to the second cycle. The isotherm shifts to lower A/A_0 and does not present hysteresis for the following cycles.

PEI/SDS pH 10: Π–*A* isotherm is characterised by a plateau at ~40 mN/m during the compression, exhibits hysteresis, presents a kink upon expansion and there is a decrease of Π from the first to the second cycle. The Π–*A* isotherm during following cycles shifts to lower A/A_0, retains the hysteresis, shows the kink upon expansion and it is reproducible.

Ellipsometry measurements were performed to follow the variation of the amount of interfacial material during the compression of the films and check their stability over time. This approach is essential to evaluate the possibility of determining the film structure when using the full-Q_Z approach of NR, as these measurements last around 30–60 min. Besides, the presence of inhomogeneities in the films will manifest themselves as temporal fluctuations of the *d*Δ values. The variation of *d*Δ as a function of time of the films spread from undercharged aggregates is shown in Figure 7.2. It is important to note that the stability of the PLL/SDS and NaPSS/DTAB films was studied at a constant area (the arrows in Figure 7.2A and B indicate the time at which the barriers were stopped). However, the PEI/SDS experiments were performed at a constant pressure of 40 mN/m due to the relative unstable nature of the spread films.[3]

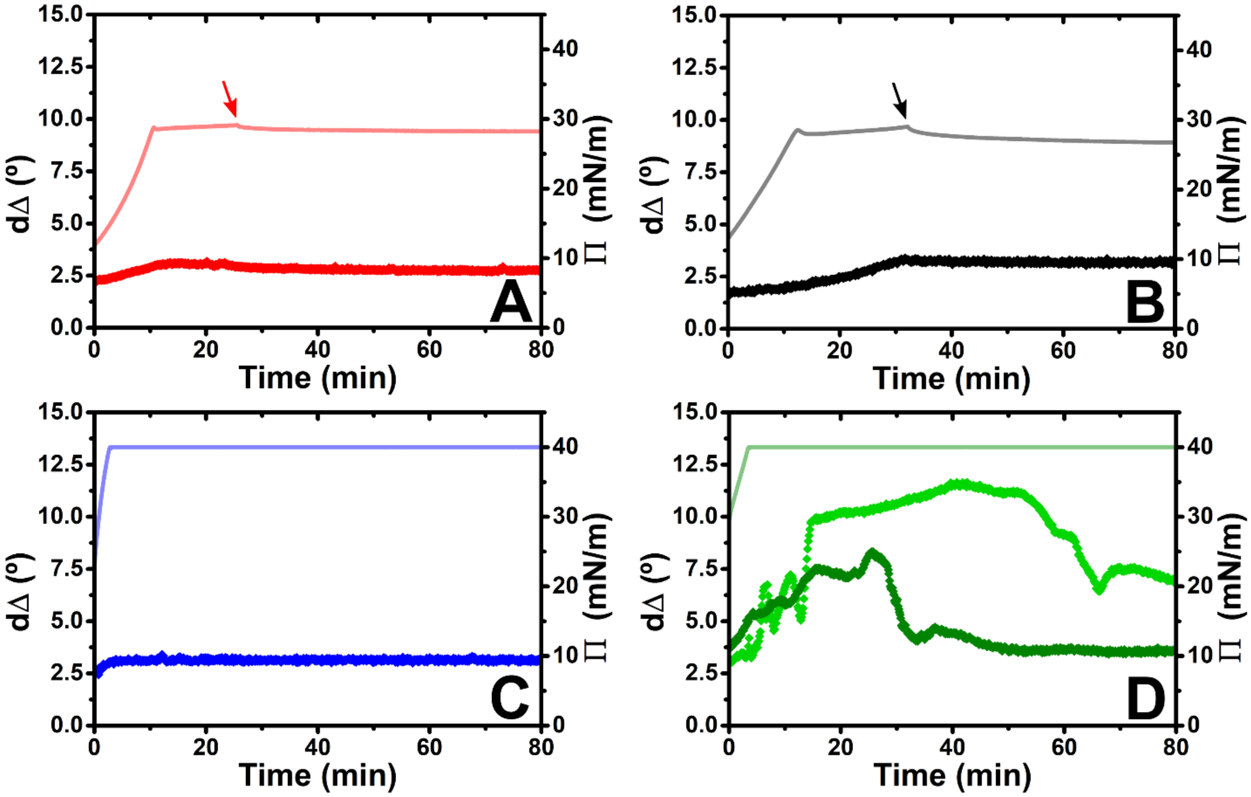

Figure 7.2. Variation of *d*Δ (diamonds) and Π (line) as a function of time of (A) NaPSS/DTAB, (B) PLL/SDS, (C) PEI/SDS at pH 4 and (D) PEI/SDS at pH 10 films spread from undercharged aggregates. Two independent ellipsometry experiments of PEI/SDS at pH 10 are shown.

NaPSS/DTAB: the collapse in Π is accompanied by a collapse in *d*Δ. The value of *d*Δ at the collapse is 2.9 and decreases once the barriers are stopped until it reaches a value of 2.7 after 80 min.

PLL/SDS: *d*Δ increases continuously even after the collapse in Π and the values reached at the minimum *A/A₀* once the barriers are stopped are very stable.

PEI/SDS pH 4: *d*Δ increases continuously during the compression of the film until reaching 40 mN/m. The *d*Δ values remain stable during the 40 mN/m Π control and the values are consistent with the presence of an SDS monolayer with PEI bound to the headgroups.

PEI/SDS pH 10: large fluctuations of *d*Δ over time during all the experiment revealing the presence of inhomogeneities in the film. Two *d*Δ independent measurements are shown to highlight the inhomogeneity of the film suggesting that aggregates may be embedded in it.

The application of BAM allows characterisation of the lateral organisation of the interfacial material present at the interface, the presence of heterogeneity and the formation of discrete ESs. In general, the presence of a homogeneous film at the interface can be observed after spreading the material due to the difference in refractive index. Compression of the film results in an increase in intensity (i.e. brightness of the images). Finally, the formation of an additional layer of ESs results in a second refractive index change resulting in the appearance of discrete regions of increased intensity.

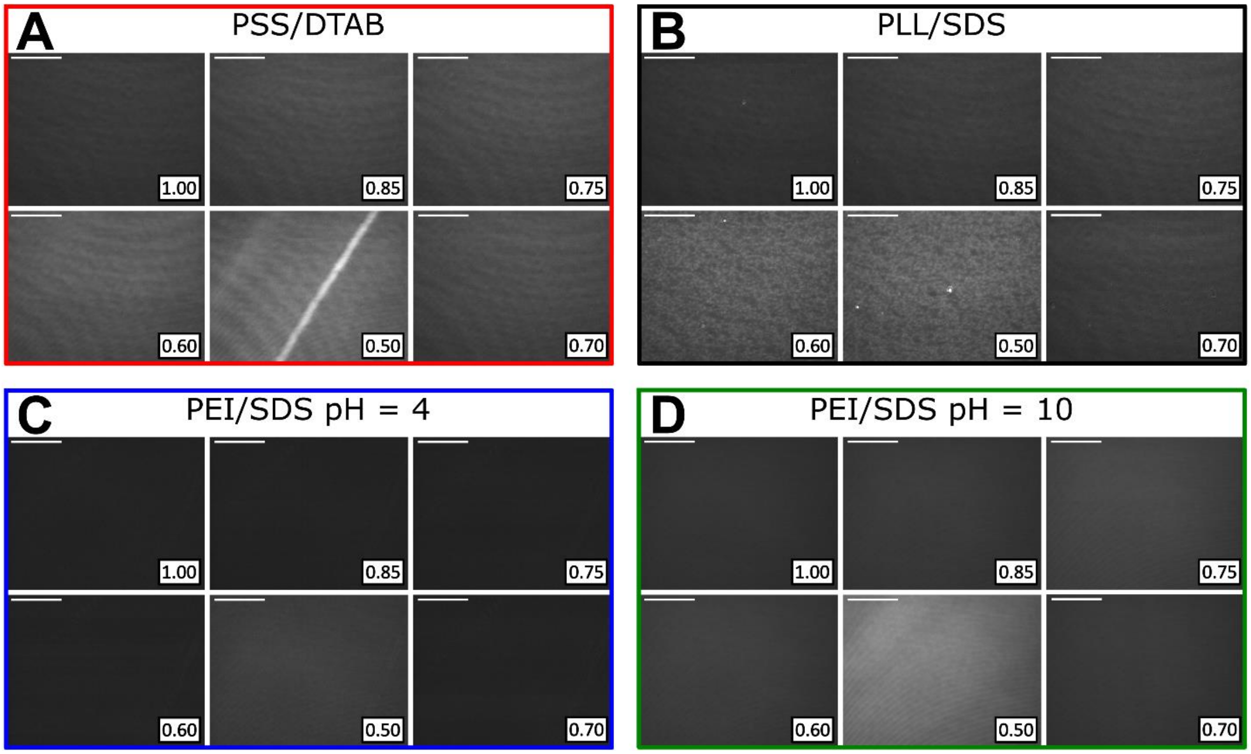

Figure 7.3. BAM images of (A) NaPSS/DTAB, (B) PLL/SDS, (C) PEI/SDS at pH 4 and (D) PEI/SDS at pH 10 films spread from undercharged aggregates at different *A/A₀*.

Figure 7.3 shows 5 BAM images during compression and 1 during expansion of the 4 systems at different values of A/A_0. The image of each film during its expansion has been included to check if film expansion results in a homogenous film again.

NaPSS/DTAB: BAM images show a homogenous film with increasing intensity with the compression prior to the collapse. A few linear white bands can be observed at the minimum values of A/A_0.

PLL/SDS: BAM images show a homogeneous film with increasing intensity as the film is compressed prior to the collapse, and discrete bright patches in the µm-scale appear after the collapse that grow in number with the compression.

PEI/SDS pH 4: BAM images show a homogeneous film with very low intensity at high A/A_0 and increasing intensity with the compression.

PEI/SDS pH 10: BAM images show a homogenous film with increasing intensity with the compression.

The application of the NR low-Q_Z approach allows following the compositional dynamics of the films, i.e., the variation of the surface excess of surfactant (Γ_S) and polyelectrolyte (Γ_P) during the compression/expansion cycles. This is particularly useful to verify if the surface excess of surfactant is higher than the full monolayer coverage indicating the formation of ESs. It is also very useful to determine if there is loss of material during dynamic compression/expansion cycles, be it polyelectrolyte or surfactant. The composition of the film also helps us to understand the nature of the binding in the film. Figure 7.4 shows the results of the compositional dynamics during 3 compression/expansion cycles of P/S films spread from undercharged aggregates.

NaPSS/DTAB: The collapse of the film is characterised by a plateau in Π and Γ_{DTAB} at 3.2 µmol/m^2, corresponding to a full surfactant monolayer. In addition, Γ_{DTAB} and Γ_{NaPSS} decreases from the first to the second cycle and there is 1:1 stoichiometry.

PLL/SDS: the collapse of the film is characterised by a continuous increase of Γ_{SDS} and Γ_{PLL} even in the Π plateau. Γ_{SDS} at the collapse is 4.0 ± 0.1 µmol/m^2 and the values reached are higher than the one expected for a full monolayer of SDS (4.2 µmol/m^2).[4] No loss of material is observed between cycles. The film presents a stoichiometry close to 1:1 before the collapse and excess of PLL after the collapse. The film composition is similar over successive cycles.

PEI/SDS pH 4: the values of Γ_{SDS} are always lower than the full monolayer coverage (4.2 µmol/m^2) and the maximum reached at the minimum A/A_0 decreases from the first (3.4 µmol/m^2) to the second cycle (3.2 µmol/m^2). The film composition shows a large excess of PEI during all the experiment. Since the Γ_{PEI} values are very noisy, with the origin of the noise unknown at this time (e.g. instrumental or sample problem), this experiment is foreseen for repetition in March 2023.

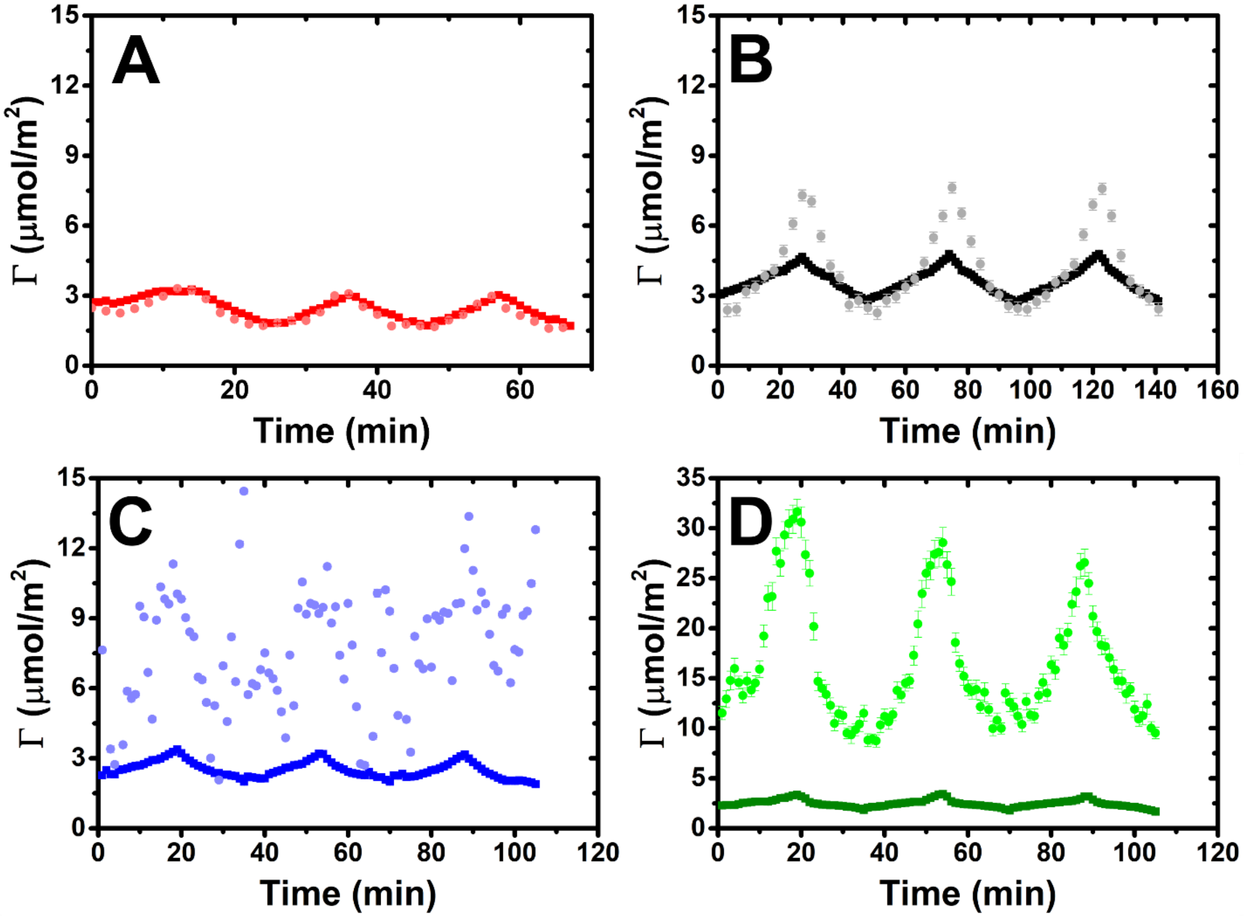

Figure 7.4. Variation of Γ_S (dark squares) and Γ_P (light circles) as a function of time of (A) NaPSS/DTAB, (B) PLL/SDS, (C) PEI/SDS at pH 4 and (D) PEI/SDS at pH 10 films spread from undercharged aggregates during 3 compression/expansion cycles.

PEI/SDS pH 10: Γ_{SDS} and Γ_{PEI} continuously increase and decrease during the compression and expansion of the film. Γ_{SDS} is always lower than the full monolayer coverage of SDS (4.2 µmol/m^2)

and reaches maximum values of 3.4 µmol/m^2. The film composition shows a very large excess of PEI during all the experiment.

Finally, the structure of the films spread from undercharged aggregates was examined using the NR full-Q_Z approach. The general procedure of fitting the data with different isotopic contrasts using a common structural model with the minimum number of layers required has been followed. In general, the structure of a surface P/S monolayer is described as a monolayer of surfactant with solvated polyelectrolyte electrostatically bound to the headgroups. The use of isotopic substitution allows the structure of these films to be resolved with high precision, allowing for example the thickness, roughness or solvent volume fraction of the surfactant tails and heads to be determined separately. The choice of the optimal contrast is an ideal tool for obtaining the desired information from the system, and it is critical when the ESs, either in static or dynamic, are resolved.[2] The presence of ESs is manifested in the reflectivity profiles by the appearance of a Kiessig fringe especially in the d-SDS/ACMW and h-SDS/D_2O contrasts in which the difference in scattering between the subphase and the surfactant forming the ESs is maximum. The reflectivity profiles of the P/S films spread from undercharged aggregates are shown in Figure 7.5 together with the model fits. The correspondent volume fraction profiles are represented in Figure 7.6.

NaPSS/DTAB: Data not measured (foreseen for recording in March 2023).

PLL/SDS: Kiessig fringe observed in the d-SDS/ACMW and h-SDS/D_2O contrasts. The structure of the film is composed of four layers: (1) SDS tails / (2) SDS headgroups + PLL / (3) PLL / (4) SDS bilayer (coverage ~25%).

PEI/SDS pH 4: No Kiessig fringe is observed. The structure of the film is composed of three layers: (1) SDS tails / (2) SDS headgroups + PEI / (3) PEI.

PEI/SDS pH 10: Slight Kiessig fringe observed in the d-SDS/ACMW contrast. The structure of the film is composed of four layers: (1) SDS tails / (2) SDS headgroups + PEI / (3) PEI / (4) SDS bilayer (coverage ~9%).

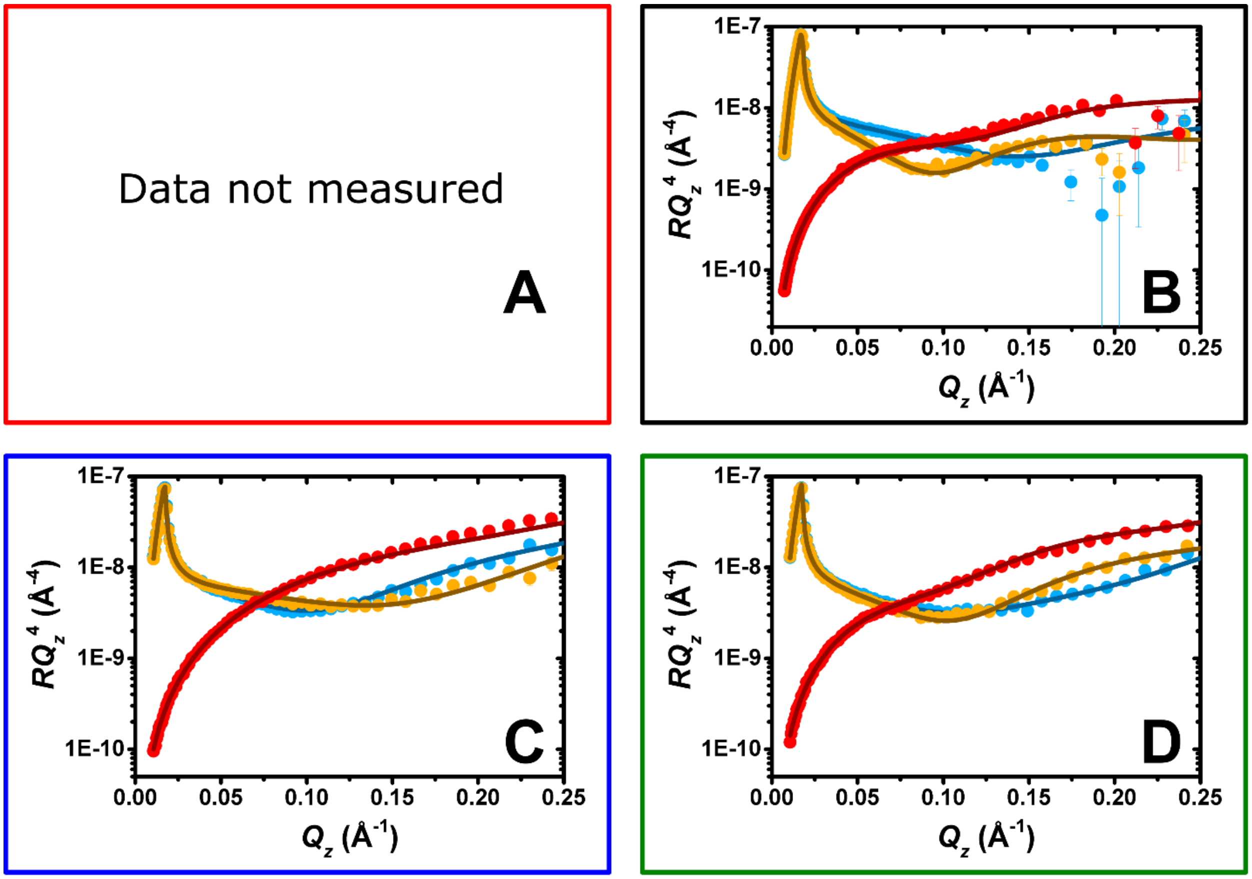

Figure 7.5. Reflectivity profiles of (A) NaPSS/DTAB, (B) PLL/SDS, (C) PEI/SDS at pH 4 and (D) PEI/SDS at pH 10 films spread from undercharged aggregates and recorded using three isotopic contrasts: d-SDS/ACMW (red), d-SDS/D_2O (blue) and h-SDS/D_2O (orange). The continuous lines show the model fits.

To conclude, the behaviour of the films spread from undercharged aggregates is summarised below, considering all the results obtained from the multi-technique approach applied.

NaPSS/DTAB: NaPSS/DTAB films show a collapse in Π, $d\Delta$ and Γ_{DTAB} during the first cycle consistent with the ejection of material to the bulk. This is further confirmed by the loss of material with time shown in the ellipsometry data and the Γ_{DTAB} values at the beginning of the second cycle lower than the first one. The behaviour of the film during the following cycle is that typical of an insoluble monolayer. Although BAM images show the presence of some white bands at the minimum A/A_0, the rest of the data shows clearly that the excess of material is loss to the bulk.

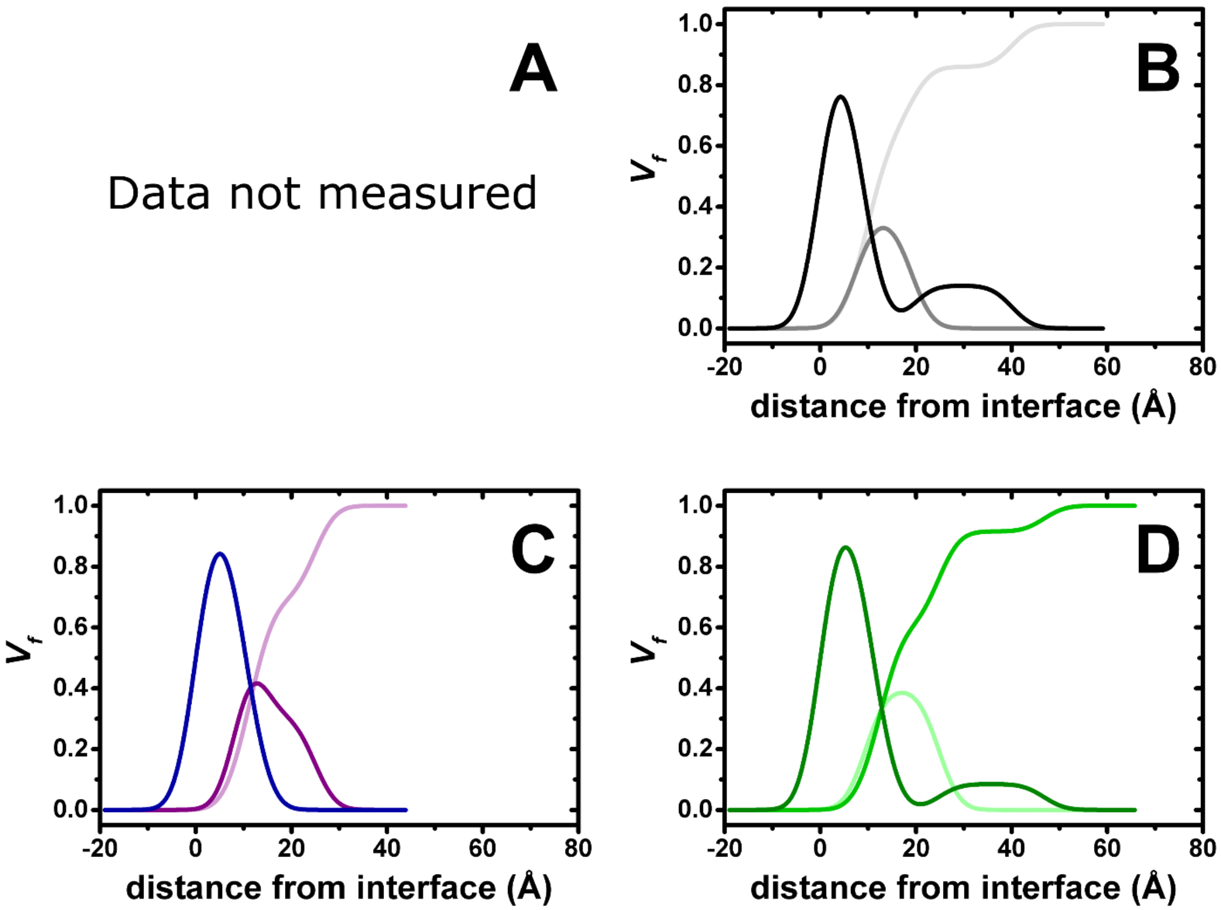

Figure 7.6. Volume fraction profiles resulting from the fits presented in Figure 7.5. where surfactant is black/blue/dark green, polyelectrolyte is grey/mauve/green and solvent is light grey/pink/light green.

PLL/SDS: PLL/SDS films are characterised by a continuous increase in $d\Delta$ and Γ_{SDS}, the appearance of discrete regions on the µm-scale during the collapse of the film and values of Γ_{SDS} higher than the full monolayer coverage, i.e. consistent with the formation of ESs. The structure of the film is composed of a P/S surface monolayer with an extra bilayer of surfactant ESs. The reproducibility of the data from one cycle to the next, as well as the high stability of the $d\Delta$ values over time, show the high stability of these films and a high efficiency to reincorporate the material expelled from the monolayer during expansion.

PEI/SDS pH 4: PEI/SDS films spread on pure water adjusted to pH 4 are characterised by collapse of the film during the first cycle, values of $d\Delta$ consistent with the presence of a P/S monolayer, uniform BAM images and Γ_{SDS} values lower than the full monolayer coverage. All the results are consistent with the structural analysis of the NR full-Q_Z data, where a model correspondent to a

PEI/SDS monolayer fits the data and the behaviour of the film corresponds to that typical of an insoluble monolayer.

PEI/SDS pH 10: The behaviour of these films is most complex. The isotherms show collapse, a kink during expansion, and are reproducible after the first cycle. The ellipsometry data show large fluctuations of *d*Δ over time consistent with the presence of regions in the film with a high amount of material. Nevertheless, the BAM images show the presence of a homogeneous film and its structure obtained from the full-Q_Z analysis consists of a P/S monolayer. Thus, the results obtained agree with the presence of embedded aggregates as indicated by ellipsometry that are smaller than the resolution of BAM and bigger than the resolution of NR.

7.2.2 Polyelectrolyte/surfactant films spread from overcharged aggregates

The Π–*A* isotherms of the films spread from overcharged aggregates are shown in Figure 7.7.

NaPSS/DTAB: Π–*A* isotherm during the first cycle shows a large plateau at ~27mN/m during the compression, exhibits hysteresis, presents a kink upon expansion and there is an abrupt decrease of Π from the first to the second cycle and a shift of the isotherm to lower A/A_0. The Π–*A* isotherm retains hysteresis over successive cycles.

PLL/SDS: Π–*A* isotherm characterised by a large plateau at ~28 mN/m during the compression, a pseudo-plateau during expansion and a final Π value close to the initial one. Large hysteresis is observed during the three cycles and the data are reproducible.

PEI/SDS pH 4: Π–*A* isotherm characterised by a continuous increase in Π during the compression and the absence of a collapse at constant Π values. There is a change in the slope that could be related to the collapse of the film understood as the onset of ESs formation. The data upon expansion is characterised by the presence of a pseudo-plateau. The Π–*A* isotherm retain the hysteresis and shows the pseudo-plateau upon expansion during following cycles, and the data are reproducible, although a slight shift of the isotherm to lower A/A_0 is observed from the first to the second cycle.

PEI/SDS pH 10: Π–*A* isotherm characterised by a continuous increase in Π during the compression of the film and the absence of a collapse at constant Π values. There is a change in the slope that could be related to the collapse of the film. The data upon expansion is characterised by the presence of a pseudo-plateau. The Π–*A* isotherm retain the hysteresis and shows the pseudo-plateau upon expansion during following cycles, and the data are reproducible, although a slight shift of the isotherm to lower A/A_0 is observed from the first to the second cycle.

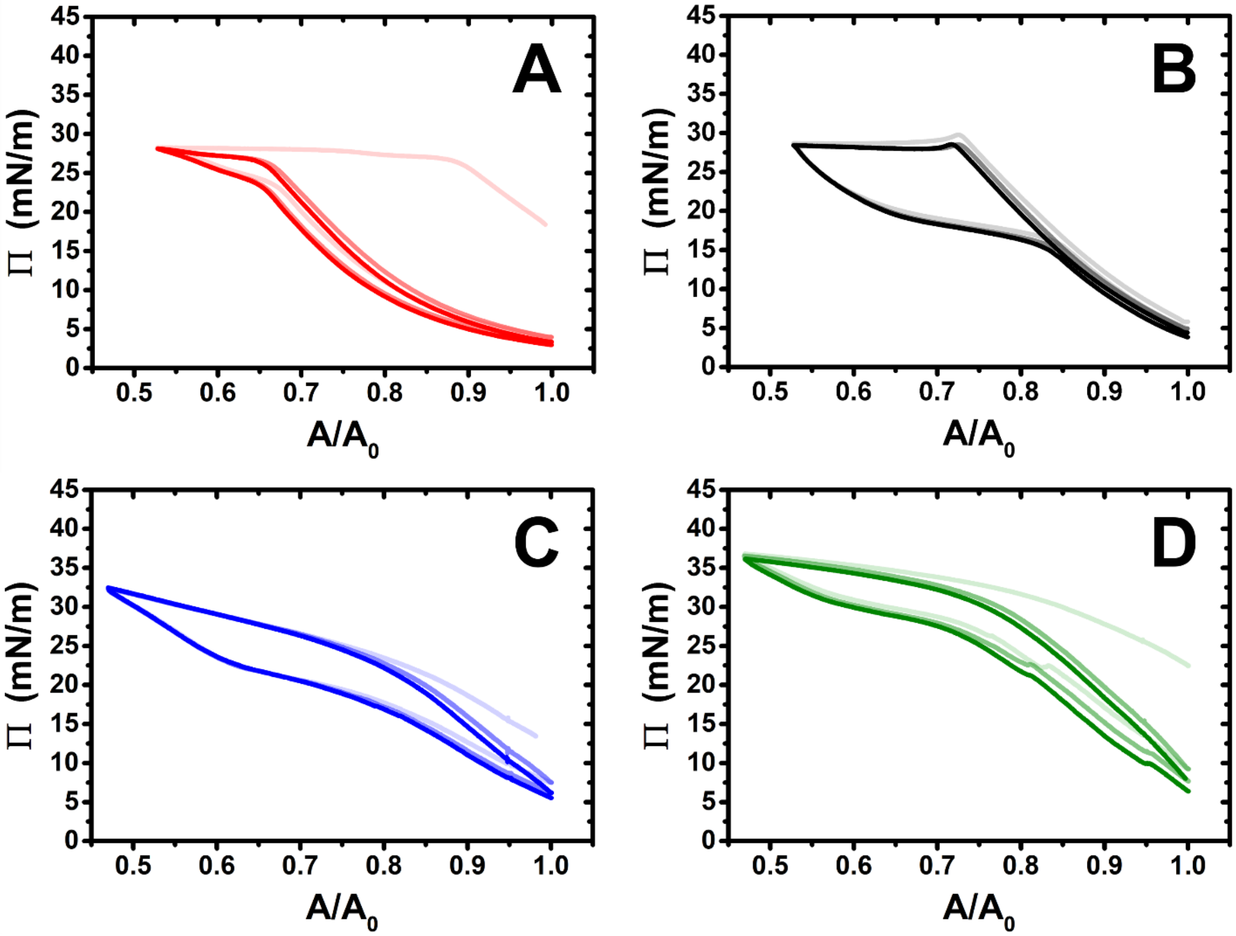

Figure 7.7. Π–*A* isotherms of 3 cycles of (A) NaPSS/DTAB, (B) PLL/SDS, (C) PEI/SDS at pH 4 and (D) PEI/SDS at pH 10 films spread from overcharged aggregates. Cycles are displayed progressively from lighter to darker.

The variation of *d*Δ as a function of time of the films spread from overcharged aggregates is shown in Figure 7.8.

NaPSS/DTAB: *d*Δ increases continuously even after the collapse in Π showing temporal fluctuations. The data show continuous temporal fluctuations of *d*Δ once the barriers are stopped, and values after 80 min close the ones obtained at the collapse of the film.

PLL/SDS: *d*Δ increases continuously even after the collapse in Π and the values reached at the minimum *A/A₀* once the barriers are stopped are very stable. The fluctuations observed during the compression can be related to domains of ESs that pass through the area illuminated by the laser beam.

PEI/SDS pH 4: continuous increase of *d*Δ during the compression of the film. Small fluctuations observed during the compression can be related to domains of ESs that pass through the area illuminated by the laser beam. The *d*Δ values remain stable during the 40 mN/m Π control and the values are much higher than the ones expected for a SDS monolayer with PEI bound to the headgroups.

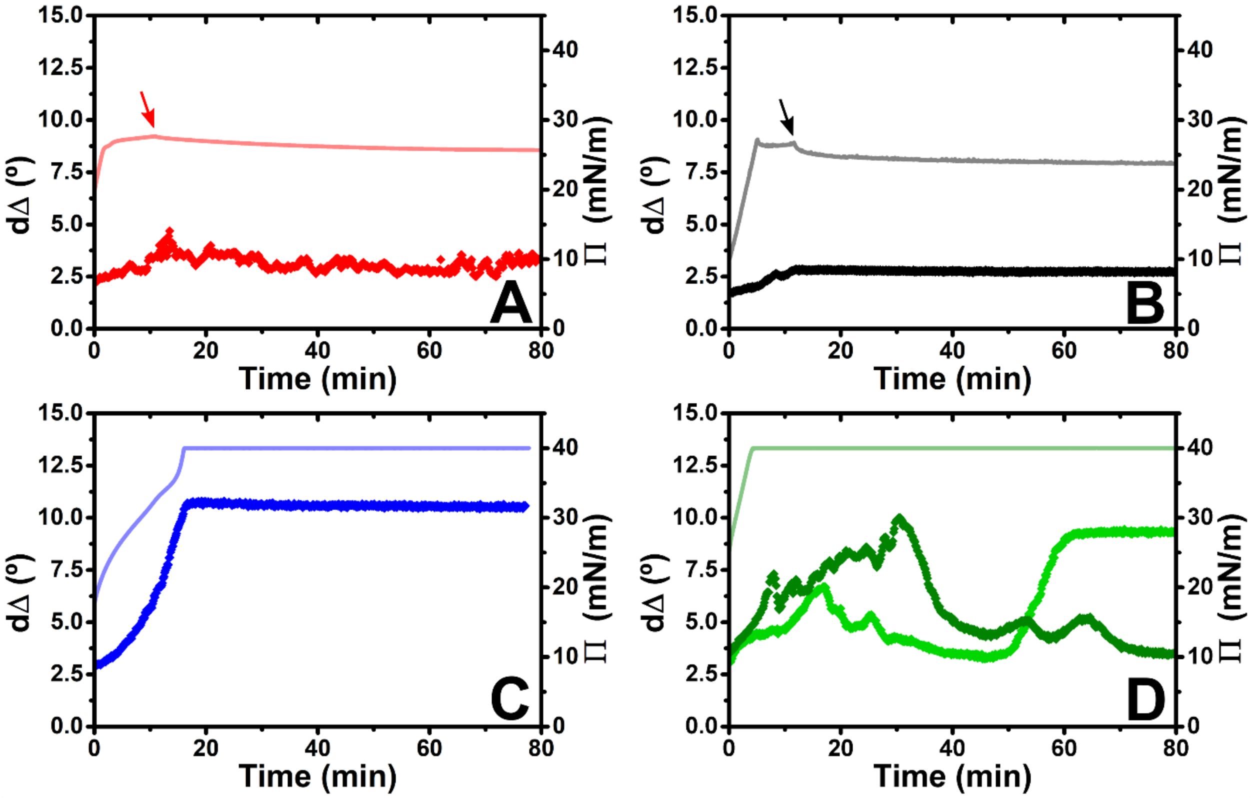

Figure 7.8. Variation of *d*Δ (diamonds) and Π (line) as a function of time of (A) NaPSS/DTAB, (B) PLL/SDS, (C) PEI/SDS at pH 4 and (D) PEI/SDS at pH 10 films spread from overcharged aggregates. Two independent ellipsometry experiments of PEI/SDS at pH 10 are shown.

PEI/SDS pH 10: large fluctuations of *d*Δ over time during all the experiment revealing that either the ESs or embedded aggregates are distributed heterogeneously in the film explaining the pronounced fluctuations when they are transported through the area illuminated by the laser beam. Two *d*Δ independent measurements are shown to highlight the inhomogeneity of the film.

The BAM images recorded during the compression and expansion of the P/S films spread from overcharged aggregates are shown in Figure 7.9. The image of the films during expansion has been included to show if the expansion results in a homogenous film again.

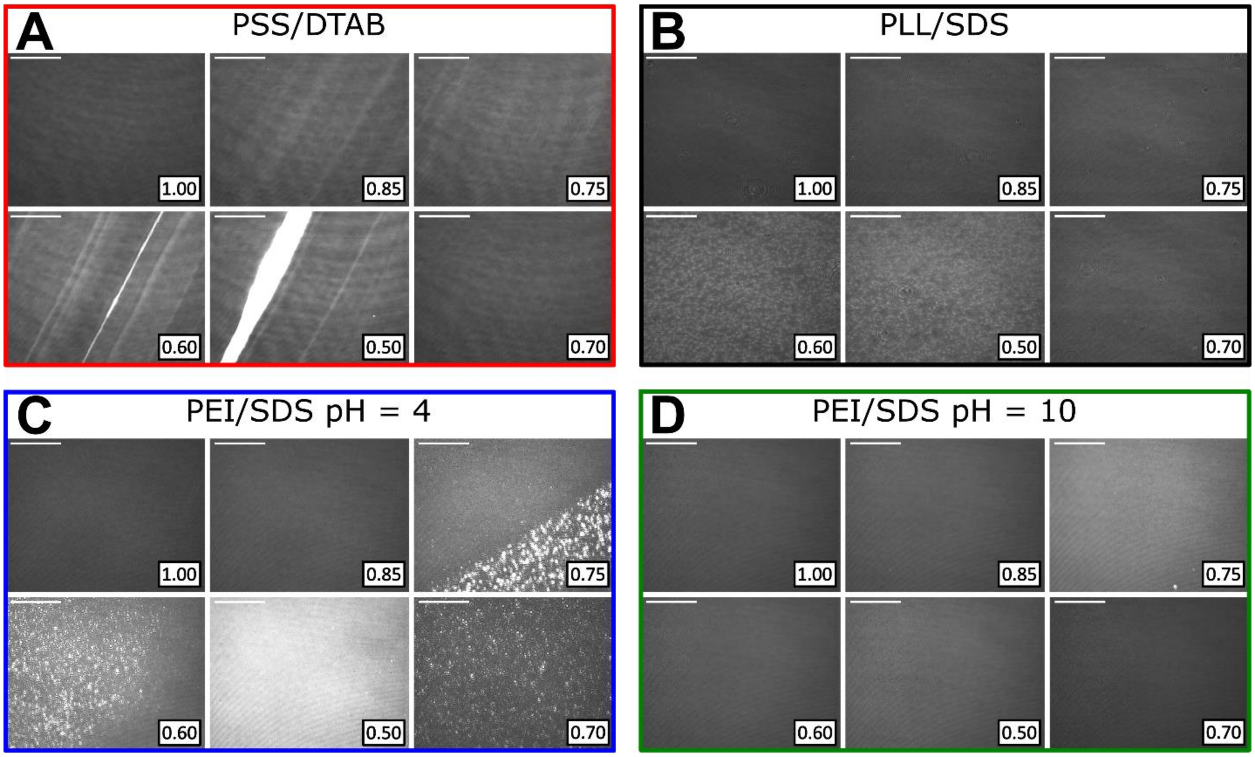

Figure 7.9. BAM images of (A) NaPSS/DTAB, (B) PLL/SDS, (C) PEI/SDS at pH 4 and (D) PEI/SDS at pH 10 films spread from overcharged aggregates at different A/A_0. Scale bars are 100 µm.

NaPSS/DTAB: BAM images show a homogenous film with increasing intensity with the compression before the collapse. Linear white bands are observed after the collapse and their number and intensity increases with the compression.

PLL/SDS: BAM images show a homogeneous film with increasing intensity as the film is compressed prior to the collapse, and the appearance of discrete bright patches in the µm-scale after the collapse that grow in number with the compression.

PEI/SDS pH 4: BAM images show a homogeneous film with increasing intensity as the compression proceeds up to A/A_0 = 0.85. Upon further compression, the coexistence of homogenous areas and areas presenting discrete bright patches can be observed until there is no observed movement in the film, suggesting the formation of a homogenous and rigid film.

PEI/SDS pH 10: BAM images show a homogenous film throughout the experiment with increasing intensity up to *A/A₀* = 0.75. However, intensity fluctuations are observed as the compression proceeds suggesting that the films are mobile in this case.

Figure 7.10 shows the results of the compositional dynamics during 3 compression/expansion cycles of P/S films spread from overcharged aggregates.

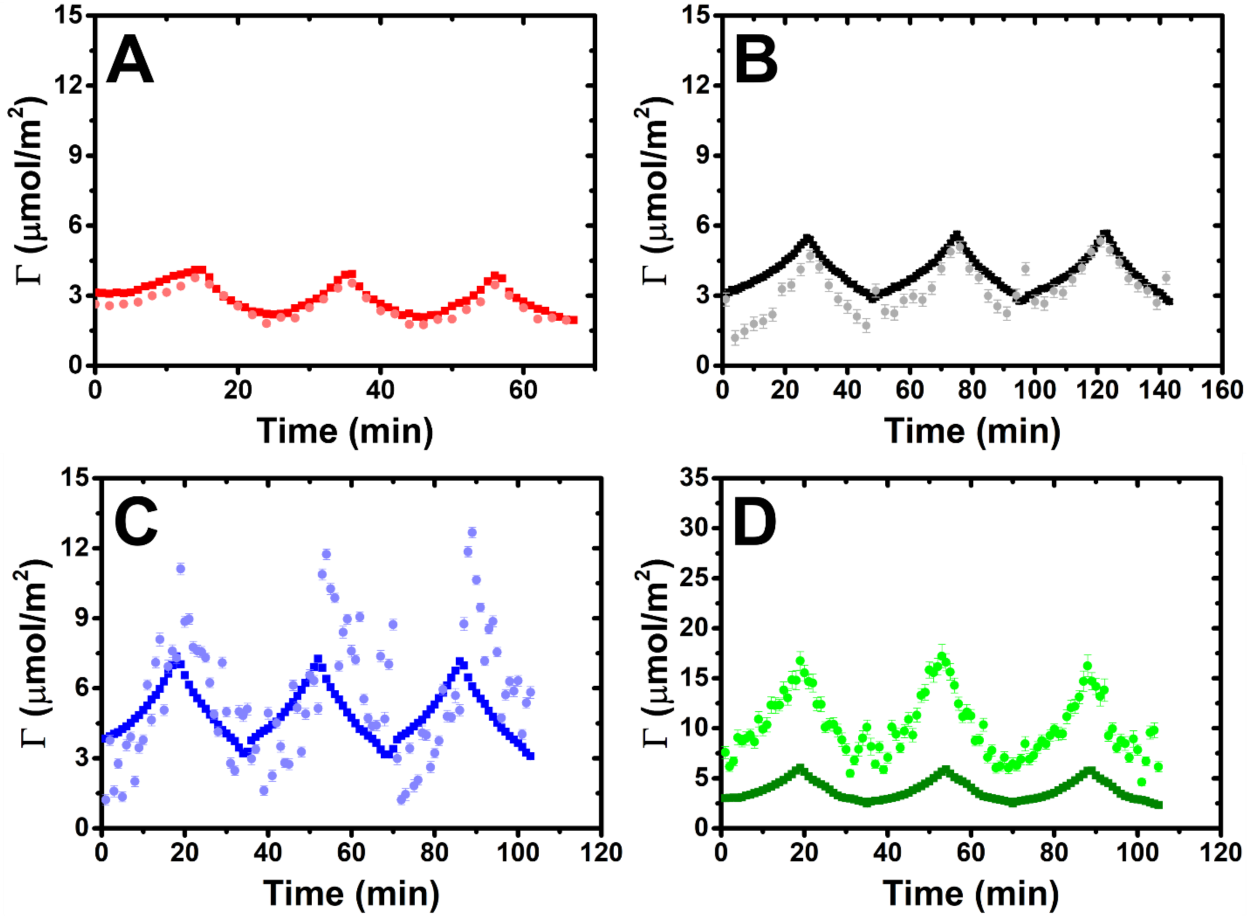

Figure 7.10. Variation of Γ_S (dark squares) and Γ_P (light circles) as a function of time of (A) NaPSS/DTAB, (B) PLL/SDS, (C) PEI/SDS at pH 4 and (D) PEI/SDS at pH 10 films spread from undercharged aggregates during 3 compression/expansion cycles.

NaPSS/DTAB: The collapse of the film is characterised by a continuous increase of Γ_{DTAB} and Γ_{NaPSS} with values of Γ_{DTAB} higher than the full monolayer coverage (3.2 μmol/m²). There is an excess of surfactant during the first compression and the film presents 1:1 stoichiometry during following cycles. Values higher than the full monolayer coverage are observed in all cycles.

PLL/SDS: the collapse of the film is characterised by a continuous increase of Γ_{SDS} and Γ_{PLL}. Γ_{SDS} at the collapse is 4.0 ± 0.1 μmol/m^2 and the values reached are higher than the one expected for a full monolayer of SDS (4.2 μmol/m^2).[4] No loss of material is observed between cycles. There is an excess of surfactant during the first cycle and evolution to 1:1 stoichiometry during the following cycles. The film composition is similar over successive cycles.

PEI/SDS pH 4: values of Γ_{SDS} higher than the full monolayer coverage (4.2 μmol/m^2) reached during the compression of the film and no loss of material is observed between cycles. Although the Γ_{PEI} data is noisy, the film composition is close to 1:1 stoichiometry.

PEI/SDS pH 10: values of Γ_{SDS} higher than the full monolayer coverage (4.2 μmol/m^2) reached during the compression of the film and no loss of material is observed between cycles. There is a large excess of PEI.

Finally, the reflectivity profiles of the P/S films spread from overcharged aggregates are shown in Figure 7.11 together with their model fits. The correspondent volume fraction profiles are represented in Figure 7.12.

NaPSS/DTAB: no Kiessig fringe is observed. The structure of the film is composed of three layers: (1) DTAB tails / (2) DTAB headgroups + NaPSS / (3) NaPSS.

PLL/SDS: Kiessig fringe observed in the d-SDS/ACMW and h-SDS/D_2O contrasts. The structure of the film is composed of four layers: (1) SDS tails / (2) SDS headgroups + PLL / (3) PLL / (4) SDS bilayer (coverage 19%).

PEI/SDS pH 4: Kiessig fringe observed in the d-SDS/ACMW and h-SDS/D_2O contrasts. The d-SDS/D_2O contrast fits a model compose of 3 layers: (1) SDS tails / (2) SDS headgroups + PEI / (3) PEI, while the other two contrasts fits to a model composed of five layers: (1) SDS tails / (2) SDS headgroups + PEI / (3) PEI / (4) SDS bilayer (coverage 33%) / (5) PEI. The absence of ESs in the d-SDS/D_2O is attributed to isotopic effects that must be discussed in the future in more detail.

PEI/SDS pH 10: Kiessig fringe observed in the d-SDS/ACMW and h-SDS/D_2O contrasts. The d-SDS/D_2O contrast fits a model compose of 3 layers: (1) SDS tails / (2) SDS headgroups + PEI / (3) PEI , while the other two contrasts fits to a model composed of five layers: (1) SDS tails / (2) SDS headgroups + PEI / (3) PEI / (4) SDS bilayer (coverage 35%) / (5) PEI. The absence of ESs in the d-SDS/D_2O is attributed to isotopic effects that must be discussed in the future in more detail.

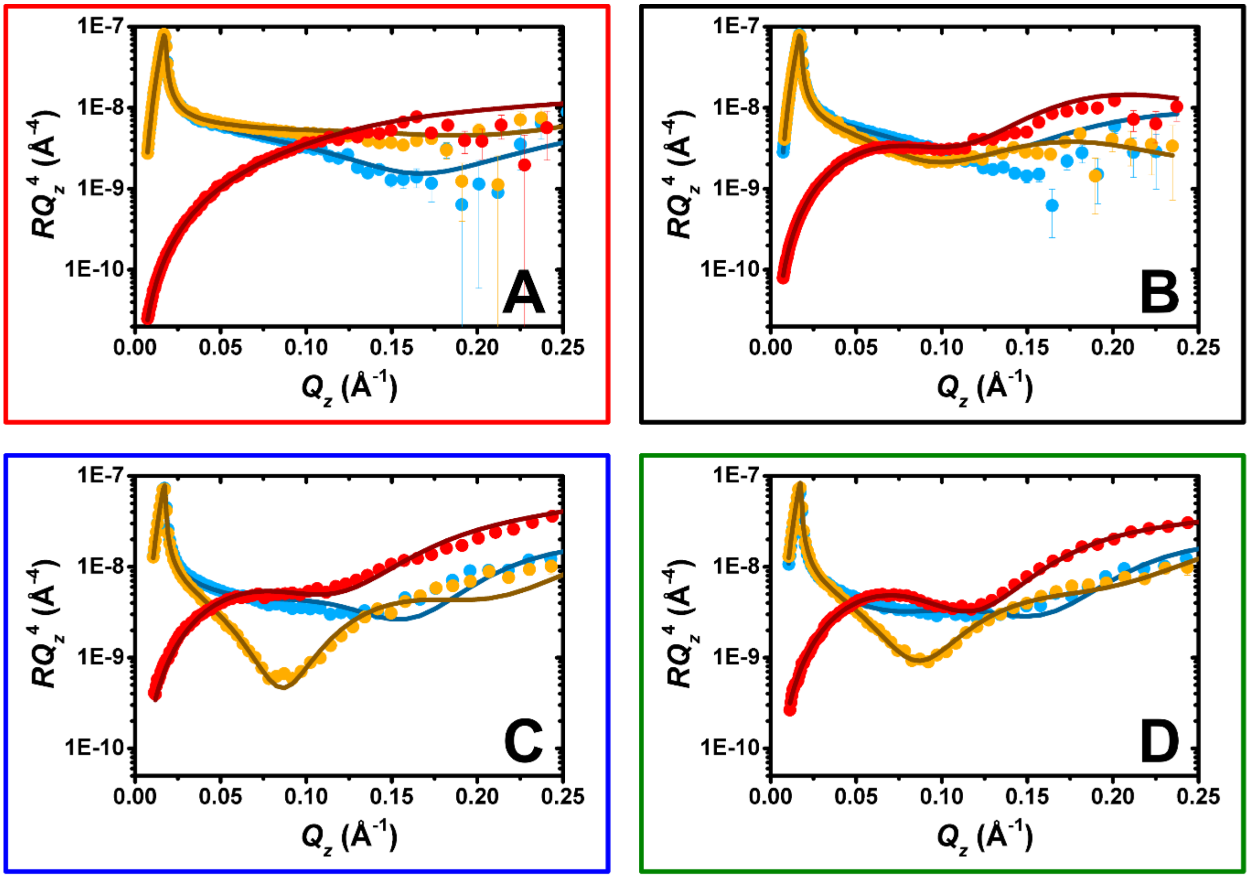

Figure 7.11. Reflectivity profiles of (A) NaPSS/DTAB, (B) PLL/SDS, (C) PEI/SDS at pH 4 and (D) PEI/SDS at pH 10 films spread from overcharged aggregates and recorded using three isotopic contrasts: d-SDS/ACMW (red), d-SDS/D_2O (blue) and h-SDS/D_2O (orange). The continuous lines show the model fits.

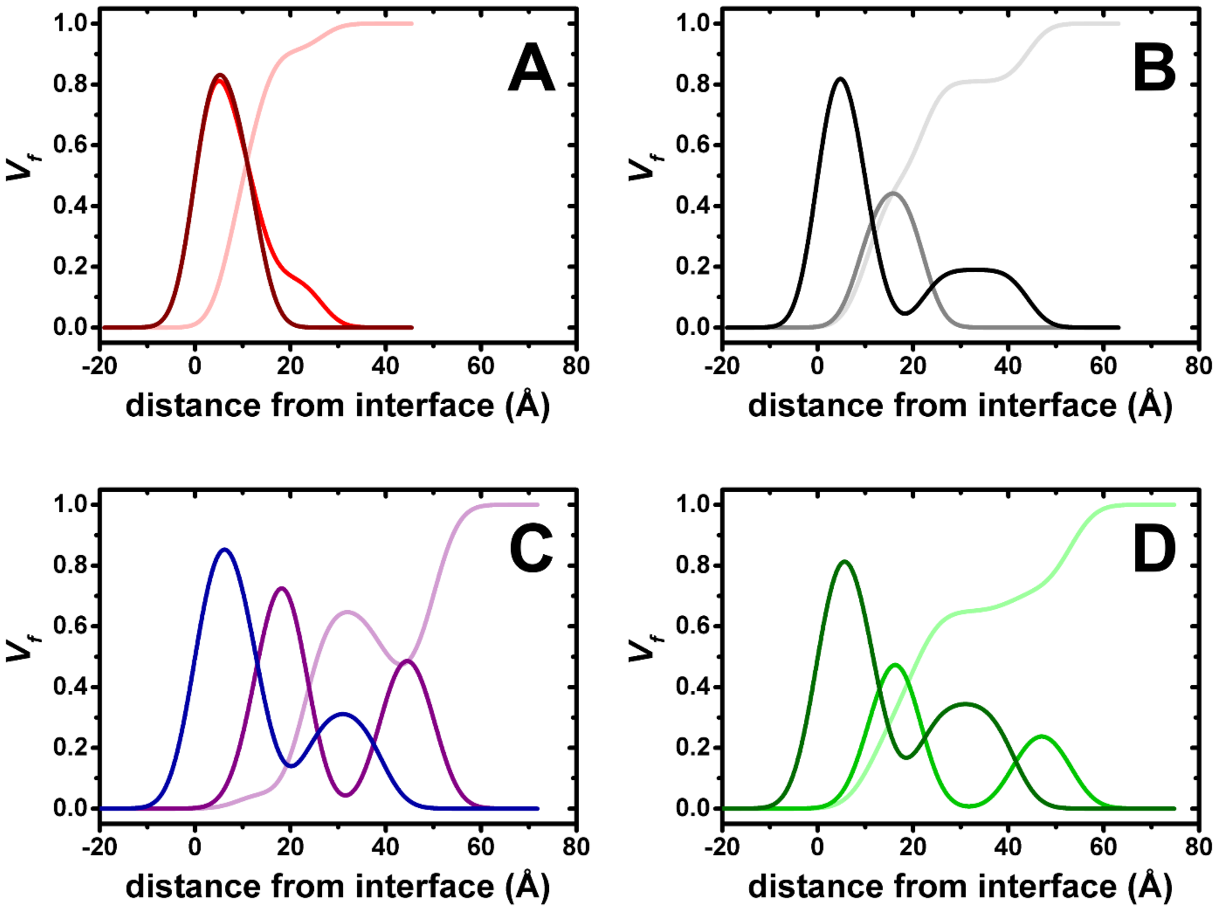

Figure 7.12. Volume fraction profiles resulting from the fits presented in Figure 7.11 where surfactant is maroon/black/blue/dark green, polyelectrolyte is red/grey/mauve/green and solvent is light red/light grey/pink/light green.

To conclude, the behaviour of the films spread from overcharged aggregates is summarised below, considering all the results obtained from the multi-technique approach applied.

NaPSS/DTAB: NaPSS/DTAB films spread from overcharged aggregates show a behaviour significantly different from the ones spread from undercharged aggregates. The first compression is characterised by a collapse in Π where the values of $d\Delta$ and Γ_{DTAB} continue to increase exceeding those related to full monolayer coverage, and BAM images show many white bands with increasing intensity with compression consistent with the formation of ESs. The kink in the data exhibited upon expansion, the retention of hysteresis over successive cycles and the Γ_{DTAB} values higher than the full monolayer coverage reached in each cycle show that the material is efficiently reincorporated upon expansion and there is repeated formation of ESs during successive cycles.

However, the $d\Delta$ values drop during time after stopping the barriers until they reach the values of a compact surface monolayer. Thus, instability of the ESs precludes resolution of the ESs using the NR full-Q_Z approach, and a typical profile of a P/S monolayer was observed.

PLL/SDS: The behaviour is very similar to that of films spread from undercharged aggregates. One of the significant differences is that while the films spread from undercharged aggregates show an excess of PLL in the minimum A/A_0, films spread from overcharged aggregates show a stoichiometry close to 1:1.

PEI/SDS pH 4: There is a continuous increase of $d\Delta$ and Γ_{SDS} during compression, the Γ_{SDS} values are higher than those corresponding to full monolayer coverage, there is appearance of bright patches and Kiessig fringes in the NR full-Q_Z data evidencing the formation of ESs. The kink in the data upon expansion and the reproducibility of the data during dynamic compression/expansion cycles show that these films are able to reincorporate efficiently the material ejected from the monolayer to the ESs upon compression. The small $d\Delta$ fluctuations observed during compression, consistent with the areas presenting bright patches observed in BAM images, can be explained as domains of ESs or embedded aggregates that pass through the area illuminated by the beam. The structural analysis of the NR full-Q_Z profiles shows that the films are composed of a PEI/SDS monolayer and SDS ESs wrapped by PEI.

PEI/SDS pH 10: Similarly to the films spread from undercharged aggregates, the ellipsometry data show large fluctuations of $d\Delta$ over time, consistent with the presence of regions of ESs or embedded aggregates and regions with $d\Delta$ values consistent with the presence of a P/S monolayer. BAM images show homogenous films, and the light intensity fluctuates throughout the experiments, indicating that the films are mobile. The values of Γ_{SDS} are higher than the full monolayer coverage and the full-Q_Z profile show Kiessig fringes, revealing the presence of ESs. The structural analysis of the NR full-Q_Z profiles shows that the films are composed of a PEI/SDS monolayer with bound ESs of SDS wrapped by PEI. However, while BAM images allude to the presence of ESs from the increasing brightness and heterogeneous character, they do not show discrete ESs. Thus, the results obtained agree with the presence of embedded aggregates as indicated by ellipsometry that are smaller than the resolution of BAM and too big to be resolved by NR.

7.3 Conclusions

The results of the four systems that are presented jointly in this chapter can be considered as the consolidation of work to understand the spreading methodology developed in 2016[5] as an efficient procedure to create P/S films at the air/water interface and precisely control their properties and structure. As demonstrated by the results presented, the use of polyelectrolytes with different architecture (linear vs hyperbranched), secondary structure (polypeptides) or persistence length (different systems), as well as P/S aggregates with different charge/structure, or a subphase with a different pH, there are many variables that allow precise control of the properties and structure of these films. In addition, we must add what is already known about the influence of the ionic strength, where its elevation reduces non-equilibrium effects and switches off ES-formation.[1]

PEI and PLL are used to form aggregates (and spread films) with SDS, and NaPSS with DTAB, where both surfactants have a dodecyl chain and one negative or positive charge in the headgroup. The differences between the results obtained on the spread films must be rationalised on differences between the polyelectrolytes used, the aggregates formed and the nature of the subphase. It is important to consider the different variables mentioned in the previous paragraph since, for example, it is known that the stiffness of the polyelectrolyte plays a very important role in stabilising the formation of ESs.[6] Previous work on the effect of aggregate charge on NaPSS/DTAB film properties demonstrated that only aggregates overcharged with an excess of surfactant in the corona activate the formation of ESs, whereas undercharged aggregates do not.[1] As the stoichiometry of the spread films, the inference was that some aggregates remain trapped in the formed films, which nucleate the formation of ESs upon successive spreading of material or compression of the surface area. But their presence was not resolved due to limitations in the various techniques applied. This physicochemical picture is similar to that of PEI/SDS at pH 4 but differs from the one of PEI/SDS at pH 10 and PLL/SDS, which show ESs formation regardless the charge of the aggregates used. In addition, it is shown that the stability of ESs varies from one system to another, which is important when evaluating possible transfer applications, which may be related to the stiffness of the polyelectrolyte and its ability to wrap the surfactant ESs.

It is important to highlight the need to use a multi-technique approach when interpreting the results obtained in the study of P/S films at the air/water interface. Without it, it would be particularly difficult to understand the behavior of the PEI/SDS system or the apparent discrepancy between the presence and absence of ESs observed when applying the low-Q_Z and full-Q_Z approaches of NR to NaPSS/DTAB films spread from overcharged aggregates.

7.4 References

(1) Tummino, A.; Toscano, J.; Sebastiani, F.; Noskov, B. A.; Varga, I.; Campbell, R. A. Effects of Aggregate Charge and Subphase Ionic Strength on the Properties of Spread Polyelectrolyte/Surfactant Films at the Air/Water Interface under Static and Dynamic Conditions. *Langmuir* **2018**, *34*, 2312–2323.

(2) Carrascosa-Tejedor, J.; Santamaria, A.; Tummino, A.; Varga, I.; Efstratiou, M.; Lawrence, M. J.; Maestro, A.; Campbell, R. A. Polyelectrolyte/Surfactant Films: From 2D to 3D Structural Control. *Chem. Commun.* **2022**, *58*, 10687–10690.

(3) Carrascosa-Tejedor, J.; Tummino, A.; Feher, B.; Kardos, A.; Efstratiou, M.; Skoda, M. W. A.; Gutfreund, P.; Maestro, A.; Lawrence, M. J.; Campbell, R. A.; Varga, I. Effects of Macromolecular Charge Density on the Properties of Spread Hyperbranched Polyelectrolyte/Surfactant Films at the Air/Water Interface. Manuscript in progress.

(4) Campbell, R. A.; Saaka, Y.; Shao, Y.; Gerelli, Y.; Cubitt, R.; Nazaruk, E.; Matyszewska, D.; Lawrence, M. J. Structure of Surfactant and Phospholipid Monolayers at the Air/Water Interface Modeled from Neutron Reflectivity Data. *J. Colloid Interface Sci.* **2018**, *531*, 98–108.

(5) Campbell, R. A.; Tummino, A.; Noskov, B. A.; Varga, I. Polyelectrolyte/Surfactant Films Spread from Neutral Aggregates. *Soft Matter* **2016**, *12*, 5304–5312.

(6) Braun, L.; Uhlig, M.; Löhmann, O.; Campbell, R. A.; Schneck, E.; von Klitzing, R. Insights into Extended Structures and Their Driving Force: Influence of Salt on Polyelectrolyte/Surfactant Mixtures at the Air/Water Interface. *ACS Appl. Mater. Interfaces* **2022**, *14*, 27347–27359.

8 Conclusions and perspectives

The aim of this PhD project has been to gain precise control of the structures self-assembled in spread polyelectrolyte/surfactant films at the air/water interface prepared from the dissociation of aggregates under static and dynamic conditions with the ambition of tuning the film properties in three dimensions and with a focus on biocompatible systems.

The specific objectives that have been addressed are:

(1) Stepping towards biocompatible systems with a view to potential applications.
(2) Gaining three-dimensional control over film structures.
(3) Tuning the film properties according to the system and various external variables.

Let us consider the advances made in aiming to meet these three objectives in turn.

8.1 Stepping towards biocompatible systems with a view to potential applications

The study of PLL/SDS and PLA/SDS systems represents an important step towards the use of the spreading methodology and the exploitation of the dynamic properties and structure of the resulting films in applications requiring biocompatibility. Ellipsometry measurements revealed that the PP/S films studied are stable for more than 1 h, making them robust and amenable for potential transfer applications. In the selection of polypeptides as a biocompatible system, it was hypothesized that the PP/S interactions in the bulk, which result in distinct secondary structures,[1–4] could be exploited in 3D structures in the films. Indeed, indications from the data suggest that this may be the case as it was the resulting stability of these films that allowed us to show using a novel implementation of NR that we could control the 3D structures of the films for the first time. The use of polypeptides combined with a fully aqueous spreading methodology, which has higher efficiency than bulk adsorption, has the potential to provide both economic and environmental advantages for potential applications as it requires less materials and generates less waste compared to other methods. Additionally, this study demonstrates that specific PP/S interactions can be exploited to fine-tune the characteristics of the films, including their morphology and mechanical behaviour, which will be discussed further below. These studies serve as a demonstration of the potential outcomes that can be attained using mixtures of two distinct polypeptides with the same surfactant, laying the foundation for developing a broad range of PP/S systems. In summary, the study of PLL/SDS and PLA/SDS films has shown not only that the spreading methodology can be extended to biocompatible systems, but also that the use of PP/S mixtures are highly suitable to control ES formation.

8.2 Gaining three-dimensional control over film structures

Inspired by the prior work of Tummino et al.,[5] this project resolved the dynamic properties, structure, and morphology of PLL/SDS, PLA/SDS, PEI/SDS films at pH 4 and pH 10 spread from aggregates overcharged with an excess of surfactant. The hypothesis was that P/S films capable of nucleating ESs formation would form and that the change in coverage of the ESs, tuned according to the maximum compression ratio reached using a Langmuir trough, may be able to tune other film properties such as their mechanics or dynamics.

All systems present qualitatively similar dynamic behavior, which is explained in the following. Marangoni spreading and dissociation of the aggregates results in the formation of the P/S surface monolayer. Compression of the surface monolayer leads to an increase in pressure due to increased molecular interactions at the interface and increased monolayer coverage. When the surface monolayer is complete, further compression causes its collapse and the excess of material is expelled from the interface in the form of ESs that remain bound to the surface monolayer. The expansion of the film is characterised by strong hysteresis and a pseudo-plateau in surface pressure during which excess material expelled during compression in the form of ESs is reincorporated at the interface. Ellipsometry, BAM and the NR low-Q_Z approach, have demonstrated that the ES coverage can be controlled by the compression ratio in all systems. The low-Q_Z approach was particularly useful in demonstrating that the excess surfactant is not expelled into the bulk but is retained by the film to form ESs. In addition, it was also shown that the amount of polyelectrolyte and surfactant at the beginning of each successive cycle is approximately the same which, together with the reproducibility of the Π–A isotherms, demonstrates the high capacity of these systems to regenerate the surface monolayer after having been subjected to significant deformations resulting even in changes of the structure's dimensionality.

Although formation of ESs in NaPSS/DTAB films was implied in previous work, the ESs were not resolved due to their transient nature.[5,6] In contrast, the structure of spread P/S films in the collapse region was resolved for the first time in this project applying the NR full-Q_Z approach to films in which ESs form that could be shown to be stable over the time required to perform structural measurements using NR, i.e. PLL/SDS and PEI/SDS films. Structural differences can be observed. For example, the thickness of the surfactant tails layer is 11 ± 1 Å for PEI/SDS films at pH 4, while it is 8.5 ± 0.2 Å for PLL/SDS films. Hence, the different nature of the systems gives rise to different interactions that have an impact on their dynamic behavior and structure, but we will return to this point later. Nevertheless, it can be concluded that the common structural model of spread P/S films in the collapse region consist of 5 layers: (1) surfactant tails, (2) surfactant headgroups with hydrated polyelectrolyte electrostatically bound, (3) polyelectrolyte, (4) surfactant ESs with a thickness corresponding to a bilayer, and (5) polyelectrolyte. The fifth layer was not resolved in some cases, e.g. for PLL/SDS films at a 2:1 compression ratio. However, its absence was attributed to the impossibility of resolving this layer when the ES coverage is low, since its presence was unequivocally confirmed when applying a 10:1 compression ratio to PLL/SDS films, and in the study of PEI/SDS films where a significantly higher ES coverage was resolved.

The application of the low-Q_Z and full-Q_Z approaches provided very detailed information on film composition during dynamic compression/expansion cycles and structure when the surface area was constant. Yet neither of these approaches had previously provided information about the structural changes taking place during film dynamics. For example, it had not been determined whether the increase in the amount of surfactant in the ESs is due to an increase in the coverage of this layer, or an increase in its thickness. In this project a new NR approach has been developed that gives access to this type of information. The mid-Q_Z methodology, so called because it uses a mid-Q_Z range where the Kiessig fringe that reveals the presence of ESs appears, was used to resolve changes in the ESs at a dynamic air/water interface for the first time. The use of this methodology demonstrated that compressing the PLL/SDS films in the collapse region enables precise control of the coverage of ESs while their thickness remains constant. Thus, the application of this methodology may help to understand the structural changes occurring during the collapse of many other types of films at the air/water interface, such as particle-laden interfaces[7] and lipid monolayers.[8]

8.3 Tuning the film properties according to the system and various external variables

During the course of this project, several variables were used to tune the interfacial properties, the dynamics, mechanical properties, morphologies and structures self-assembled in P/S films. Among these variables, three of them are directly related to the physicochemical properties of the systems, which depend on the P/S interactions: (i) PP/S interactions and maximum compression reached, (ii) charge density and architecture of the polyelectrolyte and, (iii) charge of the aggregates.

8.3.1 Polypeptide/surfactant interactions and maximum compression ratio

Previous studies showed that the interaction of PLL and PLA with SDS in bulk results in the formation of an α-helix and a β-sheet secondary structure, respectively.[1–4] Moreover, while the ammonium group of PLL exhibits only electrostatic interactions with the sulfate group, the guanidinium group of PLA exhibits additional interactions via hydrogen bonds.[9] In this project, it has been demonstrated that specific PP/S interactions can be used to tune the mechanical and structural properties as well as their resulting morphologies. BAM images showed the formation of discrete ESs in PLL/SDS films while additional macroscopic folding of the film was observed in PLA/SDS films. An approach to manipulate films through different maximum compression ratios was used to determine if higher coverage of ESs than previously observed can be obtained, and if their increased coverage affects the mechanical properties of the films.

The application of high compression ratios revealed important information. It was shown that using a 5:1 compression ratio resulted in the formation of solid and rigid films in both systems, presenting a reversible behaviour where the surface monolayer is recovered upon expansion. During the expansion it was observed that the solid PLL/SDS aggregates were more stable and gradually re-dispersed, while those of the PLA/SDS film abruptly disappeared from the area under study shortly after the beginning of the expansion. Finally, the application of a 10:1 compression ratio resulted in the irreversible collapse of the PLL/SDS films due to the fracture of the solid film into solid domains that remained trapped at the interface, while the PLA/SDS films exhibited a reversible collapse mechanism in which the film folds and respread the excess of material back to the surface monolayer upon expansion. These findings demonstrate that even subtle differences in the side group of a polypeptide can have a major influence on the film response, opening the possibility to design new biocompatible or biodegradable films with tailored properties for applications such as in tissue engineering, biosensors and antimicrobial coatings.

8.3.2 Charge density and architecture of the polyelectrolyte

The hyperbranched PEI/SDS system has been studied to evaluate the impact of polyelectrolyte architecture and subphase pH on the Marangoni spreading and aggregate dissociation as well as the structure and dynamic properties of the films spread from overcharged aggregates. The results of electrophoretic mobility, ellipsometry, BAM and NR confirm that there is a strong influence of the subphase pH on the dissociation of the aggregates and the resulting structure. Electrophoretic mobility measurements show that the amount of surfactant required to neutralize the aggregates at pH 4 (1.56 mM) is significantly higher than at pH 10 (0.57 mM). Furthermore, previous authors showed that the binding of SDS molecules to the PEI chains in the bulk aggregates is ~60% at pH 4.[10]

Results obtained from the low-Q_Z approach of NR on the spread films reveal that at pH 4 the amount of PEI is approximately equal to that of SDS, while at pH 10 the amount of PEI is approximately 3 times higher. This result supports the same physical picture with those obtained from the electrophoretic mobility measurements and the charge density of the polyelectrolyte. At pH 10, the low charge density of the polyelectrolyte and the low binding of SDS result in an excess of PEI needed to neutralize the charge on the films. In contrast, the high charge density of the polyelectrolyte at pH 4 does not seem to be sufficient to neutralize the charge of the aggregates in the bulk, where 60% SDS binding was revealed. Thus, the high impact of the pH of the subphase on the spreading is demonstrated.

Concerning the structure of the films, full-Q_Z measurements of NR revealed that the films are composed of the 5 layers mentioned above. At pH 4, the films are characterised by a thickness of 11 ± 1 Å, a compact layer of PEI with a very low volume fraction of solvent 1 ± 10%, and ESs with a thickness of 16 ± 1 Å. At pH 10, the structure is characterised by a tail thickness of 10 ± 1 Å, a PEI layer with a solvent volume fraction of 34 ± 17% and ESs with a thickness of 20 ± 1 Å. The ellipsometry shows stable $d\Delta$ values at pH 4 when the film is compressed at 40 mN/m, while large temporal fluctuations are observed at pH 10, revealing a high heterogeneity of the films. Finally, the BAM images show the formation of a homogeneous and rigid layer at pH 4, while temporal fluctuations are also detected at pH 10 but no micrometer-scale inhomogeneities are observed. Thus, it is concluded that the increase in PEI charge density when aggregates are spread on a water subphase at pH 4 results in the dissociation of most of the PEI/SDS aggregates and the formation of a homogenous compact film, while embedded aggregates remain intact and trapped at the interface resulting in a heterogenous mobile film at pH 10.

8.3.3 Charge of the polyelectrolyte/surfactant aggregates

In this project a comprehensive comparison of the film properties of the NaPSS/DTAB, PLL/SDS, PEI/SDS at pH 4 and PEI/SDS at pH 10 systems has been carried out with respect to the charge of the aggregates used in the spreading methodology.

Tummino et al. showed that only overcharged NaPSS/DTAB aggregates nucleate the formation of ESs in NaPSS/DTAB spread films. In this project, only the PEI/SDS system at pH 10 shows a similar behavior, while the PLL/SDS and PEI/SDS systems at pH 10 form ESs regardless of the charge of the aggregates. Therefore, it is shown that, although it is relevant in some systems, the charge of the aggregates is not a common parameter when it comes to nucleation of ESs. The spreading of overcharged P/S aggregates cannot be taken as a general rule to activate the formation of ESs, which is information that was not known prior to this project. Nevertheless, given that there are two steps in films formation (spreading and surface area compression), still more work is required to understand more about why undercharged aggregates can be used to generate ESs upon surface area in some systems but not others.

8.4 Perspectives

The complexity of these systems is evident from the studies conducted in this project. A change in one variable can have far-reaching effects, such as modifying the charge density and thus altering the properties of the polyelectrolyte, which in turn affects the bulk P/S binding, the dissociation of aggregates, and the structure and morphology of spread films. The use of polypeptides is a particularly complex example, as their specific interactions can change the secondary structure and make the polyelectrolyte more rigid, potentially stabilizing the ESs once formed. Although the project advances the understanding of the structural and dynamic behavior of spread films produced through the aggregate dissociation methodology, additional research is required on various systems in future work. To accomplish this goal, the spreading methodology and a multi-technique approach are crucial. The spreading methodology allows one to create P/S films rapidly and effectively through dissociation of aggregates at the interface. The use of multiple techniques has been demonstrated to be a very effective method for studying the dynamics, structure, and lateral organization of P/S spread films. The combination of different reflection techniques, which provide insights into the behavior of systems at different time and size scales, proved to be indispensable for understanding the behavior of PEI/SDS films. It is therefore essential to use the techniques presented in this project, as well as any others that yield valuable information.

The PP/S systems not only enable the control of film properties through various parameters, but they also offer additional benefits compared to traditional polyelectrolytes, such as the formation of secondary structures, which it is known to play a crucial role in determining the functionality of polypeptides.[11–13] Hence, PP/S systems offer great promise in terms of attaining even greater control over the structure, morphology, and properties of P/S films. To this end, techniques such as infrared reflection absorption spectroscopy[14] and circular dichroism[15] would play a crucial role in determining the secondary structure of polypeptides.

It has been highlighted that the deposition of P/S films holds potential for various applications. Hence, future work could focus on investigating the possibility to transfer P/S films from the air/water interface to solid substrates. Probably the best starting point would be PP/S films, which have been shown to be the most robust and reproducible, so even multiple consecutive depositions of the same layer could be explored. The Langmuir-Blodgett or Langmuir-Schaefer deposition methods,[16] well-established techniques for transferring Langmuir films from air/water interface to solids, should be employed. It would be crucial to establish the ideal deposition conditions such as the compression rate during deposition and the type of substrate functionalization. The use of atomic force microscopy could also prove beneficial to assess any structural and morphological changes that may occur during deposition. If the morphology is retained after the deposition, atomic force microscopy can provide valuable quantitative information about the in-plane organization of P/S films, such as height and size of the discrete ESs shown in PLL/SDS films.

Lastly, it has been discussed that loose analogy in the behaviour of these films can be made with lung surfactant dynamics.[17] The outstanding properties of lung surfactant films are attainable due to the formation of extended phospholipid reservoirs at the air/alveoli interface mediated by specific proteins. The design of synthetic systems capable of mimicking the properties of lung surfactant might be important in the development of new therapies for the treatment of the lack of an operative surfactant system, especially in neonates.[18,19] The use of PLL and SDS is an important step towards the use of these systems in biomedical applications. Although the maximum surface pressure reached with these systems is relatively low and no lipids have been used in this project, the multi-technique approach is a start. Further research on spread P/S films using surfactants that reach very low surface tensions or lipids, as well as a deeper understanding of the dynamics of these systems, may help researchers to develop new therapies and bridge the gap to the physicochemical processes occurring during nucleation of extended lipid reservoirs in the lung surfactant during respiration. This work has provided a source of inspiration for a project currently developed at the University of Manchester, where NR, particularly the mid-Q_z methodology pioneered in the present project, is currently being exploited to examine the structural transformations that occur during the dynamics of model lung surfactant systems.

8.5 References

(1) Buckingham, J. H.; Lucassen, J.; Hollway, F. Surface Properties of Mixed Solutions of Poly-L-Lysine and Sodium Dodecyl Sulfate. I. Equilibrium Surface Properties. *J. Colloid Interface Sci.* **1978**, *67*, 423–431.

(2) Ichimura, S.; Mita, K.; Zama, M. Conformation of Poly(L-Arginine). I. Effects of Anions. *Biopolymers* **1978**, *17*, 2769–2782.

(3) Novotná, P.; Urbanová, M. Vibrational Circular Dichroism Study of Polypeptide Model–Membrane Systems. *Anal. Biochem.* **2012**, *427*, 211–218.

(4) Novotná, P.; Urbanová, M. A Solid Phase Vibrational Circular Dichroism Study of Polypeptide-Surfactant Interaction. *Chirality* **2015**, *27*, 965–972.

(5) Tummino, A.; Toscano, J.; Sebastiani, F.; Noskov, B. A.; Varga, I.; Campbell, R. A. Effects of Aggregate Charge and Subphase Ionic Strength on the Properties of Spread Polyelectrolyte/Surfactant Films at the Air/ Water Interface under Static and Dynamic Conditions. *Langmuir* **2018**, *34* , 2312–2323.

(6) Carrascosa-Tejedor, J.; Santamaria, A.; Tummino, A.; Varga, I.; Efstratiou, M.; Lawrence, M. J.; Maestro, A.; Campbell, R. A. Polyelectrolyte/Surfactant Films: From 2D to 3D Structural Control. *Chem. Commun.* **2022**, *58*, 10687–10690.

(7) Garbin, V. Collapse Mechanisms and Extreme Deformation of Particle-Laden Interfaces. *Curr. Opin. Colloid Interface Sci.* **2019**, *39*, 202–211.

(8) Lee, K. Y. C. Collapse Mechanisms of Langmuir Monolayers. *Annu. Rev. Phys. Chem.* **2008**, *59*, 771–791.

(9) Wernersson, E.; Heyda, J.; Kubíčková, A.; Křížek, T.; Coufal, P.; Jungwirth, P. Effect of Association with Sulfate on the Electrophoretic Mobility of Polyarginine and Polylysine. *J. Phys. Chem. B* **2010**, *114*, 11934–11941.

(10) Mezei, A.; Mészáros, R. Novel Method for the Estimation of the Binding Isotherms of Ionic Surfactants on Oppositely Charged Polyelectrolytes. *Langmuir* **2006**, *22* , 7148–7151.

(11) Xiong, M.; Lee, M. W.; Mansbach, R. A.; Song, Z.; Bao, Y.; Peek, R. M.; Yao, C.; Chen, L. F.; Ferguson, A. L.; Wong, G. C. L.; Cheng, J. Helical Antimicrobial Polypeptides with Radial Amphiphilicity. *Proc. Natl. Acad. Sci. U. S. A.* **2015**, *112*, 13155–13160.

(12) Oelker, A. M.; Morey, S. M.; Griffith, L. G.; Hammond, P. T. Helix versus Coil Polypeptide Macromers: Gel Networks with Decoupled Stiffness and Permeability. *Soft Matter* **2012**, *8*, 10887–10895.

(13) Gebhardt, K. E.; Ahn, S.; Venkatachalam, G.; Savin, D. A. Role of Secondary Structure Changes on the Morphology of Polypeptide-Based Block Copolymer Vesicles. *J. Colloid Interface Sci.* **2008**, *317*, 70–76.

(14) Mendelsohn, R.; Brauner, J. W.; Gericke, A. External Infrared Reflection Absorption Spectrometry of Monolayer Films at the Air-Water Interface. **2003**, *46*, 305–334.

(15) Petralli-Mallow, T.; Wong, T. M.; Byers, J. D.; Yee, H. I.; Hicks, J. M. Circular Dichroism Spectroscopy at Interfaces: A Surface Second Harmonic Generation Study. *J. Phys. Chem.* **1993**, *97*, 1383–1388.

(16) Clifton, L. A.; Campbell, R. A.; Sebastiani, F.; Campos-Terán, J.; Gonzalez-Martinez, J. F.; Björklund, S.; Sotres, J.; Cárdenas, M. Design and Use of Model Membranes to Study Biomolecular Interactions Using Complementary Surface-Sensitive Techniques. *Adv. Colloid Interface Sci.* **2020**, *277*, 102118.

(17) Pérez-Gil, J. Structure of Pulmonary Surfactant Membranes and Films: The Role of Proteins and Lipid-Protein Interactions. *Biochimica et Biophysica Acta - Biomembranes*. July 2008, pp 1676–1695.

(18) Hudson, L. D.; Steinberg, K. P. Epidemiology of Acute Lung Injury and ARDS. *Chest* **1999**, *116*, 74S-82S.

(19) Pandit, P. B.; Dunn, M. S.; Colucci, E. A. Surfactant Therapy In Neonates With Respiratory Deterioration Due to Pulmonary Hemorrhage. *Pediatrics* **1995**, *95*, 32–36.

9 List of publications

9.1 Publications of this project

- Carrascosa-Tejedor, J.; Santamaria, A.; Tummino, A.; Varga, I.; Efstratiou, M.; Lawrence, M. J.; Maestro, A.; Campbell, R. A. Polyelectrolyte/Surfactant Films: From 2D to 3D Structural Control. *Chem. Commun.* **2022**, *58*, 10687–10690.
- Carrascosa-Tejedor, J.; Miñarro, L. M.; Efstratiou, M.; Varga, I.; Skoda, M. W. A.; Gutfreund, P.; Maestro, A.; Lawrence, M. J.; Campbell, R. A. Design of Biocompatible Films with Controllable Properties and Morphology through Specific Polypeptide/Surfactant Interactions. *Nanoscale,* in peer review.
- Carrascosa-Tejedor, J.; Tummino, A.; Feher, B.; Kardos, A.; Efstratiou, M.; Skoda, M. W. A.; Gutfreund, P.; Maestro, A.; Lawrence, M. J.; Campbell, R. A.; Varga, I. Effects of Macromolecular Charge Density on the Properties of Spread Hyperbranched Polyelectrolyte/Surfactant Films at the Air/Water Interface. Manuscript in progress.
- Carrascosa-Tejedor, J.; Tummino, A.; Efstratiou, M.; Skoda, M. W. A.; Gutfreund, P.; Maestro, A.; Lawrence, M. J.; Varga, I.; Campbell, R. A. General Physical Description of the Behaviour of Spread Oppositely Charged Polyelectrolyte/Surfactant Films at the Air/Water Interface. Manuscript in progress.

9.2 Publications resulting from collaborations

The following publications have arisen from collaboration with other research groups during the course of this project:

- Carrascosa-Tejedor, J.; Santamaria, A.; Pereira, D.; Maestro, A. Structure of DPPC Monolayers at the Air/Buffer Interface: A Neutron Reflectometry and Ellipsometry Study. *Coatings* **2020**, *10*, 507.
- Schnurbus, M.; Hardt, M.; Steinforth, P.; Carrascosa-Tejedor, J.; Winnall, S.; Gutfreund, P.; Schönhoff, M.; Campbell, R. A.; Braunschweig, B. Responsive Material and Interfacial

Properties through Remote Control of Polyelectrolyte–Surfactant Mixtures. *ACS Appl. Mater. Interfaces* **2022**, *14*, 4656–4667.

- Santamaria, A.; Carrascosa-Tejedor, J.; Guzmán, E.; Zaccai, N. R.; Maestro, A. Unravelling the Orientation of the Inositol-Biphosphate Ring and its Dependence on Phosphatidylinositol 4,5-Bisphosphate Cluster Formation in Model Membranes. *J. Colloid Interface Sci.* **2023**, *629*, 785–795.

Additionally, there are several manuscripts that are currently in progress. These manuscripts are listed below with an indication of their status at the time of the thesis submission:

- Hardt, M.; Busse, F.; Raschke, S.; Honnigfort, C.; Carrascosa-Tejedor, J.; Wenk, P.; Gutfreund, P.; Campbell, R. A.; Heuer, A.; Braunschweig, B. Photo-Responsive Control of Adsorption and Structure Formation at the Air-Water Interface with Arylazopyrazoles. *Langmuir*, submitted in January 2023. Manuscript in progress.
- Pereira, D.; Santamaria, A.; Carrascosa-Tejedor, J.; Sardo, M.; Mafra, L.; Guzmán, E.; Owen, D.; Zaccai, N. R.; Maestro, A.; Marín-Montesinos, I. Engineering Phosphatidylinositol-4,5-bisphosphate Model Membranes Enriched in Endocytic Cargo: a Neutron Reflectometry and QCM-D Structural Study. Manuscript in progress.
- Santamaria, A.; Carrascosa-Tejedor, J.; Pereira, D.; Marín-Montesinos, I.; Matsarskaiaa, O.; Prévost, S. F.; Fragneto, G.; Owen, D.; Haertlein, M.; Moulin, M., Guzmán, E.; Zaccai, N. R.; Maestro, A. Untangling Structural Molecular Details of the Endocytic Adaptor Protein Clathrin Assembly Lymphoid Myeloid Leukemia Protein (CALM) upon Binding with Phosphatidylinositol 4,5-Bisphosphate-Containing Model Membranes. Manuscript in progress.